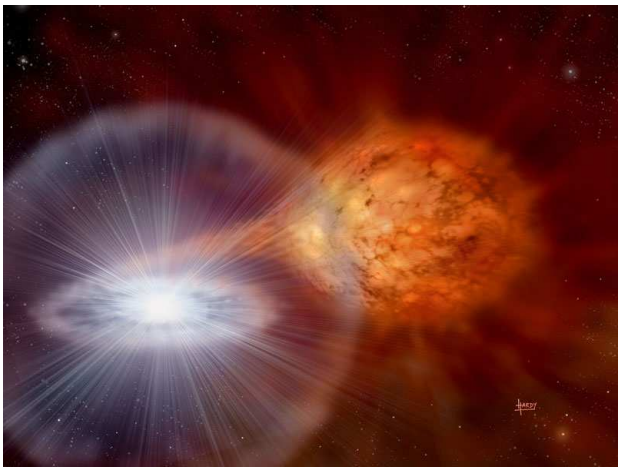

Gas and Dust Spectral Analysis of Galactic and Extragalactic Symbiotic Stars

PhD student: Rodolfo Angeloni

Supervisors
Prof. Piero Rafanelli - University of Padova
Dr. Marcella Contini - Tel Aviv University

February 2009

Dipartimento di Astronomia
Università degli Studi di Padova

Contents

Prefazione (Italian abstract)

Le stelle simbiotiche sono riconosciute come unici laboratori per lo studio di una serie di importanti problemi astro-fisici. In questa tesi di dottorato si presenta un'analisi spettrale di un campione di stelle simbiotiche galattiche ed extragalattiche. Nel primo caso, si tratta principalmente di simbiotiche di tipo D per le quali é stato effettuato uno studio comparativo con dati osservativi dal radio ai raggi X. Nel caso delle simbiotiche extragalattiche, ci si riferisce invece esclusivamente alle simbiotiche nelle Nubi di Magellano, per cui si stanno raccogliendo dati da satellite nel dominio InfraRosso.

Il quadro teorico alla base di questo studio e da cui prende le mosse l'analisi spettrale, é il *colliding-wind model*, sviluppato giá nel corso degli anni '80, sostenuto da prime evidenze osservative all'inizio degli anni '90 (soprattutto grazie a Nussbaumer e collaboratori) e, infine, ulteriormente raffinato da vari autori per mezzo di nuove simulazioni idrodinamiche, in questi ultimi anni.
Alla luce di questo scenario, si é quindi tentata un'analisi degli spettri simbiotici che fosse coerente all'interno di un unico e consistente quadro interpretativo. L'analisi spettrale é stata effettuata mediante il codice numerico SUMA, sviluppato presso l'Instituto Astronômico e Geofísico della Universitàt di São Paulo da Sueli M. Viegas (Aldrovandi) e Marcella Contini della School of Physics and Astronomy della Tel-Aviv University.
L'analisi prende solitamente avvio con un primo modelling dei rapporti di righe di emissione, che danno informazioni uniche sulle condizioni fisiche all'interno delle nebulae simbiotuche, dove agiscono sia processi di foto-ionizzazione che ionizzazione collisionale. Poi, la ricostruzione della distribuzione spettrale di energia (SED) nel continuo permette di vincolare ulteriormente i parametri caratterizzanti i modelli, e di dare un primo sguardo al sistema nel suo insieme, considerando coerentemente le sue proprietá emissive lungo tutto lo spettro elettromagnetico. Questo approccio ha anche portato a qualche previsione circa le proprietá emissive di oggetti in regioni spettrali dove dati osservativi non sono ancora disponibili.
Nella maggior parte dei casi, dopo aver verificato la bontá del modello per le nebulae da un continuo confronto tra SED e righe di emissione, si é passati poi a considerare qualsiasi tipo di informazione disponibile da letteratura sugli spettri infrarossi, al fine di caratterizzare se anche la distribuzione in shells della polvere e le proprietá chimico-fisiche dei grani fossero compatibili con le condizioni fisiche derivate nelle nebulae. Ció ha consentito di ottenere alcuni risultati del tutto sorprendenti, i quali hanno permesso di indirizzare la ricerca verso le proprietá infrarosse delle stelle simbiotiche nelle nubi di Magellano, o di pianficare proposals osservativi per esplorare le stelle simbiotiche in finestre spettrali finora poco o nulla note, come quella millimetrica.

In particolare, il capitolo 1 é concepito come un'introduzione generale al fenomeno simbiotico, secondo una prospettiva storica che muove dalle prime interpretazioni degli anni '30 fino alla moderna visione delle stelle simbiotiche come sistemi binari interagenti.

Il Capitolo 2 é una breve rassegna di alcune proprietá osservative dei venti stellari, ingrediente strutturale di ogni modello *colliding-wind*.

Nel capitolo 3, si presenta una dettagliata analisi di una serie di spettri ISO da noi pubblicati per la prma volta. La caratterizzazione delle condizioni fisiche delle polveri e del gas nelle nebulae simbiotiche ha portato ad interessanti considerazioni che fanno di questi sistemi promettenti targets per la nuova generazione di telescopi sub-mm e mm.

Il capitolo 4 é dedicato ad una analisi puntuale di H1-36. Una review dei dati di letteratura disponibli dal radio all'UV ha consentito di ipotizzare la probabile presenza in H1-36 di un jet visibile nei raggi X, che speriamo possa essere presto confermata da una nuova serie di osservazioni dedicate.

L'enigmatica CH Cyg é l'argomento dei successivi due capitoli. Nel capitolo 5 viene presentato un primo tentativo di interpretazione unitaria e coerente modellando righe di emissione e dati del continuo attraverso le diverse epoche, dall'outburst del 1978 fino allo stato quiescente che sembra caratterizzare questi ultimi anni.

Nel capitolo 6, si tenta una nuova analisi della riga Lyα emersa alla fine della fase attiva 1978-1987. Si suggerisce in particolare una nuova interpretazione dell'origine della Lyα basata sulla teoria del *charge transfer reactions*.

Il Capitolo 7 illustra alcuni recenti risultati ottenuti per BI Cru, un noto sistema con una magnifica nebulosa risolta sia in radio che in ottico, la cui struttura é una delle piú convincenti prove circa l'importanza degli shock nel modelling delle stelle simbiotiche. Durante lo studio, abbiamo voluto indagarne le condizioni fisiche analizzando tutta una serie di dati sia fotometrici e spettroscopici, dal radio ai raggi UV.

I Capitoli 8 & 9 illustrano i risultati ottenuti studiando gli spettri nel Medio-IR (ISO e VLTI/MIDI, rispettivamente) della sorprendente simbiotica di tipo D', HD330036. La presenza di silicati cristallini (che sono trovati per la prima volta in una stella simbiotica), insieme con le tracce di un chimica ricca in carbonio, ha portato allo sviluppo di un nuovo modello interpretativo in grado di spiegare la presenza di grani di polvere complessi in un ambiente cosí potenzialmente ostile.

I Capitoli 10, 11 & 12 sono invece dedicati alle stelle simbiotiche extragalattiche. Dopo una breve introduzione sulle stelle simbiotiche nelle Nubi di Magellano, si presenta il proposal osservativo AKARI *MASYS*, approvato recentemente e le cui osservazioni dovrebbero concludersi entro il mese di Luglio 2009.

La tesi si conclude con una appendice, in cui viene presentato in maniera dettagliata il codice SUMA, ampiamente utilizzato per l'analisi degli spettri discussi in questo lavoro.

Abstract

Symbiotic stars are recognized as unique laboratories for studying a large variety of phenomena that are relevant to a number of important astro-physical problems. This PhD thesis deals with a spectral analysis of galactic and extragalactic symbiotic stars. The former are mainly D-type symbiotic stars for which a comprehensive study, from radio to X-ray spectral region, has been performed. With the latter, we refer to symbiotic stars in the Magellanic Clouds, to be analyzed mainly in the IR range.

The common theoretical scenario that lies in the background of this work is the colliding-wind model, developed already during the 80's, supported by first observational evidence at the beginning of 90's (mainly thanks to Nussbaumer and collaborators), and finally completed with detailed and powerful hydrodynamical simulations by various authors in these recent years.
In the light of this scenario, we have tried to interpret gas and dust spectra of our targets in a unique and self-consistent way. The spectral analysis has been performed by means of the numerical code SUMA, developed at the Instituto Astronômico e Geofísico of the University of São Paulo by Sueli M. Viegas (Aldrovandi) and Marcella Contini from the School of Physics and Astronomy of the Tel-Aviv University.
The analysis starts usually by modelling the emission line ratios, that give unique information about the physical conditions within the symbiotic nebulae, where both photo- and collisional-ionization processes are at work. Then, the reconstruction of the continuum Spectral Energy Distribution (SED) allows to further constrain the model parameters, and to give a first, comprehensive glance at the system as a whole. This also leads to some tentative predictions about the emitting properties of objects in spectral regions where observational data are not available, yet.
In most cases, the final step consists of taking into account any kind of information on dusty infrared spectra, in order to characterize whether the dust shell spatial distribution and the dust grain properties are compatible with the physical conditions as derived from the gas nebulae. This allowed to point out some quite surprising results, which has driven the research towards, e.g., the investigation of dust in Magellanic symbiotic stars, or the exploration of symbiotic stars in the poorly-known millimeter window.

In detail, Chapter 1 is conceived as a general introduction to symbiotic phenomenon, with a historical perspective that moves from the very first interpretation, up to the modern view of symbiotics as binary interacting stars.

Chapter 2 deals with a brief review of some observational properties of stellar winds, necessary ingredient for any colliding-wind models.

In Chapter 3, a first analysis of previously unpublished ISO spectra is presented. The characterization of symbiotic gas and dust nebulae brought to interesting considerations making symbiotic stars promising targets for the new generation of sub-mm and mm observatories.

Chapter 4 is devoted to a detailed analysis of the intriguing symbiotic H1-36. A comprehensive analysis of literature data from radio to UV allowed to predict the likely presence in H1-36 of a X-ray jet, to be confirmed by a new set of observations.

The enigmatic symbiotic star CH Cyg is the topic of the next two chapters. In Chapter 5, for the first time, a comprehensive and self-consistent analysis of the system is attempted by modelling the line and continuum spectra through the different epochs, from the impressive outburst of 1978 up to the present quiescent state.
In Chapter 6, a specific analysis of the Lyα line which characterized the 1978-1987 active phase is presented. There, we suggest a new interpretation of the Lyα origin based on the theory of charge transfer reactions between ambient hydrogen atoms and post-shock protons at a strong shock front. In this context, the broad Lyα line originated from the blast wave created by the outburst, while the contemporary optical and UV lines arose from the nebula downstream of the expanding shock in the colliding wind scenario depicted in the previous chapter.

Chapter 7 presents some recent results obtained on BI Cru, a well-known system with a beautiful, resolved nebula whose structure is one of the most convincing evidence of the importance of shocks in symbiotic star modelling. Throughout the study, we wanted to find out the physical conditions in the shocked nebulae and in the dust shells, as well as their location within the symbiotic system by analyzing both photometric and spectroscopic data, from radio to UV.
An interesting result is that the spectra observed throughout the years show strong marks of the different processes at work within BI Cru, probably signatures of a evolution that followed a strong, unrecorded outburst-phase.

Chapters 8 & 9 tell us the results obtained studying the Mid-IR spectra (ISO and VLTI/MIDI, respectively) of the surprising D' type symbiotic star HD330036. The presence of crystalline silicate (found for the first time in a symbiotic system), along with signatures of a C-rich chemistry, has called for a new interpretative model that must explain the presence of complex dust grains in such a potentially hostile environment.

Chapters 10,11 & 12 deal with extragalactic symbiotic stars. After a short introduction of symbiotic stars in the Magellanic Clouds, the approved AKARI Near-IR observational proposal *MASYS* is extensively discussed, while waiting for the delivery of these promising spectra by the end of July 2009.

The thesis ends with an appendix, where detailed information about the SUMA code used in the analysis, is presented.

Part I

Symbiotic Stars in the astrophysical context

The remarkable intensity of lines requiring high excitations constitutes the chief problem of these aberrant spectra.

Paul W. Merrill (1944)

1

Introducing Symbiotic Stars

1.1 An historic perspective

During the compilation of HD catalog, several stars were found to display very strong, high ionization emission lines (e.g. HeII λ4686) superimposed on a red giant absorption spectrum (Fleming 1912). A few years later, P.W. Merrill and collaborators started focusing on such intriguing objects reporting on *the anomalous combination in a single spectrum of features that ordinarily occur near opposite ends of the sequence of stellar temperatures*, observed with the 100-inch reflector at the Mount Wilson Observatory (Merrill & Humason 1932). At that time, it was extremely difficult *to understand why a high-excitation line of ionized helium should appear along with the spectrum of a molecule* [TiO] *that is dissociated at a relatively low temperature* (Merrill & Humason 1932).
In other words, the first interpretations had to allow for the puzzling evidence of bright emission lines *requiring an excitation far above that which a low-temperature photosphere appears able to supply* (Merrill 1944).
Already during the first 30's, L. Berman envisaged a possible "deus ex machina" responsible for the production of such high excitation lines in the *close association with a faint extremely hot star*. In a prophetic report appeared in the PASP, he then suggested a qualitative binary model where the orbital *motion and the proximity of a nebular shell may account for the irregular light variations commonly observed, as well as for the complex changes in the bright line spectrum* (Berman 1932). A parallel working hypothesis was that of *pulsations in an extensive, tenuous atmosphere in which the spectroscopic effects are stratified, the nebular lines being produced in the outer one* (Merrill 1944). Nonetheless, it was fairly recognized how the observational data were so meager as to make *inadvisable to accept any hypothesis without reserve* (Merrill 1944).

Whatever the interpretation, by placing some of these peculiar objects in the Group III (*stars with combination spectra*) of his stellar classification scheme, Merrill officially opened in 1944 the attention toward the symbiotic phenomenon.

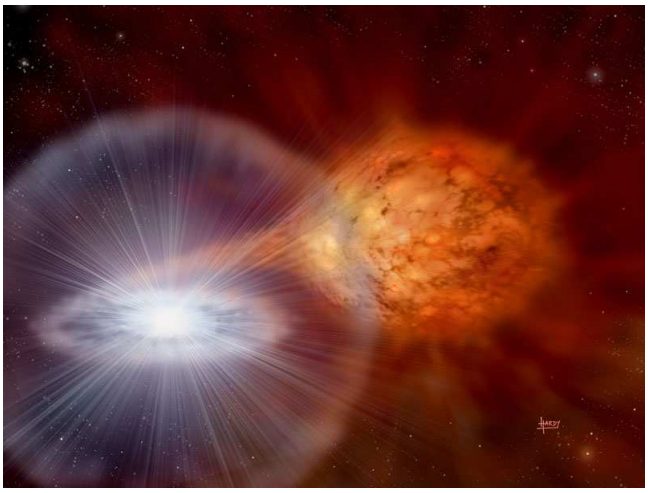

Figure 1.1: An artistic impression of a symbiotic nova system.

1.2 The symbiotic phenomenon

Symbiotic stars display a large variety of phenomenology that is hard to include in a coherent scheme, to a point that it is still debated whether they really represent a homogeneous group of objects. All kinds of ideas had been voiced about them; in a way that the class has been in the past a sort of dustbin of badly understood stellar objects.

What it is generally defined as *the symbiotic phenomenon* consists, as we have disclosed in §1.1, of 1) a composite stellar spectrum with apparently conflicting features (Fig. 1.3), and 2) large variability. As a matter of fact, the very irregular *photometric* and *spectroscopic variability* is the other major feature of the symbiotic stars, which also distinguishes them from both normal cool stars and gaseous nebulae (cfr. e.g. Friedjung & Viotti 1982, p.227).
The above mentioned variety of phenomenology, that space-based observations proofed to be present in virtually all spectral windows - from radio to hard X-ray - clearly demands a multi-wavelength approach: nowadays, any model aiming to provide a self-consistent theoretical framework can not leave aside what is told in the adjacent spectral ranges, which might provide unique information able to constrain the absolute energetic of the system: for instance, it is not conceivable anymore to deal with the dust emission properties as revealed in the infrared without taking into account the velocity and the radiation field in the shocked photoionized nebulae, as derived by the X-ray and UV emission line profiles.

Nowadays, 173 galactic symbiotic stars are known, plus 26 suspected ones (Belczynski et al. 2000). Unfortunately, this value is in striking contrast with the predicted total number of SSs in the Galaxy that, according to different

estimates, oscillates between 3 $\times$ 10^3 (Allen 1984) and 4$\times 10^5$ (Magrini et al. 2003). The actual consistency of symbiotic population is becoming a key-point to be investigated and has recently triggered specific observational campaign (e.g. Corradi et al. 2008).

1.3 Classification criteria

Sometimes it is not immediate to decide whether a peculiar stellar objects belongs to the symbiotic class or not. Nevertheless, there are some inescapable conditions that must be met to be in presence of a symbiotic star.

The optical spectra of symbiotic stars are characterized by the presence of absorption features and continuum, as appropriate for a late-type M giant (often a Mira or semi regular variable), and strong nebular emission lines of Balmer HI, HeII and forbidden lines of [OIII], [NeIII], [NeV] and [FeVII] (Fig. 1.3). Some symbiotics - the yellow symbiotic stars - contain K (or even G) giants or bright giants. The spectra of many symbiotic systems also show two broad emission features at λ 6825 Å and λ 7082 Å. These features have never been observed in any other astrophysical objects - only symbiotic stars with high-

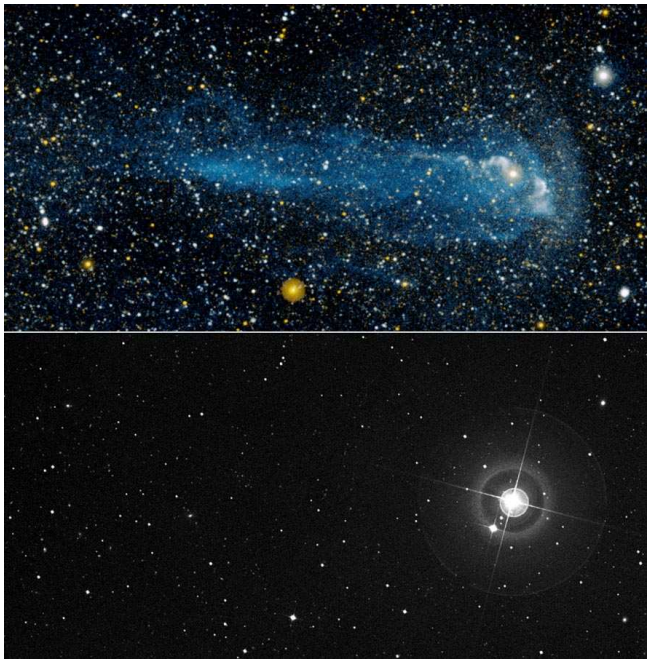

Figure 1.2: An UV Galex image (top) of Mira (o Ceti), compared with an optical one (bottom). In the UV, it becomes evident the 'cometary' tail result of the interaction between the stellar mass-loss and the interstellar medium.

excitation nebulae. For many years there was no plausible identification for these lines, but Schmid (1989) pointed out that the $\lambda\lambda$ 6825, 7082 lines are due to Raman scattering of the OVI $\lambda\lambda$ 1032, 1038 resonance lines by neutral hydrogen.
Following Belczyński et al. (2000), a symbiotic star must satisfy these criteria:

- The presence of the absorption features of a late-type giant; in practice, these include (amongst others) TiO, H_2O, CO, CN and VO bands, as well as CaI, CaII, FeI and NaI absorption lines;
- The presence of strong emission lines of HI and HeI and either emission lines of ions with an ionization potential of at least 35 eV (e.g. [OIII]), or an A- or F-type continuum with additional shell absorption lines from HI, HeI, and singly-ionized metals.
  The latter corresponds to the appearance of a symbiotic star in outburst;
- The presence of the λ 6825 emission feature, even if no features of the cool star (e.g. TiO bands) are found.

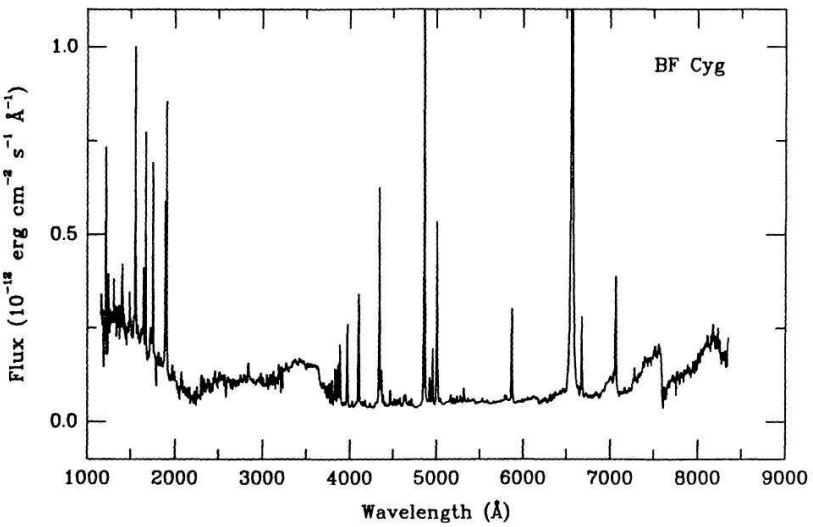

Figure 1.3: A classic symbiotic spectrum. The combined optical/ultraviolet spectrum of BF Cyg (from Kenyon 1990).

1.4 S- and D-type symbiotic stars

Once a general identification criterion has been given, the next logical step in a coherent classification scheme is to look for some internal similarities in the variety of observed phenomenology. Amongst the several grouping suggested for symbiotic stars, the most widely used is still the one proposed in the 70's by Webster & Allen (1975). On the basis of infrared spectra covering the range 1.2-3.5 μm, they split the known symbiotic population into two classes, according to whether the cool star (S-type) or dust (D-type) emission dominated the continuum spectral energy distribution (SED). A few years later, Allen (1982) introduced a third class - designated as D' type - characterized by very red colors in the far-infrared (FIR) and by a cool star of spectral type F or G, in contrast to normal symbiotics where the cool giant is a M-type star (S type) or a Mira variable (D type).

1.5 Decomposing a symbiotic star

Nowadays, a typical symbiotic star can be thought as made up of three main emitting components: a cool giant star, which is at the origin of dust formation and ejection episodes; a compact star, generally but not necessarily a white dwarf (WD), source of the ionizing radiation; and a network of gas and dust nebulae.
As we will see throughout the present work, these three components dominate the energy distribution at specific wavelength. With the S. Kenyon's words, this fact *is both a blessing and a curse: a well-defined observational program may probe a particular component of a symbiotic system, but knowledge of the complete SED is required to make progress on understanding the system as a whole* (Kenyon 1986).

1.5.1 The cool star

As we have seen, at least in our Galaxy, D-type symbiotic stars contain a Mira variables, while S-types have more normal giant branch or asymptotic giant branch (AGB) companions.
Several studies from the late 70's have tried to compare isolated and symbiotic cool giants in order to point out any difference in the physical parameters which describes these stars (mass-loss rates, pulsations, dust chemistry, etc).
The results are very interesting, even though it is not completely clear if they really highlight some intrinsic differences or just mirror biased selection effects. For example, it seems that symbiotic Miras show higher mass-loss rate than isolated one: this evidence probably does not reflect any intrinsic difference in the stellar structure, but might be easier related to the fact that for the presence of a symbiotic system, Mira mass-loss rates must be reasonably high; under a certain level, the density structure of the cool wind can not be sufficient to sustain the symbiotic phenomenon even under the action of a rush hot radiation

field.
The main difference amongst symbiotic Miras and their normal counterparts is that, in the former, there is a tight association with extended nebulae; maser emission seems rarer; whereas obscuration events are more frequent. Quite surprisingly, as we will directly show in Chapter 3, no obvious gross differences in the properties of dust around these two Mira species have been revealed.
From the theoretical point of view, it is worth mentioning a work by Soker (2002), in which it is argued how cool giant components in most symbiotic stars might possess magnetic activity on a much higher level than isolated cool giants or those in wide binary systems. This would increase the giant rotational velocity, then affecting the spatial distribution and the temporal variation of mass-loss episodes, as well as resulting in a relatively strong X-ray emission and altering the properties of jets blown by the hot compact companion. Despite it is now evident that symbiotic stars are important X-ray emitters, such hypothesis have not been convincingly demonstrated, yet.

1.5.2 The hot star

The real nature of the hot star in a symbiotic system, and its important role as engine for the symbiotic phenomenon, was fully established when IUE opened the 1200-3200 Å spectral range. In fact, most of the radiation emitted by the hot component was invisible to earth-bound observers, who could deduce its presence only on the basis of the weak, blue continuum which begins to dominate the SED at $\lambda \leq$ 4500-5000 Å. The IUE observations were thus also the definitive proof that symbiotic stars are intrinsically binary systems.

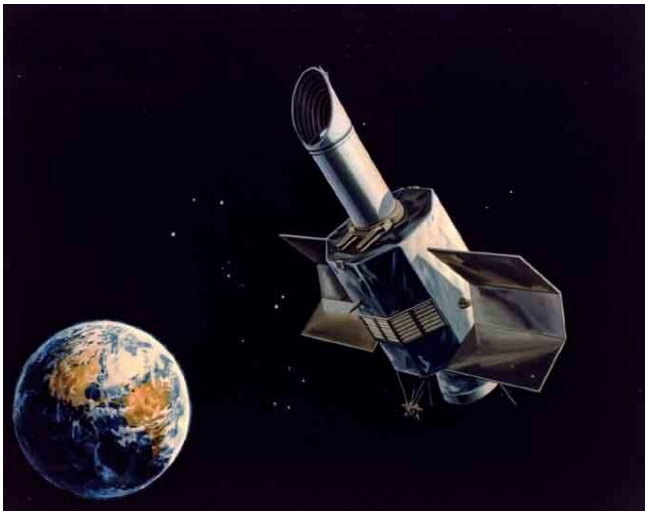

Figure 1.4: An artistic impression of the International Ultraviolet Explorer IUE.

To determine the specific physical nature of the hot star is however not trivial, since in the UV at least two radiation sources still coexist - the hot star itself and the surrounding nebula - and the interstellar extinction can be as significant as unknown.
As first pointed out by Kenyon & Webbink (1984), the UV SED of many symbiotics were consistent with a hot, compact stellar source with an effective temperature of ≈ 30.000 K to ≈ 200.000 K, and a luminosity, $L_h \sim$ 100-1000 $L_\odot$.

Some discrepancies between observed and model flux ratios in the NIII, NIV, NV emission lines brought Nussbaumer and collaborators to conclude that also the hot star possesses its own wind, whose presence could be recognized on the actual profiles of forbidden emission lines (Nussbaumer & Vogel 1989). A robust hint came from IUE spectra of AG Peg, from which Nussbaumer & Vogel (1994) derived a wind with a terminal velocity of $\sim 1000\ km\,s^{-1}$and a mass loss rate of the order of $3 \times 10^{-7}\ \dot{M}$/y. However, the first real proof of a hot star wind came from HST observations (Nussbaumer, Schmutz & Vogel 1995). The strong resonance lines from medium ionized ions showed three components: a wide foot with a P Cygni absorption, from the wind of the hot star with a speed of $\sim 1000\ km\,s^{-1}$; an additional absorption at $\sim$ -200 $km\,s^{-1}$along with a socket of comparable width, interpreted as coming from the wind collision zone; eventually, a strong narrow nebular emission with a width of $\sim 20\ km\,s^{-1}$.
Since then, any model aiming to interpret a symbiotic spectra must include a colliding wind scenario (with all the hydrodynamic implications) for being sufficiently reliable.

1.5.3 The nebula

As we have seen previously, a binary system is the most obvious explanation for the spectroscopic peculiarities of symbiotic stars, because the two observed temperature extremes can be associated with separate stellar objects.

Binarity raised the question of the origin of the nebula: in particular whether it is originated from the mass loss of the cool giant, or it is somehow related to the hot star.

Exploiting once again nebular emission lines, Schmid & Nussbaumer (1993) derived C/N and O/N abundance ratios, and compared them with those of red giants and supergiants, carbon stars, planetary nebulae, and novae. The results strongly indicated that symbiotic nebulae are mainly composed of the mass lost by the red giant. This evidence opened new ways of investigating red giants by making use of the illumination and ionization effect by the hot radiation source.

The strongest evidence of the presence of a nebula made of the wind from the red giant ionized by the hot star came from 1) line profile and radial velocity measurements of some well-studied objects (e.g. V1016 Cyg and HM Sge - Willson et al.(1984); and 2) radio surveys of a considerable number of symbiotic systems (Taylor & Seaquist 1984).
In particular, the ionization models suggested in order to reproduce the steep radio spectral index (α - $S \sim \nu^{\alpha}$) observed, assumed a spherically symmetrical

wind from the red giant, consisting of H only, calculating the Stroemgren-radius due to a blackbody radiation field from the white dwarf.
Later investigations by Ivison et al.(1991) and Ivison, Hughes, & Bode (1992) on the turnover frequency, ν_t, from optically thick to thin radio emission which contains information on the binary separation, and on the absolute values of the optically thin radio fluxes, helped to establish that the ionized emission region of D-types are far more extensive and have lower electron densities than those of S-type symbiotics.

With the advent of observations in other wavelength regions (e.g. X-rays), it was evident that models which successfully reproduced the radio continuum SED were not able to account for the new data, and that the idea of a cool stellar wind purely ionized by the hot star was fairly simplistic.
As we will briefly discuss in the last section of the next chapter, only postulating an interaction regions between two winds would allow to explain the most energetic phenomena naturally invoked from far UV and X-ray observations.

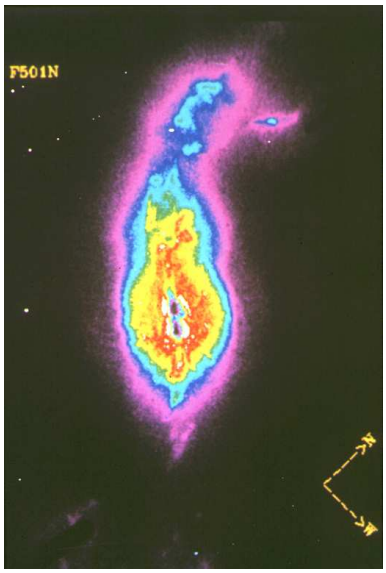

Figure 1.5: The nebula and the jet around the symbiotic D-type star R Aqr.

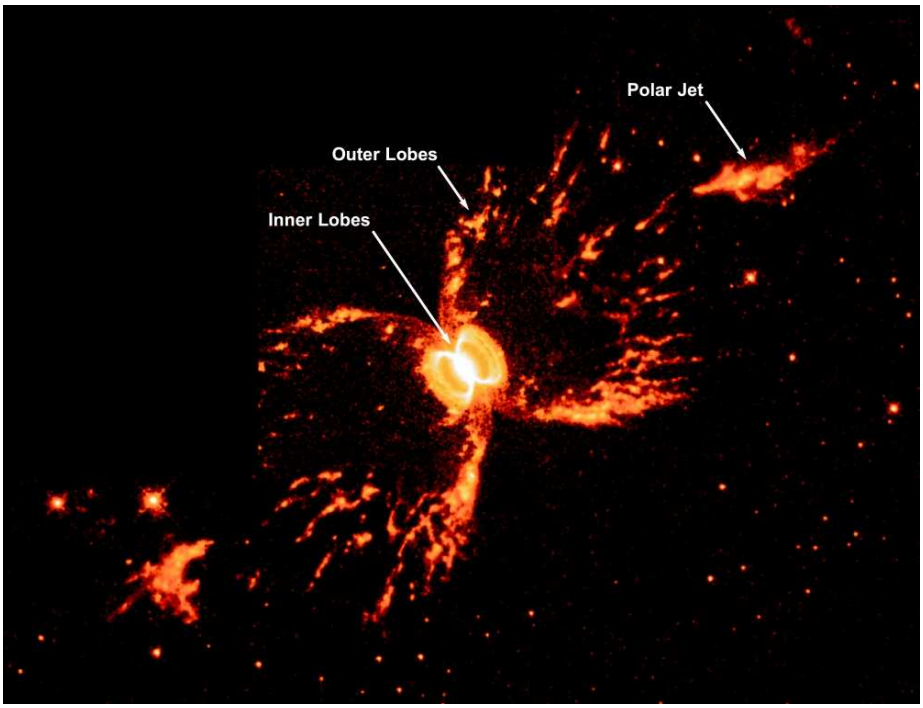

Figure 1.6: Hen2-104, the Southern Crab.

2

Notes on stellar winds, colliding-wind models, and jets

Section 2.1 is based upon, and adapted from,
Introduction to stellar winds
textbook by Lamers & Cassinelli (1999).

2.1 Observations of Stellar Winds

The two most important parameters regarding a stellar wind that can be derived from the observations are

- the *mass loss rate* $\dot{M}$ - the amount of mass lost by the star per unit time;
- the *terminal velocity* v_∞ - the velocity of the stellar wind at a large distance from the star.

For a star with a stationary spherically-symmetric wind, the mass loss rate is related to the density and the velocity at any point in the wind via the *equation of mass continuity*

$$\dot{M} = 4\pi r^2 \rho(r) v(r) \tag{2.1}$$

The distribution of the velocity of the wind with radial distance from the star is called the *velocity law* $v(r)$. Often, a very good approximation is given by a $\beta - law$, which varies as

$$v(r) \cong v_0 + (v_\infty - v_0)\left(1 - \frac{R_*}{r}\right)^\beta \tag{2.2}$$

For instance, hot stars have winds with a velocity law of $\beta \approx 0.8$. These winds experience a fast acceleration and reach 80% of their terminal velocity already at $r = 4.1R_*$.
Winds of cool stars accelerate more slowly, corresponding to larger β.

The velocity law can also be approximated by an alternative form of the $\beta - law$:

$$v(r) \cong v_\infty \left(1 - \frac{r_0}{r}\right)^\beta \tag{2.3}$$

with

$$r_0 = R_* \left(1 - \left(\frac{v_0}{v_\infty}\right)^{1/\beta}\right) \tag{2.4}$$

This form of the $\beta - law$ has the advantage that it is easier to handle when it appears in integral equations, e.g. in the expression for the column density or the emission measure.

2.1.1 The formation of spectral lines in stellar winds

Stellar wind lines can be easily distinguished from the photospheric lines because of their large width or wavelength shift due to the outflowing motion of the gas in the wind. Wind lines can appear in absorption, in emission or as a combination of the two: a *P Cygni profile*.

One can distinguish several processes for line formation in stellar winds.

Line scattering

After a photo-excitation of an atomic electron due to the absorption of a photospheric photon, the atomic electron itself de-excites to the original level emitting a photon with almost the same frequency of the absorbed one, the only difference relying in the Doppler shift due to the thermal motions of the atom. This process is called *line-scattering*, and it is important for line transitions of low atomic levels (for which the life-time for spontaneous de-excitation is small, i.e. 10^{-10} to 10^{-9} sec).
If the line transition is from the ground state of the atom, the line is called a *resonance line* and the scattering is called a *resonance scattering*.
Most of the observed P Cygni profiles are formed by resonance scattering.

Line emission by recombination

If an ion in a stellar wind collides with a free electron it can recombine.
The most likely recombination is directly to the ground state of the ion, even though the ion can also recombine to an excited state. In the latter case, the excited ion can cascade downwards in the energy level diagram by photo-deexcitation. Therefore, each de-excitation results in the emission of a line photon.

Lines from specific transitions having a high probability of being fed by recombination with subsequent photo-deexcitation may thus appear in emission. This process is responsible for the Hα emission and the infrared emission lines in the winds of hot stars.

Line emission from collisional- or photo-excitation

Excitation of an atom by collisions from the ground state to an excited state can result in subsequent photo-deexcitation to a lower level.
This process creates line-photons by converting kinetic energy into photon energy: it is most efficient in hot plasmas where collisions are frequent and energetic. It is responsible for the formation of emission lines from hot chromospheres and coronae.

Photo-excitation from the ground state it is usually not important for line formation, since it results mainly in resonance scattering.

Pure absorption

Photo-excitation of an excited atom into a higher excited state, followed by spontaneous de-excitation to another lower lever results in the destruction of the photons of the first transitions and the creation of photons of the second transitions. Nonetheless, this mechanism is not important for stellar winds because the vast majority of atoms in a stellar wind are in their ground state.

Masering by stimulated emission

If a photon travelling through a stellar wind hits an excited atom or molecule that can emit exactly the same photon by photo-deexcitation, then the process of stimulated emission becomes important. After the de-excitation, there will be two atoms with exactly the same frequency and travelling in the same direction. This is called *masering*.
This process is responsible for the very strong and usually very narrow maser emission lines of abundant molecules in the winds of cool stars.

2.1.2 P Cygni profiles

The most sensitive indicators of mass loss from hot stars are the spectral lines due to atomic transitions from the ground states, i.e. the *resonance lines*, of abundant ions.
Well-known examples are the resonance lines of C IV, N V, Si IV on the ultraviolet (UV) spectra of O to early-B type stars, the resonance lines of C II in the UV spectra of late-B to A type stars, and the resonance lines of Mg II in the UV spectra of types late-B to M (Table 2.1).

If the column density of the absorbing ions in the wind between the observer and the stellar photosphere is small (i.e. $10^{13} - 10^{14}$ ions cm^{-2}), the resonance

lines will produce a weak but observable *absorption component*, Doppler-shifted to a shorter wavelength because it is formed in a region that is moving outward from the star and toward the observer.
If the column density of the absorbing ions is high (let's say $\geq 10^{15}$ ions cm^{-2}), the lines will have a so-called *P Cygni profiles* consisting of a violet-shifted absorption component and a red-shifted emission component.

Most of the observed P Cygni profiles of the UV resonance lines in the spectra of hot supergiants are due to scattering of photons rather than to absorption.

Table 2.1: Some important UV lines that shows the effect of mass loss

Ion	Abundance (to H by number)	Ion.pot [eV]	λ [Å]	Exc.pot [eV]
C II	3.7×10^{-4}	11.26	1334.532	0.00
			1335.708	0.01
C III	3.7×10^{-4}	24.38	1175.67	6.50
C IV	3.7×10^{-4}	47.89	1548.195	0.00
			1550.770	0.00
N IV	1.1×10^{-4}	47.45	1718.551	16.20
N V	1.1×10^{-4}	77.74	1238.821	0.00
			1242.804	0.00
O VI	6.8×10^{-4}	113.90	1031.928	0.00
			1037.619	0.00
Mg II	3.5×10^{-5}	7.65	2795.528	0.00
			2802.705	0.00
Si II	3.5×10^{-5}	8.15	1526.707	0.00
			1533.431	0.00
Si III	3.5×10^{-5}	16.35	1206.500	0.00
Si IV	3.5×10^{-5}	33.49	1393.755	0.00
			1402.770	0.00
Fe II	2.5×10^{-5}	7.87	2585.876	0.00
			2598.370	0.05
			2599.396	0.00

A qualitative explanation of P Cygni profiles

The formation of a P Cygni profile can be qualitatively understood by a simple model of a spherically-symmetric outflowing wind in which the velocity increases outward (Fig. 2.1).
An outsider observer can recognize four regions which contribute to the formation of a spectral line:

- the star S which emits a continuum, possibly with a photospheric absorp-

tion component at the rest wavelength λ_0 of the line;

- the tube F in front of the stellar disk. The gas in F is moving to the observer with velocities between and $v \sim 0$ and v_∞;
- the tube O that is occulted by the star. The gas in O is moving away from the observer, but the radiation from this region does not reach him;
- the region to the sides of the star that would be observed as a halo H around the star if the wind could be spatially-resolved by the observer. The gas in H has both positive and negative velocity components along the observer's line of the sight.

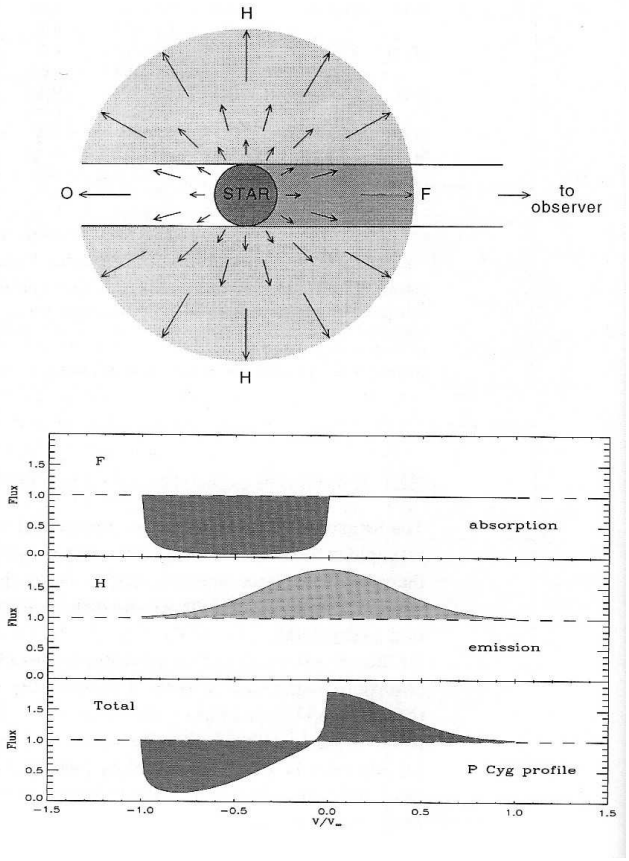

Figure 2.1: Top: the geometry of a stellar wind. Bottom: the different contribution from the system to the line profile

A quantitative explanation of P Cygni profiles

Let's consider an isotropic scattering of stellar photon in a geometrically and optically thin shell around the star at distance between r and $r + \Delta r$ with expansion velocity between v and $v + \Delta v$ (Fig. 2.2).

The absorption component extends from Doppler velocity $-v$ to $-v(1-\cos\vartheta)$ (if the intrinsic broadening by thermal motions is neglected). The emission component extends from $-v(1 - \cos\vartheta)$ to $+v(1 - \cos\vartheta)$.
The strength of the absorption depends on the column density of the number of absorbing ions in the shell; the amount of emission is equal to the amount of absorption minus the emission between Doppler velocities $+v$ and $+v(1-\cos\vartheta)$ that is occulted by the star.

A P Cygni profile formed by scattering in a wind with increasing velocity can be regarded as the sum of the contributions of many shells of different velocities. In the light of such interpretation, one can deduce that:

- the presence of a shell with an extra high density in the wind at velocity v_S will give rise to an extra absorption dip at Doppler velocity $-v_S$ and a smeared out emission component between about $-v_S$ and $+v_S$;
- if the ion that produces the line does not occur within the inner part of the wind where $v(r) < v_{in}$, the shells with a low velocity will not contribute. This gives a profile with a violet shifted absorption between $v_\infty$and $-v_{in}$, and an emission between $-v_{in}$ and $+v_\infty$, that is flat between $-v_{in}$ and $+v_{in}$;
- if the ion that produces the line does not occur at large distance in the wind where $v(r) > v_{out}$, the shells with higher velocity will not contribute. This gives a narrow P Cygni profile that does not extend to the terminal velocity;
- if the observed ion occurs only in the wind close to the star, the emission will be considerably smaller than the absorption because the occultation is significant.

The ratio between the strength of the emission and absorption component depends on the size of the wind region where the scattering occurs relative to the size of the star.
If the star emits a continuum without an absorption component, the difference between the strength of the emission and absorption component is only due to the photons that are lost by back-scattering into the star. Consequently, if the star is small compared to the scattering region, little radiation is "lost" and the emission will be about equal to the absorption. On the other hand, if the star is large compared to the size of the region in the wind where line scattering occurs, a considerable fraction of the photons are lost by back-scattering into the star: in that case the emission will be smaller than the absorption.
The presence of a photospheric absorption component complicates this relation and increases the strength of the absorption compared to that of the emission.

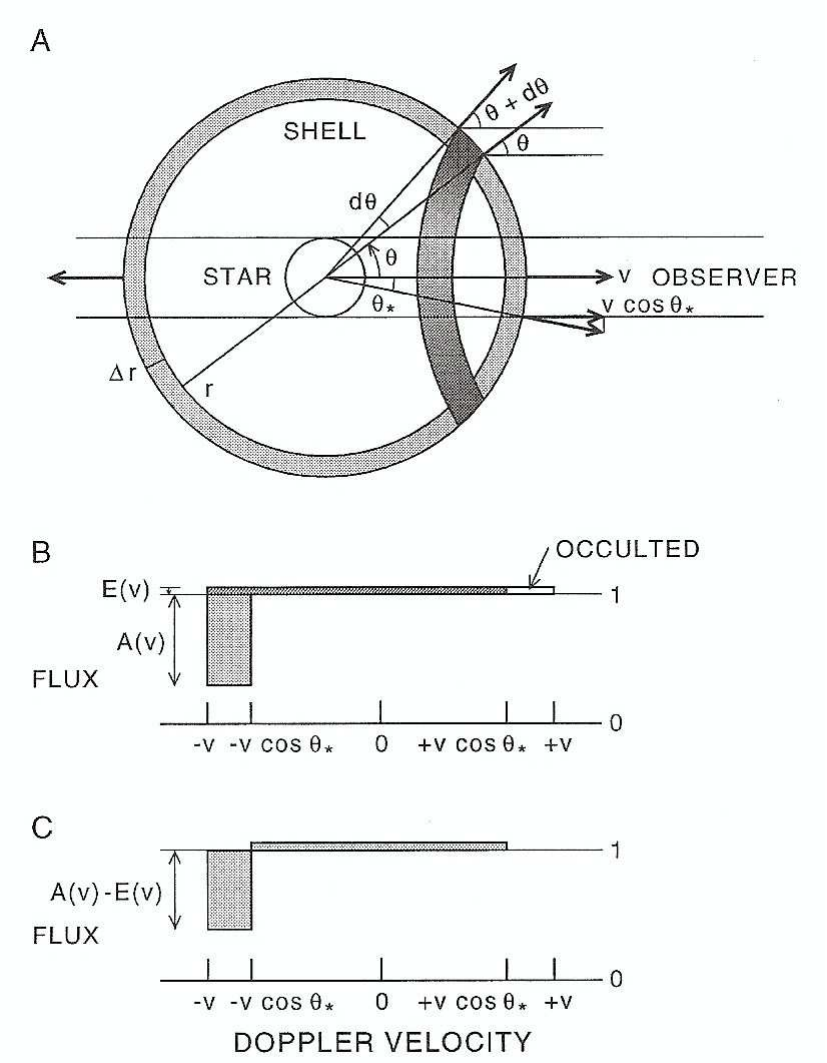

Figure 2.2: The profile of a thin scattering shell. A: the geometry of the shell. B: the resulting absorption, $A(v)$, and the flat emission, $E(v)$.

Mass loss studies of P Cygni profiles

For *strongly saturated* lines, the P Cygni profiles are mostly sensitive to the velocity law. This means that the velocity law and v_∞can be derived most accurately from the profiles of saturated lines which have a steep violet absorption edge. This violet absorption edge reaches the continuum at a Doppler velocity of $v_{edge} \sim -(v_\infty + 2v_{turb})$, where v_{turb} is the turbulent velocity in the stellar wind at a distance of $r \geq 10R_*$, where $v_\infty$is reached.

The mass loss rate can be derived from *unsaturated* P Cygni profiles on the basis of the derived radial distributions $n_i(r)$ of the observed ions in the wind. In fact, the ion density $n_i(r)$ can be converted into a density distribution $\rho(r)$ if the abundance and the ionization fraction of the observed ion is known in the wind,

$$n_i(r) = \frac{n_i(r)}{n_E(r)} \cdot \frac{n_E(r)}{n_H(r)} \cdot \frac{n_H(r)}{\rho(r)} \cdot \rho(r) = q_i(r) A_E \frac{n_H}{\rho} \frac{\dot{M}}{4\pi r^2 v(r)} \qquad (2.5)$$

where $A_E = n_E/n_H$ is the abundance of the element with respect to H and $q_i = n_i/n_E$ is the fraction of the ions in the right stage of ionization and excitation to produce the line. The ratio n_H/ρ depends on the composition of the wind (e.g. $(1.36m_H)^{-1}$ for solar composition).
By using the mass continuity equation (2.1), and known $v(r)$ and $\rho(r)$, the mass loss rate can be derived.

Summarizing, from the P Cygni profiles both the mass loss rates and terminal velocities of stellar winds can be derived. But while the terminal velocities and the velocity law can very well be determined, the determinations of mass loss rates is much more complicated because it depends crucially on the adopted ionization fractions.

2.1.3 Emission lines from winds

The strength and the profiles of emission lines provide information about the mass loss rate and the velocity law of stellar winds.
Most of the observed atomic emission lines are formed by recombination and thus have an emissivity proportional to ρ^2. This implies that the emission originates mainly from regions of high density, i.e. the lower layers of the wind close to the star, where most of the wind acceleration occurs.

The determination of mass loss rates from optically thin emission lines

The large velocity gradients in stellar winds make it easy for line photons to escape.
As soon as a line photon, created by recombination, has traveled a distance

$$l > 2v_{th}/(dv/dl)$$

with v_{th} the thermal velocity and dv/dl the velocity gradient of the wind along the path of the photon, it is Doppler shifted with respect to the surrounding gas by more than $2v_{th}$ and cannot be absorbed anymore in the same line transition. Therefore, winds with $v_\infty >> v_{th}$ are *optically thin* for line radiation. This greatly simplifies the theory and the calculations of emission line profiles.
The optically thin assumption is approximately valid for the Hα line and for the IR recombination lines from the winds of early type stars.

If the wind is completely optically thin for a line transition, the mass loss rate can be derived directly from the luminosity L_l of the line, which in turn is derivable from the spectrum if the distance to the star is known.

Let $j_l(r)$ be the *line emissivity* of the wind, namely the amount of energy generated by the emission of line photons (in $erg\ cm^{-3}s^{-1}$) at a distance r from the star. The total line luminosity is then nothing but the volume integral over the wind of emissivity, apart from a correction for the fraction of the emitted photons intercepted by the star:

$$L_l = \int_{r_{min}}^{\infty} 4\pi r^2 j_l(r)(1 - W(r))dr \qquad (2.6)$$

The integration starts at r_{min}, which is the distance where the optical depth of the wind τ_w reaches a value of about 1 for continuum radiation at the wavelength of the line. This is because line photons cannot escape if they are emitted in layers that are optically thick for the continuum radiation at their wavelength.

The factors $W(r)$ describes the probability that a photon, emitted at r in a random direction, is intercepted by the star; in another way, it is the fraction of the solid angle covered by the star. It is called *geometrical dilution factor*

$$W(r) = \frac{1}{2}\Big(1 - \sqrt{1 - (r_{min}/r)^2}\Big). \qquad (2.7)$$

The emissivity of recombination lines is proportional to the density squared, involving collisions between ions and electrons, and it is a function $f_{rec}(T)$ of temperature

$$j_l(r) = \rho^2 f_{rec}(T). \qquad (2.8)$$

By exploiting the mass continuity equation (2.1), introducing the dimensionless distance parameter $x \equiv r/R_*$ and velocity $w \equiv v/v_\infty$ and finally substituting Eqs. (2.7) and (2.8) into Eq. (2.6), one obtains

$$L_l = \frac{1}{8\pi R_*}\Big(\frac{\dot{M}}{v_\infty}\Big)^2 \int_{x_{min}}^{\infty} \frac{f_{rec}(T)}{wx^2}\Big(1 - \sqrt{1 - (x_{min}/x)^2}\Big)\, dx \qquad (2.9)$$

Eq. (2.9) shows that the line luminosity of optically thin lines is proportional to $(\dot{M}/v_\infty)^2$, or $\dot{M} \sim v_\infty\sqrt{L_l}$. This dependence makes the line luminosity an accurate indicator of the mass loss rate, once the terminal velocity from the UV P Cygni profiles is known.

2.2 Colliding winds in symbiotic stars

In the last years, colliding wind models were extensively applied to symbiotic stars in order to interpret emission line and continuum spectra as consistently as possible, along with the evidence of jets, accretion disks and other energetic phenomena that simply do not fit into a scenario of pure photo-ionization. As a matter of fact, the early 'single-wind' models suffered from a deficiency in reproducing the higher ionization against the medium or low ionization ions. Such deficiency had been at the root of the models with two mass-losing stars, briefly mentioned in Chapter 1. However, imaging is revealing that reality is much more complicated. The winds should be treated as three-dimensional colliding hydrodynamic flows, possibly influenced by magnetic fields. Furthermore, the sources of the winds move in binary orbits, which ruins any analytically comfortable density distribution.

2.2.1 A brief review

In this section we are briefly going to summarize the observational-based evidence of introducing a colliding-wind interaction region, giving the proper references to the most recent and complete colliding-wind models, that today include also a detailed treatment of non-linear hydrodynamic effects.

A first *head-on* colliding wind model was firstly suggested by Willson et al. (1984): a collision front appears at the location where the moments of the two winds are equal. Girard & Willson (1987) then presented a colliding wind model which is at the basis of further developments: namely, the winds from a late giant and from a hot WD collide between the stars and material is accumulated along the boundary, forming an initially spherical shell that is deformed by the wind of the primary (giant star): eventually, the shell reaches a steady state configuration. A large amount of turbulence perpendicular to the mean flow is expected. Both in the steady state formulation and in the dynamic shell model the shell is sufficiently thin to be considered having zero thickness.
The actual location of the collision front was later confirmed by proper hydrodynamic calculations of Stevens, Blondin, & Pollock (1992). This collision front was supposed to be at the origin of the X-ray emission which had been detected by the Einstein X-ray observatory in some symbiotic stars. On the basis of momentum conservation of the two colliding winds, they tried to calculate the geometry, mass and velocity distribution of the nebula.
Nussbaumer & Walder (1993) were the first to study wind-wind collisions for symbiotics with a hydrodynamic code: despite the assumptions being rather artificial, the calculations showed how a nebula, produced by the wind from the cool star, could evolve after the onset of a wind from the hot star, and how line profiles would react to the combined effects of winds and ionization. Much more complicated structures appear in 3D calculations, when binary motion is also included: this is the core of some simulations by Walder & Folini (2000), who pointed out that the wind-wind interaction zone is inherently unstable forming

voids high-density knots, and filaments.

The colliding wind model of Kenny & Taylor (2005, 2007) differs from previous ones because it assumes mixing of shocked material from both incoming streams instead of postulating a self-sustaining contact discontinuity. The model extends the CW model by the derivation of an adiabatic temperature, the consideration of radiative cooling, the inclusion of thermal pressures in the incoming winds, and the treatment of interaction shells of finite thickness and density. They succeed in reproducing radio images and continuum spectra (Figs. 2.3 and 2.4).

Collision of the winds and the derived shock network have thus been invoked to resolve specific discrepancies between observations and theory during the active phases of a symbiotic phenomenon. Nevertheless, in order to simultaneously reproduce the UV, optical, and IR line spectra as well as the absolute fluxes of the continuum SED from radio to X-ray (Contini 1997, Contini & Formiggini 2003, Angeloni et al. 2007a,b), the role of shocks cannot be neglected even during the quiescent phases.

2.2.2 A schematic model adapted to the calculation of the spectra

Recent works on a significant sample of dusty symbiotic stars have revealed a common trend in the IR spectrum properties, such as similar, recurrent shell temperatures and unexpected grain chemistry (Angeloni et al 2007b, 2009 in preparation).

In order to take into account the importance of dust in symbiotic stars, our model adds to the colliding wind binary system the dust shells emitted by pulsation of the cool star. The dynamical effects of instabilities, such as fragmentation, are also taken into account, as well as evaporation and sputtering of dust grains in the shells.

The shocks associated with the colliding winds are strongest along the line connecting the two stars. The interface between the two winds contains two shocks: one facing the fast wind, with $V_s \sim$ 1000 $km\,s^{-1}$but low mass flux, and one facing the slow wind, with $V_s \sim$ 30 $km\,s^{-1}$and considerably higher flux corresponding to mass loss rates of $\sim 10^{-6}$ - 10^{-5} $M_{\odot}$year^{-1}. To a first approximation, and for the purpose of the present work, they can be considered standing shocks. We will refer to the strong shock facing the WD. In the expanding region around the hot star away from the direction towards the cool star, we will refer to the expanding shock outward the system.

Throughout the present work, we will be interested in the calculations of the line and continuum spectra, so we refer to schematic nebulae: downstream of the strong standing shock between the star, downstream of the expanding shock, and downstream of the dust shell edges. The radiation emitted from the different nebulae and dust shells are summed up with different weights which depend on the orbital phase, the pulsation period of the red giant, and on activity of the WD.

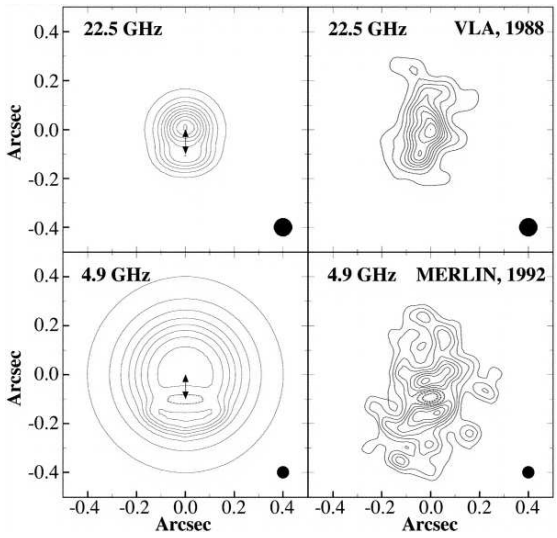

Figure 2.3: Model images of HM Sge (from Kenny et al. 1997). Model beams and contour levels are consistent with those of the observed images. The observed images are from Eyres et al. (1995). The double-headed arrows in the model images are used to locate the hot (south) and cool (north) components with respect to the model nebular structure (from Kenny & Taylor 2005).

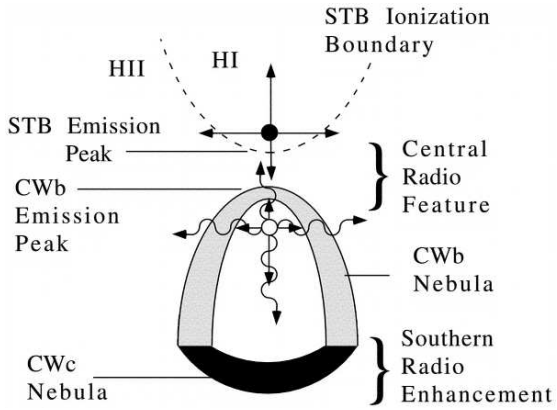

Figure 2.4: Nebular model of HM Sge. The hot and cool components are represented by the open circle and filled circle, respectively. High-energy photons from the hot component (wavy arrows) ionize the envelope of the cool component out to the dashed line. The shaded regions represent the wind interaction zones (from Kenny & Taylor 2005).

The nebulae downstream of the shock fronts are compressed by the shock and heated by both the shock and the photoionizing flux from the WD. Downstream of the reverse shock, the radiation flux from the WD reaches the shock front edge of the nebula, characterized by very high densities and by a high ionization parameter, being the shock front close to the WD. The nebula downstream of the shock expanding outwards the system is characterized by lower densities. In this configuration, the photoionizing flux from the WD, with an ionization parameter diluted by distance, reaches the edge of the nebula opposite to the shock front. Furthermore, the photoionizing flux may be obstructed by some intervening matter before it reaches the outer nebula, hence leading to shock-dominated spectra, i.e. showing only the characteristics of the shocks.

2.3 Jets in symbiotic stars

In the early 1980's bipolar mass outflow was discovered in early- and late-type stars, and jets became popular in symbiotics. As an example, Michalitsianos & Kafatos (1988), measuring the extent of the spatially-resolved jet in R Aquari and speculating that its ejection took place between 1970 and 1977, found ejection velocities between 760 and 1800 $km\,s^{-1}$; in CH Cyg, from a detailed analysis of line profiles, Solf (1987) could directly read the velocities of the jets, finding out highly collimated bipolar outflows with velocities of $\approx 800\ km\,s^{-1}$.

An important point raised since then has been to understand how much of the content and shape of symbiotic nebulae is due to jets. The last years have greatly enriched the observational information, especially on the high-energy side of the electromagnetic spectrum where even spatially-resolved images started to come. This has allowed to trace the jets back to their accelerating source, and thus to shine a light on the acceleration mechanism.
The spectra collected by Schmid et al. (2001) on the symbiotic star MWC 560 jet, give a direct proof that the initial acceleration is mainly perpendicular to the collimated jet-direction.
It is worth mentioning that jets have often been associated with colliding winds, even if the actual link is far from being fully understood. In fact, when binary motion is excluded, hydrodynamic models produce a fast mass outflow along the contact zone between the two winds; however, the binary movements mixes that outflow into a spiraling pattern within the wind of the red giant: this is unlikely to lead to prominent jets, making colliding winds unlikely jet progenitors.
Spectroscopy suggests that jets probably have their origin in a magnetically guided outflow from the close neighborhood of the spinning white dwarf, or alternatively in a strongly magnetized accretion disk. Whatever the case, it is clear that this is still an open question.

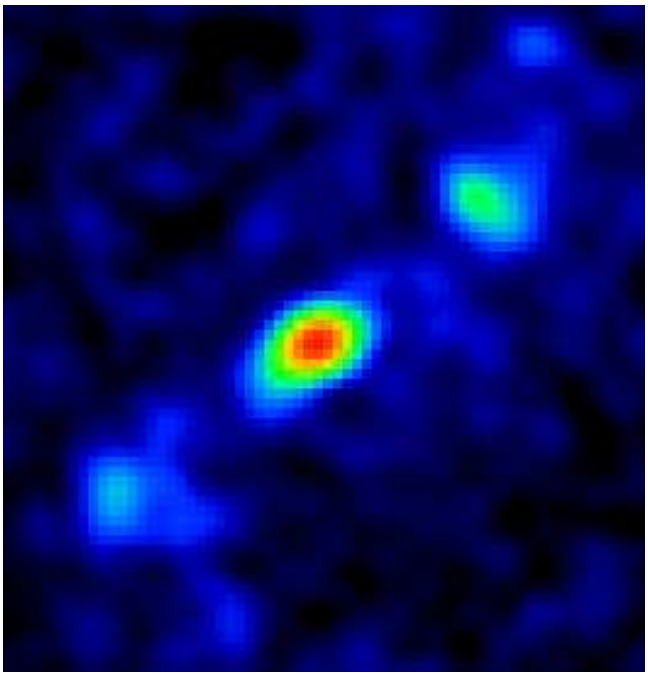

Figure 2.5: A VLA radio image of CH Cyg. The jets (green-blue spots on the sides) appeared just at the end of a powerful active phase, in 1986.

Part II

Galactic Symbiotic Stars

3

Silicates in D-type symbiotic stars: an *Infared Space Observatory* Overview

This chapter has been published in the Astronomical Journal by
Angeloni, R.; Contini, M.; Ciroi, S.; Rafanelli, P.
2007AJ,134-205A

3.1 Dust in symbiotic stars: an introduction

In a still-in-progress work, we analyze the different contributions to the continuum SED of a sample of symbiotic stars, with special emphasis on emission by dust in the IR spectral range. The results are revealing the presence of two dust shells in many systems, suggesting that multiple dust shells are common in D-type systems: the inner and hotter ($\sim$ 1000 K) shells appear circumstellar, with a typical size of 10^{14} cm, while the outer and cooler (T=300 K) with sizes of $\sim 10^{15}$ cm are likely to be circumbinary.

Since the last '60s, smooth and broad bands at 10 μm and 18 μm have been observed in the spectra of some late-type, variable stars and then in a wider variety of galactic environments. They were soon associated with silicate dust grains and were assigned to the Si-O stretching and bending modes, respectively. Furthermore, although the silicates with various composition all display these spectral features due to Si-O vibrational modes, there are differences in the spectral appearance that allow to constrain the exact composition of the silicate grains, as well. After the ISO "crystalline revolution" (Jäger et al. 1998) the whole dust profiles have been interpreted in terms of mixed crystalline and amorphous structures (e.g. Bowey & Adamson 2002, Kemper et al. 2005, Tamanai et al. 2006).

Various attempts have been carrying on to classify the different O-rich dust features on the basis of the spectral profile, by both space-based facilities, like IRAS and ISO (e.g. Little-Marenin & Little 1990; Sloan & Price 1995; Posch et al. 1999) and ground-based ones, like UKIRT (Monnier et al. 1998; Speck et al. 2000, hereafter S00). Some studies highlighted also a clear dependence on the

environment conditions: for instance, the central wavelength of the peak λ_c, of the $\sim$10 μm band is known to decrease from $>$9.8 μm in the circumstellar and diffuse-medium environments to 9.6 μm in the Taurus Molecular Clouds (TMC), while the FWHM increases from 2.5 μm to 3.3 μm (Pégourié & Papoular 1985). These changes in the profiles seem to represent the effect of mixing grains from different sources and of chemical and physical processing on the older TMC and Young Stellar Object (YSO) silicates (Bowey & Adamson 2002, Table 2) and there have been even some works which attempted, on the basis of a long series of laboratory experiments, to relate the ratio of the 10 μm and 18 μm band strength with the relative age of silicate (Nuth & Hecht 1990).
An accurate analysis of observational infrared spectra, discriminating the role played by the various environment parameters, is not trivial since not only mineralogical properties but also size, shape and agglomeration of the grains can have an influence on the shape and intensity of the distinctive spectral features. Thus, further laboratory studies on the silicate dust bands are essential for an appropriate interpretation of the observed spectra.

In the present work we analyze unexploited ISO data in order to compare the silicate dust features in D-type systems with those of "normal", isolated late-type stars and other galactic environments. We refer to the classification scheme proposed by S00 who, thanks to an infrared survey of more than 140 stars, identified similarities and differences between the features of various types of stars. As we are interested in Mira variables, that correspond to the cool component in D-type SS, which represent $\sim$ 20% of the SS in the Belczyński et al. (2000) atlas, we will focus on the three dust feature groups proposed by S00 for AGB stars: 1) *broad AGB*, where the feature extends from 8 to about 12.5 μm with little structure; 2) *broad+sil AGB*, which consists of a broad feature with an emerging 9.7 μm silicate bump; and 3) *silicate AGB*, which is the "classic" 9.7 μm silicate feature. The *silicate AGB* group is split further into four subgroups, A, B, C, D, which show a sequence of slightly different shapes from broader to narrow silicate features (S00, Fig.1).

Our aim is to study the environmental conditions in SS, both in the dust shells and in the shocked, ionized nebulæ, in order to investigate whether the "symbiosis" might affect the dust behavior, leaving its marks on the spectral profile by changing the chemical and physical properties of the grains, as well as the shell morphology and location. The sample and data reduction are described in §3.2, while in §3.3 the results are presented and discussed. Concluding remarks follow in §3.4.

3.2 The sample: observations and data reduction

The sample has been selected by cross-checking the Belczyński et al. (2000) atlas with the ISO Archive, and then by including those D-types which showed the best quality observations. It consists of 9 objects: 8 D type, namely, R Aqr (RAq), V627 Cas (V6), HM Sge (HM), V1016 Cyg (V1), RR Tel (RR), V835 Cen (V8), H1-36 (H1), BI Bru (BI), and 1 S-type, CH Cyg (CH), whose actual

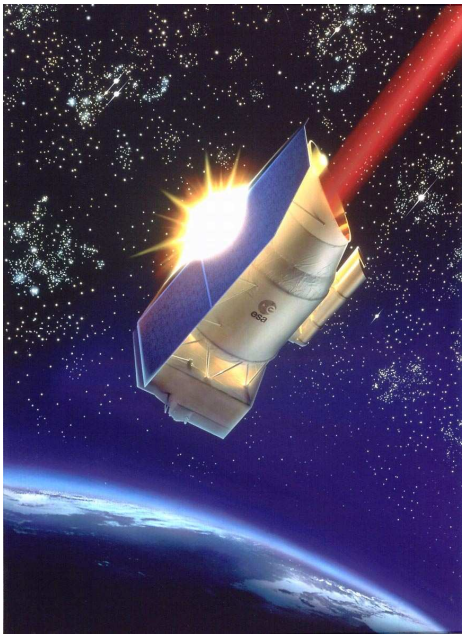

Figure 3.1: An artistic impression of the Infrared Satellite Observatory ISO.

classification is however still controversial (Hinkle et al. 2009).

We present the spectra taken with the Short Wavelength Spectrograph (hereafter SWS - de Graauw et al. 1996), used in full-grating scan mode (AOT 01) and covering the wavelength range between 2.38 and 45.2 μm. The spectra come from the "Uniform database of SWS 2.4-45.4 micron spectra" within the Highly Processed Data Products (HPDP) section of the ISO Archive. The database presents a complete set of all valid SWS full-scan 2.4-45.4 μm spectra processed from the last stage of the pipeline software and renormalized as uniformly as possible, thus representing the most processed form available from the ISO archive (see Sloan et al. 2003 for details about the algorithm used to generate the database). However, some instrumental artifacts are still present, and in specific ranges and cases the S/N level is not sufficient to derive reliable quantitative measurements: for instance, the SWS band 3E at 27.5 - 29 μm is known for its mediocre performance and beyond that wavelengths the spectral quality gradually deteriorates. Anyway, this does not affect the analysis of dust amorphous band at all, but it is reflected only in a inability to determine the very accurate values of the atomic line observed parameters. Considering the aim of the present work, we thus preferred to give only upper limits to the emission lines ratios, exploiting HM Sge as a test-case in the analysis of the emitting nebulæ (§3.3.2). In the following of the present work we focus on the 7-27 μm spectral range.

In the analysis of the dust bands at ∼10 μm and ∼18 μm we decided not to subtract any sort of "continuum", but to rely on the baseline defined by the task SPLOT within the NOAO-ONEDSPEC IRAF package software (see below) during the fitting procedure. Indeed we verified that, even when the continuum appeared moderately steep, the profile shapes did not change to the extent as to modify the basic band parameters (like λ_c and FWHM, the full width half maximum) and to prevent the classification of dust features. This has been confirmed *a posteriori* by the classification of the only star that the present sample shares with the S00 one, i.e. R Aqr. In fact, in agreement whit S00, we classified it in the *silicate AGB C* group (see §3.1).
Furthermore, the identification of the continuum to be subtracted is not trivial: S00, for instance, subtracted a 8 μm normalized 3000K blackbody representing a stellar photosphere, by explicitly assuming that in the 8-13 μm range the continuum is dominated by the stellar contribution. As a matter of fact, the modeling of ISO-SWS spectra shows that in the above mentioned range the continuum emission is predominantly caused by reradiation of hot (∼1000K) dust from the inner shells (r∼10^{14}cm). In the longer wavelength domain, i.e. around ∼ 20 μm, the continuum becomes even more composite, being the sum of contributions from at least two dust shells at different temperatures. Any kind of continuum, without a model taking into account the real physical scenario, appears hence artificial and almost meaningless. As our profiles did not change their shape substantially, we chose a direct approach to the dust band analysis.

To measure the dust profile parameters we used two different approaches. The dust profiles are clearly asymmetric therefore, by definition, the central wavelength of the band will not coincide with the peak position: a Gaussian fit is then not able in reproducing the exact, whole feature profile. Nevertheless, as we focused in the central wavelength of the peak, we performed, by means of the NOAO-ONEDSPEC task within the IRAF package software, a Gaussian fit of merely the upper portion of the band, fairly approximable by Gaussian curve. Then, to check this kind of approach, we tried to follow the same method of Bowey & Adamson (2002), i.e. to estimate the central wavelength of the peak and the FWHM of the bands "by eye". A good agreement between the two methods was found, even if this translates in moderately larger error bars. Nonetheless it is very unlikely that some not accounted for physical effects could move the real central wavelength of the band peak as much as to shift it out of the error bars. It is clear that these uncertainties do not invalidate the results presented in the next section. As regards the atomic emission lines, we performed a Gaussian fit by means of the above mentioned NOAO-ONEDSPEC task in order to measure their main observational parameters, namely the central wavelength and the FWHM.

3.3 Results and discussion

In Fig. 3.2 we present the 7-22 μm spectra for the SS of our sample. The symbiotic character of such systems can be inferred by noticing that on top of

the composite stellar-dust continuum, and even overlapped on the dust broad bands, many intense forbidden emission lines are visible.
In §3.3 we analyze and compare the amorphous silicate spectral profiles which dominate the wavelength range, and in §3.3.2, by exploiting HM Sge as a test-case, we model the IR line spectra in order to constrain the emitting properties of coupled dust-gas particles. In particular, we would like to investigate whether dust grains can survive within the shocked nebulæ and how their chemical properties might be affected by the symbiotic environment as a whole.

3.3.1 Silicate spectral features

The main characteristics of the spectra presented in Fig. 3.2 are the two broad, easily recognizable dust bands at 10 μm and 18 μm, arising from the vibrational modes of Si-O bound. These bands dominate the whole spectral range in 7 out of 9 SS: H1-36, showing a flatter continuum whose shape is due to a cooler (700-800K instead of 1000K) dust (Allen 1983) and BI, where no traces of amorphous silicate bands are recognizable and the spectrum appears almost dust featureless; nonetheless, it is worth noticing that for this last object the poor S/N of the ISO spectrum does not allow to conclusively state about the actual presence of some dust features.

The $\sim$10 μm silicate profile

The SS displaying the 10 μm band might be related, on the basis of the profile shape, to the S00 classification scheme for AGB stars. A direct comparison of our Fig. 3.3 with Fig. 1 of S00 shows that R Aqr and CH Cyg have a profile typical of the *AGB silicate C* group, HM Sge, V1016 Cyg and RR Tel belong to the *AGB silicate D* class, and V627 Cas and V835 Cen lie in the *AGB broad feature* group. No evidence for the $\sim$13 μm feature sometime present in AGB stars is found. In Tab. 3.1 and Fig. 3.4 we investigate the effect of SS environments on the band profiles, plotting the FWHM vs. the central wavelength of the peak λ_c. SS appear in a specific locus of the diagram between the proper circumstellar objects and interstellar environments, being this a clue to an increasing reprocessing of grains across the systems (see below).

It is worth noticing that the only two stars that exhibit the *silicate C* group profile (R Aqr and Ch Cyg) and that lie, in Fig. 3.4, nearest to the proper circumstellar environments (open circles) display just one dust shell ($T_d \sim 1000$K) and share similar characteristics both in the continuum SED and in the physical conditions of the ionized nebulæ. This might be just a coincidence: therefore we would like to further investigate the potential implications of such a link in the symbiotic system in a forthcoming, dedicated paper.
The three stars (HM Sge, V1016 Cyg, and RR Tel) known to have a very complex network of wakes and shock fronts and many emission lines on top of the continuum, as evidence of strong contributions from the nebulæ, display a $\sim$10 μm profile belonging to the same group, the *AGB silicate D*. Even if the FWHM of the 10 μm band appears practically identical to that of typical stellar objects,

the central wavelength of the peak is clearly at longer wavelengths ($\lambda_c \geq 10.1$ μm), probably suggesting irregularity in shapes of dust grains (Min et al. 2003). These profiles are well fitted by a combination of Mg-rich silicates and porous amorphous alumina and are interpreted in the light of a dust condensation sequence that can still be related to the specific condition of the isolated AGB star environments (Tielens 1990, Sloan & Price 1998, Speck et al. 2000).
As previously mentioned, V627 Cas and V835 Cen belong to the *AGB broad feature* group. In this case not only the λ_c appears at longer wavelength with respect to the other classes, but also the FWHM is larger (FWHM $\sim$ 2.9-3.1 μm). One of the interpretation of the larger width of the *AGB broad feature group* profile suggests a $\sim$2 μm-wide excess centred at 11.5 μm which has been attributed to the shifted peak of larger micrometer-sized grains (Jaeger et al. 1994). The presence of these larger grains could be a clue to crystalline silicates (van Diedenhoven et al. 2004), which have been observed in the D'-type SS HD330036 (see Chap. 8). New high resolution and high S/N observations would be welcome considering the other species of silicates disclosed by the ISO "revolution". As a matter of fact these data might reveal the sharp substructures due to crystalline silicates which appear superimposed on the amorphous silicate broad features. A detailed analysis of the crystalline band would then be helpful in determining the physical parameters of these environments, thanks to derived estimates of mass-loss rates (Kemper et al. 2001), dust temperature (Bowey et al. 2002) and dust geometrical distribution (Molster et al. 2002a,b,c). On the other side, new laboratory measurements are necessary for a further verification of this insight under varying environmental parameters, allowing for a better correlation between the profile shape variations and the astrophysical condition parameters.

To summarize, from this spectral comparison it follows on that dust in D-type SS appears, at least in some cases, different from the dusty environment of "normal" isolated late-type evolved stars. In particular, the sample seems to indicate a kind of sequence that moves towards objects with multiple and complicated structures of nebulæ and shells. We suggest that for these systems (the ones that differ more from typical circumstellar environment on the basis of Fig. 3.4) the different profile features can be interpreted in the light of mixed properties of the grains, being the grains responsible of the bulk of the emission both in the inner "circumstellar shell" and in the outer, circumbinary one. The symbiotic behavior seems thus to play a dominant role not only in the dynamical parameters such as location and distribution of dust by affecting both the shell radii and shapes, but also in the chemical properties of the grains, which experience physical conditions both of circumstellar and ISM environments. The signature of dust chemical disturbance due to symbiotic activity should then be assigned to the outer shells of the whole system, where the environmental conditions for grain processing and even crystallization can, in some cases, be achieved.

The ∼18 μm silicate profile

Fig. 3.2 shows that several SS have a second bump at $\sim$ 18 μm, usually attributed to Si-O bending mode in amorphous silicates. Even in this case, many emission lines are seen on top of the continuum and of the dust band.
The strength of the ∼18 μm profile decreases along with that of the ∼10 μm one; as these two features arise from different vibrational modes of the same chemical bound (Si-O), we wonder if the dust bands answer in a somewhat correlated ways to the same environmental conditions, probably periodically varying in reaction to the Mira periodic pulsations.
To verify this idea we plot in Fig. 3.5 (see also Tab. 3.1) the 10 μm vs. 18 μm λ_c. Interestingly, we find a clear increasing correlation between these two observational parameters: the longer the $\lambda_c(10)$, the longer the $\lambda_c(18)$. The least square method was performed in order to find the best linear fit to the data: $\lambda_c(18) = 1.39\lambda_c(10) + 3.73$.

Unfortunately the sample is poor in number of objects, and limited to D-type SS. We might expect that a similar behavior of amorphous silicate dust bands could also be present both in other circumstellar envelopes and galactic environments. It would be interesting if, after verified and constrained on a larger sample of different astrophysical environments, this relationship will gain some chemical and physical significances on the basis of further laboratory investigations.

3.3.2 Dust and gas conditions in the ionized nebulæ

In SS two main shocks develop from collision of the winds from the stars, one propagating outwards the system, and the other propagating in reverse towards the WD, between the stars. The nebulae downstream of the shock fronts are heated and ionized by the photoionizing flux from the hot star and by shocks. In order to include this theoretical framework in our model, we complete our investigation on dust features in SS environments by calculating dust and gas conditions downstream of the shocked nebulae. We will constrain the gas and dust physical conditions by modeling the strongest emission line ratios. The IR spectra show lines from a large range of ionization levels, including [FeVII] and [SiVII]. Radiation from the WD cannot lead to gas temperatures $\geq$ 2-3 10^4 K in the nebulae, while the collision processes heat the gas to temperatures which depend on the shock velocity ($T \propto V_S^2$). The observed lines are forbidden, therefore hardly emitted from the shells where very high electron densities lead to collisional deexcitation. Moreover, the high ionization level lines indicate high shock velocities characteristic of the nebula downstream of the reverse shock.

The models which best fit the line ratios are calculated by SUMA (Viegas & Contini 1994; Contini 1997), a code that simulates the physical conditions of an emitting gaseous cloud under the coupled effect of ionization from an external radiation source and shocks, and in which line and continuum emission from gas are calculated consistently with dust reprocessed radiation as well as with grain heating and sputtering processes. Its calculation models have been

already applied to several symbiotic stars, e.g. AG Peg (Contini 1997, 2003), HM Sge (Formiggini, Contini & Leibowitz 1995), RR Tel (Contini & Formiggini 1999), He2-104 (Contini & Formiggini 2001), R Aqr (Contini & Formiggini 2003), as well as to nova stars (V1974, Contini et al. 1997 - T Pyx, Contini & Prialnik 1997) and supernova remnants (e.g. Kepler's SNR, Contini 2004). The composite models are characterized by the parameters referring to the radiation flux (the temperature of the hot star, T_*, and the ionization parameter, U), by those representing the shock (the shock velocity, V_s, the preshock density, n_0, and the magnetic field, B_0), and by those related with dust (the dust-to-gas ratio, d/g and the initial grain radius, a_{gr}). The relative abundances to H of He, C, N, O, Ne, Mg, Si, S, Ar and Fe are also accounted for.

HM Sge: a test case

We refer to the emission line measurements of SWS spectra for HM Sge by Schild et al (2001). In Table 3.2 the observed line ratios to [NeVI] are compared with model results. We consider first the Ne lines, [NeVI]7.65, [NeV]14.32, [NeIII]15.55, and [NeII]12.82, representing four different ionization levels of the same element. [NeVI] is the strongest line while [NeII] is very weak, indicating that the temperature of the gas is high enough across the whole nebula to prevent recombination. This constrains the model to matter-bound, suggesting that the emitting nebula is located between the stars, downstream of the shock which propagates in reverse towards the hot component. The relatively high velocities indicated by the FWHM of the lines ($\sim 500\ km\,s^{-1}$, Table 3.2) confirm that we are dealing with the reverse shock. Such high velocities are in agreement with a plasma temperature of $10^{6.6}$ K deduced from the X-ray observations by Mürset et al. (1997). The profile of the density and temperature downstream which result from the hydrodynamical equations determine the stratification of the ions and thus the intensity ratios of the lines. The best fit to the data is obtained with a preshock density n_0=$5.10^5\ cm^{-3}$ which leads to densities downstream n $\sim 10^8\ cm^{-3}$, and with T_*=160 000 K and U=1. The corresponding ionizing photon flux is F_ν= 6 10^{26} cm^{-2} s^{-1}. If the radius of the ionizing source is $R_{WD} \sim 10^9$ cm and the distance to the nebula is r, we have $F_\nu R_{WD}^2/r^2$= U n c, where c is the velocity of light. We obtain r=7.8 10^{13} cm. The geometrical thickness of the nebula, D= 1.4 10^{14} cm, which is lower than the binary separation (3 10^{14} cm, Richards et al. 1999) is found by modeling.

Once the Ne line ratios are reproduced by the model, the relative abundances of the elements result from the agreement of the calculated with the observed line ratios. However, the elements different from Ne are represented by only one line in the observed spectrum, so the relative abundances are less constrained. In Fig. 3.6 top, the profiles of the electron density, n_e, of the electron temperature of the gas, T_e, as well as of the temperatures of dust grains, T_{gr}, corresponding to different initial grain radii are shown across the nebula. The vertical thin solid line shows that most of the recombination region is cut off. The fractional abundance of the Ne ions (top) and of the ions corresponding to the other observed lines (bottom) are shown in Fig. 3.7 as a function of the

electron temperature.
In Table 3.3 our results are compared with those of previous works. We find O/H and Ne/H higher than solar by factors of $\sim$ 2.3 and 4.8, respectively, revealing the strong contribution of the WD wind to the nebula between the stars (Nussbaumer & Vogel 1990, Weidemann 2003). Moreover this allows us to postulate that oxygen had an initial (i.e. pre-1975 outburst) abundance as high as to compensate any depletion caused by subsequent grain formation processes. The other metals such as Mg, Si and Fe, which are easily trapped into grains, are instead depleted relatively to the solar values. Interestingly, the depletion of Fe does not appear correlated with that of Mg and Si, being instead more than twice larger. If iron was incorporated in the silicate lattice it would return to the gas phase along with the magnesium and silicon when the silicate is destroyed (see below); iron then must be trapped in different dust material, maybe in the form of refractory species such as metallic iron or iron oxide, so that it can stay in a solid phase while the magnesium and silicon are returned to the gas phase. This insight, which provides a natural explanation of the unusual depletion pattern observed also in several lines of sight through the interstellar medium (Welty et al. 2001; Sofia et al. 2006) has been already suggested by Sofia et al. (2006) and consistently confirmed by a very recent theoretical study by Min et al. (2006). As a further and complementary proof we deduce our results on the basis of the analysis of atomic emission lines.

The rate of erosion (sputtering) of the grains can be high for $V_s \geq 200\, km\, s^{-1}$, leading to a complete destruction of the grains. Notice that even the largest ones (a_{gr}= 1 μm) are sputtered within a relative small distance from the shock front (Fig. 3.6, top). Mg, Fe and particularly Si should therefore return to the gaseous phase before the temperature drop to the values suitable to the line emission. This indicates that other effects must be considered, e.g. the lifetime of grain survival which depends on the distance downstream covered by the grains (Shull 1978, Dwek 1981). Small grains are stopped after distances of $\sim$ 7 10^{12} cm, while large grains after $\sim$ 3 10^{13} cm (Contini et al. 2004) which are of about the same order of the sputtering distances shown in Fig. 3.6.

An intriguing issue related to grain processing is that the return of silicon to the gas phase might take place in the molecular form (SiO, SiO_2), hence explaining the apparent contradiction between the high efficiency of sputtering processes we deduce from the shocks and the observed depletion calculated by the atomic lines.
It is known that SiO is a very reliable tracer of shocked gas in many astrophysical environment, and its enhancement in the gas phase has been already observed both in the bipolar outflows of young stellar objects (Martin-Pintado et al. 1992; Schilke et al. 1997) and in galaxies (Garcia-Burillo et al. 2000, 2001b; Usero et al. 2006). Moreover, there is growing evidence that different moleculæ trace distinctly different velocity regimes in shocks, with SiO associated with more energetic events, i.e., those potentially more efficient in processing dust grains (Garay et al. 2000). Although qualitatively similar, shocks characterized by different velocity regimes are expected to develop to a different extent dust grains in molecular gas: fast shocks can destroy the grain cores, liberating

refractory elements to the gas phase, while slow shocks could only be able to process the icy grain mantles. One can then conclude that an increase in the typical velocity regime of shocks will favor an enhancement of the abundance of SiO in the shocked gas.
The shock velocity characteristic of these processes, i.e. the threshold value above which the dissociation of SiO takes place, are usually $V_s \leq$ 60-70 $km\,s^{-1}$ (Martin-Pintado et al. 1992). At the bottom of Fig. 3.6 the profile of the shock velocity downstream which results from the solution of the continuity equations for our model is shown, along with the [SiVII] line formation region. As one can see, at distances sufficiently large from the shock front the velocity drops to $V_s <$ 100 $km\,s^{-1}$, indicating suitable conditions for molecular shock chemistry.
The interpretative framework is still in progress under many aspect, and it needs observational data to be more constrained. Unfortunately, so far, there is a complete lack of spectral observations for SS in the mm spectral region. We then call for mm observations at SiO transition frequencies, e.g. $\sim$ 217 GHz J=5-4 (λ=1.38 mm), $\sim$ 130 GHz J=3-2 (λ=2.3 mm), $\sim$ 86 GHz J=2-1 (λ=3.4 mm), in order to trace the shock spatial profile within and around the symbiotic nebulæ and to reveal up to what degree the sputtering processes are at work.

Consider now the nebula downstream of the shock front expanding outwards the system which is characterized by a higher D, lower velocities and lower densities, hence being the source of the rich optical and UV spectra reported and studied extensively by previous works (e.g. Nussbaumer & Walder 1993, Formiggini et al. 1995). The grains can survive to destructive processes and contribute to the IR emission even at larger wavelengths, because of the lower temperature ($T_{gr} \sim$ 300K) of dust.
The overall conditions of dust and grains within the outer expanding nebulæ are approaching those of the ISM up to a complete merge, indicating that the signature of dust chemical disturbance due to symbiotic activity, i.e. the chemical and physical reprocessing of the grains suggested on the basis of the spectral analysis, might take place and should be looked for in these circumbinary structures.

The other objects

Fig. 3.2 shows that some objects of the sample have very similar spectra, both in the dust and in the emission lines features, while some others lack highly ionized lines (e.g. R Aqr, CH Cyg) and/or dust band (e.g. BI Cru, H1-36).

For objects with an evident emission line spectrum the Ne spectral line ratios, which are independent from relative abundance effects, are compared in Table 5.2. It can be noticed that the general trend is very similar to that found for HM Sge, except RR Tel which shows [NeIII]/[NeVI] lower by a factor $\leq$ 2, and H1-36, which displays a very bright [OIV]25.89μm emission line, as well as no evident dust spectral feature (see §3.3). In Table 3.5 we present the FWHM measured for the brightest lines. The derived velocities indicate that also for these objects, as for HM Sge, we are dealing with the inner shocked nebula, which emits the detected atomic emission lines and where dust grains

can hardly survive the harsh environmental conditions. Considerations similar to those reported in the previous section about the molecular emission are still applicable.

It is noteworthy that R Aqr and CH Cyg, known to have just one hot ($T_{gr}\sim$ 1000K) and circumbinary dust shell, do not show emission lines from highly ionized elements. A plausible explanation for the absence of such strong atomic features could lie in the high density of the inner shocked nebula, up to 10^9 cm^{-3} (Contini 2006, in preparation), that prevents the formation of forbidden emission lines.

Unfortunately for some objects ISO spectra are too noisy to reveal fainter spectral feature (V835 Cen, BI Cru). Furthermore, there are still insufficient data in some spectral ranges for a consistent and thorough analysis, and even for concluding about the actual symbiotic nature of some stars, as V627 Cas (Belczyński et al. 2000). Thus we postpone to forthcoming papers a detailed discussion of the single objects.

3.4 Concluding remarks

We have investigated the IR spectral features of a sample of D-type symbiotic stars in order to constrain the emitting properties of coupled dust-gas particles across the whole systems. Having extracted the basic observational parameters of both dust bands and atomic emission lines from unexploited ISO data and having compared them with those from other astronomical sources, we have attempted to highlight the effect of the environment on grain chemistry and physics, in particular whether dust grains can survive within the shocked nebulæ and how their chemical properties might be affected by several depletion and sputtering patterns.
The main conclusions of this work are the following:

- The strong amorphous silicate emission features at $\sim$10 μm and $\sim$18 μm are found in 7 out of 9 objects of the sample. A qualitative analysis of the $\sim$10 μm dust band indicates that the profile shape is similar to that of "standard" isolated AGB stars. Nevertheless a quantitative comparison of λ_c vs. FWHM for the 10 μm silicate profile with other astronomical sources shows that SS appear between the characteristic circumstellar objects and interstellar environments, which is believed to be a clear clue of an increasing, ongoing reprocessing of grains.

- A correlation between the central wavelength of the $\sim$10 μm and $\sim$18 μm dust bands is found. It is likely that the dust bands answer in a somewhat correlated ways the same environmental conditions, probably periodically varying in response to the Mira periodic pulsations if the dust grains responsible of the bulk of the emission are mainly located in the hot, circumstellar shell. Both new high resolution and high S/N observations, as well as new laboratory measurements under varying environmental param-

eters, are necessary for a further verification of this insight, even thanks to larger samples.

- The modeling of IR spectral lines allowed to constrain the emitting properties of coupled dust-gas particles within the shocked nebulæ, showing that sputtering processes are efficiently at work in the inner nebulæ where high shock velocities are reached. The signature of dust chemical disturbance due to symbiotic activity should then be looked for into the outer, expanding, circumbinary shells where the environmental conditions for grain processing and even crystallization might in some cases be achieved.
- Both the unusual depletion values and the high sputtering efficiency could be explained by the overabundant presence of SiO moleculæ, known to be a very reliable shock tracer, hence making SS interesting targets for *mm* observations.

Table 3.1: λ_c and FWHM of the 10 μm silicate profile, λ_c of the 18 μm silicate profile, and relative uncertainties [μm] for the objects in Figs. 3.4 and 3.5.

Object	λ_c(10)	err λ_c(10)	FWHM(10)	err FWHM(10)	λ_c(18)	err λ_c(18)
Symbiotic						
R Aqr	10.0	±0.1	2.5	±0.1	17.5	±0.2
CH Cyg	10.0	±0.1	2.5	±0.1	17.6	±0.2
V627 Cas	10.4	±0.1	2.9	±0.1	18.2	±0.2
HM Sge	10.3	±0.1	2.6	±0.1	17.9	±0.2
V1016 Cyg	10.1	±0.1	2.7	±0.1	17.9	±0.2
RR Tel	10.1	±0.1	2.6	±0.1	18.1	±0.2
V835 Cen	10.4	±0.1	3.1	±0.1	18.3	±0.2
Novæ						
Aql 82	10.2	±0.1	2.9	±0.1	-	-
Her 91	10.7	±0.1	3.0	±0.1	-	-
Cas 93	9.6	±0.1	1.8	±0.1	-	-
Circumstellar						
μ Ceph	9.9	±0.05	2.5	±0.1	-	-
CU Cep	9.9	±0.05	2.5	±0.1	-	-
U Aur	9.8	±0.05	2.8	±0.1	-	-
Diffuse medium						
Cyg OB2 n.12	9.7	±0.05	2.6	±0.1	-	-
YSO, Orion Trap., TMC						
HL Tau	9.6	±0.05	3.2	±0.1	-	-
Orion Trap.	9.6	±0.05	3.5	±0.1	-	-
Taurus-Elias 7	9.6	±0.05	3.5	±0.1	-	-
Taurus-Elias 13	9.5	±0.05	3.4	±0.1	-	-
Taurus-Elias 16	9.6	±0.05	3.3	±0.1	-	-
Taurus-Elias 18	9.5	±0.05	3.2	±0.1	-	-

Table 3.2: emission lines, normalized to [NeVI] 7.65 μm, in the SWS spectrum of HM Sge.

λ [μm]	ID	iP [eV]	FWHM [μm]	observed[a]	model[b]
4.53	[ArVI]	91.01	0.01	0.09	0.09
5.61	[MgV]	141.27	0.04	0.19	0.18
6.49	[SiVII]	246.52	0.03	<0.07	0.07
7.65	[NeVI][c]	157.93	0.03	1	1
9.53	[FeVII]	124.98	0.04	0.05	0.05
10.51	[SIV]	47.22	0.04	0.04	0.04
12.81	[NeII]	40.96	0.07	<0.07	0.001
14.32	[NeV]	126.21	0.06	0.13	0.12
15.55	[NeIII]	63.45	0.06	0.08	0.08
24.31	[NeV]	126.21	0.11	0.06	0.04
25.89	[OIV]	77.41	0.10	0.09	0.08

a: adapted from Schild et al. 2001;
b: input parameters: V_s=500$km\,s^{-1}$; n_0=5 10^5 cm^{-3}; B_0=10^{-3} G; d/g=4 10^{-5} (by mass); a_{gr}=1, 0.5, 0.2 μm; D=1.74 10^{14} cm; T_{gas}=1.85 10^4 K; T_*=1.6 10^5 K; U=1;
c: absolute flux: 74 ± 0.6 10^{-12} erg cm^{-2} s^{-1}.

Table 3.3: the comparison of relative abundances in HM Sge.

element	model	NV90	solar
He/H	0.11	0.10	0.085
O/H	1.5(-3)	1.0(-3)	6.6(-4)
Ne/H	4.0(-4)	4.0(-4)	8.3(-5)
Mg/H	1.5(-5)	1.0(-4)	2.6(-5)
Si/H	8.0(-6)	2.0(-4)	3.3(-5)
S/H	3.6(-5)	1.0(-4)	1.6(-5)
Ar/H	6.3(-6)	6.0(-6)	6.3(-6)
Fe/H	6.0(-6)	3.0(-5)	4.0(-5)

NV90: Nussbaumer & Vogel (1990).

Table 3.4: the brightest Ne emission lines[a] visible on top of continuum.

Symb	$[NeV]_{14.32}$	$[NeIII]_{15.55}$	$[NeV]_{24.31}$
R Aqr	-	-	-
CH Cyg	-	-	-
V627 Cas	-	-	
HM Sge[b]	0.13	0.08	0.06
V1016 Cyg	<0.3	<0.1	<0.2
RR Tel	<0.2	<0.05	<0.1
BI Cru	-	-	
V835 Cen	<0.05	-	
H1-36	<0.5	<0.2	<0.15

a: normalized to [NeVI] emission line @ 7.65 μm;
b: adapted from Schild et al. 2001.

Table 3.5: FWHM [μm] of the brightest atomic emission lines.

Symb	$[NeVI]_{7.65}$	$[NeV]_{14.32}$	$[NeIII]_{15.55}$	$[NeV]_{24.31}$	$[OIV]_{25.89}$
R Aqr	-	-	-	-	-
CH Cyg	-	-	-	-	-
V627 Cas	-	-	-	-	-
HM Sge	0.03	0.06	0.06	0.11	0.10
V1016 Cyg	0.03	0.05	0.05	0.11	0.11
RR Tel	0.03	0.06	0.06	0.09	0.10
BI Cru	-	-	-	-	-
V835 Cen	0.03	0.06	-	-	-
H1-36	0.03	0.05	0.06	0.10	0.11

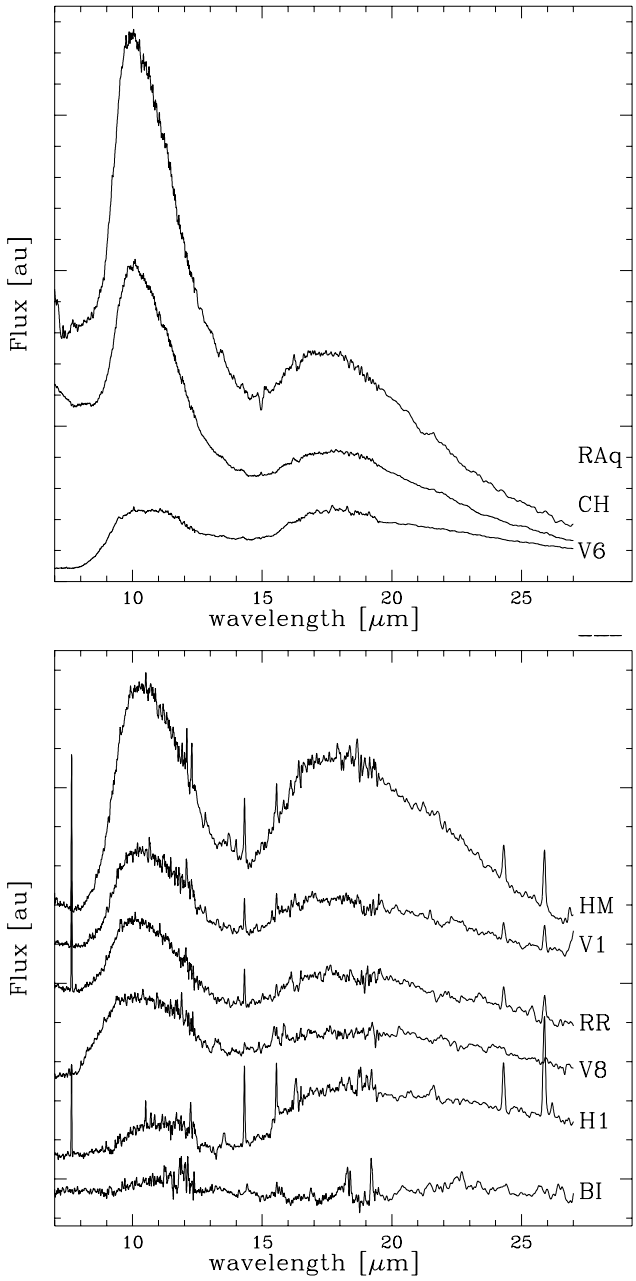

Figure 3.2: The 7-27 μm region of the ISO-SWS spectra for the SS of the sample. Notice the similarities and the differences in the continuum SED, in the dust band profiles at ~ 10 and ~ 18 μm (e.g. likely absent in BI Cru, even if the poor S/N of the spectrum does not allow to conclusively state about it) and in the intensities of atomic emission lines.

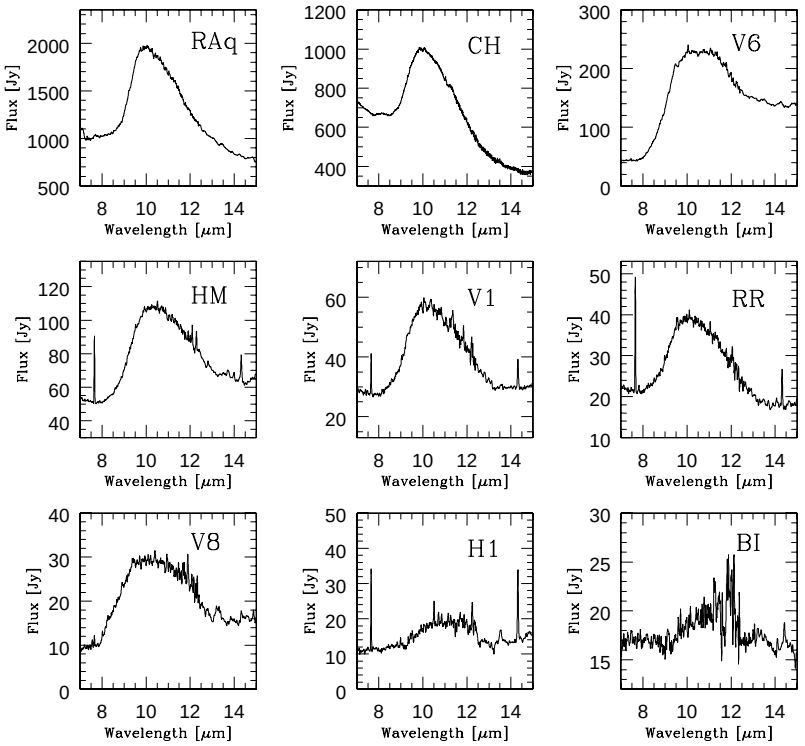

Figure 3.3: The 7-15 μm range. The amorphous silicate profile at $\sim$10 μm is dominant in 7 out of 9 SS.

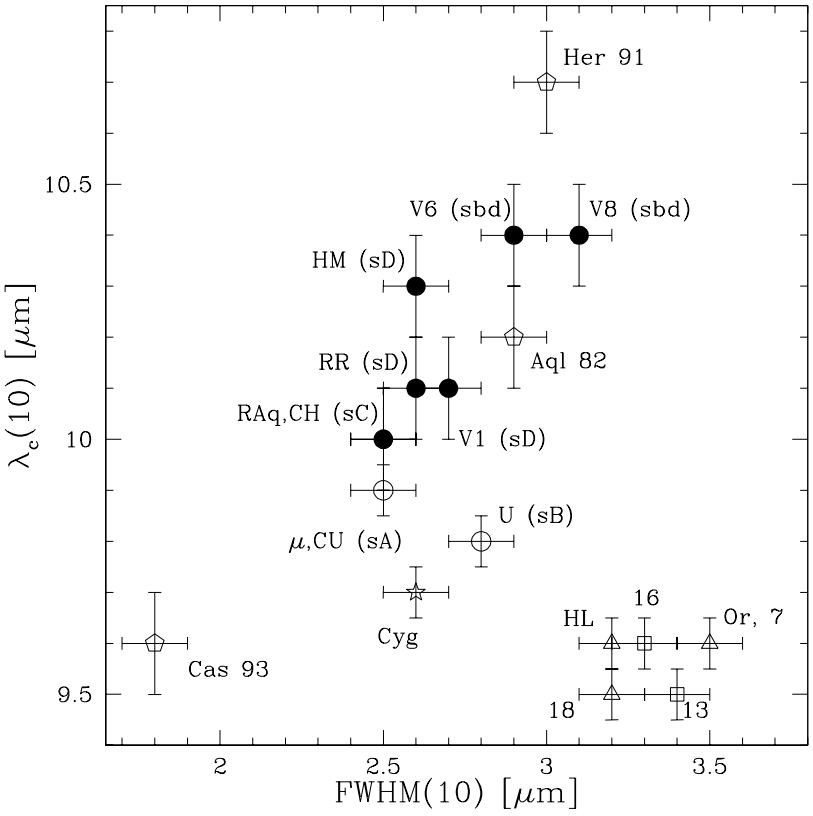

Figure 3.4: Effect of environment on the 10 μm silicate profile. Filled circles: SS; open pentagon: Novæ (Aql82, Her 91, Cas 93 - Evans et al. 1997); open circles: circumstellar (CU Cep, U Aur, μ Cephei; Russell et al. 1975); open star: diffuse medium (Cyg OB2 n. 12); open triangles: YSO and TMC (HL Tau, Taurus-Elias 7 and 18) and Orion Trapezium (Gillett et al. 1975); open squares: quiescent TMC (Taurus-Elias 16 and 13).

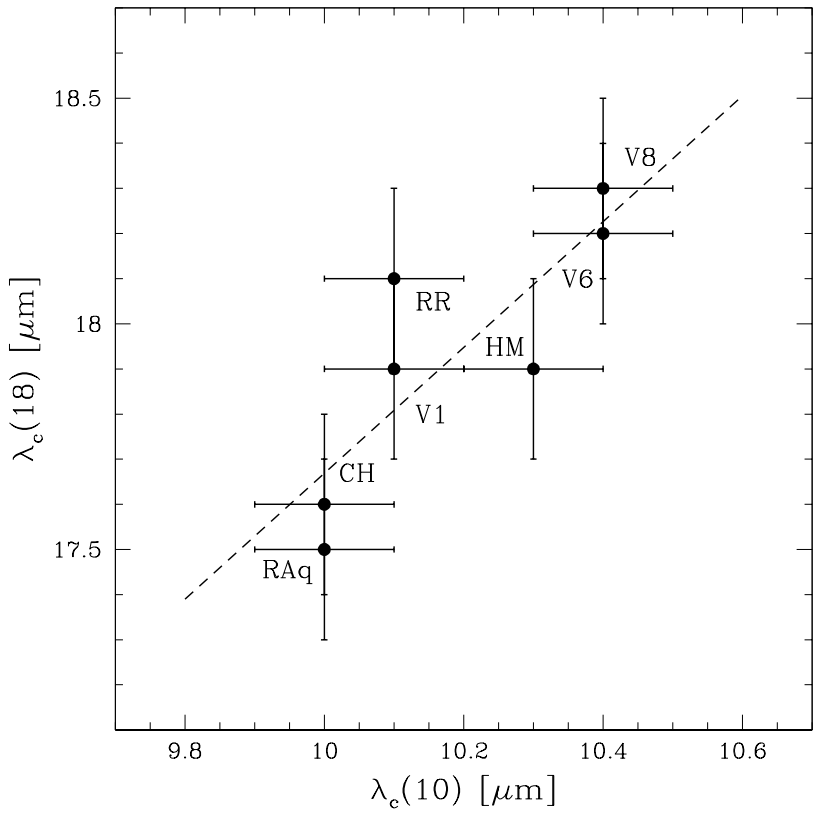

Figure 3.5: The peak wavelength of the 10 μm vs. 18 μm amorphous silicate bands. The dashed lines is the best linear fit with the data.

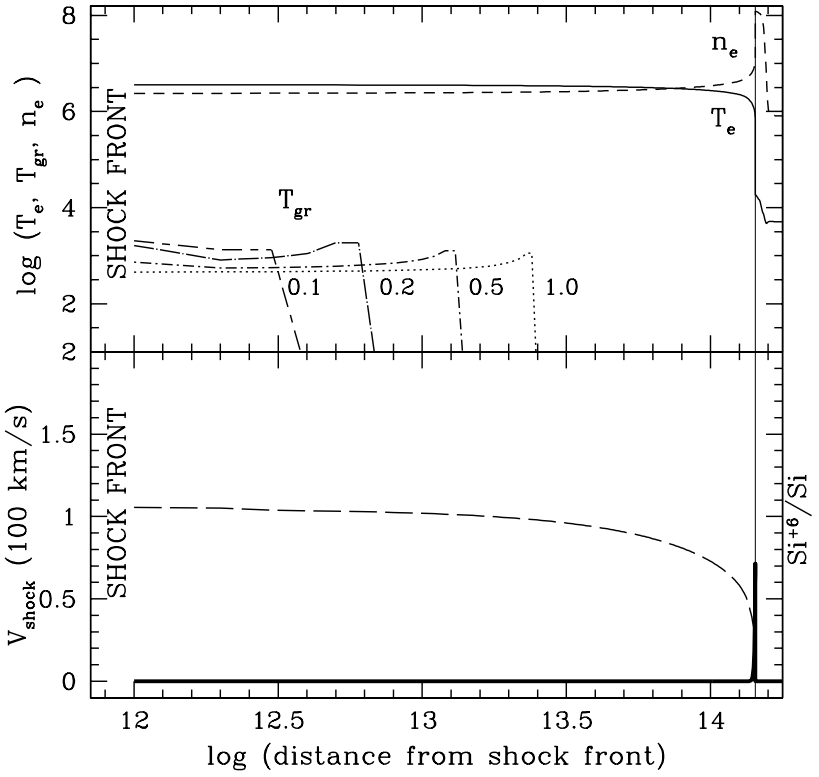

Figure 3.6: Top: the profile of electron density, electron temperature and grain temperature relative to different initial grain size (in μm) downstream across the reverse shocked nebula in HM Sge. The vertical thin solid line represents the edge of the matter-bound model. Numbers near the grain temperature line indicate the initial grain radius, a_{gr}. Bottom: the profile of shock velocity, V_s, and the distribution of the Si^{+6}/Si fractional abundance (thick solid line).

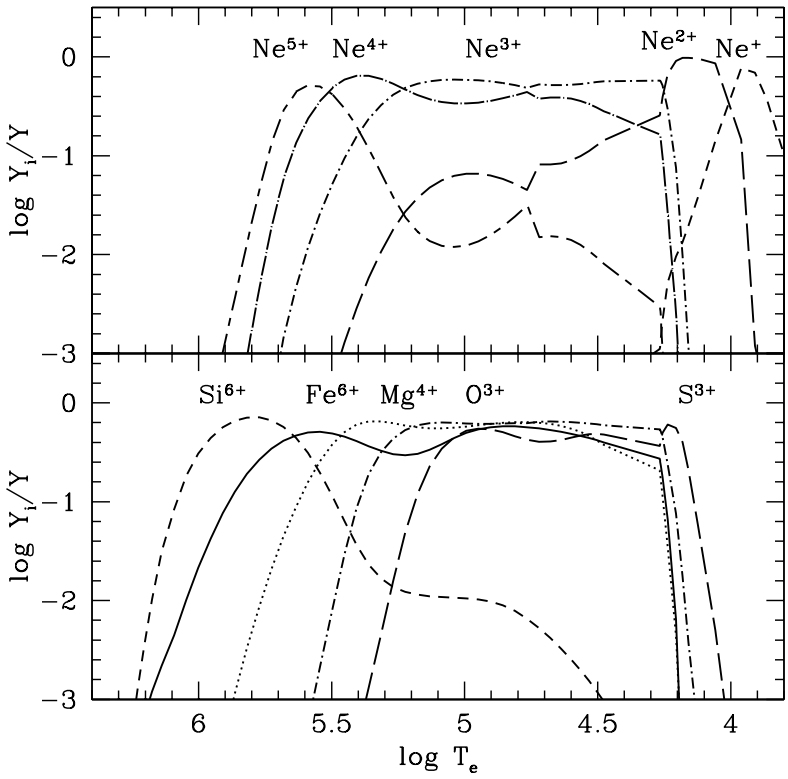

Figure 3.7: The fractional abundance of the ions downstream as function of the temperature across the nebula for HM Sge.

4

The symbiotic star H1-36. A composite model of line and continuum spectra from radio to ultraviolet

This chapter has been published in Astronomy & Astrophysics by
Angeloni, R.; Contini, M.; Ciroi, S.; Rafanelli, P.
2007A&A,471-825A

4.1 Introduction

H1-36 was among the most interesting objects in the extensive Purton's radio survey of emission-line stars (1982). The particular attention that was drawn to it since the Haro's discovery (1952) was due to a curious set of misunderstood and genuine insights: cataloged as planetary nebula despite its extremely high-excitation emission line spectrum and its imposing infrared excess, H1-36 was even thought to be, now we know erroneously, the optical counterpart of the *Uhuru* hard X-ray source 3U 1746-37 (Giacconi et al. 1974). Finally, Allen permanently classified H1-36 as a D-type SS by including it in his catalog (Allen 1981) and dedicating to it a paper (Allen 1983) that so far still represents the most complete observational work on such object.

One of the most important results emerging from that study is that the Mira star experiences an extraordinary reddening ($A_v \sim 20$ mag.), especially when compared to the one towards the emission-line regions (only 2.2 mag.): this allowed Allen to point out that the cool component is heavily embedded in its own circumstellar dust shell, illuminated from the outside by a $T_* \sim 150.000$ K star. The derived cool star and dust temperatures would then be, respectively, $T_M \sim 2500$ K and $T_d \sim 700$-800 K.
Another interesting feature of H1-36 lies in the radio range: as a matter of fact, it is one of a small number of radio sources whose spectra are flat at high frequencies but turn towards a spectral index near +1 at lower frequencies (Purton 1977). Several papers hence tried to explain this behavior in terms of free-free emission from the ionized cool star wind, unfortunately without taking

into account the possibility of any outflow from the compact star (for a further description of this models, see Sect. 4.3.2).
The following papers, which presented both imaging (e.g. Bhatt & Sagar 1991; Corradi et al. 1999, who resolved the complex nebula at radio and optical wavelengths) and new spectra (e.g. Costa & de Freitas Pacheco 1994; Pereira 1995; Pereira et al. 1998), have not substantially modified the original scenario drawn by Allen's analysis, whose physical parameters have still to be considered as the most reliable ones available in literature. Interestingly, H1-36 is the only SS known to support OH- (Ivison et al. 1995), as well as SiO- (Allen 1989) and H_2O- masers (Ivison et al. 1998).

In this chapter, we aim to model H1-36 (Table 4.1) by combining literature observations from radio to UV collected over a period of about 30 years (Sect. 4.2). Within a colliding-wind scenario and by means of the SUMA code, we start modelling more than 40 emission lines from IR to UV in order to constrain the physical conditions across the whole system (shocked nebulæ, dust shells, hot and Mira stars). In the light of the derived parameters, we are then able to fit the composite continuum SED in a self-consistent way. The results of this cross-checked method are extensively presented in Sect. 4.3. Concluding remarks appear in Sect. 4.4.

4.2 Observational details

4.2.1 Radio-mm observations

In Table 4.2 we present the data we collected from literature in order to ensure as much a complete spectral coverage in the radio-mm range as possible.
The most important references about the H1-36 radio spectrum remain Purton's papers (Purton 1977, 1982), in which observations from about 2 GHz to 90 GHz obtained with the CSIRO 64-m telescope at Parkes, Australia, the NRAO 11-m telescope at Kitt Peak, USA, and the NRAO three-element interferometer at Green Bank, USA, are presented. In the next years several works, focused mainly on the mass loss properties of the cool stellar component (e.g. Jones 1985) and on the presumed correlations among different spectral bands (Seaquist et al. 1993), performed observations at intermediate frequencies. They allowed us to extract a well defined radio profile and eventually to confirm that the object has not been significantly variable in the last 30 years.
This ensures that collecting data coming from a wide temporal range is, at least for this SS, a reliable approach. Summarizing, we are able to present a radio-mm profile composed by 16 points from 843MHz to 230GHz (Fig. 4.1, bottom panel).

Table 4.1: The main parameters of H1-36 D-type symbiotic star.

-	-	Ref.
α (J2000)	17 49 48.1	Belczyński et al. (2000)
δ (J2000)	-37 01 27.9	Belczyński et al. (2000)
WD temperature	$1.5\ 10^5$ K	Allen (1983)
Cool star spectrum	Mira - M4-M5	Allen 83 - Medina-Tanco & Steiner (1995)
Mira temperature	2500 K	Allen (1983)
Mira pulsation period	450-500 d	Whitelock (1987)
Dust temperature	700 K	Allen (1983)
Distance	4.5 kpc	Allen (1983)
Binary separation	$3\ 10^{16}$ cm	Allen (1983)
Orbital period	$\geq$10 $D^{3/2}$ yr	Allen (1983)
Other names	PK 353-04 1=Hen2-289= =Haro 2-36=IRAS 17463-3700	Belczyński et al. (2000)

4.2.2 Infrared data

D-type SS are known to be variable systems in the IR range, where we observe the contributions of different emitting components, i.e. cool star and dust shells. Quite surprisingly, as in the radio case, the H1-36 IR spectra do not show dramatic variations in the data flux over the years we are going to discuss (Table 4.3, Fig. 4.1, top panel): indeed, IRAS points (1982) agree well with ISO-SWS spectrum (taken in 1996) and with the 34.6 μm measurement presented in He et al. (2005); also the accordance with the MSX6C photometric points (Egan et al. 2003) is reasonably good. At NIR wavelengths the Allen's NIR bands are slightly shifted with respect to the DENISE and 2MASS bands, especially the H and J bands which feel the increasing contribution of the cool star. This is confidently due to the Mira variations, whose period is about 450-500 days (Whitelock 87).

4.2.3 Optical spectra and UV spectrophotometry

Also in this case the analyzed data are a collection of different observing sessions from 1975 to 1979. These are presented in Allen (1983), where the reader is sent for further technical details. Moreover, in that paper it is explicitly stated that the optical data "are combined in the belief that variability of the lines is slight". This has been even more reconfirmed by recent spectra, which in fact did not show relevant changes in the line and continuum flux level (Costa & de Freitas Pacheco 1994, Pereira 1995, Pereira et al. 1998).

4.3 Modelling the spectra

In this section we present the models which best reproduce the whole properties of H1-36. The models dealing with the observed line spectra appear in Sect. 4.3.1. They are cross-checked by the continuum SED (Sect. 4.3.2) until a fine tuning of line and continuum spectra is found: we refer in particular to the SED in the radio range, where the turnover frequency and the steeper spectral index of the bremsstrahlung at lower frequencies are highly sensitive to the physical conditions of the gas.

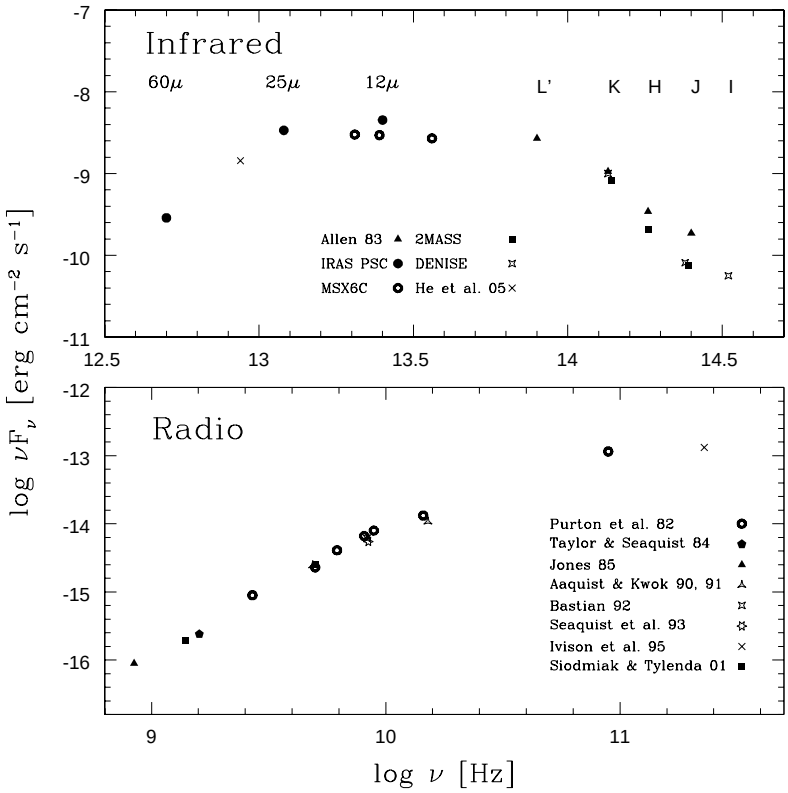

Figure 4.1: Observational data. Top panel: IR spectral range - for sake of clarity we don't show the ISO spectrum. Bottom panel: radio spectral range.

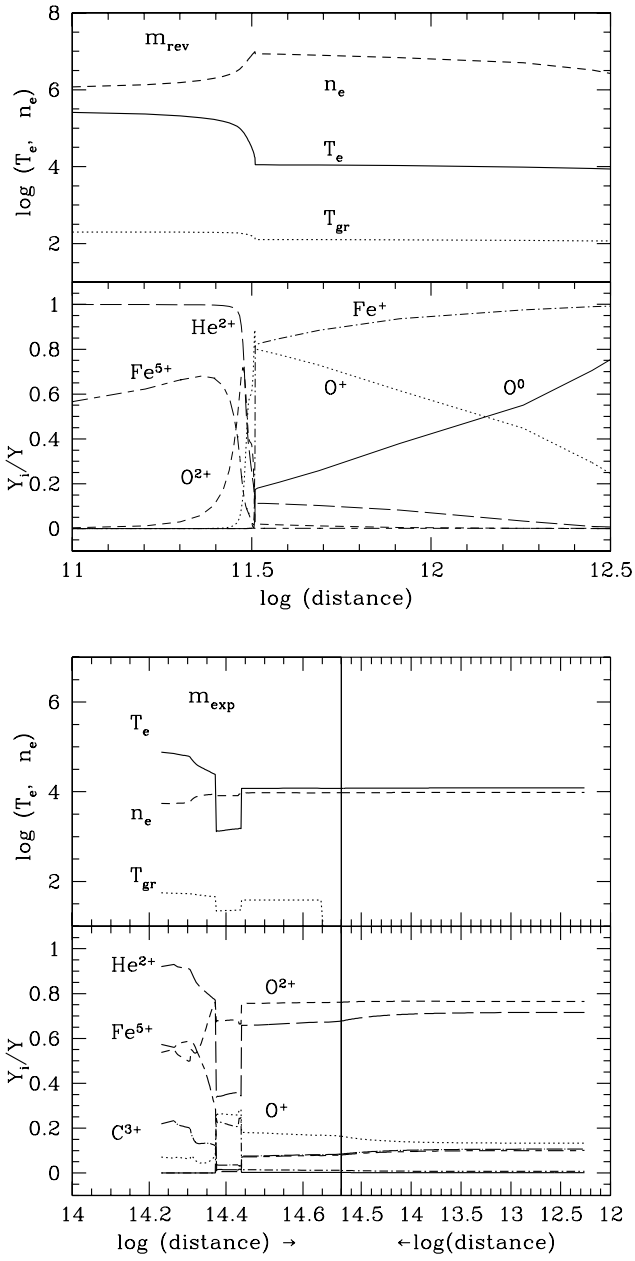

Figure 4.2: The profile of the electron temperature, of the electron density and of the temperature of the grains (a_{gr}=0.2 μm) downstream of the reverse (top diagram) and of the expanding shock front (bottom diagram). The stratification of the most significant ions is shown in the bottom panels. For both diagrams, shock front is on the left side.

Table 4.2: The radio-mm data references.

ν [GHz]	Flux [mJy]	Ref.
0.843	10.6±1.2	Jones (1985)
1.4	13.5	Siodmiak & Tylenda (2001)
1.6	15	Taylor & Seaquist (1984)
2.7	33±4	Purton et al. (1982)
4.885	50	Aaquist & Kwok (1990)
5.0	46±10	Purton et al. (1982)
5.0	50	Siodmiak & Tylenda (2001)
6.2	65±10	Purton et al. (1982)
8.1	82±7	Purton et al. (1982)
8.31	73.5	Bastian (1992)
8.44	65.3±3.3	Seaquist et al. (1993)
8.9	90±15	Purton et al. (1982)
14.5	90±10	Purton et al. (1982)
14.965	72	Aaquist & Kwok (1991)
90.0	127±53	Purton et al. (1982)
231	55±16	Ivison et al. (1995)

Table 4.3: The infrared data references.

λ [μm] (phot. band)	Flux [Jy]*	Ref.
1.20 (J), 1.64 (H), 2.22 (K), 3.8 (L')	1.55 - 2.1 - 4.8 - 7.1	Allen (1983)
8.28, 12.13, 14.65	7.454 - 11.93 - 14.67	MSX6C PSC, Egan et al.[b] (2003)
1.235 (J*), 1.662 (H*), 2.159 (K*)	0.0312 - 0.115 - 0.594	Ramos-Larios & Phillips[c] (2005)
0.9 (I_C), 1.25 (J), 2.22 (K)	0.0167 - 0.034 - 0.741	DENISE[d]
12, 25, 60	18.13 - 28.16 - 5.75	IRAS PSC[e]
34.6	16.6	He et al. (2005)[f]
2.5-45.5 SWS	- - -	ISO IDA[g]

* 2MASS Photometric System; a: out of Allen, expressed in 10^{14} erg s^{-1} cm^{-2} A^{-1}; b: The Midcourse Space Experiment Point Source Catalog Version 2.3 (October 2003); c: 2MASS NIR measurements of galactic planetary nebulae; d: The DENIS consortium (third release - Sept.2005); e: IRAS Catalogue of Point Sources, Version 2.0 (IPAC 1986); f: The 35 μm absorption line towards 1612 MHz masers; g: ISO Data Archive (@ http://www.iso.vilspa.esa.es).

4.3.1 The line ratios

The spectra derived from Allen's observations are shown in Table 4.4, col. 2; the models calculated for the reverse (m_{rev}) and for the expanding shock (m_{exp}) are presented in cols. 3 and 4, respectively; their weighted sum appears in col. 5.

The input parameters of the models appear in Table 4.5. They are constrained by the observations, namely, the shock velocity V_s is roughly determined by the FWHM of the line profiles (in agreement with Allen 1983); the preshock density, n_0, is constrained by the slope of the radio continuum and by the ratios of characteristic lines (e.g. [SII] 6717/6731); the preshock magnetic field, B_0, is characteristic of symbiotic systems (Crocker et al. 2001); the stellar temperature, T_*, is taken from the analysis of Allen (1983); the ionization parameter, U, is determined phenomenologically; the geometrical thickness, D, is

constrained by the radio continuum slope and by the ratios of the lines to Hβ ; eventually, the relative abundances of the elements are determined by the line ratios. Unfortunately, in the present case, the dust-to-gas ratio *(d/g)* cannot be directly determined because the bump of the dust reprocessed radiation is covered by the emission from the summed dust shell and Mira black body fluxes.

The line ratios calculated by m_{rev} and m_{exp} are summed up adopting the weights w shown in Table 4.5, last row. They are the same as those adopted in Fig. 4.3 to suite the continuum SED.

The observed line ratios are reproduced by the summed model within a factor of 2, except a few lines which are badly fitted, e.g. [NI] 5200, since they have a particularly low critical density for collisional deexcitation and are very faint at the relatively high density of m_{rev} and m_{exp}. We suggest that the observed HeII 1640/ Hβ may be blended with the rather high OIII 1640/Hβ ratio, whose calculated value is > 3. An improved fit of the [OIII] 5007/[OIII] 4363 ratio could result from a reverse shock with lower densities, which are however incompatible with the radio SED: as a matter of fact the [OII] 3727 and [OIII] 5007 lines are mostly emitted from the expanding shock.

Model m_{rev} shows N/H and O/H slightly higher than solar by factors of 1.7 and 1.3 respectively, while Fe is strongly depleted both in m_{rev} by a factor of 10 and in m_{exp} by a factor of 5: this is not surprising as iron, a refractory element, is easily trapped into dust grains.

In Fig. 4.2 we present the profile of the electron density, electron temperature and the fractional abundances of the most significant ions throughout the nebula downstream of the reverse (left diagram) and expanding shock (right diagram). It is worth noticing that model m_{rev} is matter-bound: this is characteristic of the interbinary symbiotic nebulae, where the geometrical thickness is constricted by the colliding wind region.

4.3.2 The continuum SED

In Fig. 4.3 we present the modelling of the continuum. The SED is the result of the emitting contributions from the cool and hot stars, as well as of the fluxes from the dust shells and of the bremsstrahlung from the shocked nebulae downstream of the shock fronts, which emit the UV and optical line spectra.
The bremsstrahlung from the nebulæ shows two main peaks. At higher frequencies the continuum is emitted from gas collisionally heated by the shock at relatively high temperatures: the peak frequency depends therefore on the shock velocity. The peak at $\sim 10^{14}$Hz, on the other hand, depends on the volume of gas at temperatures of $\sim$ 1-3 10^4 K, which is heated and ionized mainly by the photoionizing flux: the peak frequency is therefore more sensitive to the radiation parameters, T_* and U. Also a contribution to the SED by synchrotron radiation, not so exotic in objects where shocks are at work, can not be ruled out (Fig 4.3).
As a matter of fact, without more constraining data it remains puzzling to determine whether the measured flux densities at $\sim 10^{11}$Hz are dominated by synchrotron, by bremsstrahlung or by thermal emission from cold dust, also

Table 4.4: The fluxes of the UV and optical spectral lines, normalized to Hβ .

line	obs[a]	m_{rev}	m_{exp}	av$_{m_{rev}+m_{exp}}$
CIV 1549	18.78	19.7	27.3	22
HeII 1640	7.88[b]	1.1	5.2	2.6
NIII] 1749	5.15	2.24	2.	2.2
CIII] 1909	27.2	9.3	18.	13.0
[NeV]+OIII 3425	4.24	0.13[c]	0.13[c]	0.22[c]
[FeVI] 3662	0.006	0.0043	0.0047	0.0044
[OII]+ 3727	0.576	0.04	2.6	0.99
[NeIII] 3869+	2.12	1.5	2.2	1.78
[SII]+ 4070	0.18	0.38	0.08	0.27
Hγ	0.42	0.44	0.45	0.44
[OIII] 4363	0.61	1.29	0.80	1.1
HeI 4471	0.056	0.036	0.023	0.044
[FeIII] 4658	0.015	0.01	0.015	0.012
HeII 4686	0.55	0.16	0.76	0.4
Hβ 4861	1	1	1	1
[ArIV] 4711	0.02	0.0013	0.13	0.049
[NeIV]+ 4714	0.11	0.14	0.08	0.12
[ArIV] 4740	0.097	0.011	0.15	0.063
[OIII[5007+	19.1	2.	35.	14.2
[FeVI] 5146	0.017	0.007	0.03	0.016
[FeII] 5159	0.03	0.039	0.0017	0.025
[FeVI] 5176	0.03	0.018	0.033	0.023
[ArIII]5191	0.005	0.017	0.012	0.015
[NI] 5199	0.006	0.0002	0.0005	0.0003
[FeVI] 5335	0.011	0.0018	0.017	0.008
[NII] 5755	0.15	0.43	0.04	0.28
HeI 5876	0.11	0.18	0.07	0.14
[FeVII] 6087	0.12	0.002	0.005	0.003
[OI] 6300+	0.4	0.47	0.013	0.3
[SIII] 6312	0.08	0.14	0.13	0.136
[NII] 6548+	1.0	0.2	1.4	0.63
Hα	4.5	3.5	3.1	3.4
[SII] 6717	0.02	0.002	0.057	0.022
[SII] 6731	0.039	0.0035	0.10	0.039
[ArIII] 7136	0.24	0.14	0.24	0.14
[ArIV] 7170	0.007	0.023	0.009	0.018
[OII] 7319+	0.55	2.6	0.48	1.8
[FeII] 8617	0.0027	0.0027	0.0011	0.002
[SIII] 9069	0.33	0.06	1.3	0.5
Hβ abs.[d]	-	1.13	0.0075	-

a: observed values from Allen (1983);
b: blended with OIII 1640;
c: the calculated flux refers only to [NeV];
d: Hβ absolute flux calculated at the nebulæ [erg cm^{-2} s^{-1}].

taking into account that emission from either mechanism could fluctuate in response to variable mass-loss episodes.

The radio continuum

In an important paper on radio emission of mass-losing stars, Wright & Barlow's (1975) presented an analytic study of the spectral flux distribution produced by completely ionized, uniform, spherically symmetric mass loss flow in early type star. Though under idealized hypothesis, they tried to interpret the radio data

for some recently observed objects in the light of thermal free-free emission which would result in a power-law spectrum $S_\nu \propto \nu^{0.6}$. They also discussed deviations from the ideal treatment caused by e.g., non-uniform mass-loss rates or by the actual ionization structure of the emitting circumstellar envelope.

In effect, the Purton's radio survey (Purton 1982) pointed out that there were some objects (with a high incidence of SS) whose radio spectral index was systematically steeper than α=0.6 (in the range 0.8-1.5), therefore implying an envelope density profile quite far from the inverse-square one assumed by Wright & Barlow (1975). In any event, no attempt was made by Purton to fit a detailed physical model to the data.

Few years later, Seaquist et al. (1984) and Taylor & Seaquist (1984) presented a model (hereafter STB model) which explained the H1-36 radio properties in light of the mounting evidence for the binary nature of symbiotic stars: by assuming that the emitting region arises from the portion of the cool component wind photoionized by the WD, they performed a fit to the Purton's data with a least-square criterion as a function of the so called X parameter (related to the shape of the ionized nebula), of the turnover frequency ν_t, and of the flux density at ν_t. The model was successful in reproducing many of the observed properties of radio symbiotics, such as the spectral index, the spectral turnover, the correlation between the radio emission and the spectral type of the cool component. Nonetheless, it was soon recognized that the actual radio sources were more complex than those assumed in the STB model, and that any derived

Table 4.5: The model input parameters.

parameter	m_{rev}	m_{exp}
V_s $(km\,s^{-1})$	140	70
n_0 (cm^{-3})	2.5e5	3.5e3
B_0 (gauss)	1e-3	1e-3
T_* (K)	1.5e5	1.5e5
U	2e-3	2.5e-3
D (cm)	2.8e12	1e15
d/g	1e-14	1e-14
He/H	0.1	0.1
C/H	3.3e-4	3.3e-4
N/H	1.5e-4	9.1e-5
O/H	8.6e-4	6.6e-4
Ne/H	8.3e-5	8.3e-5
Mg/H	2.6e-5	2.6e-5
Si/H	3.3e-5	3.3e-5
S/H	1.6e-5	1.6e-5
Ar/H	6.3e-6	6.3e-6
Fe/H	3.2e-6	6.2e-6
log w	-11.05	-9.1

physical property had to be treated with particular caution. Furthermore, more recent observations by Seaquist & Taylor (1993) at millimeter and submillimeter wavelengths showed that several objects might differ considerably from the STB model.
As with regards to the specific case of H1-36, the STB model failed e.g. to reproduce the 843MHz flux presented by Jones (1985). Moreover, the assumed density profile appeared too simplistic: even the two-layer model discussed by Costa & de Freitas Pacheco (1994) referring to the inner structure of the emitting nebulae cannot be considered adequate since SS have such important density gradients that do not even allow to adopt unique values for electron temperature and densities.
Unfortunately, so far there are no papers which try to interpret the radio spectra taking into account the possibility of any outflow from the compact star.

In the following we fit the existing radio-mm data we have presented in Table 4.3 and Fig. 4.1 - bottom panel, within a colliding-wind scenario. Our approach is shown to be self-consistent with the continuum profile of the system along the whole electromagnetic range, as well as cross-checked by the spectral line emission.

Three main slopes are seen between 10^8 and 10^{11} Hz.
The flattest one, with a spectral index of 0.75, can be explained by synchrotron radiation created by the Fermi mechanism at the shock front (Bell 1978a,b): a cut-off at the lower limit is given by Ginzburg & Syrovatskii (1965) ($\nu \sim 20$ N_e/B, with N_e $\sim 10^6$ cm^{-3} and B=10^{-3} Gauss at the shock front), explaining the SED profile at $\sim 10^{11}$Hz. The unabsorbed bremsstrahlung explains the slope of the SED between about 10^{10} and 10^{11} Hz. At $\nu < 10^{10}$ Hz the bremsstrahlung shows the high slopes which are produced by free-free self-absorption. The optical depth $\tau = 8.24\,10^{-2} T^{-1.35} \nu^{-2.1} E$ (where T is to be measured in K, ν in GHz and E, the so called *emission measure* $E = \int n_e n^+ ds$, in $\mathrm{cm}^{-6} pc$ - Osterbrock 1988) is low for gas at relatively high temperatures: however, in the downstream nebulae of H1-36 we found large regions (i.e. large ds) of gas at T $\sim 10^4$ K (Fig. 4.2) which make $\tau > 1$. The other parameters which vary from slab to slab are the density, which is calculated through the compression equation, and the geometric thickness of the slab. At this point we would like to emphasize that the calculation of the density profile is not assumed *a priori* in our models accounting for shocks, but consistently calculated across the whole emitting nebula (Sect. 4.3.1). In this case, the thinner the slab the better the approximation of the calculated spectra. Therefore the densities must be sufficiently high to give a sensible absorption. The turnover corresponds to different frequencies for different slabs and the final bremsstrahlung results from the integrated flux throughout the whole length of the nebula. The actual turnover frequency ν_t indicates then the transition from the optically thin to the optically thick case.

Eventually, it is worth highlighting that higher densities generally refer to the nebula downstream of the shock front facing the WD between the stars (model m_{rev}), while the densities downstream of the expanding shock (model m_{exp}) correspond to an optically thin nebula. Therefore, the radio spectrum

observed in SS may be emitted by the gas between the stars, with an important, more increasing contribution from the expanding nebula at lower frequencies. Interestingly, this agrees with the variable size of the radio nebula, which becomes gradually larger at lower frequencies (i.e. 0.6 arcsec at λ=2 cm and 5 arcsec at λ=6 cm - Taylor 1988).

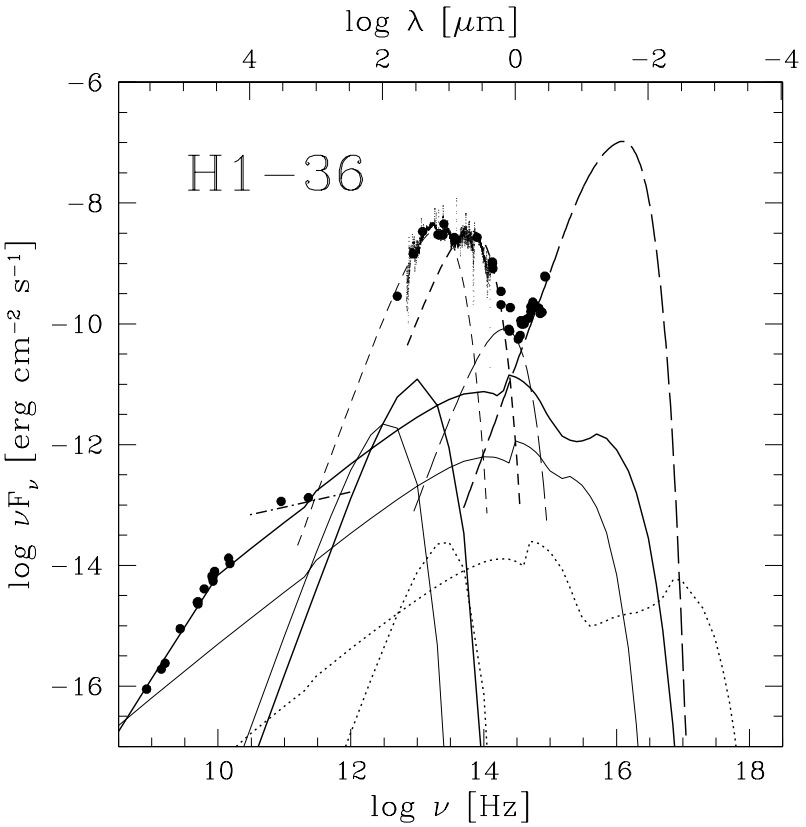

Figure 4.3: The H1-36 continuum SED, from radio to UV. Thin short-dashed line: 250 K dust shell; thick short-dashed line: 800 K dust shell; thin long-dashed line: Mira (2500 K) stellar component; thick long-dashed line: hot stellar component; dot-dashed line: synchrotron; thin solid line: m_{exp}; thick solid line: m_{rev} (see Table 4.5 for details about the model input parameters); dotted line: the *jet* (see Sect. 4.3.3). Notice that for m_{rev}, m_{exp} and the *jet* models there are two curves: one is the bremsstrahlung emission from radio to X-rays, the other represents the consistently calculated reprocessed radiation by dust in the IR.

The IR continuum

One of the most intriguing aspect of the symbiotic phenomenon in D types pertains to the dusty environment. As a matter of fact, these systems show a broad IR excess which has been attributed to emission from circumstellar dust since the first IR surveys. Early observations already showed that in D type objects the dust excesses have colour temperatures near 1000 K (Feast et al. 1983); nevertheless today, thanks to the IR astronomy developments, it has been realized that it is difficult to explain the observed IR spectrum by a single temperature. Theoretical models too, confirmed that different "dust" temperatures should be combined in order to reproduce the NIR-MIR data (e.g. Anandarao et al. 1988, Schild et al. 2001, Angeloni et al. 2009, in preparation).

In H1-36, the temperature of the dust shells is derived by modelling the IR data we collected which, quite surprisingly, agree in the overlapping frequency range: this proves that variability, even if present as in all symbiotic IR spectra, has not been as large as to substantially modify the dust continuum emission and then invalidate our results (see Sect. 4.2, Fig. 4.1 and Table 4.3).
It is worth noticing that the cooling rate is very strong at the densities typical of the region closer to the shock front downstream, which corresponds to the maximum temperature of dust: this implies that the flux from the shell corresponds mainly to the maximum temperature of the grains and can be modelled by a black body (bb). As a matter of fact, Fig. 4.3 shows that the whole IR continuum can be well explained by the combination of two bb curves, corresponding to temperatures of 800 K and 250 K. By comparing the models with the data we obtain the η factors: they depend on the radius of the dust shell, r, and on the distance of the system to Earth d $(\eta = r^2/d^2)$, being the fluxes calculated at the nebula and the data, obviously, measured at Earth. Adopting d=4.5 kpc (Allen 1983), we find r= 4.4 10^{14} cm and 4.7 10^{15} cm for the shells at 800 K and 250 K, respectively. Both the derived inner shell temperature and radius are in good agreement with what found by Allen (1983), who suggested that the cool component is heavily embedded in its own dust shell, specifically the hot shell is circumstellar.
An interesting issue is related to the outer shells: if we relied on the Allen's proposed binary separation (3 10^{16} cm), then even this shell would be circumstellar, namely, well comprised within the system. Allen himself admitted such a large binary separation was striking, though; moreover, he stated that, translated in an angular separation of $\sim$0.5 arcsec according to the suggested distance of 4.5 kpc, this binary separation would have been large enough to be resolved by careful infrared astrometry, as well as by high-resolution optical and radio observations. As a matter of fact, few year later Taylor (1988) succeed in resolving the radio nebula. Conversely, Bhatt & Sagar (1991) failed in detecting any nebulosity in the optical emission lines, arguing that if this was actually present, it should be smaller than $\sim$2 arcsec. Corradi et al. (1999) finally resolved the optical nebula and found out that it appeared also in a continuum image, therefore suggesting that it might be a reflection nebula.

At this point, we would like to stress that the unusual large size of the

system has been constrained so far by observations of gaseous emitting nebulæ, and that the binary stellar components have never been resolved: this might be a clue that the actual binary separation is overestimated, therefore implying that the outer shell we found directly by modelling the IR data may even be circumbinary, surrounding both the stars. This would not be so out of ordinary for D-type SS, since this dichotomy in the dust shell distribution (with a hot shell being circumstellar, and a cool one circumbinary) has been confirmed by recent studies (Angeloni et al. 2009, in preparation).

H1-36 appears as an extreme SS: only further observations at higher spatial resolution and in different spectral ranges will be able to investigate the actual size and physical properties of the dust and gas nebulæ.

The UV continuum

For sake of completeness we would like to note that longward of $log\ \nu$=14.5 the UV data are well fitted by a T_*=150.000 K bb curve (Fig. 4.3), in agreement with the Allen's (1983) derived hot star temperature: the WD flux dominates in that range over the bremsstrahlung emission. However, it is worth reminding that between $log\ \nu \sim 16.4$ and $log\ \nu \sim 17.7$ absorption of X-rays is quite strong, therefore implying that X-rays, if present, would be soft and mainly due to bremsstrahlung emission arising from the high-velocity component we deduce from the IR line features (see Sect. 4.3.1).

4.3.3 A jet in H1-36?

In a previous analysis of ISO SS infrared spectra (see previous chapter, or Angeloni et al. 2007a - hereafter Paper I), we found broad emission lines, indicating high-velocity components in many objects of the sample (Paper I - Fig. 1, Table 4). In H1-36, the FWHM of these line profiles correspond to velocities of 500 $km\,s^{-1}$; we remind that high-velocity components were not observed in the optical-UV spectra presented by Allen (1983) which showed FWHM $\leq$ 200 $km\,s^{-1}$. Consequently, since the ISO-SWS spectrum shows several highly-ionized and broad Ne and O lines, not compatible with the physical models derived by the optical-UV spectra, we decide to include these new results in order to draw out an as most large and consistent as possible interpretation. We then calculated a further model, characterized by higher shock velocities and lower densities, able to reproduce the observed IR lines without making the previous fit worse.

In Paper I we found that, in H1-36, the [NeVI] 7.65 μm line dominates, followed by the [OIV] 25.89 μm, [NeIII] 15.55 μm, [NeV] 24.31 μm, and [NeV] 14.32 μm lines.
The model calculated with V_s=500 $km\,s^{-1}$, n_0=10^4 cm^{-3}, U=8, and D=10^{16} cm well reproduces the observed intensity ratio: in fact we obtain [NeII]12.8 / [NeVI]7.65=0, [NeV]14.32/[NeVI]7.65=0.47, [NeIII]15.55/[NeVI]7.65=1.3e-4, and [NeV]24.31/[NeVI]7.65=0.05, in agreement with the observed upper limits, respectively [NeV]14.32/[NeVI]7.65<0.5, [NeIII]15.55/[NeVI]7.65<0.2 and

[NeV]24.31/[NeVI]<0.15. Moreover, the same model represents a non negligible contribution only on the high ionization level lines, particularly to CIV 1549, [NeV] 3425, [FeII]6087, and a relatively strong contribution to HeII 1640.

We can now calculate the distance of this high-velocity structure from the WD. A WD T_*=150.000 K corresponds to a ionizing photon flux of 4 10^{26} photons cm^{-2} s^{-1}: this flux is related to the ionization parameter and to the gas number density, in the radiation dominated zone, by $F_\nu(R_{WD}/r_j)^2 = Unc$. Adopting an average density of n=10^5 cm^{-3} after compression, and a WD radius of 10^9 cm, we obtain log η = -16.2. This value allows to place the bremsstrahlung emission from this component in the continuum SED diagram of Fig. 4.3, and to verify that its contribution to the radio spectrum is negligible when compared to the bremsstrahlung from the nebulæ. Conversely, on the high-energy side of the spectrum, it is interesting to notice that V_s=500 $km\,s^{-1}$ would correspond to a temperature in the immediate postshock region of ∼3.6 10^6 K, hence indicating that a soft X-ray emission may be actually present in H1-36.

Eventually, after this consistent analysis, we would like to stress the possibility that this high-velocity component in H1-36 is a jet-like feature. This suggestion, if confirmed, would be fascinating, as only recently it has been recognizing that SS are a class of jet-producing objects. Furthermore, the two SS X-ray jets that have been discovered to date (R Aqr, Nichols et al. 2007 and CH Cyg, Karovska et al. 2007) both show a X-ray structure more extended than their radio ones (Sokoloski et al. 2006). This would explain why this 10^{16} cm jet has not been seen in the radio image (with comparable angular resolution) and drive us to indicate SS as promising X-ray targets.

4.4 Concluding remarks

In this study we have analyzed the spectra of D-type SS H1-36 within a colliding-wind theoretical framework. After having constrained the relative physical conditions by modelling more than 40 emission lines from radio to UV, we have been able to confidently explain the continuum SED by taking into account all the emitting contributions arising from both the stars, the dust shells and the gaseous nebulæ. A comprehensive model of the radio spectra allowed to reproduce the different slopes of the radio profile and the turnover frequency, as well as the size of the observed nebulæ at several frequencies in light of different contribution from the expanding and reverse shocks. The IR continuum unveiled the presence of two dust shells with characteristic radii and temperatures: the inner shell is confirmed to embed the Mira star, while the outer one may be *circumbinary*, i.e. surrounds the whole binary system. We believe that the presence of multiple dust shells is not a unique characteristic of H1-36, but it may somehow represent a distinctive feature of D-type SS. Furthermore, the broad profiles of the IR lines directed us to investigate whether a high-velocity component (perhaps an X-ray jet) may be present. This insight led us to indicate H1-36 as a promising X-ray target and represents a further support to the emerging interpretation of SS as a class of jet-producing objects. We then

encourage new observations and studies which consistently take into account the complex nature of SS throughout the whole electromagnetic spectrum.

5

The symbiotic star CH Cyg I. An analysis of the shocked nebulae at different epochs

This chapter has been recently submitted to
Astronomische Nachrichten - arXiv:0807.1480
by *Contini, M.; Angeloni, R.; Rafanelli, P.*

5.1 Introduction

The symbiotic star (SS) CH Cygni (CH Cyg) has been observed since the late '80s of the XIX century. It was identified as an anonymous red semiregular variable by Gaposchkin's 1952 analysis of Harvard patrol plates, and classified as a M6-M7 spectrum star with a 90-100 day period and about one-magnitude amplitude. This classification seemed to be suitable until 1963 when a hot blue continuum appeared, along with a late-type spectrum and emission lines of H, He, [FeII] and [CaII], evidence of a composite nature. This drove Deutsch (1964) to recognize in CH Cyg the brightest SS at visual wavelengths. Since then, active and quiescent phases have been alternating without a predictable trend.

At a distance of 270±66 pc (according to the Hipparcos parallax measurements - Munari et al. 1997) CH Cyg is one of the most studied, yet poorly understood SSs. It has been observed in the last thirty years both photometrically and spectroscopically from radio to X-ray wavelengths (Kenyon 2001).

The basic configuration of the CH Cyg system is still debated, despite the large amount of multi frequency observations carried out since the first recorded symbiotic activity. In particular, it is discussed whether it is a binary or a triple star, and, in the latter case, whether composed of a red giant/white dwarf pair with a G star companion (Hinkle et al. 1993) or a red giant/white dwarf pair with an additional red giant companion (Skopal et al. 1996). The explanation of the total hot component luminosity in a binary star scenario might be a crucial problem: specifically, the suggested binary orbital parameters

(e.g. Mikolajewski et al. 1992) would imply an accretion rate onto the white dwarf not in agreement with that requested by the observed hot component luminosity. On the other hand, adopting the binary star scenario the orbital solution of the triple model (Hinkle et al. 1993) would require a low inclination angle. This is in contrast with the jet appearing in the plane of the sky, implying an accretion disk and/or an orbital plane virtually edge-on. Furthermore, the low inclination implied by Hinkle et al. (1993) would result in an unrealistically low mass (0.2 $M_{\odot}$) white dwarf. Finally, the similarity of the 756 day period of CH Cyg with non-radial pulsations in a few semi-regular variables drove Schmidt et al. (2006) to interpret this periodic trend more as a non-radial pulsation of the cool component rather than a real orbital period.

Several theoretical papers have appeared presenting SSs as colliding-wind (CW) binary systems (e.g. Kenny & Taylor 2005). The observational evidence that actually both the component stars of a SS lose mass through strong stellar winds (Nussbaumer et al. 1995), along with the presence in CH Cyg of radio, optical and X-ray jets (Karovska et al. 2007), have confirmed the importance of shocks for a real understanding of such outstanding system.

CH Cyg is characterized by the presence of an eruptive white dwarf, showing episodes of accretion fed by the high-density wind coming from the M star, and of wind-wind interaction leading to shock waves. The nebulae downstream of the shock fronts show the spectroscopic marks of a turbulent kinematics, resulting in an inhomogeneous and highly disrupted envelope.

In this chapter we review the recent history of CH Cyg, in the light of a colliding wind scenario (e.g. Girard & Willson 1987, Kenny & Taylor 2005) that has been used to explain many SSs (e.g. Formiggini, Contini, & Leibowitz 1995, Contini 1997, Contini & Formiggini 1999) and recently updated including a detailed analysis of dust features (Angeloni et al. 2007a,b,c).

We interpret the observational data throughout both the active and quiescent phases, from the 1978 great outburst up to date, with the aim of investigating the physical and morphological conditions of the system by modelling the line and continuum spectra emitted from the different nebulae.

We adopt the binary scenario, considering the $\sim$ 756 day period as due to the giant pulsation mode, and the $\sim$ 15 year period as the actual orbital period.

Following the method used in previous SS investigations, we analyze the continuum spectral energy distribution (SED) in different epochs, instead of the light curve through the years. At each epoch we model the data collected from radio to X-ray constraining the results by the analysis of the line spectra. The continuum accounts for bremsstrahlung and dust reprocessed radiation from the shocked nebulae, radiation from dust shells, as well as radiation from the stars. Our method is particularly suitable for disentangling the multiple contributions of gas and dust in different conditions at different phases.

We focus on the *nebulae* within the shocked wind-wind interaction regions and on the *shells* ejected by the giant star, constraining the models by the observed *absolute* fluxes.

A short summary of observational history of CH Cyg is presented in Sect. 5.2. The next sections are devoted to the analysis of the individual active and

quiescent phases. As CH Cyg has not been observed regularly in the different wavelength ranges, except of the optical one, the SED profiles in some epochs present some data gaps: for instance, there are no UV and X-ray observations for the 1988-1990 quiescent phase, nor mid-IR data for the 1998-2000 active phase. This led us to focus on specific physical processes in each phase: the basic models which result by disentangling the different contributions to the SEDs and to the line ratios at different days during the active phase 1978-87 are presented in Sect. 5.3; in Sect.5.4, different types of IR obscurations occurred during the 1988-90 quiescent phase are indicated; near-UV and IR variability during the 1991-95 active phase are discussed in Sect. 5.5, while Sect. 5.6 (1996-97 quiescent phase) deals with the complex nature of the radio emission. The very expanded nebulae and the X-ray emission are modelled throughout the 1998-2000 latest active phase (Sect.5.7) up to date (Sect. 5.8). Concluding remarks and a summary of the results are presented in Sect. 5.9.

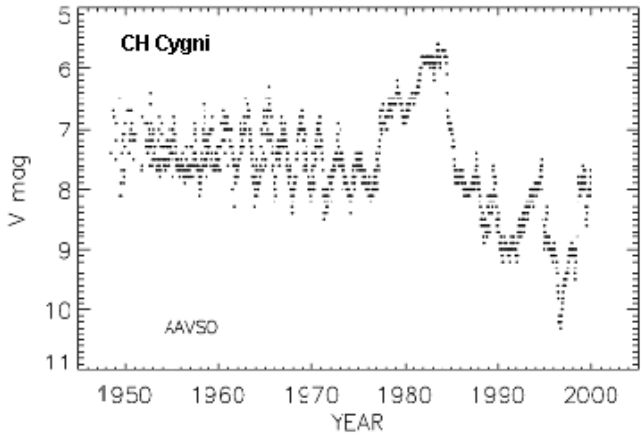

Figure 5.1: AAVSO light curve (10-day means of observations) of CH Cyg from 1948 to 2000.

5.2 Observational progress

The symbiotic classification was introduced on the basis of optical spectral features, however, a real understanding of SSs, and CH Cyg in particular, has been possible only by space-based astronomy.

A key-role was played by the long-lived IUE, which opened the UV window allowing to monitor the temporal evolution of many emission lines arising from the nebulae and the continuum coming from the hot star. This great effort revealed that CH Cyg is much more complex than thought before. Its puzzling nature triggered a series of new radio observations (e.g. Taylor et al. 1985, 1986) attempting to understand the actual origin of the nebular emission and

to constrain a self-consistent view in the light of the most accepted scenario at the time. It was concluded that the symbiotic behavior was due to the dense cool wind photoionized by the hot star radiation (e.g. Taylor et al. 1988).

The optical and near IR spectrophotometry throughout the years (e.g. Taranova & Yudin 1988, 1992; Munari et al. 1996; Skopal et al. 1996, 1997, 2000, 2002, 2004, 2007) have allowed to follow small changes in the emitting properties of CH Cyg, without leading to a substantial breakthrough.

Unexpected results came from the first X-ray observations (e.g. Leahy & Taylor 1987) that for the first time made clear that the energetic of the whole system was hard to explain in term of standard photoionization models. It became evident that shocks, and in general hydrodynamic phenomena (e.g. fluid instabilities), play a primary role in shaping the energy distribution along the whole spectral interval. Further observational evidence of stellar wind collision in CH Cyg derived from the most recent X-rays observations (Ezuka et al. 1997, Galloway & Sokoloski 2004, etc).

The IR spectral range is not yet fully explored. It was suggested that "symbiotic dust" carries as much information as symbiotic emission lines (Angeloni et al. 2007c), and the unique CH Cyg mid-IR spectra recorded by the ISO satellite (Schild et al. 1999) complicated furthermore the system overall picture. Multiple dust shells, mixed grain chemistry, equilibrium between grain formation and destruction processes in the turbulent nebulae (Angeloni et al. 2007a) are worth investigating with the new era of mm-IR facilities, such as ALMA and Herschel.

Fig. 5.1 shows the light curve of CH Cyg throughout many years. The first ever recorded symbiotic activity of CH Cyg started in September 1963 and was over by August 1965, followed by an other period of increased activity in the years 1967-1970. Then, CH Cyg experienced a dramatic eruption in 1978 when it became as bright as to be visible by unaided eye (visual mag. 5.6). This great outburst ended in 1986 with the emission of bipolar radio and optical jets (Solf 1987) and by a decline of about 2.5 visual magnitudes (Taylor et al. 1986). After 1986, the decline in magnitude continued, even though not regular nor smooth. Meanwhile, shorter and dimmer outbursts (1991 - 1995, 1998 - 2000) have been accompanying the fading trend (Fig. 5.1). Between these periods of activity the spectrum has exhibited almost exclusively red giant characteristics, and U B V light curves with significant variations at a level of about 1.5 mag.

Since the beginning of the 2000, CH Cyg persists in a quiescent phase at rather bright magnitude, despite a 2 mag decline in the U B V light curves during the 2006 June-December period (Skopal et al. 2007). An apparently anomalous extreme IR fading has been recently pointed out by Taranova & Shenavrin (2007).

In the Appendix, we present the references to the observational data we collected from the literature. In the quoted works the reader can find the journal of observations, so in the Tables we have indicated only the spectral domain and the year, addressing to the specific reference for any further information or technical detail.

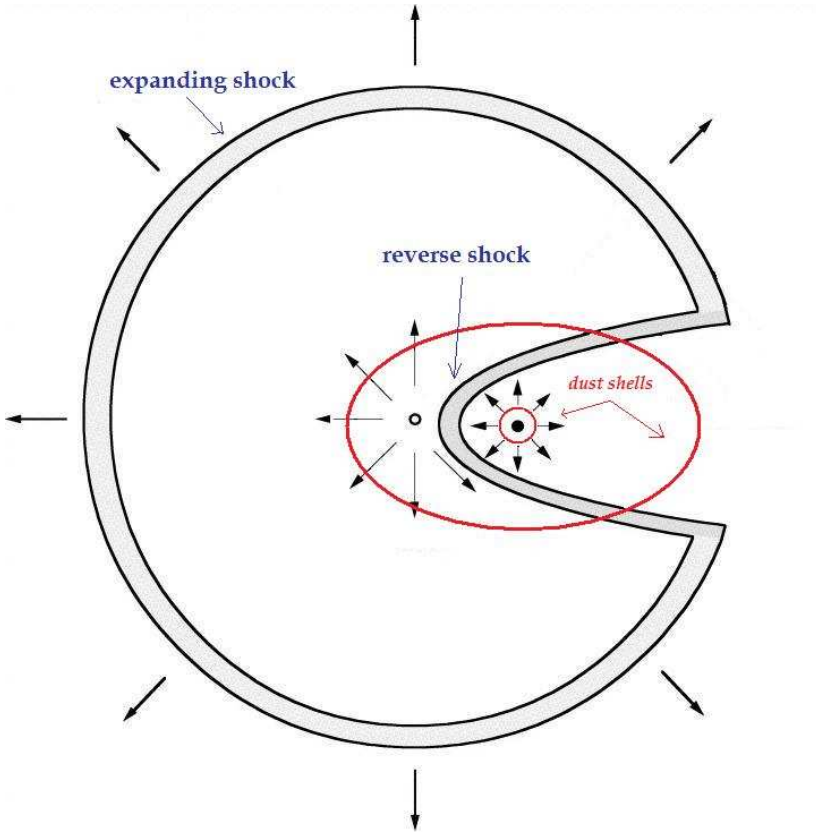

Figure 5.2: A very schematic picture of the CW model and the dust shells (adapted from Kenny & Taylor 2005).

Table 5.1: The models

	$m1_{shell}$	$m2_{shell}$	m^a_{600}	m^a_{1200}	$m1^a_{exp}$	$m2^a_{exp}$	$m3_{exp}$
n_0 (cm^{-3})	1.5e9	2.e9	5.e7	1.e7	1.e5	1.e7	2.e7
$V_s(km\,s^{-1})$	40	60	600	1200	150	100	70
B_0 (gauss)	2.e-3	3.e-3	3.e-3	3.e-3	1.e-3	1.e-3	1.e-3
T_*(K)	1.5e5	1.5e5	1.5e5	1.5e5	3.5e4	3.5e4	3.5e4
U	0.5	1	6	2	0.01	0.001	0.001
D^b (cm)	4.0e14	3.6e13	1.e14	1.e14	5.e15	3.e17	3.e17
d/g^c	4.e-4	4.e-4	4.e-4	4.e-4	4.e-7	4.e-7	4.e-7

[a] radiation dominated (U≠0);
[b] upper limit in radiation-bound models;
[c] by mass.

5.3 1978-1986 active phase: the models

Since the emission lines better constrain the physical properties of a nebula than the continuum, we start by modelling the composite line spectra.

5.3.1 The line spectra

Permitted and forbidden lines were observed along the whole outburst episode. Hack et al. (1988) reported that in quiescence only Hα and Hβ appeared as broad, relatively strong emissions, while the other Balmer lines were faint absorbed and severely blended with the neutral metallic lines. The FW0M of Hβ varied from about 400 $km\,s^{-1}$at the beginning of the outburst to 600-700 $km\,s^{-1}$from early 1978 to the middle 1981; then it remained at 600 $km\,s^{-1}$until mid 1984, increasing to 750 $km\,s^{-1}$in July 1984; in November 1984 and 1985 it reached about 1200 $km\,s^{-1}$. At the same epoch, high resolution UV spectra showed a strong and broad (4000 $km\,s^{-1}$) Lyα emission, never present at previous epochs. The origin of the broad Lyα is discussed by Contini et al. (2007).

Before 1985 the overall spectra did not show strong emission features except [SII] 4068+, [OI] 6300+ in the optical and OI 1304, 1358, SiIII] 1892, CIII] 1909, and MgII 2800 in the UV (Mikolajewska et al. 1988). Emission lines of HeI 5876 were present during the whole outburst except in the beginning. The [OIII] 4363 and 5007 lines appeared only in November 1984, when the outburst was almost over. At the same epoch the UV spectrum indicated that several high ionization emission lines (NV, CIV, SiIV, HeII, OIII]) had appeared (Selvelli & Hack 1985, Mikolajewska et al. 1988). The decrease in density at the end of the outburst was indicated by the ratio of FeII/[FeII] and CIII] 1906/1909.

The UV line ratios suggested electron densities of 10^8-10^{10} cm^{-3}, characteristic of winds close to the stars. On the other hand, the forbidden optical lines indicated densities $< 10^6$ cm^{-3} and were therefore emitted from the nebulae downstream of the expanding shock front.

Since the structure and evolution of the nebulae are very complicated, we adopt three schematic types (Tables 5.1-5.2): 1) downstream of a shock with velocities of 600 - 1200 $km\,s^{-1}$corresponding to the reverse shock, 2) downstream of a shock expanding outwards with velocities ≤ 150 $km\,s^{-1}$which can be either radiation dominated, namely, the nebula is reached by the photoionizing flux from the WD, or shock dominated, i.e. the conditions in the nebula are those corresponding to a pure shock, and 3) downstream of a shock with velocities of $\sim$ 40-60 $km\,s^{-1}$and a high n_0 ($\sim 10^9$ cm^{-3}) propagating outwards the red giant star, which represents its own dust shells. As a matter of fact, the shock velocities of the shells are ≤ 30 $km\,s^{-1}$, but the velocity increases when the shock propagates throughout the circumstellar environment with a negative density gradient.

We can now explain the evolution of the spectra in the 1978-86 active phase. A complete grid of models was run and the models which appear in Table 5.1 were selected from those which best fit the observed line and continuum spectra.

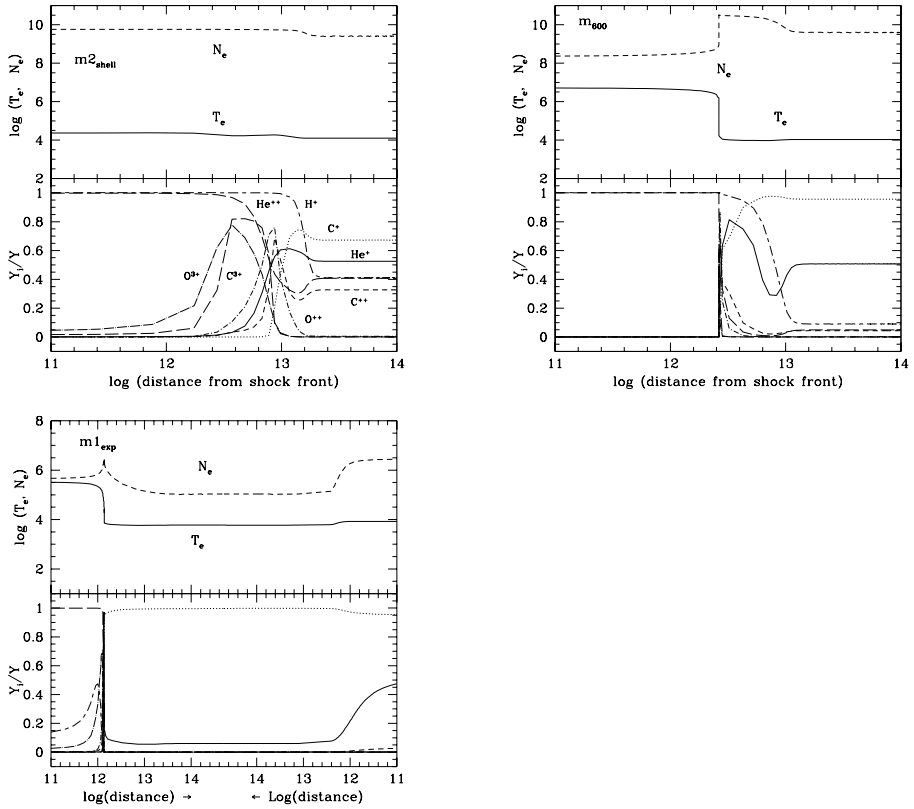

Figure 5.3: Top left diagram: The profile of the electron temperature and electron density throughout the dusty shell for model m2$_{shell}$ is shown in the top of the diagram. The fractional abundance of the most significant ions is shown in the bottom of the diagram. Top right diagram: the same as in the left figure throughout the nebula downstream of the reverse shock corresponding to the model (m$_{600}$). Symbols are the same as in the left diagram. Bottom: the same as in the diagrams on the left for the expanding nebula (m1$_{exp}$). The X axis units are *cm*.

In Fig. 5.3 we show the profile of the electron density, electron temperature and of the fractional abundances of the main ions, which explain the spectra.

In particular, each diagram represents the profile of the physical conditions in the gas downstream of a shock front. We have chosen three very different models. The diagrams correspond to shocked nebulae. The shock front is on the left. The diagrams on top of Fig. 5.3 show the case in which radiation from the WD reaches the very shock front edge. In fact the diagram on top left represents the nebula downstream of a gas+dust shell ejected by the Mira. It is characterized by a high preshock density and a low V_s. The shell propagates towards the WD.

The top right diagram represents the conditions downstream of the reverse shock, facing the WD. The shock velocity is roughly determined by the FW0M of the line profile, while the range of the preshock density is dictated by the line ratios.

The diagram on the bottom of Fig. 5.3 represents the nebula downstream of the shock front propagating outwards the system. The X-axis scale is logarithmic and symmetric with respect to the middle of the nebula in order to show the conditions in both edges with similar high resolution, because, in this case, the shock and the radiation flux act on opposite edges. The physical conditions on the two sides of the nebula (the collisional dominated and the radiation dominated) are bridges by the secondary diffuse radiation from the hot slabs of gas.

The top right diagram of Fig. 5.3 and the left side of the bottom diagram show the characteristics of a shock dominated regime, namely, the temperature of the gas decreases from $T = 1.5\,10^5 (Vs/100\,km\,s^{-1})^2$ immediately behind the shock-front. However, the recombination coefficients are low at high temperatures. Therefore, a long region of high temperature gas survives downstream, emitting, by the way, X-rays and coronal lines. The cooling rate is proportional to n^2. When the temperature reaches about 10^5 K the bulk of the UV and optical lines are emitted leading to a strong decrease of the temperature. The abrupt cooling is followed by the calculation code by reducing the geometrical thickness of the slabs (down to even 10^5 cm) by $(T_{i-1} - T_i)/T_{i-1} < 10$, where T_i and T_{i-1} represent the temperatures of two close slabs. After the drop, the temperature is maintained at about 10^4 K by the primary and secondary radiations. Recall that photoionization alone hardly heats the gas to temperatures $>$ 2-3 10^4 K. In a pure shock case (U=0) the temperatures decreases rapidly below 1000 K and the neutral lines are thus strong.

The situation is different in the shell (top left diagram) with a relatively low temperature even close to the shock front. The radiative ionization rates prevail on the collisional ones which depend strongly on the temperature, so the picture is very similar to that of a pure photoionization regime. The density is very high and the optical thickness of the slabs is high enough to reduce the primary and secondary fluxes at a certain distance from the shock front. The gas therefore recombines. The case presented for the shell is matter-bound due to fragmentation at the shock front.

Spectra from the reverse shock

As mentioned before, in the epoch corresponding to the outburst the FWHM of the Balmer lines evolve from 400 to 1200 $km\,s^{-1}$. These lines are emitted from the nebula downstream of the reverse shock bounding the wind-wind collision region between the stars (Contini 1997, Angeloni et al. 2007a). Model m_{600} is adopted to represent the high velocity shock: it shows relatively high Hβ , HeII and HeI line ratios (Table 5.2).

The FWHM of the broad line profiles suggests the range of the shock velocity V_s. High velocities are characteristic of the reverse shock between the stars, a high n_0 is dictated by the range of densities in the star atmosphere.

Recall that the temperature in the immediate post-shock region is $\propto V_s^2$, so the temperatures are high ($\geq$ 2.4 10^6 K) for $V_s \geq$ 400 $km\,s^{-1}$, recombination coefficients are low, and even compression (n/n_0) downstream is low close to the shock front, because the densities would correspond only to $\sim 4\ n_0$ (*the adiabatic jump*). The radiation flux related to the H and He lines and the continuum can be as strong as to be observable only at temperatures $\leq 10^6$ K. The densities play a dominant role in the cooling rate ($\propto n^2$, where n is the density) in order to recover those temperatures downstream of a strong shock. In fact, the density must be high enough ($n_0 \geq 10^7\ cm^{-3}$) to reduce the temperature to T$\leq 10^6$ K within the nebula downstream of the reverse shock. This nebula therefore should have a geometrical thickness D smaller than the binary separation (10^{13} - 10^{14} cm).

This shows that V_s, n_0, and D are the main input parameters constraining the choice of the model. Moreover, a strong transverse component of the magnetic field can reduce compression and a high dust-to-gas ratios may speed up the cooling rate of the gas through the collision heating of dust grains (Contini 2004). The ionization parameter and the star temperature affect particularly the ionization structure of the gas.

The radiation flux emitted from the gas downstream is calculated in each slab downstream and integrated throughout the nebula. The input parameters are even more constrained by comparing the calculated flux F_c with the flux F_o observed at Earth throughout the continuum SED (Fig. 5.4). Recall that $F_c\ r^2 = F_o\ d^2$, where r is the distance of the nebula from the system center and d is the distance to Earth. For instance, $F_c = 2\ 10^8$ erg cm^{-2} s^{-1}at ν=5 10^{14} Hz is calculated downstream of a shock front with V_s=600 $km\,s^{-1}$and $n_0 = 5\ 10^7\ cm^{-3}$. For r$\sim 2\ 10^{13}\ cm$ and adopting d= 270 pc, F_o results $\sim 10^{-7}$ erg cm^{-2} s^{-1}, in agreement with the observations (Fig. 5.4). In this case the emission lines corresponding to the heavy elements are very weak because the low temperature ($\leq 10^6$ K) zone in the nebula is narrow, while the Balmer and permitted He lines are high enough to be observed, due to a high ionization parameter U (> 1).

The parameters are refined in order to obtain the best fit to observations in different epochs, considering that V_s increases with time during the 1978-1986 active phase and therefore n_0 must decrease.

Spectra from the shells

At the earliest epochs (1978-1984) the models are constrained by the relative strength of OI 1304, 1358, SiIII] 1892, CIII] 1909, and MgII 2800. The spectra before November 1984 showed relatively strong low ionization lines which are explained by model $m1_{shell}$ (Tables 5.1 and 5.2) with V_s=40 $km\,s^{-1}$. The CIV/CIII] line ratio depends on the geometrical thickness D of the nebula namely, the larger D, the lower the CIV/CIII] ratio. Therefore, the observed CIV/CIII] < 1 suggests to represent the shells by matter-bound models relative to a quite extended nebula (D=4 10^{14} cm).

The parameters describing the shells are chosen considering that dust shell characteristic velocities are $\sim$ 30-50 $km\,s^{-1}$and that the densities must be suitable to the giant atmosphere ($\geq 10^9\ cm^{-3}$). They are slightly modified in order to obtain line ratios fitting the observations. Notice that adopting low V_s (30-60 $km\,s^{-1}$) and high densities, the temperatures downstream are $< 6\ 10^4$ K and the permitted UV lines emitted from the heavy elements are high enough to be observed.

Spectra from the expanding shock

The eclipse (Skopal et al. 1996) at the end of 1984 indicated that the system had rotated and the spectra were hence emitted from a different nebula, namely, the nebula downstream of the expanding shock.

In November 1984, [OIII] and [NIII] in the optical domain, and several high ionization lines (e.g. CIV, SiIV) appeared. The models best fitting both line and continuum spectra are shown in Table 5.3 where the line ratios are compared with the observations of Mikolajewska et al. (1988).

The parameters corresponding to the expanding shock are dictated by the FWHM of the forbidden lines, by the densities that must avoid collisional de-excitation of the forbidden lines (e.g. [OIII] 5007), and by the consistent fit of the observed continuum SED and of the line ratios.

In particular, the UV line ratios to Lyα =10 calculated by model $m1_{exp}$ are compared with the observations by Mikolajewska et al. (1988, Table 5.3) at JD 2446086 (20/1/1985). This model is shock dominated, as the spectrum is emitted from gas in the external side of the expanding nebula, facing the observer. Notice that a perfect fitting of the observations is not sensible due to the approximation of the models. Therefore we have focused on the line ratios which unequivocally describe a physical situation.

The model is constrained by the CIV:CIII]:CII] line ratios. The shock dominated model $m1_{exp}$ cannot explain the observed HeII 1640 line. which is better approximated by model $m2_{shell}$. Also in the optical range model $m2_{shell}$ shows HeII 4686 and HeI 5876 lines as intense as to be observed (Table 5.2), while OI 1304 and SiII 1814 are underestimated. In conclusion, also the shells contributed to the line spectra as well as to the continuum.

Table 5.2: Calculated line ratios to Hβ

line	m1$_{shell}$	m2$_{shell}$	m$_{600}$	m1$^{a}_{exp}$
NV 1240	0.003	0.23	0.001	4.15
OI 1304	0.04	0.02	0.006	0.006
CII 1335+	0.8	1.65	0.15	3.
OI 1356	0.42	0.19	0.06	0.05
OIV]+				
SiIV1400	0.34	1.8	0.02	8.
NIV] 1486	0.03	0.27	0.002	3.
SiII 1531	0.06	0.03	0.013	0.02
CIV 1550	1.0	7.2	0.09	14.
HeII 1640	3.8	4.7	1.9	0.06
OIII] 1663	0.25	0.9	0.05	2.
NIII] 1744+	0.1	0.4	0.002	1.3
SiII 1814	0.37	0.2	0.1	0.08
SiIII] 1892	0.7	1.	0.4	2.5
CIII] 1907+	1.2	2.	0.08	5.6
CII] 2326	1.5	1.2	0.25	3.2
MgII 2798	1.1	0.5	3.	0.5
[NeIII] 3869+	0.008	0.004	0.001	0.3
[OIII] 4363	0.008	0.004	-	0.45
HeI 4471	0.04	0.02	0.03	0.63
HeII 4686	0.55	0.65	0.28	0.005
[OIII] 5007+	0.001	0.002	-	1.47
HeI 5876	0.14	0.08	0.1	1.12
[OI] 6300+	0.002	0.0004	0.001	0.25
Hβ [b]	7.6e8	1.9e8	5.8e8	0.75

[a] shock dominated;
[b] in erg cm^{-2} s^{-1}.

Table 5.3: 1978-86: modelling the line ratios at JD 2446086 (20/1/1985)

line	obs_{6086}	$m2_{shell}$	$m1^a_{exp}$
HI 1215	10	10	10
NV 1240	1.6	0.02	0.8
OI 1304	3.3	0.02	0.01
CII 1335+	0.87	0.13	0.6
OIV]+SiIV 1400	0.83	0.15	1.3
NIV] 1486	0.19	0.02	0.43
SiII 1531	0.77	0.002	0.02
CIV 1550	1.8	0.58	2.7
HeII 1640	1.4	0.4	0.01
OIII] 1663	0.69	0.007	0.4
NIII] 1744+	1.1	0.03	0.2
SiII 1814	1.23	0.02	0.02
SiIII] 1892	0.89	0.08	0.5
CIII] 1907+	1.2	0.16	1.1

[a] shock dominated

5.3.2 The continuum SED

In Fig. 5.4 we present the modelling of the observations (Table 5.5) at some significant days during the 1978-86 active phase. The top left panel of Fig. 5.4 displays the data on a large frequency range (from radio to X-ray), while in the top right one the optical-UV range is zoomed in. The two bottom panels focus, respectively, on the IR and optical-UV flux variations: in particular, the bottom left panel shows the time-evolution of the SED in the near-IR, characteristic of a significantly variable absorption by dust.

Model results are plotted over the data in the top panels of Fig. 5.4. The models are cross-checked by the line spectra previously analyzed and constrained by the strong self-absorption in the radio range (top left panel). The high velocity models m_{600} and m_{1200} are needed to explain the X-ray datum (top left panel). The models characterized by $V_s > 600\ km\ s^{-1}$reproduce the Balmer line FW0M, but lead to UV-optical lines negligibly weak, so they were not included in Tables 5.2 and 5.3.

Dust is collisionally heated by the gas to high temperatures in a strong shock velocity regime and sputtering reduces the grain sizes; the smaller the radius, the higher the temperature reached by the grains. Reprocessed radiation by dust downstream of the shock fronts appear in the top left diagram of Fig. 5.4. Model m_{600} can reproduce both the optical and radio continuum slopes.

The dusty shells which fit the data in the optical-UV domain at maximum of activity (JD 2444937-2445720 = 28/11/1981-20/1/1984) contribute also to the CIV and CIII] lines in agreement with observations. Dust in the shells is mainly heated by radiation from the hot star: this was already found by previous investigations (Munari et al. 1996, Angeloni et al. 2007b,c). Throughout

expansion, the dust shells gradually fragmented by interaction with the environment, may reach the external edge of the binary system ($> 10^{14}$ cm), becoming circumbinary and playing a primary role in the complex obscuration episodes of CH Cyg.

At JD 2446212 (26/5/1985) and 2446776 (11/12/1986 - Fig. 5.4, right panels) at the end of the active phase a *flat* component appears in the near-UV SED. This is interpreted by model $m1_{exp}$ which represents the nebula downstream of the shock propagating outwards the system. Model $m1_{exp}$ is shock dominated (U=0) and explains most of the line ratios observed by Mikolajewska et al. (1988) at JD 2446086 (20/1/1985 - Table 5.3). The slopes at JD 2446212 (26/5/1985) and 2446776 (11/12/1986) can also be fitted by the same $m1_{exp}$ model in the radiation dominated case, adopting a relatively low U. However, in this case, the calculated line ratios are lower than observed. Recall that the line spectrum and the continuum were observed at different, although close, days. This is a further evidence that if the medium surrounding the system is clumpy enough, the radiation flux throughout its path from the WD to the external shock can be flickering.

During the brightness minimum in 1985, CH Cyg showed X-ray emission (Leahy & Taylor 1987). Simultaneous radio observations with the Very Large Array (VLA) revealed a radio outburst and expanding jets (Taylor et al. 1986). The X-ray datum in Fig. 5.4 was taken at the end of 1984, therefore constraining the models at that time. For earlier times, when no data are available, Leahy & Taylor suggested a flux lower by a factor of ∼80. We agree with them that the very large column density of the downstream nebulae led to large absorption in the 0.05 - 1.5 keV range.

5.3.3 Radii of shells and nebulae

Comparing the bremsstrahlung calculated at the nebula with the data observed at Earth we obtain the factors $\eta = r^2/d^2$, where r is the distance of the nebula from the system center and d is the distance to Earth.

The reverse shock (model m_{600}) was hence located at a radius of $2\ 10^{13}$ cm. The top right panel of Fig. 5.4 points out that the bremsstrahlung from the shell in the optical-UV range, represented by model $m2_{shell}$, can explain the data at two different days, JD 2443877 (3/1/1979) and JD 2444937 (28/11/1981). The calculated radii are $2.88\ 10^{13}$ and $9\ 10^{13}$ cm, respectively, to which would correspond a shell expansion of $\sim 6\ 10^{13}$ cm in 2.9 years. This, in turn, would correspond to a velocity $< 7\ km\ s^{-1}$, much lower than the shock velocity (V_s=60 $km\ s^{-1}$), unless the two shells were ejected at different times. The latter hypothesis seems more realistic, as the pulsation frequency of the cool component is actually ∼756d.

The expanding shock reached a radius of $8\ 10^{16}$ cm. The geometrical thickness Δ of the cool region ($T \leq 10^4$ K) within the downstream nebula is constrained by the relatively strong self absorption of free-free radiation in the radio. The optical thickness τ is $\propto n^2\ \Delta$, where the density n ($\leq 10^6\ cm^{-3}$ considering compression downstream) is constrained by the slope of the bremsstrahlung: a

larger n would lead to a steeper bremsstrahlung in the UV-optical range. This allows us to give a lower limit to the geometrical thickness of the cool region : $\Delta > 2\ 10^{15}$ cm.

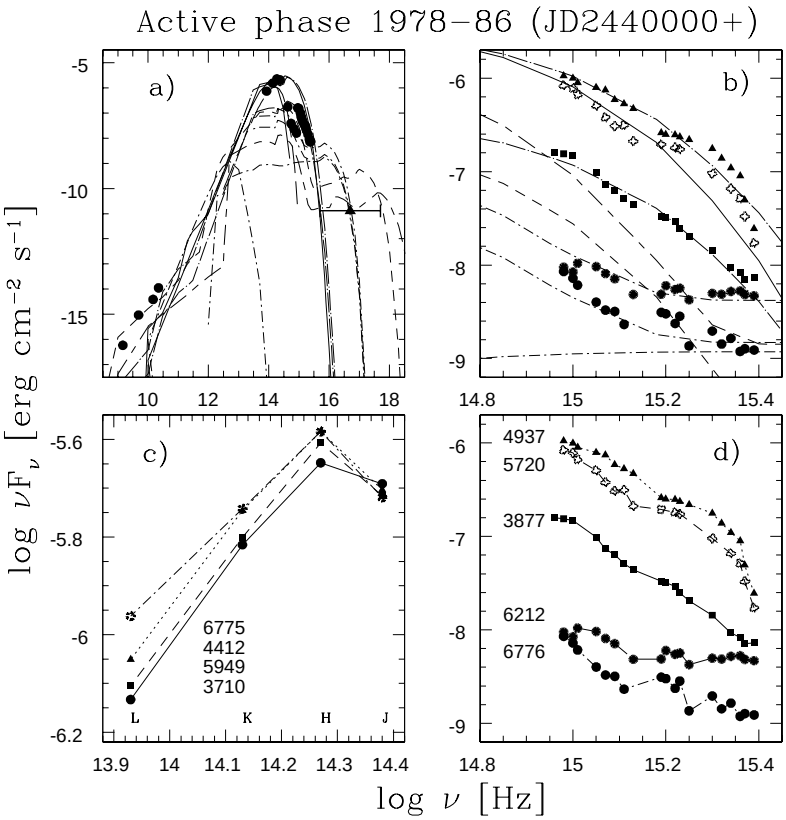

Figure 5.4: Modelling the active phase 1978-86. Top panels: comparison of the models with data from radio to X-ray (left) and a zoom in the optic-UV range (right). Thick-solid line: bb (2000 K); long dash-dotted lines: $m2_{shell}$; solid line: $m1_{shell}$; short-dashed lines: m_{600}; short-long-dashed lines: m_{1200}; short dash-dotted lines: $m1_{exp}$. Bottom panels: comparison of time variations in the IR and in the optic-UV range at different days.

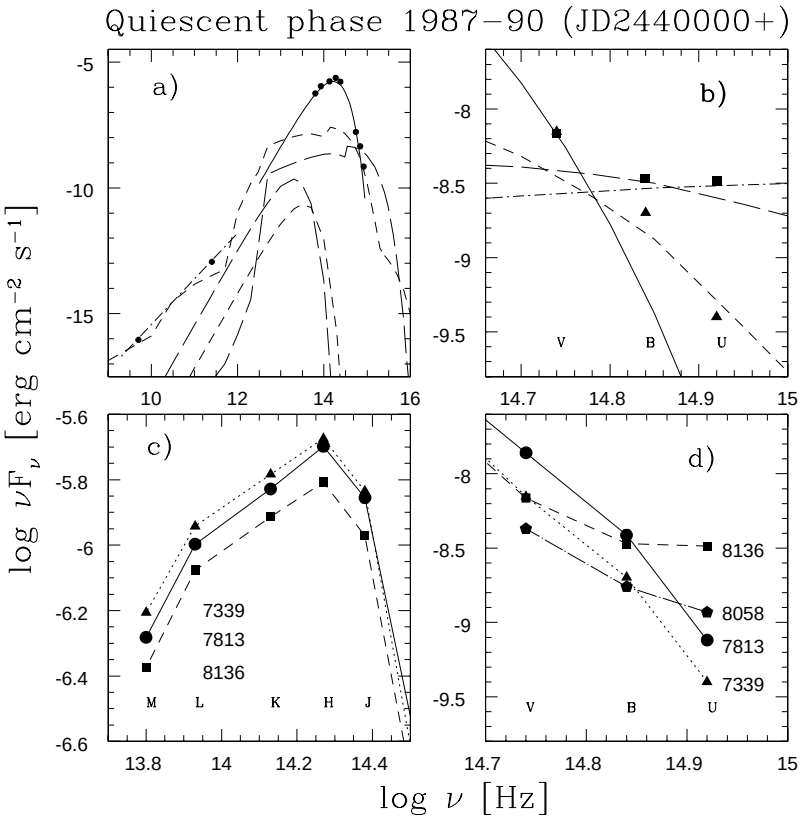

Figure 5.5: Modelling of the quiescent phase 1987-90. The figure is structured as Fig. 5.4. Top panels: Solid line: bb (2000 K); short-dashed lines: $m3_{exp}$; long-dashed lines: $m2_{exp}$; dot-dashed lines: model $m1_{exp}$. The models refer to Table 5.1.

5.4 1987-1990 quiescent phase: the obscuration effect

5.4.1 The line spectra

Taranova & Yudin (1992) stated that the optical spectra taken in 1988 did not reveal any emission lines (Mikolajewski et al. 1990) or revealed only very week Hα and Hβ lines (Andrillat 1988, Bopp 1990). In 1989, before the next outburst, an emission line spectrum with FeII, [FeII], [SII] 4068, and faint one-component Hβ was lying upon numerous absorption lines. The spectrum can be roughly explained by the expanding nebula represented by model m1$_{exp}$ with V_s=150 $km\,s^{-1}$. At JD 2448122 (18/8/1990), Tomov & Mikolajewski (1992) observed numerous emission lines from the shell which can be explained by model m2$_{shell}$.

5.4.2 The continuum SED

In Fig. 5.5 we present the SEDs observed during the quiescent period 1987-1990 between the two active phases 1978-86 and 1991-95. Fig. 5.5 is structured as Fig. 5.4. In the top right panel the V data are fitted by the bb flux from the cool star, while the B and U data showed a flat slope that can be reproduced by models m1$_{exp}$ and m2$_{exp}$, corresponding to different preshock densities (Table 5.1). So we constrain the models by the line ratios, recalling that the optical spectra observed in 1988 did not reveal any emission lines or very week Hα and Hβ . This excludes the shock dominated model m1$_{exp}$ that was used to fit the flat slopes at the end of the 1978-86 active phase and the line spectrum at JD 2446086 (20/1/1985).

The models which best fit the slopes at JD 2448136 (1/9/1990) and JD 2447339 (26/6/1988), m2$_{exp}$ and m3$_{exp}$, respectively, are both shock dominated with $V_s \leq 100\ km\,s^{-1}$and relatively high n_0, which lead to negligible line emission downstream. They indicate that the outflowing shock is propagating through a denser medium, perhaps a residue of matter ejected during previous eruptions.

Finally, let us compare the near-IR fluxes during the 1978-86 phase with the ones during the 1987-90 phase (bottom left panels of Figs. 5.4 and 5.5, respectively): while in the former case the slopes showed a dust absorption clearly wavelength-dependent, during the quiescent phase minimum the IR flux decreased equally throughout the whole near-IR range, suggesting an obscuration effect by an external shell.

5.5 1991-1995 active phase: the black body radiation from the WD

A new active phase began in December 1991 with a large flux rise in U, a smaller one in B and a negligible one in V. This trend was sustained until March 1992.

Then, from the beginning of 1993 the U band rose again until summer 1994. The eventual drop in summer 1995 informed that the outburst was running out.

It is worth noting that during this 1991-95 high state, the bb continuum flux from the hot star became gradually detectable (right panel of Fig. 5.6). As a matter of fact, the appearance of a hot continuum source with T_{eff}=150,000 K was taken as the indication of the beginning of the outburst by Skopal et al. (1996). To obtain an initial hint about the system during this active phase, we compare the evolution of the slopes in the U-B-V during the 1978-87 and 1991-95 active phases in Fig. 5.6. An impressive difference can be noticed comparing the right and left panels: in particular, the left one shows that in the first active phase the trend in the UB range cannot be explained by the bb flux from the hot star which vice-versa is evident (right diagram) during the 1991-95 outburst. The direct contribution of the hot star to the U band is shown at the 1991-95 active phase maximum (JD 2449598 $\equiv$ 2/9/1994). In Fig. 5.6, the low frequency tails of the black body curves correspond to T_*=100,000 K (dashed line) and T_*=35,000 K (dotted line). These temperatures represent the maximum and minimum one, respectively, during and after the outburst (Corradi et al. 2001). The slopes of both bb fluxes in the UB frequency domain are slightly different than observed, and are even less fitting the data before (thin lines) and after maximum (thick lines). We suggest that the WD was hidden from a direct view in the 1978-86 active phase, while it became visible during the 1991-95 maximum.

The two deep minima in U recorded at the end of September 1992 and in October 1994 lasted 81 and 127 days, respectively. They were attributed to the eclipse of the active component by the cool one in the light of the triple star model (Skopal et al 1996), but they are hardly explained by the binary interpretation which ascribes the 756d periodicity to a non-radial pulsation of the M giant. Fig. 5.6 (bottom panel) shows that the eclipses of September 1992 just before JD 2448900 (4/10/1992) and of October 1994 involved only the B and U bands, the WD and the shocked nebula being eclipsed most probably by dust shells. The V band in fact was not involved as it recovered its range of magnitudes that were shifted during the bursts by the contribution of the nebulae. Similarly, the relatively weak maxima immediately after the "eclipses" were due to emission from the shocked nebulae. We suggest that the minima were due to absorption by the dusty shells that are ejected in tune with the pulsation of the red giant. Recall that the dusty shells are highly fragmented therefore this effect cannot be observed periodically.

5.5.1 The line spectrum

At JD 2448094 (21/7/1990), a dramatic change led to broad hydrogen absorption profiles and at JD 2448095 (22/7/1990) CH Cyg displayed faint emission in Hα with corresponding velocities around -67 $km\,s^{-1}$. Then, in August 1991, the appearance of absorption terminal radial velocities of -1000 and -900 $km\,s^{-1}$for Hα and Hβ , respectively, might have been a consequence of the rotation of the system. This would have allowed us to see the reverse shock in front of the WD.

Eventually, the absorptions turned into emissions with velocities up to 1800 for Hα and 1600 $km\,s^{-1}$ for Hβ : these velocities disappeared at the beginning of the 1992. From JD 2448883 (17/9/1992) the Hβ emission increased, whereas no absorption lines were observed.
High velocities had been observed also during the previous active phase and there explained by the reverse shock model.

The spectral region around [OIII] 5007 showed complicated structures consistent with more components. During the outburst (1992 onwards) strong emission lines of FeII, [FeII], [SII], and H were observed, while [NeIII]3869+ and [FeIII] 4659-4670 were still faint, increasing later. Also, [OIII]4363 and [OIII] 5007+ were relatively faint and varied rapidly during the active phase. The overall scenario, with multiple emission line components and structured line profiles, may be qualitatively understood by Richtmyer-Meschkov (R-M) and Kelvin-Helmoltz (K-H) instabilities (Graham & Zhang 2000). R-M is an interfacial instability between two fluids of different density driven by shock waves. The K-H instability leads to the consequent fragmentation of matter at the shock front (Contini & Formiggini 2001). The clumpiness of the nebula might then contribute to flickering episodes.

On September 1992, the M-giant was even more apparent due to the eclipse. The red part of the spectrum was dominated by the M-giant molecular spectrum, overlayed by strong Hα , [OI]6300, and HeI 5876 emissions. There were simultaneous emission lines of [SII], [NeIII], and [FeIII]; notice that the HeII 4686 and 1640 lines were not present during the outburst. We suggest that the line spectrum is most probably emitted from a disrupted shock dominated expanding nebula ($m1_{exp}$) characterized by low HeII lines (Table 5.2).

In May 1993 the UV emission line spectrum showed Lyα , OIV], SiIV 1400, CIV 1550, OIII] 1666, SiIII] 1892, CIII] 1909, CII] 2325, [OII] 2470. These lines are reproduced by the model for the expanding nebulae $m1_{exp}$. Moreover, numerous FeII multiplets appeared, together with MgII 2796, 2803 doublet, and sharp emission lines, ArIII 2187, 2191. In August 1994, a sharp absorption cutting the emission line profiles at V_s=150 $km\,s^{-1}$ most likely shows that the expanding nebula is facing the observer. In fact, the strongest emission came from the line core while a very broad and smooth absorption up to -1600 $km\,s^{-1}$ was seen.

5.5.2 The continuum

The SEDs of the continuum are shown in Fig. 5.7 diagrams. The models which appear in the top left diagrams, covering the whole spectral range, were selected by the consistent fit of the data in the optical-UV range (zoom in the top right diagram), of the radio and of the X-ray data.

We start by presenting the modelling in the optical-UV range because it is more constraining. Around maximum at JD 2449598 (2/9/1994), the flux SED corresponding to the sum of the expanding shock ($m1_{exp}$) bremsstrahlung and the bb flux from the hot star (T_*=150,000 K) reproduces the slope of the U-B-V SED. At JD 2449583 (18/8/1994) the bb component was not visible. This may

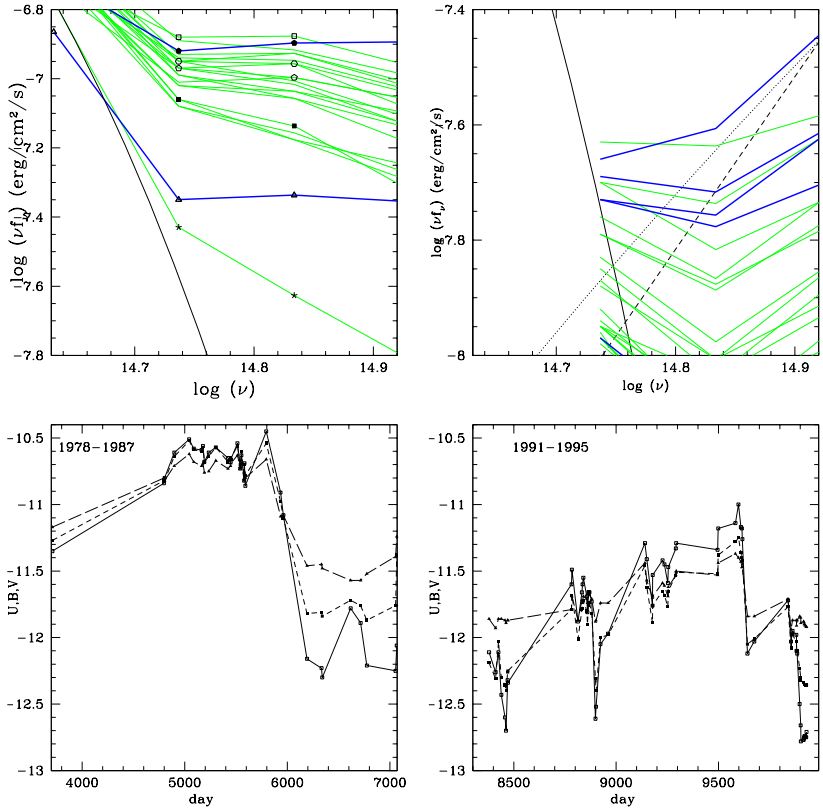

Figure 5.6: Top. Left: the SEDs in different days (1978-87) from Taranova & Yudin (1988). Right: the SEDs in different days (1991-95) from Munari et al. (1996). Thin lines represent the epochs before the U band maximum, thick lines refer to later epochs. Bottom (JD 2440000+). Left: the light curves during 1978-87 (in erg cm^{-2} s^{-1}Å^{-1}). U: open squares connected by solid lines; B: black squares connected by short-dashed lines; V: black triangles connected by long-dashed lines. Right: the light curves during 1991-95.

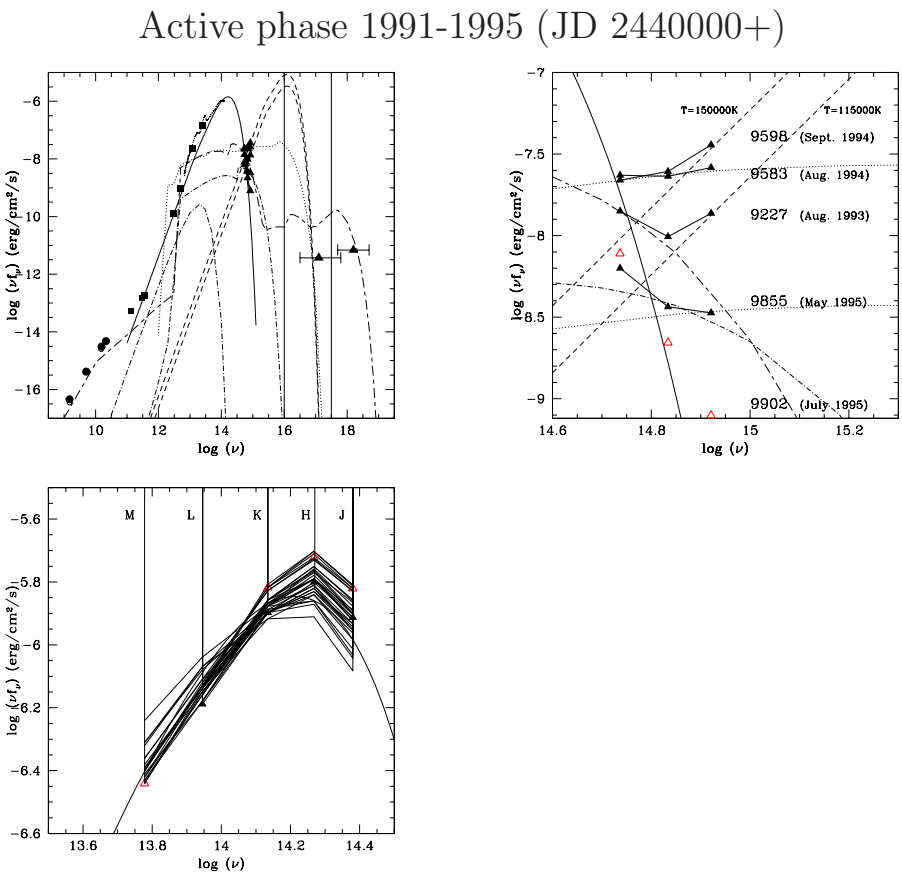

Figure 5.7: Modelling the 1991-1995 active phase on a large frequency range (top left diagram). Dotted line: model $m1_{exp}$; dot-dashed: $m2_{exp}$; long-short-dashed: m_{1200}; thick solid: bb (2000 K); short-dashed: bb from the WD (see text); thick dotted line: data from ISO; black circles: JD244922, black squares: JD 2448818 (Skopal et al. 1996), small black triangles: data from Munari et al (1996); large black triangle: X-ray. Thin vertical lines indicate the frequency region of high X-ray absorption. Top right diagram: optic-UV range. Black triangles: JD are labeled for each epoch; empty triangles : JD 2449902. Bottom diagram: variability in the IR. Data from Munari et al. (1996). Black symbols show the slopes of the lines; empty triangles: JD 2449902.

be explained by the fragmented nature of the shells which screen the flux from the WD, confirming Eyres et al. (2000) claim that flickering cannot be observed during the eclipse.

Similarly, the flux SED which best reproduces the trend of the data at JD 2449227 (27/8/1993) results from the sum of model m_{1200} with the WD bb flux: recall that broad lines were still emitted in 1993. In May 1995 we observed only the expanding shock corresponding to model $m2_{exp}$.

Fig. 5.7, top right diagram shows that the bb flux from the WD grew by a factor of 2.75 between JD 2449227 (27/8/1993) and JD 2449598 (2/9/1994), corresponding to an increase of the WD temperature from $\sim$ 115,000 K to 150,000 K.

We can now examine the data on a large scale, from radio to X-ray. The radio slope between 1992 and 1993 as observed by MERLIN, VLA, and JCMT (Skopal et al 1996) is once again explained by bremsstrahlung with a strong self-absorption at longer wavelengths. The best fit is obtained with a model corresponding to V_s=1200 $km\,s^{-1}$in the reverse shock. This model also explains the data in the optical-UV range and the hard X-ray. Models $m1_{exp}$ and $m2_{exp}$ give a negligible contribution in the radio. Skopal et al. (1996) proposed a velocity of $\sim$ 310 $km\,s^{-1}$in order to match the contemporary angular radius observed by MERLIN: this discrepancy is easily explained as we deal with disrupted nebulae downstream of head-on shocks in a highly turbulent regime.

The soft X-ray datum by ASCA was modelled by Ezuka et al. (1998) as two optically thin thermal plasma emissions. We find (Fig. 5.7, left diagram) that the soft X-ray is emitted downstream of the expanding shock, while the hard X-ray would correspond to the reverse shock between the stars with a velocity of 1200 $km\,s^{-1}$.

An impressive systematic evolution of the JKLM band flux appears in the bottom diagram of Fig. 5.7, indicating that dust is involved in the obscuration process.

Finally, by exploiting the η factors above defined we can calculate for the reverse shock a radius of 4 10^{13} cm and for the expanding nebulae which best fit the data a corresponding radius of 10^{16}-3 10^{17} cm. Similar dimensions of the system were found by HST imaging in the 1998-2001 active phase by Eyres et al (2002) after about 5 years. Adopting en expanding velocity $\leq$ 100 $km\,s^{-1}$the radius increment is relatively small ($<$ 2 10^{15} cm).

5.6 1996-1997 transition phase: the contribution of radio synchrotron radiation

During the quiescent phase 1996-97 some interesting radio observations were taken between March and October 1997 by Karovska et al. (1998). The data (Fig. 5.8, top left), along with an intriguing flux variability, followed the trend of an absorbed bremsstrahlung as was found in previous phases adopting a high

velocity model (V_s=1200 $km\,s^{-1}$). A particular investigation of the radio range is shown in Fig. 5.8, bottom left diagram. The slope of the data at 8 and 43 GHz observed between May and August 1997 could be fitted by synchrotron emission created at the shock front by the Fermi mechanism in the non-relativistic case (Bell 1978) with a characteristic spectral index α = -0.35. This is not surprising because non-thermal emission was also invoked by Crocker et al. (2001) in order to explain the radio data between 1985 and 1999, adopting a magnetic field of the order of 1-3 mG. Interestingly, we have reached the same values of the magnetic field (B_0 = 1-3 mG, Table 5.1) by consistent modelling of line and continuum spectra in the different phases. Nonetheless, the datum at 22 GHz is highly under predicted by the synchrotron radiation and may refer to a completely different emission process, e.g. bremsstrahlung from the downstream nebula. A high velocity model is in fact requested by the optical-UV data, as presented in Fig. 5.8 (top diagrams).

Regarding the infrared range, it is worth reminding some results of 1997 ISO observations, unfortunately still no fully exploited. Schild et al. (1999), who did a preliminary analysis of the spectra, found no strong emission lines but [OI]63 μm, and strong OH and weak H_2O molecular emission on top of a rapidly decreasing continuum. This continuum can be fitted by a single dust shell model ($T_d \sim$ 1000K, Fig. 5.8), in contrast with other SSs which seems to display multiple dust shells with characteristic radius and temperatures (Angeloni et al. 2007c).
The dust chemistry was quite surprising, since weak PAHs (at 6.3 μm) coexisted with dominant amorphous silicate (at 9.7 and 18 μm). Unfortunately, a comparative study of dust spectroscopy capable of investigating the grain formation and destruction processes throughout both the active and quiescent phases is still not possible for lacking of data (see Angeloni et al. 2007a for a comparison of emission lines and silicate dust features, from ISO spectra, in a various sample of SSs including CH Cyg). ISO-SWS observed the system twice during this quiescent phase, and in Fig. 5.9 we show a comparison of the two recorded spectra. As one can notice, the maximum flux variation seems to be in correspondence of the strong silicate emissions, while the underlying dust continuum appears not so sensitive to the environment variation due to the giant pulsations. How this can be related to the actual dust formation and processing is far from understood.

5.7 1998-2000 active phase: jets and X-rays

5.7.1 The line spectra

As noticed by Eyres et al. (2002) in the HST imaging, the very inner regions of CH Cyg contributed mainly to continuum, and very little to the line emission. In our interpretation this is not surprising since the nebulae emitting the line spectra would correspond to the expanding nebulae that are moving towards the outside of the system.

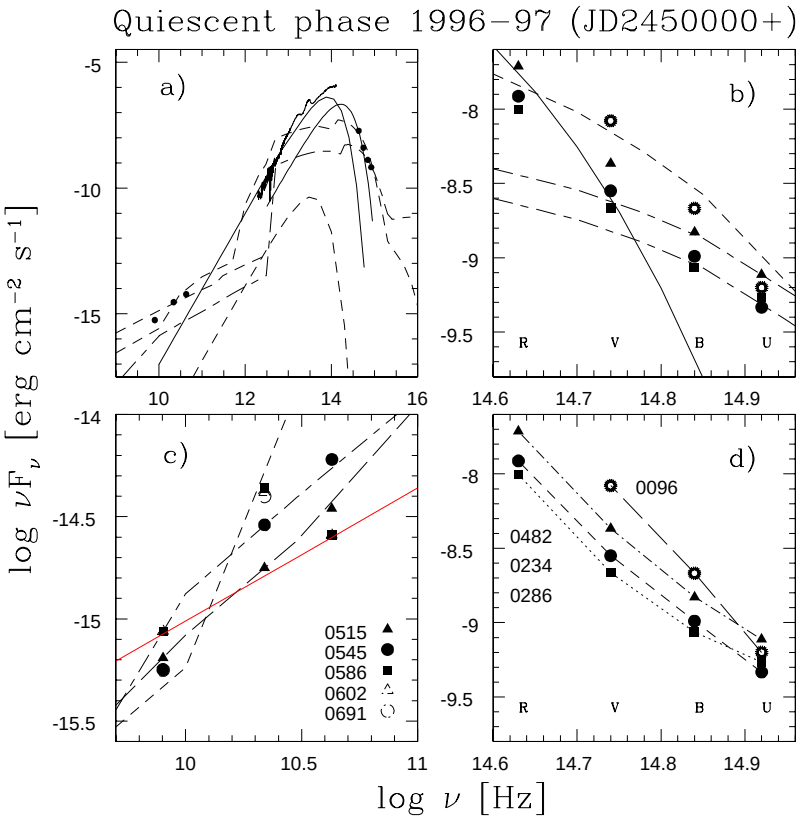

Figure 5.8: Modelling the SED of the transition phase 1996-1997 on a large frequency range (left top) and in the optic-UV range (right top). The figure is structured as Fig. 5.4. Long-short dashed lines: m_{1200}; dashed lines: $m3_{exp}$; thick solid line: bb flux (2000 K); thin solid line: dust bb radiation at 1000 K. Diagram on the bottom left: variability of the radio flux in 1997. The data by Karovska et al (1996) are connected by thin solid lines; thick solid (red) line: synchrotron radiation corresponding to α=-0.35; short-dashed lines: $m3_{exp}$; short-long-dashed lines: m_{1200}; long-dashed lines: m_{600}.

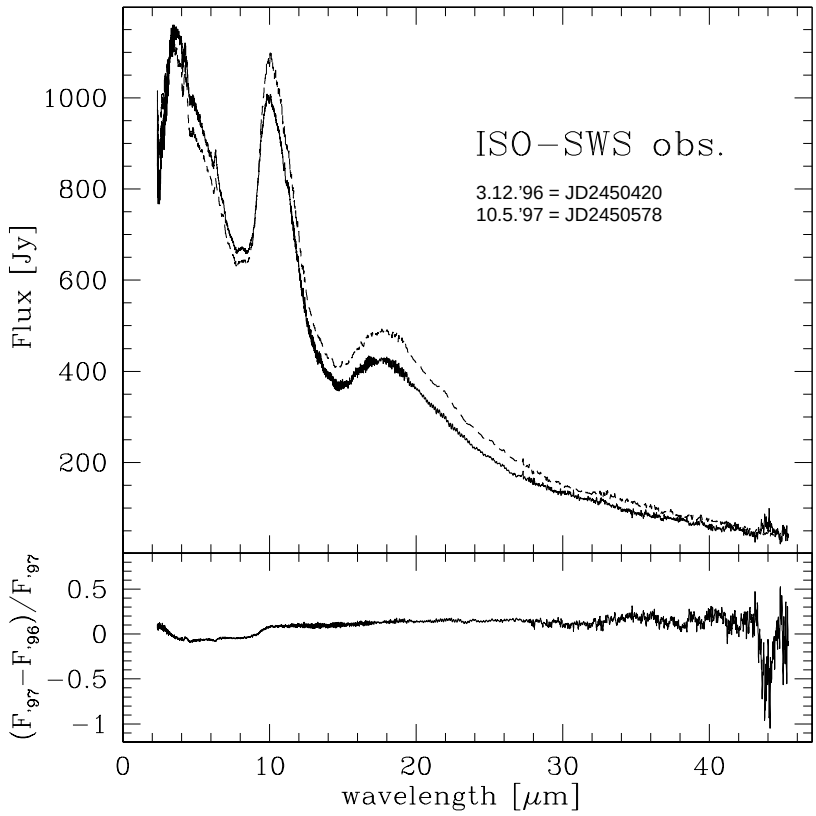

Figure 5.9: The two ISO-SWS spectra. Top panel: the spectra displayed in arbitrary units. It is noticeable the variations in the 9.7 μm silicate profile. Bottom panel: the relative ratio of the fluxes, showing that the main variations seems to be due to the silicate emissions, and not to the underlying dust continuum.

Balmer lines Hα , Hβ , Hγ, all double peaked, lay upon a broad feature 1200 $km\,s^{-1}$wide confirming that a fast reverse shock of V_s=1200 $km\,s^{-1}$was present within a small radius $< 10^{13}$ cm. The fast shock can explain also the X-ray Chandra observations of 2001 at $\sim$ 0.26 and 2 keV reported by Galloway & Sokolowski (2004). Indeed, the temperature in the immediate post shock region corresponding to that V_s, is 2.16 10^7 K, decreasing downstream to $\sim$ 1.5 10^7. The cooling rate is not so strong because recombination coefficients are low at such high temperatures.

The HST images by Eyres et al. (2002) revealed strong [OIII], which can be explained by the expanding nebulae m3$_{exp}$ modelled by fitting the SEDs.

In September 1998 the OI, HeI, HeII, FeII, and TiII were probably emitted from the shells. [OIII] 5007 was also evident, while [OIII] 4363 absent both in and out the eclipse. We have run some further models corresponding to expanding nebulae (ME$_{exp}$ and ME1$_{exp}$) which, in agreement with the observations, predict relatively low [OIII] 4363 (Table 5.4). The input parameters are shown in the bottom of Table 5.4. The models are shock dominated (U=0). The dust-to-gas ratios adopted in these models are 4 10^{-4} by mass.

Corradi et al. (2001) indicated strong [OII] and [NII] lines in the 1999 images. These strong low ionization lines are characteristic of shock dominated models, e.g. ME$_{exp}$ and ME1$_{exp}$, which might occur from the collision of the expanding jets with the surrounding ISM. The radius of these shocked nebulae are calculated by fitting the continuum SED. The η factors lead to a radius $>$ 3 10^{16} cm.

5.7.2 The continuum SED

In Fig. 5.10 we present the modelling of the 1998-2000 active phase. Some significant UBV data are taken from Eyres et al (2002, Fig. 2). Fig. 5.10 (left diagram) shows that the best fit of the UBV slopes are obtained by model m2$_{exp}$ in December 1998 during the maximum, while at later epochs the slopes are reproduced by model m$_{1200}$. This can be explained considering that at maximum the relative position of the different system components (stars, nebulae, shells) is such that we cannot see the reverse shock, which appears only after some months.

The fitting of the models to the data in Fig. 5.10 (right diagram) leads to similar factors η for the two models. However, we know that the radius of the reverse shock is much smaller than that of the expanding shock by at least a factor of 100. This question is resolved invoking the filling factor as a key parameter. The radii of the expanding shell at maximum of the active phase and of the reverse shock at later epochs result of 1.3 $10^{12}/ff$ cm and of 1.4 $10^{12}/ff$ cm, respectively, leading to corresponding filling factors of $\sim$ 0.001 and 0.1, to recover more sensible radii. Small ff are suitable to the fragmented character of matter throughout the expanding shock deriving from dynamical instabilities e.g. R-M and K-H (Contini & Formiggini 2001).

Fig. 5.10 (left diagram) shows also that the d/g ratio adopted by model ME$_{exp}$ is just a lower limit, because the flux corresponding to reradiation by

dust is constrained by the SED, definitively dominated by bb from the cool star in that wavelength range. The low velocities of these models indicate that the expanding nebulae swept up a large amount of interstellar matter, whose d/g actually corresponds to $d/g \geq 4\ 10^{-4}$. This matter probably existed before the start of this outburst, and might be considered as a sort of remnants from the former bursts which have then propagated throughout the ISM.

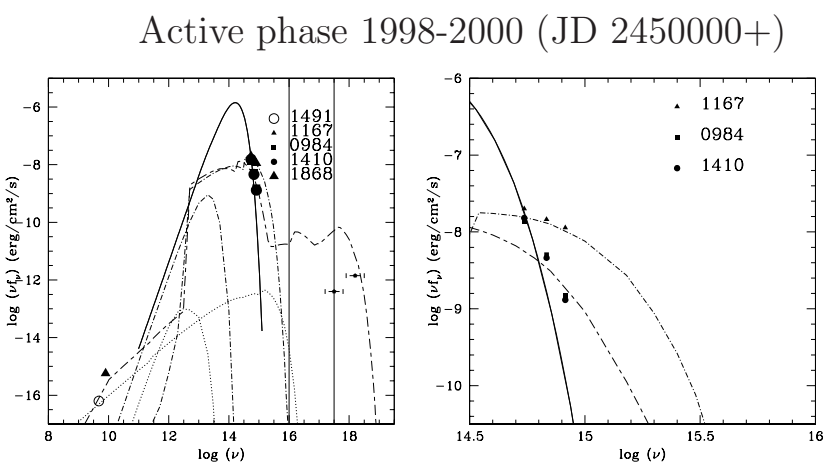

Figure 5.10: The 1998-2000 active phase. Left diagram: modelling the SED from radio to X-ray. Right diagram: the optical frequency range. Long-short-dashed lines: m_{1200}; dash-dotted lines: $m2_{exp}$; dotted lines: ME_{exp}; solid line: bb (2000 K). Large black triangle: data from Karovska et al (2007). The vertical thin lines show the range of strong absorption in the X-ray domain.

5.8 From 2001 up to date

Since 2001, CH Cyg persists in a quiescent phase recovering from the latest high state, at a rather bright magnitude (U$\sim$10 or less, V=7-8, B=8.7-9.4). During the last months it showed a $\sim$ 2mag decline in the optical bands (2006 June-December, Skopal et al. 2007) and a most significant, anomalous, IR fading (Taranova & Shenavrin 2007).

In April 2004, high-resolution optical data by Yoo (2006) detected double-peaked emission components for the Hα and Hβ profiles, with an interesting V/R <1, where V and R stand for the intensities of the blue and red wings, respectively. This has been taken as a proof, along with the vanishing of the blue continuum, that at that time an accretion disk was already present, although highly processed. Moreover, the multiple-peaked profiles of the emission lines led to suggest a strong non-homogeneous envelope, result of the collision between some outflowing matter and the circumstellar shells.

A few months later, in October, new observation revealed (Yoo 2007) a

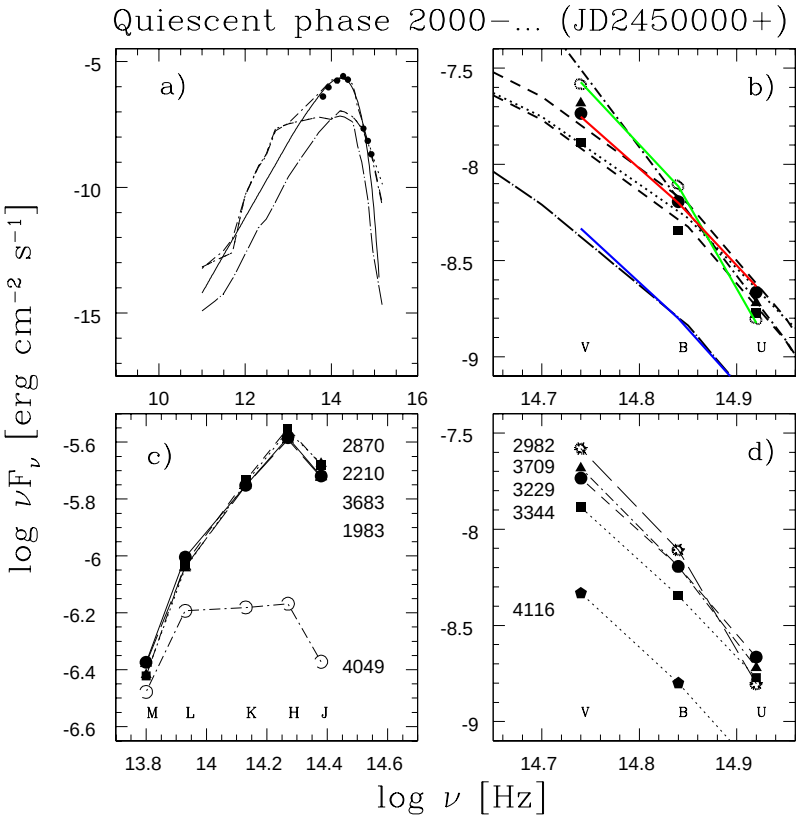

Figure 5.11: Red line: the SED at maximum of U; green line: the SED at maximum of V; blue line: the SED towards minimum. Short dashed line: model m1$_{exp}$; short-dash-dotted line: w1 m1$_{exp}$ + w2 bb$_{2000}$, where w1=$10^{-12.5}$ and w2=$10^{-14.4}$ are the relative weights, respectively; long-dash-dotted: w1 m1$_{exp}$ + w2 bb$_{2000}$ where w1=$10^{-13.35}$ and w2=$10^{-16.0}$ are the relative weights, respectively; dotted: w1 m1exp + w2 m3$_{exp}$ where w1=$10^{-12.5}$ and w2=$10^{-18.9}$ are the relative weights, respectively.

Table 5.4: Line ratios to Hβ in the extended nebulae (jets)

line	ME$_{exp}$	ME1$_{exp}$
[OII] 3727+	40.	19.
[OIII] 4363	2.6	2.18
HeII 4686	0.016	0.027
[OIII] 5007+	35.3	25.7
HeI 5876	0.4	0.58
[OI] 6300+	0.37	0.40
[NII] 6584+	8.9	6.42
Hβ (erg cm^{-2} s^{-1})	0.0013	0.0025
$V_s(km\,s^{-1})$	70	100
n_0 (cm^{-3})	5.e3	5.e3
B$_0$ (gauss)	1.e-3	1.e-3
D (cm)	1.e15	1.e15

rapidly developing framework, with single-peaked Hα and Hβ emissions and no absorption component at their line centres. The V/R ratio became $<<$ 1, indicating that the accretion disk might have been destroyed within the April-October time interval. Variability in the Hα blue component intensity has been explained as the actual expansion effect of some jets. Moreover, the blue continuum became so dim as to unveil the M giant even at short wavelengths, while a contemporary enhancement of the emission lines allowed to detect conspicuous [OIII] 4959 and [OIII] 5007, along with broad emission components of [NeIII] lines. This emission might have originated in an extended, expanding shell constructed by the outflowing matter from the WD.

In the X-ray, Mukay et al. (2006), analyzing Suzaku observations of 2006 January and May, found CH Cyg in a soft X-ray bright, hard X-ray faint state. While the soft X-ray flux level was similar to the 1994 ASCA observation, the hard one was much lower, confirming that the hard component is more variable than the soft component (Ezuka et al. 1997), which in turn may be spatially distinct. Assuming a binary period of $\sim$14.5 years, the entire binary should be extended $<$0.4" (100AU at $\sim$270 pc), explaining why Chandra was not able to resolve the system and, at the same time, in agreement with an extended X-ray emission region, comparable with the size of the binary, as expected in the colliding wind interpretation demonstrated by consistent modelling.

The hard X-ray component, more directly sensitive to the variable symbiotic activity, is the manifestation of those non-thermal emission processes (such as synchrotron) which once again prove the key-role played by shocks in accelerating relativistic particles responsible for the bulk of emission at hν $>$10 (De Becker et al. 2007).

In Fig. 5.11 we present the modelling of the UBV and JHKLM data presented by Skopal et al. (2007) and Taranova & Shenavrin (2007), respectively. The models which best fit the slopes of the data are the combination of those used in previous epochs (see caption of Fig. 5.11). Three main slopes can be

noticed. That at maximum of U (red) shows a contribution of two nebulae with different densities. The curve with the highest V (green) have a conspicuous contribution from the giant bb radiation. This contribution decreases and even disappears at minimum (blue curve), indicating that the whole binary system is obscured by the expanding nebula, as was found in previous epochs.

5.9 Discussion and concluding remarks

The complex nature of the SS CH Cygni has been investigated by modelling the line and continuum spectra at different epochs, from the impressive outburst of 1978 up to date. Our results give an approximated picture of the shocked nebulae throughout the system because our approach implies a plane parallel geometry for the different shock fronts. This is constrained by the composite models which account for both photoionization from the WD and shocks created by the collision of the winds. However, the plane-parallel geometry can be justified for relative large radii and in particular situations characteristic of SS.

The present analysis has revealed that similar developing trends may be recognized throughout the active phases and throughout the quiescent phases. In the light of a colliding-wind scenario, we have specifically focused on the role of the nebulae created by collision of the winds from the hot and the cool stars, in order to build up a comprehensive view of the system as a whole, namely to self-consistently interpret the variable line spectra, the radio emission, the IR photometric properties, the fluxes in the U B V bands and the X-ray observations. The most important result of our method that can be applied to all the SSs, consists in recognizing the different sources of radiation (stars, nebulae, dust) throughout the continuum SED.

We have found that bremsstrahlung from the nebula downstream of the shock front facing the WD between the stars explains the continuum slopes observed during the active states. These fast shocks seem to be always present during the outbursts, proving that the wind collision is playing a primary role in the spectral properties of the symbiotic phenomenon (e.g. radio and X-ray wavelength region). The circumstellar dusty shells define the optic-UV SED , also contributing to the line spectra during the active phases.

The WD may be related to flickering during the active phases, either by appearing directly (1991-95) or by photoionising the shells throughout a disrupted medium (1978-87). Towards the end of the active phases, the expanding shock propagating outward the system is visible both in the continuum SED and in the line spectra.

During the quiescent phases the circumbinary expanding shocks dominate. We have found that these shocks propagate throughout a relatively dense medium which may be interpreted as matter ejected in previous outbursts. This leads to a relative strong synchrotron radiation from the shock front at some epochs.

The jets observed by Corradi et al (2001) imply the presence of an accretion disk. The modelling of the low-ionization lines (e.g. [NII, [OII]), that are strong in their images, confirms that the jets expanding in the ISM, have reached a

radius > 0.01 pc from the SS.

We have shown, by consistent modelling, that soft and hard X-rays are emitted downstream of shock fronts corresponding to quite different velocities, namely, the expanding shock ($V_s \sim$ 100-150 $km\,s^{-1}$) propagating outwards the binary system would explain the soft X-ray emission, while the hard X-rays correspond to the high velocity shock between the stars, in agreement with the recent results discussed by Karovska et al. (2007) on the basis of radio, optical and X-ray imaging.

Dust grains within the nebulae are collisionally heated by the gas in a strong shock velocity regime ($\geq$ 600 $km\,s^{-1}$), while, in the dusty shells, grains are mainly heated by radiation from the hot star. The dust expanding disrupted shells might reach, in some cases, the external edge of the symbiotic system (r> 10^{14} cm), becoming circumbinary and therefore contributing to the complex obscuration episodes of CH Cyg.

It should be emphasized that the interpretation of CH Cyg spectral evolution is further complicated by the relatively short orbital period ($\sim$14.5 years): in fact, the orbital motion combined with the unpredictable recurrent activity leads to different system configuration as seen from Earth. We have tried to explain them by combining the radiation fluxes from the several emitting contributors with different, variable weights.

For the sake of clarity, we schematically summarize the results of our modelling:

1978-1987 active phase

- Emission lines with FWHM of 400 $km\,s^{-1}$- 1200 $km\,s^{-1}$correspond to the reverse shock;
- before 1984 November, low-ionization lines come from the shells;
- after 1994, higher level lines are emitted both by the expanding nebula and the dusty shells;
- at days JD2446212 and JD2446776, UV and optical lines from the expanding nebulae appear;
- at the end of the active phase, shock dominated models explain both line and continuum spectra.

1988-1990 quiescent phase

- The expanding nebula propagates throughout matter ejected in previous eruptions;
- in the IR the system is obscured independently from wavelength.

1991-1995 active phase

- In 1991, at the onset of the new active state, the lines display FWHM< 100 $km\,s^{-1}$, indicating a disrupted expanding nebula;
- in August 1991, broad Hα and Hβ are seen in absorption, suggesting that the reverse shock is absorbing the WD flux;
- by 1992 absorption lines disappear and M-giant molecular bands are observed. In May 1993, UV lines are emitted from an expanding nebula with a radius of 10^{16} - 10^{17} cm.

1996-1997 quiescent phase

- The radio flux shows a synchrotron component created by the Fermi mechanism at the shock front.

1998-2000 active phase

- . A fast reverse shock of 1200 $km\,s^{-1}$may explain the X-ray Chandra observations in 2001;
- the HST images by Eyres et al. (2002) reveal strong [OIII], which can be explained by the expanding nebulae in agreement with the fit of the SED;
- in 1998 Sept the OI, HeI, HeII, FeII, and TiII lines are emitted from the shells. Moreover, [OIII] 5007 is evident and [OIII] 4363 is absent both in and out of the eclipse. These lines come from shock-dominated expanding nebulae with relatively low velocities ($\sim$70-100 $km\,s^{-1}$) and relatively low densities ($n_0\sim$ 5000 cm^{-3}). In fact the corresponding [OIII] 4363 lines are relatively low;
- the 1999 images of Corradi et al. (2001) indicate strong [OII] and [NII] lines: they are characteristic of a shock dominated nebula with a relative low n_0=5 10^3 cm^{-3}.

2001-up to date

- three different slopes are observed in the optical-IR range. They are modelled by the combination of different expanding models with the bb flux from the cool component star.
- the decline observed by Taranova & Shenavrin in the IR is consistent with the decline in the optical-UV range and is explained by the eclipse of the whole system.

Observational references

Table 5.5: Observation references for the 1978-86 active phase.

	Observation date	References
radio	1984 Apr - 1985 May	Taylor et al. (1985, 1986, 1988)
IR	1983	IRAS CPS[a]
	1978-82	Ipatov et al. (1984)
	1978-87	Taranova & Yudin (1988)
optical	1977-86	Hack et al. (1988)
	1978-82	Ipatov et al. (1984)
	1978-87	Taranova & Yudin (1988)
	1980-87	Bondar & Shakhovskaya (2001)
UV	1978-87	Taranova & Yudin (1988)
	1981 Nov 29	Mikolajewska et al. (1988)
	1985 Jan 24	Mikolajewska et al. (1988)
	1986 Jul 16	Mikolajewska et al. (1988)
X-rays	1985 May 24	Leahy & Taylor (1987)

Table 5.6: Observation references for the 1987-90 quiescent phase.

	Observation date	References
radio	1989 Mar 7-12	Altenhoff et al. (1994)
	1988 Oct 14	Ivison et al. (1991)
IR	1988-90	Taranova & Yudin (1992)
optical	1988-90	Taranova & Yudin (1992)
UV	-	-
X	-	-

Table 5.7: Observation references for the 1991-95 active phase.

	Observation date	References
radio	1992 Jul 24	Skopal et al. (1996)
	1993 Jun 17 - Aug 19	Skopal et al. (1996)
	1993	Skopal et al. (1996)
IR	1991-95	Munari et al. (1996)
optical	1989-95	Skopal et al. (1996)
	1989-94	Skopal et al. (1996)
	1991-95	Munari et al. (1996)
UV	1989-95	Skopal et al. (1996)
	1991-95	Munari et al. (1996)
	1992 Nov 24	Skopal et al. (1996)
	1993 May 27	Skopal et al. (1996)
X-rays	1994 Oct 19	Ezuka et al. (1997)

Table 5.8: Observation references for the 1996-97 quiescent phase.

	Observation date	References
radio	1997 Mar 8 - Aug 31	Karovska et al. (1998)
IR	1997 May 10	Schild et al. (1999)
optical	1995 Dec 18 - 1997 Mar 11	Skopal et al. (1997)
	1996-97	Corradi et al. (2001)
UV	1997 Jul 10	Corradi et al. (2001)
X	-	-

Table 5.9: Observation references for the 1998-2000 active phase.

	Observation date	References
radio	1999 Sep 26	Eyres et al. (2002)
IR	1999-2003	Taranova & Shenavrin (2004)
optical	1998 Sep 5 - 2000 Oct 15	Eyres et al. (2002)
	1998 Jun 29 - 2001 Nov 28	Skopal et al. (2000, 2002)
	1999 Aug 12	Eyres et al. (2002)
UV	1999 Aug 12	Eyres et al. (2002)
	1998-2000 Apr	Eyres et al. (2002)
X-rays	-	-

Table 5.10: Observation references for the most recent period 2001-07.

	Observation date	References
radio	-	-
IR	1999-2007	Taranova & Shenavrin (2007)
optical	2001 Nov 28 - 2003 Nov 2003	Skopal et al. (2004)
	2003 Nov 8 - 2007 Jan 15	Skopal et al. 2007
	2004 Apr 9-11	Yoo (2006)
	2004 Oct 2-5	Yoo (2007)
UV	-	-
X	2001 Mar 27	Galloway & Sokoloski (2004)
	2006 Jan 04/05 - May 28/29	Mukai et al. (2006)

6

The symbiotic star CH Cyg II. The broad Lyα emission line explained by shocks

This chapter has been accepted for publication in
Astronomy & Astrophysics - arXiv:0807.1473
Contini, M.; Angeloni, R.; Rafanelli, P.

6.1 Introduction

As we discussed in the previous chapter, CH Cygni (CH Cyg) is amongst the most studied yet still discussed SSs. There, we have attempted a comprehensive and self-consistent modeling of continuum and line spectra in different epochs within the CW framework.

In particular, in 1977, CH Cyg underwent a powerful outburst that lasted until 1986. Towards the end, bipolar radio and optical jets appeared (Solf 1987) and spectral variations were observed in the UV and optical ranges. A remarkable characteristic of the 1985 spectrum was the appearance of a broad, strong Lyα emission line (Fig. 6.1), never evident in previous spectra (Selvelli & Hack 1985). This very peculiar spectral feature was, however, disregarded in the previous models, because it could not be explained by the CW model alone. The overall model of CH Cyg has been amplified and is presented in this paper.

We discuss the origin of the Lyα line appearance in 1985 and suggest an alternative interpretation accounting for shock waves that accompany the WD outburst during the active phase. In Sect. 6.2 we briefly review the observational trend and the previous theories suggested to explain the composite Lyα line profile. In Sect. 6.3 we describe the colliding-wind scenario and the resulting picture at the end of the 1977-1986 active phase. Consequently, adopting Chevalier's (1982) theory on the interaction of the outburst with the circumstellar medium, we apply the results by Heng & Sunyaev (2008, hereafter HS08) about the Lyα broad line formation at high-velocity shock fronts. A discussion appears in Sect. 6.4, while concluding remarks follow in Sect. 6.5.

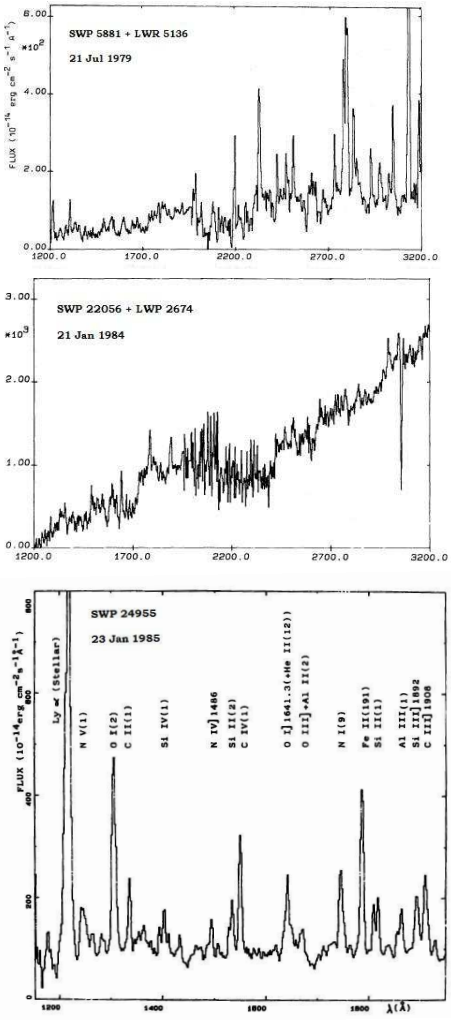

Figure 6.1: IUE spectra of CH Cyg, showing the appearance of a strong and unusually broad Lyα in 1985, at the end of the 1977-86 active phase (adapted from: MSH88, top and central panels - Selvelli & Hack 1985, bottom panel)

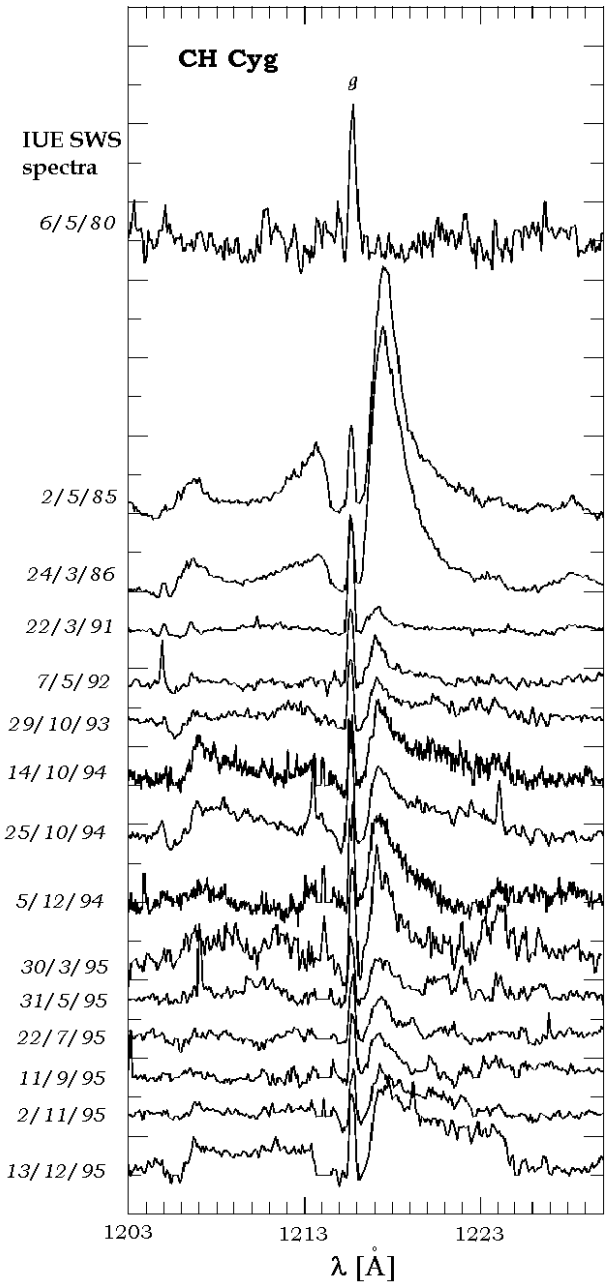

Figure 6.2: Evolution of the Lyα profile in the high-resolution IUE spectra, from 1980 to 1995. On the left, the observation date are indicated; the g marks the position of the narrow Lyα geocoronal emission (adapted from Skopal et al. 1998).

6.2 The broad Lyα line: observations and former interpretations

During the outburst started in 1977, no Lyα emission from CH Cyg was recorded. Then, towards the end of the active phase (January 1985), a strong and broad Lyα emission line, as wide as 20 Å, appeared (Figs. 6.1 and 6.2), with a strong redward-shifted wing, suggesting expansion velocities up to 4000 $km\,s^{-1}$. This outstanding behavior has not been repeated during the subsequent evolution throughout the active and quiescent phases. For instance, during the 1990-91 and 1995 quiescent stages, the Lyα virtually disappeared, together with the hot UV and optical continuum, while during the active phase 1992-1995 the Lyα line was similar in profile (Fig. 6.2), but 2-3 times weaker than in 1985 (Skopal et al 1998).

The standard Lyα profile has been decomposed into two - stable and variable - components (Skopal et al. 1998). While the former emission has usually been attributed either to the atmosphere of the red giant (Selvelli & Hack 1985) or to some circumbinary material (Skopal et al. 1998), the latter, i.e. the variable part of the profile that extends up to a high velocity ($\sim$ 2200 $km\,s^{-1}$), has been explained as a fast outflow in the vicinity of the hot star. An asymmetric high-velocity outflow (2000 $km\,s^{-1}$) was also indicated by the broad Balmer lines occurring in the spectrum on short time scales (Iijima et al. 1994). Such velocities and variabilities are similar to those characteristic of the shock between the stars created by collision of the winds. Therefore, they are less anomalous than the broad (4000 $km\,s^{-1}$) Lyα line observed at the end of the 1977-1986 active phase.

A mechanism for explaining this broadening was proposed by MSH88 who claimed that, according to Johansson & Jordan (1984), the Lyα line with an enhanced red wing, typical of line formation in an acceleration outflow, may be broadened by scattering by a high opacity. However, a stellar origin is difficult to reconcile with the sudden appearance of the broad Lyα line. MSH88 then proposed a formation region displaced from the orbital plane, connected with outflowing material, while the Balmer lines might originate in an accretion disk.

6.3 Theoretical scenarios

We would like to explain the exceptionally broad Lyα line emission in the frame of the shock-front network in CH Cyg. The results of the wind-collision model led to a detailed physical and morphological picture of the emitting nebulae within the SS. In particular it was demonstrated that the spectra depend on the system phase. In January 1985, at the end of the active phase that started in 1977, the UV and optical line ratios revealed that we were facing the circumstellar medium of the WD opposite the red giant. In this region, the dynamical consequences of the WD outburst can be compared with those of a supernova explosion, though on a different scale. Following Chevalier (1982), 8 years after

the burst, the expanding blast wave reached a relative large radius and the velocity of the shock front is in the range of those characteristic of broad Lyα line emission by charge-transfer reactions (HS08).

6.3.1 Results of the colliding-wind model

Collision of the winds (Girard & Willson 1987, Kenny & Taylor 2005) from the two-component stars leads to two main shocks: the head-on shock between the stars, facing the WD, and the head-on-back shock expanding from the system outwards (called the *reverse* and *expanding* shocks, respectively).

According to the colliding wind model, during the active phase, the broad Hβ lines with FW0M of 400-1200 $km\,s^{-1}$were emitted downstream of the head-on shock between the stars (Angeloni et al. 2007a). Although this shock is actually a standing shock, it may be accelerated throughout the decreasing density of the atmosphere by the massive wind from the red giant. The broad Balmer lines emitted downstream are particularly strong because the intensity of permitted lines depends on the temperature of the star T_* and on the ionization coefficient U. T_* can reach more than 100,000 K during the outburst and U is relatively high (> 1) because the emitting gas is close to the hot star. The broad lines decline both in intensity and width during quiescence because T_* becomes $\leq$ 30,000 K and the high velocity wind slows down. In a shock dominated regime, Rayleigh-Taylor (R-T), Richtmyer-Meshkov (R-M), and Kelvin-Helmholtz (K-H) instabilities at the shock fronts lead to fragmentation. Adopting a filling factor between 0.001 and 1, a maximum geometrical thickness of the filaments $\sim 10^{14}\ cm$, and an average velocity of 600 $km\,s^{-1}$during outburst, the variability time scale is between $\leq$ 1 hour and $\leq$ 1 month. The time scale increases during quiescence depending on the velocity decrease.

The sudden appearance of the broad (4000 $km\,s^{-1}$) Lyα line looks quite anomalous. Such a broad line could not even come from the nebula downstream of the expanding shock, which corresponds to $V_s \leq$ 150 $km\,s^{-1}$. Interestingly, the broad Lyα line appeared at about the same time as the line spectrum observed after November 1984, when the outburst was almost over. The spectrum revealed [OIII] 4363 and [OIII] 5007 lines, as well as high ionization UV emission lines, e.g. NV, CIV, SiIV, HeII, OIII] (Selvelli & Hack 1985, MSH88). Forbidden optical lines cannot survive the densities of 10^8-$10^9\ cm^{-3}$ that are characteristic of the shock between the stars. They must have been emitted from the nebula downstream of the shock expanding outward throughout the external region of the system, which in accordance with the colliding wind model (Girard & Willson 1987), is located on the side of the WD circumstellar region opposite the red giant. Consequently, the Lyα line, appearing at this very epoch, was emitted from high-velocity gas outflowing throughout the extended hemispherical region on the side of the WD less disturbed by the dynamical effects of the red giant wind.

6.3.2 The blast wave from the outburst

We adopt MSH88 suggestion that the broad Lyα emission region is connected with the outflow material.

Following Chevalier (1982), we consider the interaction of the outburst with circumstellar matter on the assumption that is built up by a steady wind. If the ambient density is described by $\rho \propto r^{-s}$ (ρ= 1.4 m_H n, where n is the density in number cm^{-3} and m_H the mass of the H atom), the steady wind corresponds to s=2. The interaction of the freely expanding matter with the surrounding medium gives rise to a high-energy density region bounded by shock waves. Two shock fronts develop, one proceeding inward in the high-density region, the other expanding outward in the circumstellar medium.

The case of uniform expansion gas is described by s=2 and γ=5/3. For s=2 the radius of the outer shock is given by the Primakoff solutions: R_{BW}=(3 E/2 π A)$^{1/3}$ $t^{2/3}$ (Chevalier 1982, Eq. 5), where E is the total energy, ρ_0 = A R^{-2} (ρ_0= 1.4 m_H n_0, where n_0 is the pre-shock density of the gas upstream), and t is the time elapsed from the burst.

This equation is valid for times longer than the time of change t_s = 0.677 $M^{3/2}$/A $E^{1/2}$, between that of the interaction of freely expanding matter with the surrounding medium and the following one, i.e. when the flow tends toward the self-similar solution for a point explosion in a power-low density profile (Sedov 1959). Here M stands for the ejected mass.

The velocity V_s= dR/dt is constrained by the observed FW0M of the Lyα line 8 years after the burst. After some algebra we obtain n_0=1.45 10^{-47} E. The mass ejected by the WD in the CH Cyg system during the 1977-86 outburst is about a few (2-3) 10^{-6} $M_\odot$(Taylor & Seaquist 1985). The total energy is half thermal and half kinetic (Chevalier 1982). The high velocity observed after January 1985 presumes that the velocity of the ejecta was $\sim$ 14,000 $km\,s^{-1}$at t=1 year. If all the ejecta had a velocity of 14,000 $km\,s^{-1}$, the associated kinetic energy would amount to 6 10^{45} erg, the total energy E=1.2 10^{46} erg, and consequently n_0 = 0.2 cm^{-3}. This in turn gives R_{BW}=2.25 10^{17} cm.

To check this result we calculate for instance, n_0 close to the WD ($n_{0_{WD}}$) at a radius $R_{0_{WD}}$ = 2 10^{13} cm. We choose the distance that was found for the standing shock between the stars by modeling the continuum SED observed in May 1985. Although the interbinary region shows mixing of the winds from the stars, the standing shock facing the WD reflects the composition of the WD (e.g. Contini 1997). From $n_{0_{WD}}$ =$n_{0_{BW}}$ $R^2_{BW}/R^2_{0_{WD}}$ where $n_{0_{BW}}$ = 0.2 cm^{-3}, we find $n_{0_{WD}}$ = 2.5 10^7 cm^{-3} in good agreement with the preshock density n_0 =5 10^7 cm^{-3} adopted to explain the continuum SED at that epoch. Constraining t_s within a maximum radius of $\sim$ 2. 10^{17} cm and adopting n_0=0.2 cm^{-3}, we find t_s= 5.2 years, confirming that Chevalier's model is valid in this case.

We can now adopt the theory of HS08, who treated the blast wave shocks in the SNR case. Their results show that broad Balmer and Lyman lines are produced by charge transfer reactions between the post-shock protons and the ambient atoms. A population of post-shock atoms follows with a broad velocity distribution (broad neutrals). For $V_s \geq$ 500 $km\,s^{-1}$the broad neutrals can pro-

duce Lyα that is blue- or red- shifted by resonance with the stationary atoms, hence providing an escaping way for the protons. For shocks with $V_s \geq$ 4000 $km\,s^{-1}$, the luminosity ratio $\Gamma_{Ly\alpha/H\alpha}$ is $\geq$ 10 (HS08, Fig. 1), so the Lyα line would be strong.

6.4 Discussion

As previously mentioned, the broad Lyα appeared at about the same phase as the expanding shock within the colliding wind scenario. The radius of the expanding nebula $R_{exp} \sim 8\ 10^{16}\ cm$ results from modeling the observed spectral energy distribution of the continuum. Notice that the radius of the blast wave R_{BW} calculated in Sect. 6.3.2, is about three times that of R_{exp}, while the physical parameters, V_s=4000 $km\,s^{-1}$and n_0=0.2 cm^{-3} of the blast wave, and V_s=150 $km\,s^{-1}$and n_0=10^5 cm^{-3} of the expanding shock, are very different. This is not surprising, considering that the blast wave stems from the outburst, while the expanding shock derives from the wind collision. The two shock fronts will hardly interfere even in the orbital plane, because R-T and K-H instabilities lead to fragmentation of matter at the shock fronts with filling factors < 0.01 (Contini & Formiggini 2001).

A velocity of $\sim$ 4000 $km\,s^{-1}$was evident from the Lyα line profile after January 1985 in CH Cyg. The other UV and optical lines showed narrow FWHM profiles. In contrast, UV lines indicating expansions of 3000-4000 $km\,s^{-1}$were observed after the 1985 eruption of the recurrent nova RS Ophiuci (Snijders 1987; Shore et al. 1996) and also optical lines after the last outburst in 2006 (Bode et al. 2007 and references therein) showed high-velocity expansion. The UV and optical lines strong enough to be observed can be emitted downstream of a strong shock if the preshock density is high enough to speed up the cooling rate ($\propto n^2$) downstream. Consequently the temperature will drop below 10^6 K, leading to recombination. However, the densities are constrained by the critical densities for collisional deexcitation of the different ions, which are relatively low ($< 10^6\ cm^{-3}$) for forbidden lines. In order to emit strong enough forbidden lines (e.g. [OIII]), a shock with V_s=4000 $km\,s^{-1}$should propagate throughout a medium with $n_0 \leq 10^4\ cm^{-3}$ The lines are emitted from the gas beyond the temperature drop characteristic of shock-dominated regimes downstream, at a distance from the shock front of $\geq 7\ 10^{16}\ cm$. Lower densities correspond to stronger forbidden lines at larger distances from the shock front. Strong [FeVII]6087, [FeX] 6375, and even [FeXI] 6986 are predicted at such high V_s. The UV lines are generally permitted or semi-forbidden, therefore they can also be emitted at higher densities. The OVI 1034 and CIV 1500 lines will be particularly strong. These predictions imply a preshock magnetic field of B_0=10^{-3} Gauss.

Such densities are not unusual in the circumstellar medium, as they were found by modeling the [OII] and [NII] lines during the active phase 1998-2000 of CH Cyg. The high preshock density would indicate that the shock is interacting with mass lost by either the progenitor star or by the SS in a previous burst.

However, such high velocities were never seen in the line profiles of CH Cyg, except for the broad Lyα in 1985.

Interestingly, the energies calculated from the temperature ($\sim$ 2.94 10^9 K) downstream of this strong shock front correspond to $\sim$ 250 keV, not far from the gamma-ray energy range, while energies of $\sim$ 21 keV (2.4 10^8 K) correspond to V_s=4000 $km\,s^{-1}$. We suggest that the observations of symbiotic star outbursts beyond hard X-rays might lead to interesting results.

The escape velocity of the WD is v_{esc} =$(2\ G\ M_{WD}/R_{WD})^{1/2} \sim 1.6\ 10^{13}/R_{WD}^{1/2}$, adopting a mass $M_{WD} \sim 1M_{\odot}$. We recover a velocity of 14,000 $km\,s^{-1}$similar to what is predicted at early times for the Lyα line FW0M profile, adopting a WD radius $R_{WD} \sim 1.36\ 10^8\ cm$ in the CH Cygni system.

6.5 Concluding remarks

In 1985, at the end of the active phase 1977-1986, a broad (4000 $km\,s^{-1}$) Lyα line was observed that had never been present in previous spectra from the symbiotic system CH Cygni.

We have noticed that the broad Lyα line appeared contemporaneously with the optical-UV spectrum emitted downstream of the shock created by collision of the winds from the stars. This shock expands throughout the extended circumbinary region located on the side of the WD circumstellar region opposite to the red giant; as a result, the Lyα line originates somewhere in the hemispherical region opposite the WD, where the dynamical consequences of the burst are less affected by the red giant wind. The overall situation is similar to that of an SN explosion. This suggests that the broad Lyα emission line and the other optical and UV lines observed at the same phase could be emitted from different shocked nebulae. We consider that the broad Lyα line stems from the WD outburst.

Applying the theory developed by Chevalier (1982) for Type II supernovae to the interaction of the WD outburst with circumstellar matter, we have found that the expanding blast wave had reached a radius $R_{BW} \sim 2.25\ 10^{17}\ cm$ 8 years after the burst for a shock velocity of 4000 $km\,s^{-1}$. We then applied the theory developed by HS08 for high-velocity shock fronts in SNR, namely, the broad Lyα line is produced by charge transfer reactions between the blast wave post-shock protons and the ambient pre-shock atoms. For shocks with $V_s \geq$ 4000 $km\,s^{-1}$, the luminosity ratio $\Gamma_{Ly\alpha/H\alpha}$ is $\geq$ 10 (HS08), so the observed Lyα line is strong.

The energy involved with the outburst is E $\sim$ 1.2 10^{46} erg, and the ambient density consistent with a velocity of 4000 $km\,s^{-1}$is $n_0 \sim 0.2\ cm^{-3}$. Higher velocities of about 14,000 $km\,s^{-1}$predicted by the Sedov solution at early times, lead to temperatures in the downstream region of such a strong-shock front, corresponding to emission in the near gamma-ray frequency range. Such emission was not observed at that time, first because of technical inadequacy and also because, during the active phase, the WD circumstellar region opposite the red giant only become visible in 1985 when the broad Lyα appeared. The velocities

had already decreased to about 4000 $km\,s^{-1}$. Actually, the SEDs in the VBU range during the 1977-86 period, presented in the previous chapter, show that the black body flux from the hot star does not appear.

According to previous results, the hard X-rays are emitted from a small region between the two component stars, while the soft X-ray are emitted from the extended circumbinary region. The results of this paper suggest that the hardest radiation ($\sim$ 250 keV) comes from the WD circumstellar region close to the WD on the opposite side of the giant star, while hard X-rays could also be observed at distances $\leq$ 0.08 pc from CH Cyg.

Finally, the complex light curves of CH Cyg (Eyres et al. 2002) show that the nebulae created by collision of the winds and the dusty shells ejected from the red giant, expanding outward beyond the binary system, lead to temporary obscuration. We suggest that the shock front at a relatively large radius corresponding to the blast wave may also contribute to obscuration episodes.

7

The symbiotic star BI Cru
The shock-front network

This chapter has been recently submitted to MNRAS
by *Contini, M.; Angeloni, R.; Rafanelli, P.*

7.1 Introduction

Symbiotic stars (SSs) are interacting binary consisting of a cool giant and a hot companion, in most cases a white dwarf (WD). Today it is known that both components loose mass in the form of stellar winds: while AGB winds are relatively well-known (typical flow velocity of $\sim$30 $km\,s^{-1}$), the observation evidence of winds from WD is more recent (Nussbaumer et al. 1995, Eriksson et al. 2007) and their characteristic velocities much higher ($\sim$1000 $km\,s^{-1}$). The inevitable collision of stellar winds with such different properties, inside and outside the system, leads to a complex network of shocked nebulae. The spectra emitted from these shocked nebulae along the whole wavelength range are generally rich in permitted and forbidden lines, giving fundamental informations about the local physical conditions. Because of the intense radiation field of the WD, also photoionization is an important energy source: this means that for a comprehensive analysis of SSs one needs models able to take into account the role of both photoionization and shocks.

Several SSs clearly show composite line profiles that reveal symmetric broad emissions characteristic of fast ($\geq$ 800 $km\,s^{-1}$) expansion in jets and lobes (Tomov 2003). The velocities in the lobes can be as low as $\sim$ 200 $km\,s^{-1}$, e.g. as deduced from the optical spectra of CH Cyg (Corradi et al. 2001) and of He2-104 (Corradi et al. 1999b). The question about whether the low velocities depend on geometrical projection can be resolved by the FWHM of the line profiles. In any case, the striking similarity of the nebulae and jets observed by Schwarz & Corradi 1992 (hereafter SC92) in the dusty SS BI Cru and He 2-104 suggests that the evolutionary link between SSs and bipolar nebulae is very strong (Corradi & Schwarz 1993, hereafter CS93).

In a few SSs (e.g. CH Cyg, BI Cru, etc), another interesting aspect refers

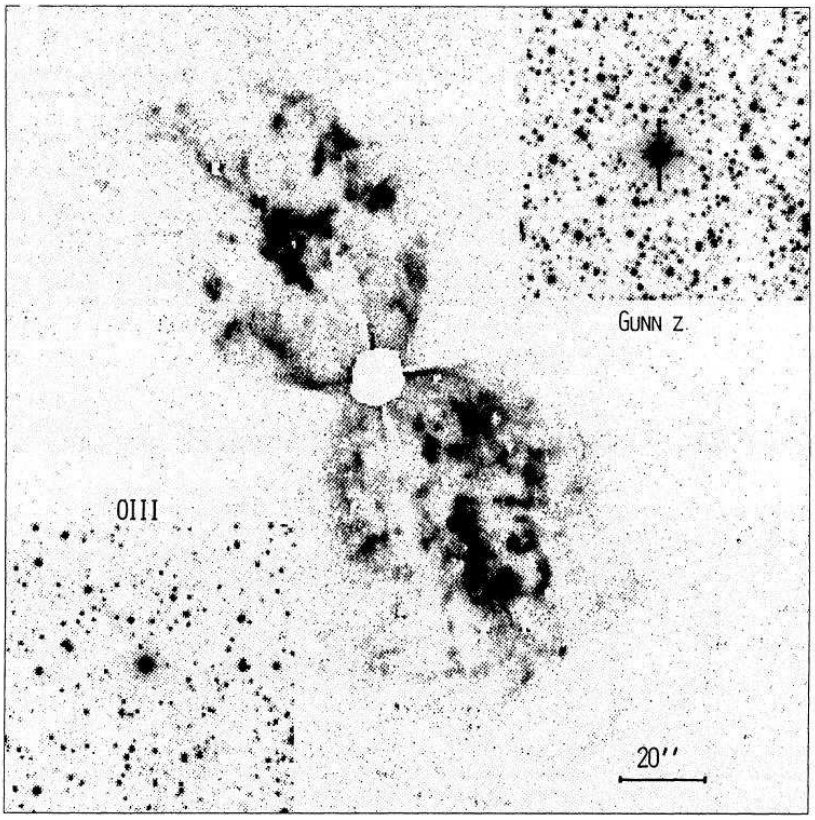

Figure 7.1: The image of BI Cru, from SC92: central image is in [NII] with [NII] continuum subtracted to remove the many background stars; top right is the Gunn z image, and bottom left the [OIII] frame.

to the hydrogen lines. As a matter of fact, broad ($\geq$ 3000 $km\,s^{-1}$) Balmer and Lyman lines were sometimes recorded and usually attributed to scattering in a dense stellar atmosphere (e.g. Mikolajewska et al. 1988). However, the recent modelling of the very broad Lyα appeared in CH Cyg at the end of the active phase 1977-1986 (Contini et al. 2008b) suggests that at that epoch we were actually seeing the blast wave of the outburst propagating in the circumstellar side of the WD less affected by the companion wind. There, the broad lines can be explained by charge transfer reactions between hydrogen atoms and protons in collisionless shocks, as in supernova explosions (Heng & Sunyaev 2008).

In this study we focus on BI Cru, a dusty symbiotic system (Kenyon 1986, Schmeja & Kimeswenger 2001) that hosts an early Mira whose pulsation period is 280d (Allen 1974), and a hot star of T_*=26500 K (Rossi et al. 1988, hereafter R88). With respect to other dusty SSs, BI Cru shows a less strong IR excess which can be attributed to thermal emission of relatively cool dust (Angeloni et al. 2007a). At a distance of 2 kpc and with a total extent of 1.3 pc, BI Cru seems to have a dynamical age of 3000 yrs, and appears morphologically (Fig. 7.1) very similar to He2-104 even if it is likely at a slightly different evolutionary age (CS93). Bipolar jets and lobes suggest the presence of an accretion disk, whose formation may be plausible assuming a typical accretion rate of 10^{-7} $M_{\odot}yr^{-1}$ (Morris 1987).

Specifically, we analyze the spectral and morphological appearance of BI Cru investigating the dynamical origin of the emission fluxes at different epochs. The modelling of line and continuum spectra makes use of SUMA, a code that simulates the physical conditions of an emitting gaseous nebula under the coupled effect of photoionization from an external source and shocks.

These composite models have been extensively used to explain SSs since 1995, e.g. RS Ophiuci (Contini, Orio & Prialnik 1995) and HM Sge (Formiggini, Contini & Leibowitz 1995), whereas a detailed analysis of the complex spectra from the extended nebulae was applied to AG Peg (Contini 1997) and RR Tel (Contini & Formiggini 1999). Spectra emitted downstream of shock fronts created by the interaction of jets and lobes with the ISM were also modelled in He 2-104 and R Aqr (Contini & Formiggini 2001, 2003, respectively).

The important role of dust is investigated in a sample of particular objects, such as H1-36 and HD 330036 (Angeloni et al. 2007a, b, c). Recently, the complex SS CH Cyg was explained through the line and continuum spectral analysis in different epochs by a model including colliding winds, dust shells and the blast wave in the WD circumstellar medium after the main outburst (Contini et al. 2008a,b).

In the following, the observations of BI Cru at different epochs are presented in Sect. 7.2. The line spectra are analyzed in Sect. 7.3 and the spectral energy distribution (SED) of the continuum in Sect. 7.4. Discussion and concluding remarks follow in Sect. 7.5.

7.2 Observational data

SSs are rarely observed with a clear long-term strategy through the years. For most objects, the data from the literature are either the result of specific observations or belong to large surveys of those generally said "peculiar emission-line stars" such as PNe, Novae, CVs, etc. Unfortunately, this is also the case of BI Cru, since its discovery on Michigan-Mount Wilson Southern Hα Survey plates in 1949. In the following, we summarize the data we have exploited in order to constrain our physical interpretation of this SS.

7.2.1 Photometric data

Besides the two upper limits (namely, missed detections) reported in Purton et al. (1982), the only information we have about the radio-mm wavelength range in BI Cru comes from the survey by Ivison et al. (1995 - Fig. 7.2, bottom panel). Unfortunately, this implies that there is no way to investigate any radio variability, which may be expected according to its specific nature of SS.

With regards to the IR photometric data, it is worth mentioning that there is a reasonable agreement between observations taken at different times (Fig. 7.2, top panel). This means that our discussion of the continuum SED is not invalidated by the well known IR variability mainly ascribed to the Mira pulsations. The data come from the IRAS Point Source Catalog (the 60 μm point being actually an upper limit) and the Midcourse Space Experiment Point Source Catalog (Version 2.3, Egan et al. 2003) for the longer wavelengths, and from Munari et al. (1992) and the 2MASS survey for the NIR range.

7.2.2 Spectroscopic data

The absence of a long-term strategy in observing BI Cru has not prevented to recognize an intrinsic variability of both emission and absorption lines since the late '40s. In particular, variations in Hα intensity were suspected already by Henize & Carlson (1980, hereafter HC80), which pointed out that the line was stronger in 1950-51 than in 1949. Moreover, they reported on a Mount Stromlo slit spectrogram obtained in 1962 which shows an emission line spectrum of relatively high excitation, superposed on a weak bluish continuum (HC80, Table 1).

In the 70's, Lee (1973) noticed on a spectrum taken in 1968 the presence of strong unusual emission features, probably due to FeII, as well as a very strong Hβ , and a moderately strong Hγ. Allen (1974), on the other hand, recorded more than 40 lines of FeII, [FeII], weak lines of HeI, and also suspected [OI], in addition to Balmer emission lines. Interestingly, he found rather broad emission lines and a weak violet component to Hγ displaced from the principal line by several hundred $km\,s^{-1}$.

In any case, the most remarkable difference between the 1962 and 1974 spectra is the presence of [OIII], [NeIII], and [SII] with different FWHM in 1962, and their absence in 1974 (HC80).

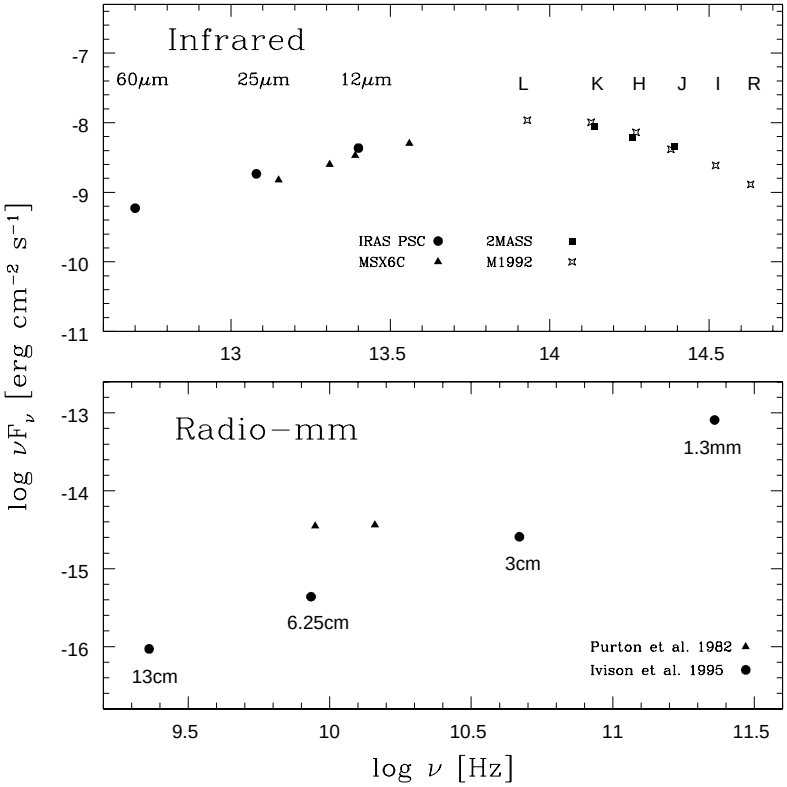

Figure 7.2: Observational data. Top panel: IR spectral range. The 60 μm IRAS point is an upper limit. Bottom panel: radio spectral range. The two data points from Purton et al. (1982, triangles) are also upper limits.

In the 80's, Whitelock et al. (1983) presented some infrared photometry, from which they deduced the evidence of a possible secular decrease in intensity between 1979 and 1982, as well as new optical spectra taken in 1974 just 55 days before the Allen's spectrum. In these spectra, surprisingly, a strong Hα emission was evident showing blue displaced P Cyg absorption and extensive emission wings with FWHM of $\sim$ 1500-2000 $km\,s^{-1}$, and FeII lines with a P Cyg profile where the E-A radial velocity difference was of 145 $km\,s^{-1}$.

A few years later, R88 analyzed a spectrum taken in 1983 with the 1.5m ESO telescope at La Silla. Strong Hα emission and prominent HeI lines confirmed that BI Cru was in a fairly high ionization stage. Several FeII emission lines were also present (Fig. 7.3). The spectrum observed by R88 shows strong Hα and blend of FeII. R88 calculated a minimum black body (bb) T=26500 K for the hot star and referred to two emission components in Hα of 110 and 350 $km\,s^{-1}$, with a violet shifted absorption extending from 0 to -300 $km\,s^{-1}$.

In the 90's, SC92 finally reported the discovery of a bipolar nebula associated with BI Cru (Fig. 7.1), whose morphology and derived expansion velocity (420 $km\,s^{-1}$) immediately suggested an evolution similarity with He2-104, the "Southern Crab". The 1986 low resolution and 1988 high resolution spectra presented there and in the following papers (such as in CS93) pointed out significant optical-UV spectral changes between 1986 and 1987, on a time-scale $\leq$ 1 year. Since then, the link between SSs and bipolar planetary nebulae has become stronger, demonstrating the need of improved models to explain such complex sets of data.

7.3 The modelling

The several emitting components recognizable in a symbiotic spectrum can be alternately visible or hidden from view depending on the different configuration with respect to the line of sight, as well as on the activity phase of the system. For instance, the modelling of CH Cyg in different phases of outburst and quiescence (Contini et al. 2008, and references therein) led to recognize some main dynamical mechanisms, that can be summarized by: the collision of the stellar winds which leads to shocked nebulae at different location on the orbital plane, the formation of a disk as a consequence of accretion phenomena, the ejection of jets and lobes perpendicularly to the orbital plane, and the outburst of the WD, at the origin of the blast wave propagation outwards in the ISM. Furthermore, also the dust shells emitted by the Mira contribute to the line and continuum spectra and might be responsible for obscuration episodes.

In the following we first identify the emitting nebulae through their emission signatures. Then, we try to interpret the spectra on the basis of the orbital motion and of the activity status of BI Cru.

Previous studies by Morris (1987) proposed a binary model for the formation of bipolar planetary nebulae via variable accretion rates onto the WD. Jets and fast winds would be thus naturally created, but for a meaningful modelling of BI Cru at least two other elements should be taken into account: the bipolar

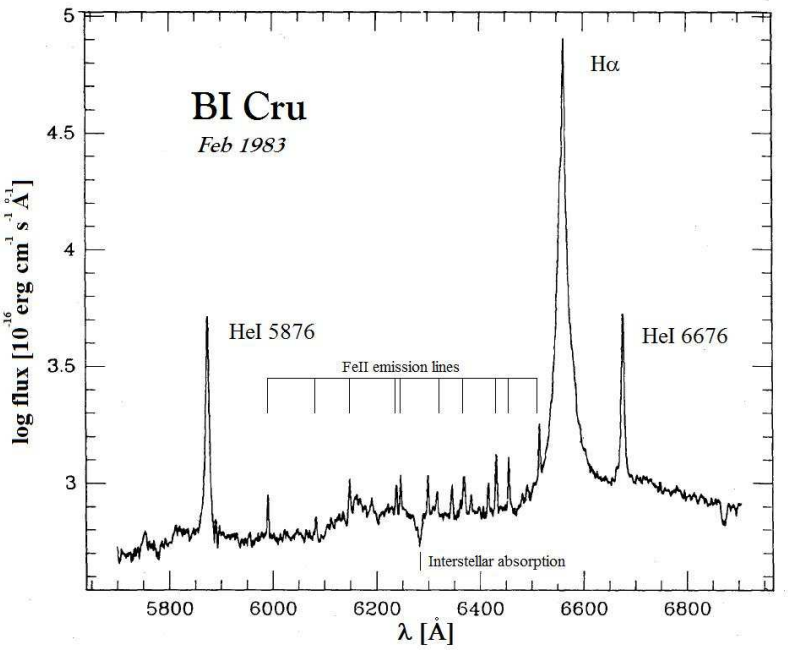

Figure 7.3: Low-resolution spectrum of BI Cru in Feb 1983: Hα and HeI 5876 and 6676 are very strong. Several FeII emission lines are also noticeable, as well as the 6284 band of interstellar origin (adapted from R88).

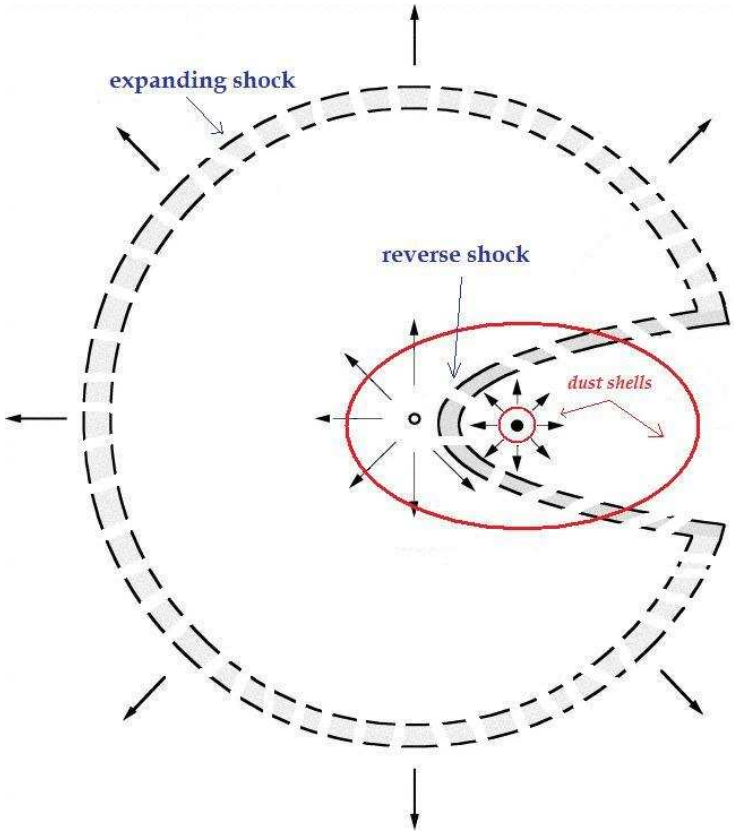

Figure 7.4: A schematic model of a colliding-wind system applied to BI Cru. The reverse and expanding shocks, as well as the location of the dust shells discussed in the text, are indicated.

nebula expands at as high velocities as the jets (200 $km\,s^{-1}$- CS93), and there is evidence of multiple events at least for He-104 which shows a very similar morphological appearance to BI Cru. CS93 claim that periodic hydrogen shell flashes may have occurred on the WD surface (every ∼1000 yr) on the basis of a M_{WD} of 1 $M_{\odot}$and an accretion rate of 10^{-8} $M_{\odot}yr^{-1}$. We will check these conditions in BI Cru in the light of our results (Sect. 7.3.3).

Anyway, we have to account for episodes of wind collisions, ejection of lobes and jets due to the accretion processes, and expansion of the blast wave in the surrounding medium as a consequence of past outbursts of the WD.

In the case of the present work, we can derive quantitative informations for our modelling only from the 1962 spectrum presented in HC80, which provides intensities and velocities of several observed lines. Further, important informations are obtained by the observation of the broad Hα line reported by Whitelock et al. (1983) and by the polarization of its wings discussed by Harries (1996). Eventually, some upper and/or lower limits to the physical parameters derived from the spatial distribution of some important emission lines (e.g. [OII], [OIII]) were found by SC92.

7.3.1 The colliding wind scenario

In the last years, several observing evidence has been accumulating that compact hot stars, regardless they belong to a SS or not, loose mass through fast (1000 km/s), low-density wind.

Regarding SSs, Nussbaumer et al. (1995) were the first that, by analyzing observations of a fast wind from the compact object, referred to a colliding-wind scenario.

Violation of hydrostatic equilibrium in a star leads to a stellar wind. This condition translates into $L^* > L_{Edd}$, where L^* is the luminosity of the star (Prialnik 2000). The Eddington luminosity $L_{Edd} = 3.2\ 10^4\ (M/M_{\odot})(\kappa_{es}/\kappa)$ $L_{\odot} \sim 10^{38}$ erg s^{-1} adopting $\kappa_{es}/\kappa \sim 1$ (where κ_{es} and κ are the opacity from electron scattering and the opacity coefficient, respectively) and M=1 $M_{\odot}$.

The luminosity of the star at maximum can be calculated by $L^*=\sigma\ {T_*}^4\ 4\ \pi$ R^2_{WD}, where σ is the Stefan-Boltzmann constant. One thus finds that a stellar wind develops from the hot component star when $T_*>$ 200,000 K for $R_{WD} \sim 0.1$ $R_{\odot}$. If the ratio of the opacities is < 1, T_* can be lower. Such high temperatures are not unusual in SSs (e.g. HM Sge, Formiggini et al. 1995).

The winds from the hot and the cool stars collide within and outside the system, hence creating a complex network of wakes and shock fronts that result in a complicated structure of gas and dust nebulae (Nussbaumer 2000). In the light of this scenario, one can consider that two shock-fronts develop from the head-on collision of the winds between the stars the *binary* colliding wind configuration discussed in some theoretical works, e.g. Girard & Willson (1987), Kenny & Taylor (2005): one strong shock-front facing the WD (the reverse shock) and the other, very weak, facing the red giant. Similarly, in the extended circumbinary region, two shock fronts develop from the head-on-back collision of the winds: one expanding outwards and the second, virtually negligible, facing

the system center. This shock network corresponds to the *concentric* colliding wind configuration of e.g. Kwok (1988a), which is a theoretical basis to the more realistic picture of shock fronts disrupted by instabilities (Fig. 7.4).

Generally, we can figure out that for all shock waves there is an *upstream* region where the gas enters into the shock front, and a *downstream* region on the opposite side. The shock front discontinuity is very thin, the thinner the faster the shock velocity.
The gas entering the strong shock front is thermalized and a high temperature region appears immediately behind the discontinuity, in the downstream region. On the opposite side of the shock front, upstream, the temperature of the gas is slightly increased by precursor radiation from the hot slabs of the gas downstream and by radiation from the WD, without reaching temperatures as high as those in the immediate post-shock region, though. The gas recombines following a high cooling rate due to the high pre-shock densities and to compression downstream.

The key parameter is obviously the shock velocity, V_s. For high-velocity shocks, the very high temperature reached in the post-shock region leads to the X-ray emission observed in some SSs. Moreover, broad strong lines can also be observed along the whole electromagnetic spectrum, particularly the coronal lines in the infrared (e.g. Angeloni et al. 2007a): therefore, from the spectral point of view, different line profiles trace different velocity regimes, allowing to highlight the different physical conditions within a symbiotic system.

Also BI Cru shows the signatures of the colliding-winds, because the range of velocities observed in literature (Sect. 7.2.2) fit with both the head-on shock between the stars ("high-velocity" regime) and the expanding shock front outward the system ("low-velocity" regime), and cannot be reconciled with a single velocity model. For instance, the [OIII] 4959 line observed in the central system corresponds to $\sim$ 400 $km\,s^{-1}$, while [NII] lines observed in the lobes display widths of $\sim$ 200 $km\,s^{-1}$. Lower velocities ($\sim$ 50 $km\,s^{-1}$) of optical-UV lines appear also in the 1962 spectra reported in HC80.

In the frame of the CW model already exploited to interpret many others symbiotic spectra (Contini et al. 2008b and references therein), we schematically refer to the nebulae downstream of the main shock fronts: 1) the head-on shock between the stars facing the hot star (named hereafter *reverse shock*) and 2) the head-on-back shock propagating outward the system (hereafter *expanding shock*). Moreover, we will consider 3) the shock front accompanying the expansion of the lobes. The nebula downstream of the reverse shock between the stars is thus characterized by photoionizing radiation and shocks acting on the same edges of the shocked nebula, while the models describing the expanding shock propagation outside the system are characterized by photoionization and shocks acting on opposite edges. For both the inverse and expanding shocks, the shock velocity is suggested by the FWHM of the line profiles, while the other physical conditions in the emitting region downstream are constrained by the observed line ratios.

The models must then account consistently for shocks and photoionization. Furthermore, since the matter is highly inhomogeneous at the shock fronts (Fig.

Table 7.1: Optical line ratios to Hβ and model parameters.

line	Vel.	obs[a]	m1	m2	m3	m4	m_{av}
[NeIII]3869+3896	-152	0.17	0.26	0.004	0.154	0.06	0.113
[SII] 4068+4077	-174	0.03	0.001	0.0	0.3	0.008	0.02
[OIII] 4363	-189	0.09	0.11	0.001	0.15	0.09	0.06
HeI 4471	-79	0.17	0.048	0.11	0.89	0.05	0.13
HeII 4686	-227	0.13	0.0016	0.2	5.e-4	0.005	0.11
[OIII] 5007+4959	-480	0.33	0.6	0.043	1.6	0.44	0.35
Hβ [b]	-	-	1.37e4	6.2e-3	0.086	1.0	-
$V_s(km\,s^{-1})$	-	-	190	150	70	400	-
n_0 (cm^{-3})	-	-	2e5	1.6e3	3e4	1.e5	-
B_0 (10^{-3} gauss)	-	-	1	1	0.1	1	-
U	-	-	15	25	-	1	-
type[c]	-	-	RDo	RDo	SD	RD	-
D (10^{15} cm)	-	-	1	1	5	0.1	-
log w	-	-	-7.0	-0.045	-2.2	-5	-
N_e (cm^{-3})	-	1e6-1e7[d]	-	-	-	-	-
T_e(K)	-	$\sim$5.5e4[e]	-	-	-	-	-

[a] reddening corrected (from HC80);
[b] in erg cm^{-2} s^{-1};
[c] RDo: radiation dominated model with radiation flux and shock acting on opposite edges of the nebula; RD: radiation dominated model with radiation flux and shock acting on the same edge; SD: shock dominated model (U=0) - see text for details;
[d] from HC80;
[e] evaluated from the observed [OIII]5007+4959/[OIII]4363.

7.1) because of instabilities at the fluid interface (e.g. the Rayleigh-Taylor (R-T), Kelvin-Helmholtz (K-H), Meshkov-Richtmyer (M-R) instabilities), different physical conditions should be accounted for, particularly regarding the density.

The models are calculated by the code SUMA[1].

7.3.2 The 1962 spectrum explained by colliding winds

We start analyzing the spectrum presented by HC80 and taken on 14 June 1962. We focus mainly on the BI Cru emission lines in 1962, because there are too few forbidden lines in the 1983 spectrum reported by R88 to allow a reliable modelling of the nebulae.

In 1962, the complex and unusual spectrum includes HeII 4686 and blended NIII 4634,41,42, while [OII] is not visible. HeI 4043 and 4026 show absorptions and P Cyg profiles. These lines led HC80 to suggest that one component of the system possesses an expanding atmosphere with an improbably large velocity of 1940 $km\,s^{-1}$, and to conclude that the forbidden lines may arise in a region apart from the one in which the permitted lines occur.

The analysis of the ion velocities shows three distinct velocity regimes: one at -55 $km\,s^{-1}$represented only by HI, a second at -115 $km\,s^{-1}$which includes

[1] http://wise-obs.tau.ac.il/$\sim$marcel/suma/index.htm

HeI and FeII, and a third at about -180 $km\,s^{-1}$which includes HeII and the forbidden lines. The individual velocities give an approximate mean error of $\pm$ 20 $km\,s^{-1}$. Only the [OIII] 4959 line shows a velocity of $\sim$ 377 $km\,s^{-1}$. In Table 7.1, the observed intensities corrected for reddening, and the FWHM are shown for the forbidden lines and the Balmer lines.

Modelling the line spectrum

The modelling of a line spectrum is based on some points. The most significant are the following:

1) recombination lines (e.g. Hβ , HeI, HeII) depend strongly on the temperature of the star and on the ionization parameter.

2) line ratios of a single element from the same ionization level but corresponding to a different quantum configuration depend on the physical conditions of the emitting gas (density, temperature, etc).

3) line ratios of single elements from different ionization stages depend on the ionization rates: radiative and/or collisional. The radiative ones are strong at temperatures $\leq 10^5$ K, while the collisional ones are strong at high temperatures. Therefore collisional ionization rates are important when shocks are at work.

4) ratios of lines from different elements are strongly linked to the relative abundances.

For a spectrum with a rich number of lines, these rules act together and constrain the models. Generally, in SSs the spectra from different nebulae must be accounted for at the same time. The results will depend on the relative weights adopted to sum up single nebula spectra.

The spectrum from Bi Cru in 1962 shows the HeI and HeII line ratios to Hβ which are described in point 1) and the [OIII] 5007+4959/[OIII]4363 ratio which refer to point 2); however, lines from different levels refer to different elements leading to an uncertain modelling. Moreover, each line is characterized by a different FWHM, indicating that a pluri-nebula model must be adopted.

We have tried to complete the insufficient informations derived from the line ratios from the modelling of other SSs. For instance, the model with V_s=400 $km\,s^{-1}$is accompanied by a high pre-shock density ($\sim 10^5\ cm^{-3}$) because located between the stars. R88 indicated a WD temperature of at least $\sim$ 26500 K , Bohigas et al. (1989) proposed a preshock magnetic field of $\sim 10^{-3}$ gauss in SSs similar to that of isolated giants. This value was confirmed e.g. in the CH Cyg system by Crocker et al. (2001) and Contini et al. (2008a). The nebula network throughout SSs is further complicated because each of the nebulae is characterized by relative abundances suiting either those of the WD atmosphere or those of the red giant (Contini 1997). We discuss the abundances in the following. In our first trial we have used solar abundances (Allen 1973).

The selected models

We have run a grid of models covering reasonable ranges of all the input parameters, also the ones roughly indicated by the observations, in order to find the

best and most consistent fit of calculated to observed line ratios. The results appear in Table 7.1.

Four models are selected amongst the best fitting ones and are described in the bottom of Table 7.1. For each of them, T_*= 26500 K and d/g= 4 10^{-4} by mass are adopted.

Models labeled with RDo indicate a radiation-dominated case where radiation flux and shock act on opposite edges of the nebula (*expanding shock*): it describes matter farthening from the hot star. Models labeled with RD deals with a radiation dominated case for which radiation flux and shock act on the same edge (*reverse shock*); the models labeled with SD are shock dominated (ionization parameter U=0).

Models m1 and m2 show different pre-shock densities by a factor of $\sim$ 100, and a slightly different ionization parameter. Shock velocities through clouds of different densities are inversely proportional to the density square root ratio: this is evident when comparing $V_s$and n_0 of models m2 and m3 and indicates that the expanding shock front is disrupted propagating in a highly inhomogeneous medium. In turn, model m2 shows both lower $V_s$and n_0 than model m1, thereby indicating that the corresponding nebula has reached a larger distance from the central system than that corresponding to the model m1.

Model m3 represents the shock dominated case, i.e. the ionization conditions throughout the nebula are dictated only by the shock, the flux being absorbed by some intervening matter (a dust shell?). Model m3 shows a very high HeI 4471/Hβ ratio and a low V_s, in agreement with the FWHM reported by HC80.

Model m4 is radiation dominated and represents the shocked nebula downstream of the shock front facing the hot star. The high shock velocity (400 $km\,s^{-1}$) suites the FWHM of the [OIII] 4959+5007 lines. The other input parameters are purposely chosen in order to give a negligible contribution to the other lines which show narrow profiles. In the frame of the colliding wind picture, model m4 represents the reverse shock front between the stars adopted to explain the spectra of D-type SSs (Angeloni et al. 2007a), while models m1, m2, and m3 represent the disrupted expanding shock front.

The models are summed up adopting different relative weights w (model m_{av}, Table 7.1). Notice that calculated [NeIII]/Hβ and [SII]/Hβ can be ameliorated adopting relative abundances of Ne and S slightly higher than solar by a factor of$\sim$ 1.5. We can deduce directly from the results the abundances of Ne and S because they are not strong coolant. Ne/H and S/H higher than solar are characteristic of the WD atmosphere although in BI Cru they are highly diluted by merging with the ISM.

The electron density N_e and the electron temperature T_e measured from the observations appear in the bottom of Table 7.1.

Using SUMA, the spectra emitted from each nebula result from integration throughout different gas regions downstream characterized by different physical conditions which derive from the cooling rate, from radiation transfer of the primary and secondary (diffuse) radiation flux, and from compression which characterizes models which account for the shocks. We present in Fig. 7.5 the profiles of the electron density N_e, electron temperature T_e, and of the fractional

abundance of the most significant ions which lead to the different lines ratios. The lines in Table 7.1 correspond to low and intermediate ionization levels, meaning that most of the lines are emitted from gas at $\leq 5\ 10^4$ K.

Finally, we refer to the several permitted FeII lines, often recorded in BI Cru spectra (Fig. 7.3) but not included in Table 7.1, which deserve a special discussion. Emission lines of FeII are seen in the ultraviolet spectra of many SSs (e.g. RR Tel, AG Peg). In some objects, optical multiplets of FeII are also seen in emission, indicating that the ultraviolet resonance lines are optically thick (Penston 1987).

Transitions between even 5-eV levels and even 3-eV levels correspond to the permitted optical multiplets 27, 28, and 29, around 4000 Å, and to the well-known feature at $\sim$ 4570 Å(Collin & Joly 2000), which are all observed in BI Cru, while forbidden [FeII] lines are rarely observed. Therefore, an overabundance of iron cannot help to explain the FeII emission by a photoionization model, but the FeII region should be heated by an additional mechanism; that is, the FeII spectrum is not produced directly by photoionization but more probably by shocks. Indeed, it is generally believed that collisional excitation is responsible for the bulk of the FeII emission, and it has been shown how these lines may represent, especially in SSs, one of the most direct traces of fast outflows of WD winds (Eriksson et al. 2007). Inelastic collisions with electrons excite the odd parity levels near 5 eV which then decay into the optical and UV lines. Self-fluorescence and fluorescent excitation by Lyα are also important sources of excitation (Sigut & Pradhan 2003).

Verner et al. (2000) have shown that at low densities ($n_e \leq 10^2$ - 10^4 cm^{-3}) the permitted optical Fe II lines are relatively weak, the reason being that the 63 lowest levels, the most populated at these densities, are all of the same (even) parity and are able to radiate only forbidden lines. The situation dramatically changes near 10^6 cm^{-3} because, then, levels of odd parity are populated by collisions, enough to produce the permitted lines. So if both the permitted Fe II and forbidden lines were produced in the same region, the density should be larger than 10^6 cm^{-3} and lower than 10^8 cm^{-3} because forbidden lines would be collisionally deexcited (Veron-Cetty et al. 2004).

In the case of BI Cru, it is interesting to note that models m1 and m4 correspond to 2 10^5 cm^{-3} and 10^5 cm^{-3}, respectively, which lead to $n_e > 10^6$ cm^{-3} downstream. In this density range, the FeII lines can then be produced without invoking a different emission region for permitted and forbidden lines, conversely to what was stated by HC80.

7.3.3 The broad Hα line

Whitelock et al. (1983) reported on a strong Hα with blue displaced P Cyg absorption at -228 $km\,s^{-1}$and extensive emission wings with FWHM of $\sim$ 1500-2000 $km\,s^{-1}$ in the 1974 spectra. On Feb 1984, R88 observed the Hα region, noting a double emission with a strong and broad violet-shifted absorption extending to about -300 $km\,s^{-1}$. The Hα absorbed portion was thought to arise from gas in front of an HII region with a large velocity gradient, hence suggesting

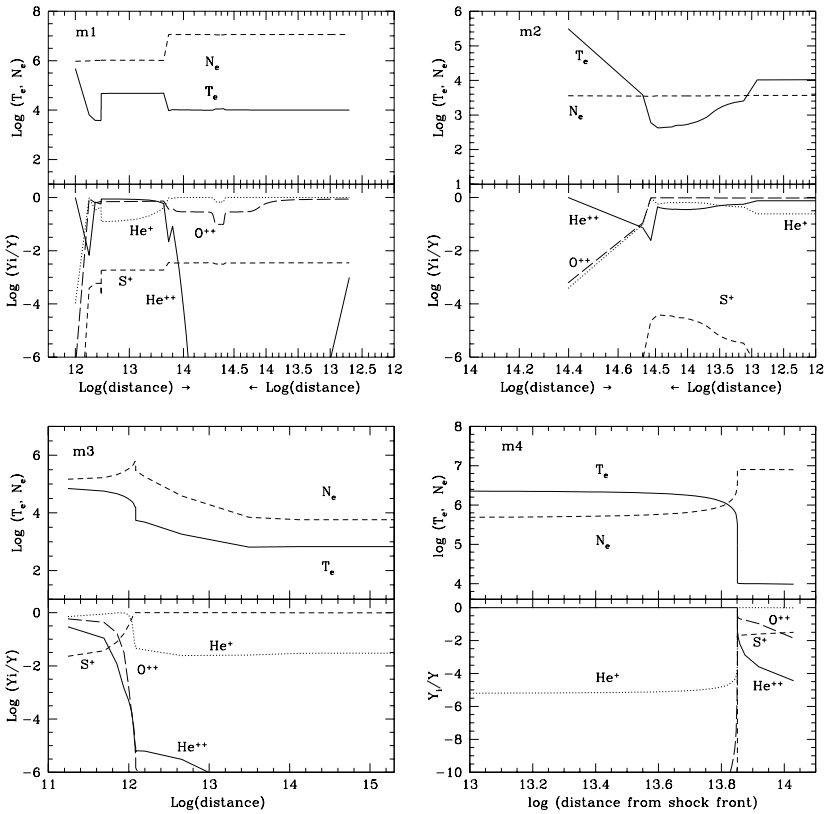

Figure 7.5: The profiles of T_e, N_e (top panels) and of the fractional abundances of the most significant ions (bottom panels) in the different models described in Table 7.1. For all diagrams the shock front is on the left.

a possible location in the cool giant wind accelerated by the intense radiation of the hot component. SC92 recorded, on a high-resolution spectrum taken in 1988, an Hα line with a FWZI of more than 3000 $km\,s^{-1}$(Fig. 7.6): such velocities are generally explained by scattering in an accretion disk (Robinson et al. 1989).

Linear spectropolarimetry of BI Cru was presented by Harries (1996). Interestingly, he found that the broad blue Hα wing is unpolarized, while the red one is strongly polarized. As already suggested by R88, Harries (1996) proposed that the Hα emission is produced in two separate velocity regimes: the central narrow peak being formed in the slow moving part of the cool component wind, while the broad component in the part of the wind approaching the hot source. The spectropolarimetric observations supported this hypothesis, although Harries (1996) believed the source of the high velocity material has to be identified in the bipolar flow.

Our analysis of such a broad Hα focuses on the evidence that the blue wing is unpolarized, meaning that this part of the line is formed out of the scattering region and excluding the broadening by scattering by a high opacity (Mikalojewska et al. 1988).

Note that in Fig. 7.3 the Hα line appears abnormally broad, whereas the other strong permitted lines (e.g. He I 5876 and 6676) which should be emitted from the same emitting gas region, are both much narrow.

Similarly to what proposed interpreting the appearance in the CH Cyg spectra of a broad Lyα at the end of the active phase 1977-1986 (Contini et al. 2008b), we would like to explain the broad Hα line in BI Cru by means of the theory of charge transfer reactions between ambient hydrogen atoms and post-shock protons at a strong shock front (Heng & Sunyaev 2008). Particularly, recall that in the circumstellar side of the WD opposite to the red giant, the effect of symbiosis is less enhanced. Here, we can apply to the WD outburst the theory developed by Chevalier (1982) for Type II supernovae.

We relay on the hypothesis of CS93 that multiple bursts could occur in BI Cru, similarly to He2-104. The WD temperature $\sim$ 26500 K found by modelling the line spectra is an indication that the last burst is completely run out. Whitelock et al. (1983) reported on FeII narrow lines and Allen's (1984) spectrum is rich in NIII and HeII lines which could be emitted from the expanding region. According to the CW model, the expanding shock front is located in the circumbinary side of the system opposite to the red giant star. Therefore we can apply Chevalier's theory.

The interaction of the freely expanding matter with the surrounding medium gives rise to a high-energy density region bounded by shock waves. Two shock fronts develop, one proceeding inward in the high density region, the other expanding outward in the circumstellar medium. Following Chevalier, we consider the interaction of the outburst with circumstellar matter on the assumption that is built up by a steady wind. If the ambient density is described by $\rho \propto \mathrm{r}^{-s}$ (ρ= 1.4 m_H n, where n is the density in number cm^{-3} and m_H the mass of the H atom) the steady wind corresponds to s=2.

By 3D hydrodynamic simulation in the case of RS Ophiuci, Walder et al.

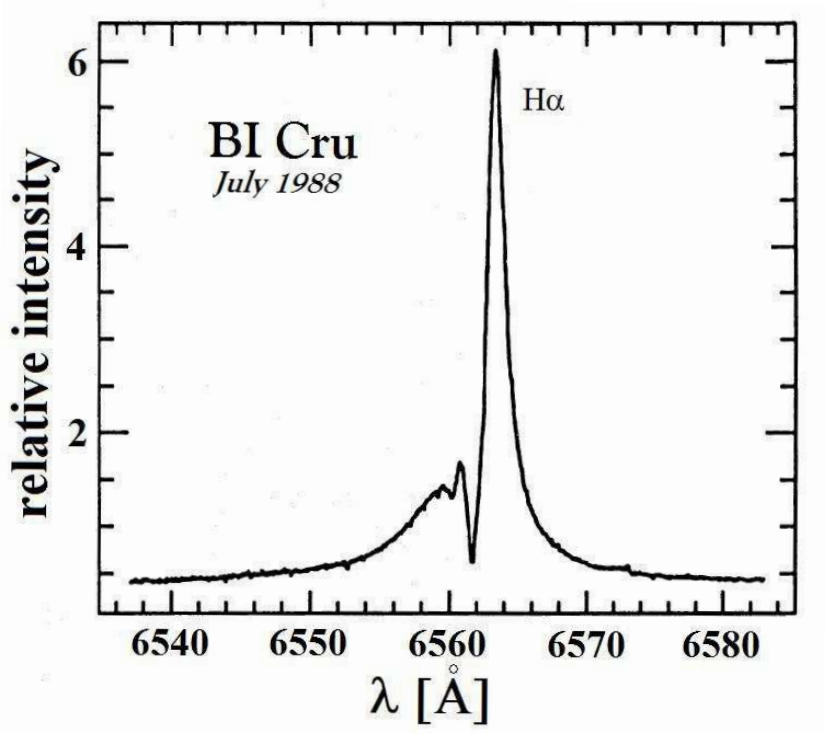

Figure 7.6: High-res spectrum of Hα as recorded in July 1988 (adapted from SC92).

(2008) found that the density decreases throughout the nova remnant as $1/r^2$ *in average*. Accordingly, we will use the case of the uniform expanding gas described by s=2 and γ=5/3.

For s=2, the radius of the outer shock corresponding to the blast wave R_{BW} (where BW stands for blast wave) is given by the Primakoff solutions (Chevalier 1982, eq.5) :

$$R_{BW} = (3E/2\pi A)^{1/3} t^{2/3} \quad (7.1)$$

where E is the total energy (twice the kinetic energy), ρ_0 = A R_{BW}^{-2}, ρ_0= 1.4 m_H n_0, and n_0 the density of the gas upstream.

This equation is valid for times longer than a specific time, called the time of change

$$t_s = 0.677 M_{ej}^{3/2}/AE^{1/2} \quad (7.2)$$

(M_{ej} is the ejected mass) between that of the interaction of freely expanding matter with the surrounding medium and the following one, i.e. when the flow tends toward the self-similar solution for a point explosion in a power-low density profile (Sedov 1959).

The velocity of the blast wave is:

$$V_{BW} = dR_{BW}/dt = 2/3(3E/2\pi A)^{1/3} t^{-1/3} \quad (7.3)$$

On the basis that no burst has been observed in the last 60 years, we adopt t$\sim$60 years as a lower limit. Following the method indicated by Contini et al. (2008b) for CH Cyg, a blast wave velocity V_{BW}= 1500-2000 $km\,s^{-1}$60 yr after the outburst, would correspond to $V_o \sim$ 5800-7700 $km\,s^{-1}$within one year. A velocity of $\sim$ 5800 $km\,s^{-1}$is about the maximum predicted by the models of Yaron et al (2005, hereafter Y05) for nova outbursts. A period less than one year after Bi Cru burst would lead to higher velocities. We will cross-check whether one year from the burst is compatible with the time of change t_s (eq. 2). In this case we will adopt an initial velocity of 5800 $km\,s^{-1}$as the escape velocity.

The results of Y05 and Prialnik & Kovetz (1995) models of nova outbursts, indicate that a velocity of 5800 $km\,s^{-1}$is possible for a 1.25 $M_\odot$WD and an accretion rate of 10^{-11} -10^{-12} $M_\odot yr^{-1}$. The corresponding ejected mass M_{ej} would be $\sim 4\ 10^{-5}$ $M_\odot$and the recurrence period $> 3\ 10^6$ yr. For a WD mass of 1.4 $M_\odot$and an accretion rate of 10^{-10} $M_\odot$yr-1 they find a maximum velocity of $\sim$ 5300 $km\,s^{-1}$, M_{ej}= 7 10^{-7} $M_\odot$and a period of 5.9 10^3 yr.

Considering an escape velocity of 5800 $km\,s^{-1}$and a WD mass M_{WD}=1.4 $M_\odot$, we obtain the radius of the WD, $R_{WD} \sim 9.35\ 10^8$ cm. This in turn corresponds to L* $\sim 10^{36}$ erg s^{-1} for T_*=200,000 K, still below the Eddington luminosity (Sect. 7.3.1). Therefore, a stellar wind could not develop from BI Cru and we will refer to a nova-type wind.

The radius of the blast wave in BI Cru 60 years after the outburst, is calculated by R_{BW} = 3/2 V_{BW} t, leading to R_{BW}=4 10^{17} cm. The ejected mass is then calculated by eq. 2. Notice that A = 1.4 m_H n_0 R_{BW}^2 is a constant. We assume that the preshock density n_0 at a radius of 4 10^{17} cm from the binary

system is of the order of that of the ISM (0.1 - 10 cm^{-3}). Then, if t_s = 1 year, $M_{ej}/\ n_0 = 4.8\ 10^{-6}\ M_\odot cm^3$, in agreement with model results by Y05 and Prialnik & Kovetz (1995).

We can calculate by A that a density of $10^9\ cm^{-3}$ could be found within a radius of $\leq 1.2\ 10^{13}$ cm from the WD.

7.3.4 The bipolar lobes

The central image of BI Cru taken by SC92 (Fig. 7.1) is in the [NII] light. No [OIII] and [OII] appear in the lobes. In the 1986/87 spectra they have identified: HI,HeI,II,OI,II,III, [OIII],NII,III,[SII], SiII, FeII,[FeIII],[FeVI], [ClIII],[ClIV]. The 1987 spectrum much richer than the 1986, confirms the important variability of the object.

The ejecta (jets) interact with the ISM with velocities $\leq 200\ km\,s^{-1}$, similarly to what happens in the He 2-104 'crab legs'. Two lobes are seen in the [NII] light but not in the [OII] and the [OIII] in both BI Cru and He2-104. Contini & Formiggini (2001) have modelled and discussed the formation of the "crab legs" in He2-104: therefore we follow the same modelling approach. First, we constrain the models by [NII]/[OII] and [NII]/[OIII] $\gg 1$. We have run a shock dominated (U=0) grid of models with $V_s$between 200 and 250 $km\,s^{-1}$as measured by SC92. Fig. 7.7 shows that the critical line ratios result easily for V_s=200 $km\,s^{-1}$. The pre-shock densities are $\geq 10^4\ cm^{-3}$, high enough to reduce the [OII] line intensity by collisional deexcitation. The magnetic field is B_0=10^{-3} Gauss, the same as that found in the system center. The geometrical thickness of the filaments in the lobes is D=10^{17} cm, leading to radiation-bound models.

Fig. 7.8 shows N_e, T_e, and the fractional abundances of the most significant ions in the lobes.

7.4 The continuum SED

The observed SED of the continuum, calculated in the light of the colliding-wind model that was extensively presented in the previous sections, is shown in Fig. 7.9. There are no data for the continuum flux in the years corresponding to the 1962 line spectra (Sect. 7.2.1). We are thus forced to refer to later data, having already checked that the intrinsic flux variations at different epochs are not as strong as to invalidate the results. At high frequencies ($\geq 10^{15}$ Hz) there are no data, so we constrain the models on the basis of the radio-IR-optical data presented in Sect. 7.2.

As we have shown in previous papers (e.g. Contini et al. 2008a), a few schematic models can describe the variable spectra of SSs: therefore we compare the combination of models calculated by the fit of the line spectrum on the basis of a data-set taken on a certain time, with a mosaic of continuum data observed at very different epochs. The modelling is presented in Fig. 7.9, left diagram. The models are scaled according to the weights shown in Table 7.1, last row.

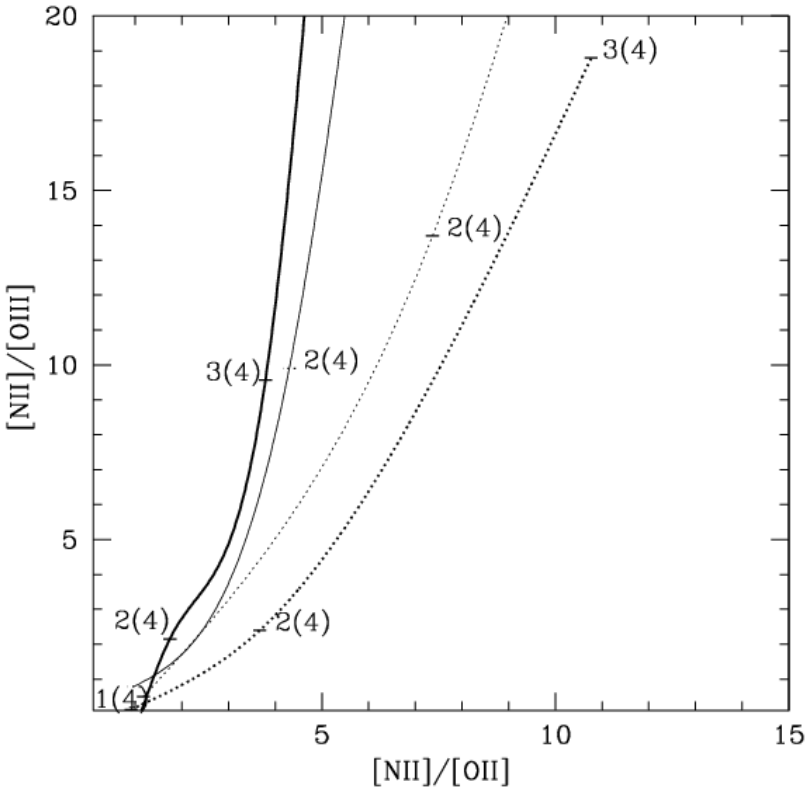

Figure 7.7: The ratio [NII]6584+6548/[OIII]5007+4959 vs [NII]6584+6548/[OII]3727+3729 for different models. Thick lines: V_s=250 $km\,s^{-1}$; thin lines: V_s=200 $km\,s^{-1}$; solid lines: B_0=10^{-4} Gauss; dotted lines: B_0=10^{-3} Gauss. Labels refer to n_0 in $10^4 cm^{-3}$.

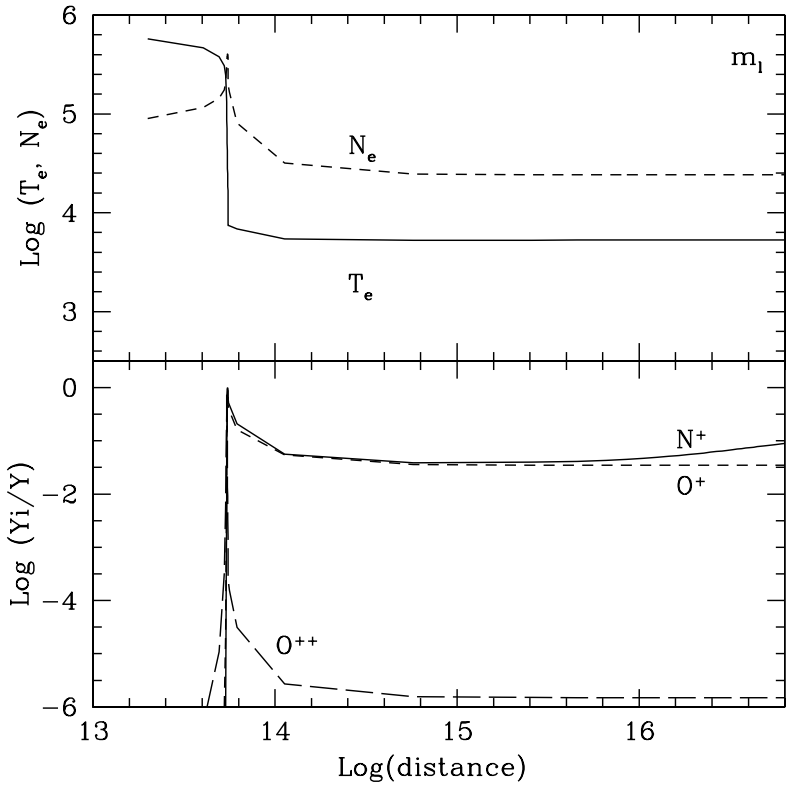

Figure 7.8: The profiles of T_e, N_e (top panels) and of the fractional abundances of the most significant ions (bottom panels) for model m_l representing the conditions in the lobes .

Model m4 (Fig. 7.9, left diagram, green lines) shows the characteristic self-absorption in the radio range already found in other SSs (e.g. H1-36, Angeloni et al. 2007b). It describes the physical conditions of the nebula downstream of the reverse shock which is characterized by relatively high densities downstream ($> 10^6\ cm^{-3}$). This model shows that X-rays could be expected in 1962. Emission in the UV - soft X-ray is suggested by model m2 (black lines) which explains also the data at longer wavelengths. This model represents the nebula expanding with V_s=150 $km\,s^{-1}$. The bremsstrahlung emitted from the shock dominated model m3 (violet lines) is not directly seen throughout the SED, however, the reprocessed emission from dust corresponding to a model with 70 $km\,s^{-1}$, contributes to very far IR emission ($\nu < 10^{12}$ Hz).

In the right diagram of Fig.7.9 model m_l, which represents emission from the lobes (SC92) is compared with the data.

We suggest that the presence of many shock fronts in BI Cru should be confirmed by synchrotron radiation in the radio range, produced by the Fermi mechanism.

The line spectra are generally modelled referring to the line *ratios*, while the SED of the continuum is modelled on the basis of *absolute* fluxes. Since the observations are taken at the Earth, while the models are calculated at the nebula, we define the factor η =(ff r/d)^2, where r is the distance of the nebula from the SS center, d the distance to Earth ($\sim$ 2 kpc for BI Cru), and ff the filling factor, in order to compare models with data. The η factors, depending on the distance of the nebulae from the system center, further constrain the models.

Adopting a continuum SED similar to that observed in later epochs, we find that the radius of the different nebulae which contribute to the 1962 line spectrum are r_{m1} = 6. 10^{13} cm, r_{m2} = 1.8 10^{17} cm, and r_{m3}= 1.5 10^{16} cm, adopting ff=1.

The distance of the reverse shock from the hot star results r= 5.4 10^{12} cm, considering that for model m4, U=1 can be combined with T_* by F_ν (R^2_{WD}/r^2)=U n c, where F_ν is the flux in number of photons cm^{-2} s^{-1} corresponding to T_*= 26500 K, and adopting R_{WD}= 7.9 10^8 cm (Sect. 7.3.3).

In Fig. 7.9, right diagram, we refer to the modelling of the lobe spectra (Sect. 7.3.3). We select a model (m_l) representing the filaments in the lobes, with V_s=210 $km\,s^{-1}$as indicated by SC92, n_0=2 10^4 cm^{-3}, B_0=10^{-3} Gauss, D=0.33 pc. The bremsstrahlung calculated by model m_l is then compared with the data in Fig. 7.9 (right diagram, blue lines), leading to log η=-12.5. SC92 indicate that the lobes had expanded to a radius $r_l\sim$1.3 pc. Combining η with r_l we obtain $ff \leq$ 0.001.

According to its nature of *dusty* SS, also BI Cru confirms that in order to reproduce the NIR-MIR continuum slopes, different "dust" temperatures should be combined (e.g. Anandarao et al. 1988, Angeloni et al. 2008, in preparation). In BI Cru, two dust shells result from the continuum SED modelling, an internal one at a temperature of 800 K with a radius of 1.5 10^{14} cm, and the other one at 250 K with a radius of 1.6 10^{15} cm.

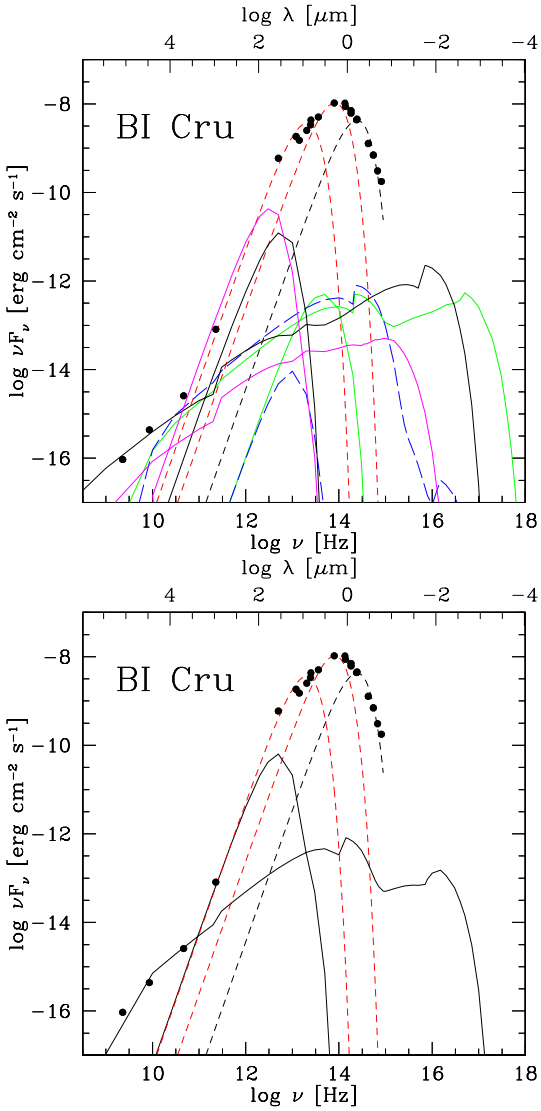

Figure 7.9: The observed BI Cru continuum SED, from radio to UV. Thin short-dashed line (red): 250 K dust shell; short-dashed line (red): 850 K dust shell; thick short-dashed line (black): Mira component. Left diagram: solid lines (green): m4; long-dashed lines (blue): m1; thick solid lines (black): m2; thin solid lines (violet): m1. Both bremsstrahlung and reradiation by dust are shown for each model. Right diagram: solid lines (black): model m_l.

7.5 Discussion and concluding remarks

We compare in the following the interpretation of the observed spectra of the SS BI Cru as given by the observers themselves with our model results.

HC80 admits that *whether the differentiation of velocities arises in a stratified atmosphere, in gas streams, in binary orbital motion or in a combination of all three is impossible to say.*

R88 suggest that *Hα is probably formed in the outer part of the cool giant's wind facing the hot star and ionized by the UV radiation which is also accelerating the wind velocity. The thick FeII emission lines are formed in the denser parts of the Mira's wind.*

SC92 claim that *the disk loses mass by excreting in the equatorial plane. The presence of cool dust is thus explained. The fast outflow mass comes from the disk or the hot secondary, the collimation being provided by the large density gradient of the thick excretion disk.*

The common conclusion is that different lines form in different regions of the binary system.

We have reached more quantitative results analyzing the line spectra observed in 1962 from BI Cru within a colliding-wind theoretical framework (Sect. 7.3). The data of the continuum were observed many years later than the 1962 line spectra. Even considering a minimum set of prototypes, the emerging picture of the BI Cru nebular network is consistent and reliable.

The result obtained by modelling the line spectra indicates that in 1962 BI Cru may have been in a post-eruption "classical" phase, with two main shock networks created by the collision of the stellar winds. The shock front between the stars, facing the hot star, has a velocity of V_s=400 $km\,s^{-1}$, while the expanding shock shows different components with V_s= 70-190 $km\,s^{-1}$, in agreement with the observed FWHM. The shock velocities are thus similar to those found in other SSs for the reverse and expanding shocks (Angeloni et al. 2007a,b,c).

The physical conditions (e.g. $n_e \geq 10^6$ cm^{-3} downstream) which result from line modelling, are responsible for self-absorption of free-free radiation in the radio range, and also indicate that both permitted and forbidden FeII lines can be emitted from the same region.

In 1992 the lobes observed by SC92 expanding out to 1.3 pc are dominated by the [NII] 6584 line. We have modelled the filaments in the lobes by constraining the model by the absence of [OII] 3727 and [OIII] 5007. The fit of the calculated model to the observed continuum SED leads to a filling factor in the lobes of about 0.001

Summarizing our results for BI Cru, the spectrum in 1962 indicates that we were seeing the internal region between the stars. The broad Hα reported in 80's and 90's indicated that we were seeing the system from the side of the WD opposite to the Mira. We wonder whether these insights are sufficient to suggest a likely orbital period for BI Cru of about 100 years.

In particular, the model developed by Chevalier (1982) to explain the hy-

drodynamical picture in SNae after the explosion, combined with the Heng & Sunyaev (2008) theory of broad Lyman and Balmer emission line production, is invoked to interpret the observed broad Hα .

The broad blue wing of the Hα line observed by Whitelock et al. (1983) in 1974 is explained by emission throughout the blast wave shock created by a past ($\geq$60 years ago), unrecorded outburst which has now reached a radius > 0.1 pc. We have demonstrated that even if no outbursts have actually been observed in BI Cru, at least in the last 60 years of historical observations, this does not invalidate our analysis; on the contrary, this negative evidence is exploited as a temporal constrain in the calculations.

Regarding the origin of the Hα broad blue wing, let us examine whether accretion disks appear in SSs. Accretion in SSs does not necessarily implies an accretion disk. Nevertheless, theoretical studies have demonstrated that disk formation around a WD when accretion occurs from a wind (and not via Roche-lobe overflow) is not impossible (Livio et al. 1986, Livio 1988). It was found that flickering variability in the X-ray from symbiotic systems (e.g. RT Cru, Luna & Sokoloski 2007) and in the optical observations of MWC 560, RS Ophiuci, etc. (Gromadzki et al. 2006) is likely powered by accretion through a disk and that jet production appears to be common in flickering symbiotics (Harries 1996, Sokoloski 2003). In the case of BI Cru, the only hint to an accretion disk is by the resolved nebula that shares a lot of features with PPNae and Post-AGB stars.

We argued that the broad blue wing of Hα could not be emitted from the accretion disk because the blue wing and the red wing show different polarization. Lines emitted from an accretion disk are generally double peaked with asymmetry in peak heights. Following Robinson et al. (1994) in SSs that are believed to contain an accretion disk, eclipses are invoked to explain unequal emission peaks. The modelling by Robinson et al. (1994) leads to two peaks with similar intensity. Therefore, the intensity of the blue peak calculated from the accretion disk eventually summed up with the broad Hα calculated in the frame of the Heng & Sunyaev (2008) theory would overcome the red peak. The observations do not confirm it, the opposite is true. Therefore, the broad blue wing of the Hα line is emitted from the extended region beyond the WD.

Robinson et al. (1994) also propose alternative sources, e.g. the Strömgen sphere surrounding the hot component of the system leading however to single-peaked lines, or Thomson scattering off free electrons present within the wind material. Anyway, the different polarization in the two Hα wings suggests a different origin.

Adopting the Robinson et al. (1989) model of line formation from the accretion disk, the broad Hα line emission should originate from the innermost regions of the disk, being always perceived only if the accretion disk is face-on, but hardly seen in other configurations. On the other hand, by Chevalier's theory (Sect. 7.3.3) the broad Hα line appears from the system edge (> 0.1 pc) and is seen only from the side of the WD opposite to the Mira.

The blast wave velocity of $\sim 5800\ km\,s^{-1}$estimated at very early times after the outburst, is higher by a factor ≥ 1.5 than the velocity of the nova ejecta

in RS Ophiuci immediately after the 1985 outburst ($\sim$ 2700-3900, Shore et al 1996), while Walder et al (2008) adopt velocities of $\sim 3500\ km\,s^{-1}$after the 2006 outburst. The first SWP spectrum dominated by two strong broad emission lines, OI+SiIII1300 and NIII] 1750, was taken about 6 days after brightness peak (Shore et al. 1996).

In the broad-line phase OI and NIII] show FWZI of the line profiles of 7000 $km\,s^{-1}$(Shore et al 1996). The data of BI Cru are not enough to make comparisons with the broad-line spectra of RS Ophiuci. On the other hand, after the start of the narrow line phase, emission from [MgV]2783 and [FeXI]1467 and [FeXI]2648 coronal lines appeared (Shore 1996). Models m1, m2, and m4 (Table 1) for BI Cru indeed lead to relatively strong [MgV] and [FeXI] lines in the UV. They correspond to FWZI $< 200\ km\,s^{-1}$. Model m3 with V_s=70 $km\,s^{-1}$is unsuitable, because the shock velocity is too low.

Moreover, the detection of X-rays from RS Ophiuci explained by shocks by e.g. Bode & Kahn (1992), could be expected also from BI Cru as can be seen in Fig. 7.9. The X-ray emission, the onset of the narrow line emission , and the peak of the radio curve (Taylor et al 1989) were simultaneous (Shore et al 1996) in RS Ophiuci. Interestingly, as can be seen in Fig. 7.9 (top diagram), a single model (m2) contribute to the X-ray, as well as to the narrow lines, and nicely reproduces the radio data of BI Cru.

Concluding, in this study we have modelled the different spectra emitted in different epochs from BI Cru. Particularly, an observed abnormal wide Hα requested an explanation based on Heng & Sunyaev theory of charge transfer between ambient hydrogen atoms and post-shock protons at a strong shock front. This was possible considering that this line was emitted from the region in the WD atmosphere opposite to the red giant, i.e. less affected by the Mira wind. Applying the self-similar theory for a point explosion in a power-law density profile (Chevalier 1982) we have calculated an escape velocity at the burst of $\sim 5800\ km\,s^{-1}$.

By checking the results of our calculations with the models calculated by Y05 and Prialnik & Kovetz (1995), we found that a nova outburst based on a thermonuclear flash could occur adopting a very low mass transfer rate ($\leq 10^{-10}$ $M_{\odot}$yr-1 and a WD mass between 1.25 and 1.4 $M_{\odot}$. We calculate an ejected mass $\geq 10^{-6}$ $M_{\odot}$, in agreement with Y05 models. Consistently, a density of $\sim$ 1 cm^{-3} is found at a distance $>$ 0.1 pc from the binary system.

Finally, some considerations about the properties of jets in symbiotic systems. By comparing the results obtained for BI Cru with those obtained for He2-104, R Aqr and CH Cyg, all objects showing lobes and jets extending outwards, we can see that the temperatures of the hot star are within the range of moderately WD at quiescence ($\leq$ 30000 K - BI Cru) and those ($\geq$ 100000 K - CH Cyg) that power the typical high ionization emission line spectra of SSs; R Aqr, with T_*=80000K, is just in between. Ionization parameters, shock velocities, pre-shock densities, pre-shock magnetic fields, and geometrical thickness of the disrupted filaments are rather similar in BI Cru and He2-104. The relatively high geometrical thickness of the nebula downstream of the reverse

shock in He 2-104 would result in a large binary separation, but the large ranges of physical conditions in the expanding fragments of BI Cru firmly indicate that its surrounding medium is actually more inhomogeneous.

The jets in R Aqr have a different aspect due to a complex combination of shock dominated and radiation dominated spectra with a low U, indicating strong dilution of the ionizing radiation. By consistent modelling of the UV spectra emitted from the reverse nebula in R Aqr, Contini & Formiggini (2003) confirmed that the inverse shock is a standing shock and that a strong shock does not form in R Aqr, even if the lines show a large FWHM. In contrast, a strong shock appears in BI Cru (V_s=400 $km\,s^{-1}$), and can be very strong ($V_s \leq$ 1500 $km\,s^{-1}$) in CH Cyg.

8

Gas and dust spectra of the D' type symbiotic star HD330036

This chapter has been published in Astronomy & Astrophysics by
Angeloni, R.; Contini, M.; Ciroi, S.; Rafanelli, P.
2007A&A,472-497A

8.1 Introduction

In 1982, Allen introduced a third, new class of SSs designated as D' type, characterized by very red colours in the far infrared (FIR) and by a cool star of spectral type F or G, in contrast to ordinary symbiotics where the cool giant is a M-type star (S type) or a Mira variable (D type). The D' types are quite rare objects, and nowadays only eight out of about 200 SS are known to belong to this class (Belczyński et al. 2000).

In the last years several studies allowed to highlight the distinctive features of D' types: for instance, both Smith et al. (2001) and Munari et al. (2001) showed that these stars display enhancements of the s-process elements that are synthesized via slow neutron captures during stellar evolution along the asymptotic giant branch (AGB). Moreover, Pereira et al. (2005, hereafter P05) and Zamanov et al. (2006, hereafter Z06), measuring the rotational velocity of the cool star, pointed out that in the D' type SS the cool component rotates faster than the isolated giants, at a substantial fraction of the critical velocity (e.g. $v \sin i \sim 0.6\ v_{crit}$ in the case of HD330036). This high rotational velocity can result in large mass loss rates, likely enhanced in the equatorial regions, and inevitably will affect the dusty environment (Soker 2002) by leading to a disk-like circumbinary structure in which the high gas density enhances dust formation and growth. It would be the dust temperature stratification in such a disk, already noticed in some D' SS (e.g. V417 Cen, Van Winckel et al. 1994), to be at the origin of the observed IR excess.
Furthermore, under the hypothesis that the D' type orbits are synchronized, Z06 argue that the orbital periods would be relatively short (4-60 days) and the interbinary distance about 2 - 5 times the cool star radius.

One of the most intriguing aspects of the symbiotic phenomenon in these cases pertains to the dusty environment. As a matter of fact these systems show a broad IR excess which, since the first IR surveys, has been attributed to emission from circumstellar dust. While in D type objects the dust excesses have colour temperatures near 1000 K (Feast et al. 1983), in the D' SS their presence is revealed only beyond ~ 3 μm, suggesting a lower temperature, which Allen (1984) stated to be not higher than 500 K.
Whichever symbiotic type (D or D'), thanks to development of IR astronomy it was soon realized that it was difficult to explain the observed IR spectrum by a single temperature component, and theoretical models too, confirmed that several "dust" temperatures should be combined in order to reproduce the NIR-MIR data (e.g. Anandarao et al. 1988, Schild et al. 2001, Angeloni et al. 2007, in preparation).

As with regards to the emission line spectra, D' types SS closely resemble planetary nebulæ (PN), leading to a long controversy about the exact evolutionary status of these stars. It is noteworthy that D' types were even classified by some authors as young, compact PN with a binary core (Feibelman 1983, 1988; Lutz 1984, hereafter L84; Bhatt 1989, van Winckel et al. 1994, Corradi et al. 1999). However, Schmeja & Kimeswenger (2001) pointed out that the NIR colours provide a reliable tool to distinguish symbiotic from genuine PN. Finally, based on the ongoing interaction between the cool giant and the nebula, Schmid & Nussbaumer (1993, hereafter SN93) favor a classification of D' type systems as symbiotic stars.

Among D' type SS one of the most intriguing object is HD330036 (CN 1-1). Unfortunately, many physical parameters of this enigmatic system remain inconclusive.
The estimate of the hot star temperature, for instance, ranges from 60000 K (SN93), 10^5 K (L84), up to $2.5\,10^5$ K (Bhatt & Mallik 1986, hereafter BM86). The interpretation of polarization measurements is also uncertain: as a matter of fact Schulte-Labdeck & Magalhaes (1987) considered the polarization observed ($\sim 3\%$) in HD330036 of purely interstellar origin; whereas Bhatt (1989) argued that, at least to some extent, the polarization can be intrinsic to the system and due to scattering by dust grains in an asymmetric nebula, calling for a bipolar morphology.
More debatable is the distance to Earth, an important parameter in the context of this analysis. L84 estimated a distance of $\sim$450 pc based upon the colour excess versus distance for stars within 20' of HD330036, but based on the cool star luminosity there are several arguments that led P05 to assume a distance of 2.3 kpc; the difference between the estimates of L84 and P05 being in someway caused by different values of the reddening. Summarizing, the probable limits for the distance to HD330036 lie within $\sim$0.6 to 2.3 kpc, with upper values being more likely.
On the other hand, the cool star is rather well known despite its evolutionary status is still controversial: P05 obtained $L = 650 L_{\odot}$, T_{eff}=6200$\pm$150K, log g=2.4$\pm$0.7 where L is the luminosity, T_{eff} the effective temperature, g

the gravity; this implies R_g=22$R_\odot$, M_g=4.46$M_\odot$ (using R_g and log g), and P_{rot} $\leq$10.4$\pm$2.4 d, where R_g, M_g and P_{rot} stand for radius, mass and rotational period, respectively.

These parameters would be theoretically sufficient for an estimate of the mass loss rate (not found in the current literature); but the problem is to understand if the formulæ for dust-enshrouded red giants and supergiants and oxygen-rich AGB stars remain valid when extended to a G-F giant. As a matter of fact, when we attempt to calculate $\dot{M}$ by using several proposed relations (Wachter et al. 2002, van Loon et al. 2005) and assuming the Pereira's stellar parameters, we find discordant results. Furthermore these values are too low ($\dot{M}< 10^{-9} M_\odot/yr$) in order to sustain any interaction of the binary stars that must be at the origin of the observed symbiotic activity (Kenyon 1988). Unfortunately, modelling of motions in the atmospheres of yellow giants and supergiants only managed to emphasize that the subject is still not well understood, resulting in the lack of reliable empirical mass loss rates or terminal wind velocities for normal G-F giants and supergiants (Achmad et al. 1997). Hence in this study we decided to attempt a completely alternative approach (Kemper et al. 2001) deriving the mass loss rate by means of the crystalline dust feature recognizable in the infrared spectrum (see §8.4.3).

Concerning the dusty environment of HD330036, Allen (1984) realized its uniqueness among the known symbiotic stars in exhibiting infrared emission bands at 3.3 and 11.3 μm, suggesting a C-rich nature of this object. A few years later BM86, on the basis of IRAS observations, noticed that there were two distinct components of infrared emitting dust in HD330036: one at a temperature of $\sim$ 215K and the other much hotter at $\sim$ 850K; interestingly, in order to obtain a likely dust to gas ratio, these authors postulated the existence of large dust grains ($a_{gr}> 1$ μm).

In the present work, we aim to model HD330036 in the light of the nowadays widely accepted interpretation of SS as colliding-wind binary systems by combining UV and optical observations (reported in L84 and SN93) together with the IR ISO-SWS (Short Wavelength Spectrograph) spectrum, analyzed here for the first time. The observed line ratios allow us to constrain the physical conditions in the emitting nebulae, while the ISO data, combined with other IR photometry points from IRAS and 2MASS, reveal the properties of dust by constraining temperature, size and chemical composition of the HD330036 dusty environment.
We start by analyzing HD330036 UV and optical line spectra in §8.2. Subsequently, cross-checking the continuum and line ratio results, we select the models which best explain the gas and dust emission. We then derive the grain conditions and location by comparing the dust reprocessed radiation flux with the IR data (§8.3). In §8.4 we review the main characteristics of dust features by carefully analyzing the ISO-SWS spectrum. Discussion and concluding remarks follow in §8.5.

Table 8.1: The UV and optical emission lines.

line	obs[1]	m1	obs[2]	m2	m3	line	obs[1]	m4	m5	m6
NV 1239	1.46±0.32	1.68	-	0.04	0.09	[OII] 3727+	10±5	8.	4.	6.3
NIV 1468	6.02±0.81	7.66	4.3	5.8	7.3	[NeIII] 3869+	200±50	197.	140.	155.
CIV 1548	48.9±4.57	44.8	46.	40.0	44.7	[CIII] 4068	< 5±4	0.07	0.07	3[5]
HeII 1640	1.65±0.25	2.28	1.1:	0.9	0.3	HI 4340	40±11	46.	45.	45.
OIII] 1662	5.61±0.76	4.8	5.3	4.4	4.25	[OIII] 4363	70±18	50.	71.	84.
NIII] 1750	6.12±0.71	5.0	5.7	4.8	5.03	HeI 4471	< 5±4	4.4	5.7	6.
CIII] 1911	19.11±1.51	19.6	21.	19.2	19.2	HeII 4686	5±4	18.	9.	6.3
Hβ 4861	-	2	-	2	1.5	Hβ 4861	100	100	100	100
Hβ 4861[3]	-	1.75	-	2.5	2	Hβ 4861[4]	-	6.57	0.15	0.098
-	-	-	-	-	-	[OIII] 5007+	1145	1150	970.	1074.
$V_s(km\,s^{-1})$	-	300	-	150.	150.	-	-	30.	50.	50.
n_0 (10^6 cm^{-3})	-	2	-	40.	40.	-	-	0.15	0.15	0.15
B_0 (10^{-3} Gauss)	-	1	-	1	1	-	-	1	1	1
$T_*(10^5$ K)	-	1.04	-	0.6	0.6	-	-	1.04	0.6	0.6
U	-	10	-	4.5	4.	-	-	0.007	0.013	0.08
d/g (10^{-4})	-	12	-	4	0.2	-	-	20	4	0.04
$a_{gr}(\mu$m)	-	0.2	-	0.2	2.	-	-	0.2	0.2	2.
C/H (10^{-4})	-	5.3	-	5.3	5.3	-	-	3.3	3.3	3.3
N/H (10^{-4})	-	5.1	-	5.1	5.1	-	-	0.91	0.91	0.91
O/H (10^{-4})	-	7.6	-	7.6	7.6	-	-	6.6	6.6	6.6

[1] fluxes in 10^{-12} erg cm^{-2} s^{-1}(Lutz 1984); [2] fluxes in 10^{-12} erg cm^{-2} s^{-1}(Schmid & Nussbaumer 1993); [3] absolute fluxes in 10^5 erg cm^{-2} s^{-1}; [4] absolute fluxes in erg cm^{-2} s^{-1}; [5] blended with [SII].

8.2 The line spectra

Low resolution ($\sim$ 7 Å) IUE spectra were taken in 1979 September, 1980 June, and 1981 April (L84), while optical spectra were obtained on the 4m and 1m telescopes at Cerro Tololo Inter-American Observatory (CTIO) during 1977, 1978, and 1979 (L84). The IUE observational data by SN93 were taken in 1984, July 26.
The observed UV and optical lines are shown in Table 8.1.

8.2.1 The UV lines

The data come from L84 and from SN93. Notice that the two spectra in the UV (left side of Table 8.1) observed in different times show compatible line ratios, considering that the Lutz (L84) spectrum is reddening corrected while Schmid & Nussbaumer (SN93) give the observed fluxes. However, the NV 1239 line which was observed by Lutz, is absent in the SN93 spectrum. This is a crucial line, which can be explained not only by a higher T_*, but also by a relatively high shock velocity. Indeed, the shock velocity is responsible for the heating of the gas downstream in the immediate post shock region where T$\propto {V_s}^2$.

We have calculated the spectra by different models, m1, m2, and m3 (Table 8.1, bottom). Model m1 leads to the best fit of the calculated line ratios to those observed by Lutz and is characterized by a high V_s (300 $km\,s^{-1}$) and a high T_* (100,000 K). Model m2 explains the line ratios observed by Schmid & Nussbaumer, who derived a temperature of the hot star T_*= 60,000 K. Such a relatively low temperature is valid to explain the UV spectra which do not show lines from relatively high ionization levels (e.g. NV). Model m3 is characterized by a large a_{gr}, which is consistent with crystalline grain formation. The relatively high magnetic field adopted ($B_0 = 10^{-3}$ Gauss) is characteristic of SS

(e.g. Crocker et al. 2001). Notice that changing one input parameter implies the readjustment of all the other ones.
The models which explain the UV line ratios correspond to different temperature of the hot star and different grain radius. T_*= 100,000 K and V_s=300 $km\,s^{-1}$which are used in model m1 to explain the UV spectrum observed by Lutz, particularly the NV 1240 line flux, are less suitable because such high velocities are not seen in the FWHM profiles. Moreover, T_*=100,000 K leads to HeII4686/Hβ higher by a factor of $\sim$ 3 than observed in the optical domain. Adopting T_*=60,000 K both the UV line spectra (SN93) and the optical ones (L84 - see §8.2) are satisfactorily explained.
Higher preshock densities are adopted by models m2 and m3 to compensate for the lower compression downstream which results from a lower V_s (=150 $km\,s^{-1}$).
Notice that the shock velocity is higher in the reverse shock (V_s=150$km\,s^{-1}$) than in expanding shock (V_s=50$km\,s^{-1}$). The velocity of the reverse shock is rather high (V_s= 150-300 $km\,s^{-1}$) compared with the ones obtained from the radial velocity measurements by L84 (Table 5 therein), which are $\sim$ 12-16 $km\,s^{-1}$. The densities in the reverse shock are too high to give a contribution to the optical forbidden lines (e.g. [OII]).
At the bottom of Table 8.1 the model input parameters are shown. The relative abundances C/H, N/H, and O/H appear in the last rows. The other elements (H, He, Ne, Mg, Si, S, Ar, Fe) are adopted with solar abundance (Allen 1973) because no lines of these elements are available. Indeed, P05 indicate a near solar Fe/H. The relative abundances adopted for models m1, m2, and m3, consistently calculated, are C/O=0.70, N/O=0.67, and C/N=1.04 in the reverse shock, while L84 found C/O=0.79 and N/O= 1.00 and SN93 C/O=0.73, N/O=0.67, and C/N=1.1. The relative abundances of C, N, and O adopted to reproduce the UV spectra are in good agreement with those obtained by SN93 for symbiotic stars. Moreover, the models lead to CIII]1909/SiIII]1892 <1, which indicates that HD330036 is less adapted to the PN class.

8.2.2 The optical lines

The optical spectra observed by Lutz (Table 8.1, right) contain several forbidden lines which refer to relatively low critical densities for deexcitation, particularly the [OII] lines. The radial velocities observed by Lutz are rather low and applicable to those found in the winds close to the giants, typical of 20-30 $km\,s^{-1}$. The densities tend to decrease with distance from the giant center: therefore the outward shocks most likely accompany the wind close to the system.

Lutz found that the emission line region is characterized by electron densities $n_e \sim 10^6$ cm^{-3} and temperatures of $T_e\sim$ 1.5 10^4 K. Actually, the weakness of the [OII] lines compared to the [OIII] lines and the strong [OIII] 4363 line are indicative of relatively high T_e and n_e. The presence of strong optical forbidden lines constrains the density to $\leq 10^6$ cm^{-3}. Recall that the densities downstream are higher than the pre-shock ones by about a factor of 10 due to compression. The agreement of the calculated optical line ratios with the data, adopting solar

abundances, indicates that the shock is sweeping up the IS matter. Moreover the models lead to grain temperatures < 100 K.

The results of model calculations reproduce the data within the errors (20-30 %), except the observed HeII 4686 line in model m4, which is overpredicted by a factor of ≥ 3: therefore this model is less reliable.

In Fig. 8.1 the profiles of the electron temperature and density downstream of the reverse shock (left) and of the expanding shock (right) are given as well as the distribution of the fractional abundance of the most significant ions (bottom panels). The photoionizing source (hot star) is on the left for all diagrams: therefore in the diagrams on the right of Fig. 8.1, which refer to the case in which the photoionizing flux and the shock act on opposite edges, the distance scale is logarithmic and symmetrical with respect to the center of the nebula with the highest resolution towards the edges of the nebula. In the top diagrams models m1 (left) and model m4 (right) appear: notice that in the nebula downstream of the reverse shock represented by model m1, sputtering is very strong and the grains are destroyed after a small distance from the shock front. In the middle diagrams the physical conditions for models m2 (left) and m5 (right) are described, while bottom diagrams refer to models m3 (left) and m6 (right). The comparison between the middle and bottom diagrams shows that relatively large grains ($a_{gr} = 2\ \mu$m) affect the distribution of the physical conditions downstream, particularly, the distribution of the ions.
The d/g ratios is selected cross-checking the modelling of the continuum: a high d/g enhances the cooling rate downstream, changes the distribution of the physical conditions and, consequently, the emitted line intensities.

8.3 The continuum SED

In Fig. 8.2 we present the modelling of the continuum SED. The data in the IR come from the ISO archive (see §8.4 for more details), the IRAS Catalog of Point Sources and the 2MASS database, while the data in the UV are extracted from the IUE archive and refer to the 1984 spectrum already analyzed by SN93. The radio points are from Milne & Aller (1982) and the optical ones (B and V Johnson magnitude) from Kharchenko (2001).

The SED of the continuum results from the contributions of the fluxes from the cool and hot stars, as well as the fluxes from the dust shells, the free-free radiation from the ionized nebulae downstream of the shock fronts (which emit the UV and optical line spectra) and the reprocessed radiation from dust.

At a first guess, the flux from the stars and the dust shells is approximated by black body radiation. We find that a black body of 6000 K fits the NIR data corresponding to the cool star, in agreement with P05, while the temperature of the hot star is calculated phenomenologically by modelling the line spectra (§8.2).

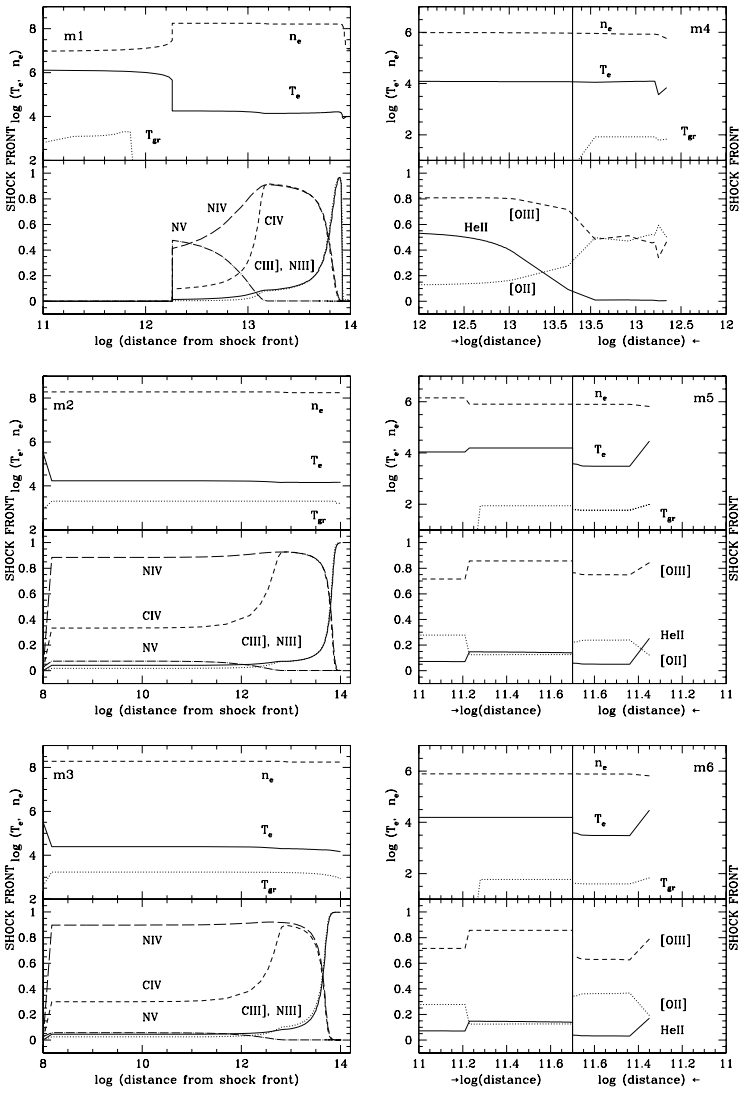

Figure 8.1: Top left diagram. Top panel: the profile of the electron temperature (solid line), of the grain temperature (dotted line), and of the electron density (dashed line) downstream of the reverse shock for model m1; bottom panel: the distribution of the fractional abundance downstream. Top right diagram: the same downstream of the expanding shock for model m4. Middle left diagram: the same for model m2. Middle right diagram: the same for model m5. Bottom left diagram: the same for model m3. Bottom right diagram: the same for model m6.

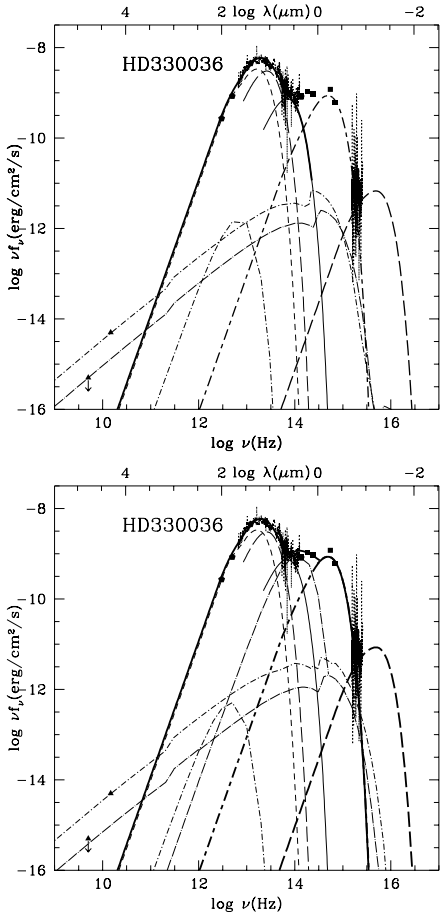

Figure 8.2: The SED of the continuum. Data (black squares) from the IUE archive (UV range), from ISO archive, IRAS catalog of Point Sources and 2MASS database (IR range), from Kharchenko 2001 (B and V Johnson magnitude) and from Milne & Aller 1982 (black triangles - radio range). The bb at 60,000K (thick long-dashed); the bb at 6000K (thick long-short dashed); the bb at 850K (thin solid); the bb at 320K (thin long-dashed); the bb at 200K (thin short-dashed). Top diagram: the free-free emission calculated by model m2 (long-dash dot); the free-free and relative dust emission by model m5 (short-dash dot); the summed SEDs of the dust shells (thick solid). Bottom diagram: the free-free and relative dust emission calculated by model m3 (long-dash dot); the free-free and relative dust emission by model m6 (short-dash dot); the summed SEDs of the dust shells, reemission by dust from the reverse shock, and the cool star bb (thick solid).

8.3.1 The shells

The dust grains form in the atmosphere of the giant star where the temperature has dropped below $\sim$ 2000 K and the densities are $\sim 10^9$ - 10^{10} cm^{-3}. Their temperature results from the coupled effect of the photoionization flux from the WD and collisional heating by the gas. The flux emitted from the region closer to the shock front downstream, which corresponds to the maximum temperature of dust, is calculated by the Plank-averaged absorption coefficient of dust. The cooling rate is very strong downstream at such densities, therefore the flux from the shell corresponds mainly to the maximum temperature of the grains and can be modelled by a black body. The temperature of the dust shells is derived by modelling the ISO and IRAS data which agree in the overlapping frequency range: this suggests that variability, at least in the IR domain, has not been as so large as to substantially modify the dust continuum emission. Fig. 8.2 show that the data can be explained by the combination of at least three black body (bb) fluxes, corresponding to temperatures of 850 K, 320 K, and 200 K.

By comparing the models with the data we obtain the η factors: they depend on the radius of the dust shell, r, and on the distance of the system to Earth d ($\eta = r^2/d^2$), being the fluxes calculated at the nebula and the data measured at Earth. Adopting d=2.3 kpc, we find r= 2.8 10^{13} cm, 4 10^{14}cm, and 10^{15} cm for the shells at 850 K, 320 K, and 200 K, respectively. Interestingly, this implies that all the dust shells are circumbinary, with the coolest ones extending well beyond the two stars if we assume an upper limit for binary separation of $\sim$ 8 10^{12} cm (5 R$_g$), as suggested by Z06. According to the D' type nature of this star, the dust shell at $\sim$ 1000 K generally observed in D type SS does not appear in HD330036.

8.3.2 The shocked nebulæ

The radiation emitted from the shocked nebulae accounts for both free-free and dust reprocessed radiation, which are calculated consistently in the downstream region. The fluxes are integrated from the shock front throughout regions of gas and dust in different physical conditions. The reradiation IR bump from dust is in fact wide because it accounts for the stratification of the temperature downstream. The free-free emission covers a large wavelength range, from radio to UV.

In the previous sections we have presented some alternative models which were selected from the best fit of the line spectra. Since the models m1 and m4, calculated adopting a hot star temperature of T$_*\sim 10^5$ K, fail in reproducing the HeII 4686/Hβ ratio, in the following we consider only the remaining ones (Table 8.1). The continua calculated by these models are compared with the observations in the diagrams of Fig. 8.2: in the top one the models m2 and m5, representing the nebulae downstream of the reverse and of the expanding shock respectively, and calculated with a hot star temperature of T$_*$=60,000 K and an initial grain radius a$_{gr}$=0.2 μm, appear; in the bottom one, models m3 and m6, calculated with T$_*$=60,000 K and a$_{gr}$=2 μm, are shown. Models

with μm-size grains are justified by the presence of silicate crystalline features (e.g. Vandenbussche et al. (2004)) at the top of the IR continuum, as we will discuss in details in §8.4.3. In Fig. 8.2 diagrams we have added also the UV data in order to constrain the free-free emission fluxes in the UV range, while the modelling of the IR data is constrained by the d/g ratios.
The calculated line ratios and the continuum have been then cross-checked until both the line spectra and the SEDs were fitted satisfactorily.

The SED of the free-free emission is constrained by the radio data, and the dust reradiation peak by the IR data in the 1-3 μm range. Generally in D-type SS the cool star is of Mira type with temperatures of 2000-3000 K, therefore their fluxes cover the data in the NIR range. However HD330036 shows a cool star temperature of 6000 K, therefore adopting the bb approximation, the emission peak results shifted toward higher frequencies and the 1-3 μm continuum data are most probably explained by hot dust.

The bottom diagram of Fig. 8.2 shows that the contribution of the reprocessed radiation of dust from the shocked nebula downstream of the reverse shock (m3) is significant in this range, while the grains downstream of the reverse shock calculated with a_{gr}=0.2 μm (m2) reach temperatures of $\sim$ 1900 K and easily evaporate: therefore model m2 is not significant in the modelling of the hot dust. The contribution of the dust downstream of the expanding shock which reaches temperatures of $\sim$ 100K cannot be seen in the SED because hidden by the dust shell radiation flux.

The d/g ratio for models m2 and m5 is 4 10^{-4}, of the order of d/g in the ISM; for models m3 and m6 the d/g ratio is even lower, being reduced by factors > 10.
Recall that dust emissivity at a temperature T_d is calculated by $4\pi\ a_{gr}^2\ B(\lambda,T_d)\ d/g\ n_{gas}$ (Viegas & Contini 1994), where $B(\lambda,T_d)$ is the Plank function. A lower d/g, which is constrained by the data, compensate for a higher a_{gr}. Therefore, in the two diagrams of Fig. 8.2 which account for models calculated by different a_{gr}, the intensities of the reradiation peak of dust relative to free-free are similar.

We can now calculate the radius of the nebulae by the η factors. Adopting d= 2.3 kpc and models m2 and m5, the reverse shock and the expanding shock have r=1.9 10^{13} cm and r=4.9 10^{15}cm respectively, while adopting models m3 and m6 the reverse and expanding shocks have radius r=1.8 10^{13} cm and r=8.7 10^{16} cm, respectively.
It is worth noticing that the reverse shock radius is an upper limit because we have adopted the maximum value for the distance (d=2.3 Kpc) and the η is constrained by the datum at 5 GHz, which in turn is an upper limit. Fig. 8.1 (bottom left) shows that the temperature of dust calculated with model m3 is $\leq$ 1500 K at a distance $> 10^{12}$ cm from the shock front, in agreement with a shell radius of $\sim 10^{13}$ cm calculated from the η factor by fitting the SED in Fig. 8.2 (bottom diagram).

Finally, the datum at 14.7 GHz in the radio range constrains the free-free, whereas the other one at 5 GHz is just an upper limit (Milne & Aller 1982). Incidentally, the physical conditions downstream of models m1, m2, and m3, representing the reverse shock, lead to an optical thickness $\tau > 1$ at $\nu < 10^{12}$ Hz

(Osterbrock 1988), indicating that self absorption of free-free radiation reduces the flux. On the other hand, the conditions downstream of models m4, m5, and m6, which represent the expanding shock, lead to $\tau < 1$ at 14.7 GHz but to $\tau \geq 1$ at 5 GHz.

Summarizing, we have found that the physical parameters which best explain the shocked nebulae are T_*=60000K, V_s=150 $km\,s^{-1}$, n_0=4 10^7 cm^{-3}, a_{gr}=0.2 μm for the reverse shock, while for the expanding shock we found V_s=50$km\,s^{-1}$, n_0=1.5 10^5 cm^{-3} and grains of both sizes,a_{gr}=0.2 μm and 2 μm.

8.4 The solid state features in the ISO spectrum

8.4.1 Observations and Data Reduction

HD330036 was observed by ISO on 1996, September 18.
In this work we focus on the spectrum taken with the Short Wavelength Spectrograph (hereafter SWS - de Graauw et al. 1996), used in full-grating scan mode (AOT 01) and covering the wavelength range between 2.38 and 45.2 μm (Fig. 8.3, top). The spectrum comes from the "Uniform database of SWS 2.4-45.4 micron spectra" within the Highly Processed Data Products (HPDP) section of the ISO Archive. This database presents a complete set of all valid SWS full-scan 2.4-45.4 μm spectra processed (from the last stage of the pipeline software) and renormalized in as uniform a manner as possible: in particular, the processing produces a single spectrum for each observation from the 288 individual spectral segments, which are the most processed form available from the ISO archive (see Sloan et al. 2003 for details about the algorithm used to generate the database). However some instrumental artifacts are still present (e.g. the strong "glitches" at $\sim$ 18 μm and $\sim$ 28 μm, whose profiles show a characteristic vertical flux increase followed by an exponential decrease, revealing then their fake origin): obviously, these features are not considered in deriving physical conclusions and we point them out whenever the real origin of such structures remains ambiguous.

We have analyzed the data with the IRAF package software. In particular, we have defined a continuum for the ISO-SWS spectrum by means of a spline-fit function: although this continuum has not necessarily a physical meaning, it merely aims to enhance the sharp structures visible on top of the spectrum and to offer an easier identification of the solid state features. The continuum subtracted spectrum of HD330036 appears in Fig. 8.3, bottom. In spite of the low quality, particularly at long wavelengths, many dust bands are recognized.

The spectrum appears substantially different with respect with the other SS ISO spectra analyzed by Angeloni et al. (2007a), where the mid-infrared range is dominated by the strong emission of amorphous silicate dust. Conversely, in HD330036 it can be clearly split into two regions: the short wavelength one (up to $\sim$15 μm) dominated by PAH prominent emission bands and the long one showing a blending of narrow and characteristic emission profiles, often concentrated in specific wavelength regions (named *complexes*), whose carriers

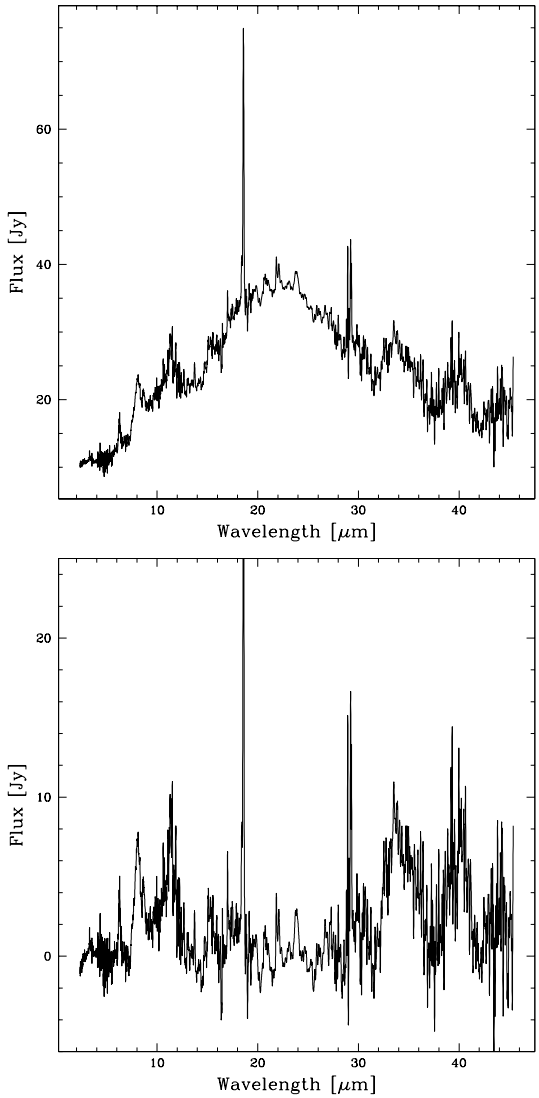

Figure 8.3: Top: ISO-SWS spectrum of HD330036. The strongest spectral features at $\sim$ 18 μm and $\sim$ 28 μm are instrumental artifacts (see §8.4.1). Bottom: continuum subtracted ISO-SWS spectrum of HD330036. Notice the bands usually attributed to Polycyclic Aromatic Hydrocarbons (at 3.3, 6.2, 8 and 11.3 μm). At longer wavelengths we found evidence for emission from crystalline silicates (clearly visible the strong complexes at $\sim$ 33 μm and $\sim$ 40 μm)

are believed to be crystalline silicates. Only after the ISO mission these dust species were noticed to be present outside our own solar system, allowing for the first time a mineralogical analysis of the dust composition in a wide range of astrophysical environments. In the following, we study the specific solid state features visible in the ISO-SWS spectrum.

8.4.2 PAHs

A wide variety of astronomical sources show some strong emission bands at 3.3, 6.2, 7.7, 8.6 and 11.3 μm: the so called unidentified infrared (UIR) emission features (Puget & Leger 1989, Allamandola et al. 1989). Though some features remain still unidentified, the UIR spectrum as a whole is linked to PAHs, or to small grains containing PAHs, whose variety and complexity suggest a mixture of ionized and neutral PAH molecules.
HD330036 exhibits all these UIR bands (Fig. 8.4). In this section we analyze their profiles and peak positions, in order to investigate the PAH local conditions and formation history.

The 3.3 μm feature

HD330036 shows a prominent feature at $\sim$ 3.29 μm (Fig. 8.4a) usually attributed to the C-H stretching mode ($v = 1 \rightarrow 0$) of highly excited PAHs. The profile is clearly asymmetric, with the blue wing steeper than the red one: the peak position and the FWHM (3.292 and 0.037 μm, respectively) look similar to other 3.3 μm profiles seen in e.g. the Orion bar, even though these characteristics seem to be not so common in astronomical sources (van Diedenhoven et al. 2004).
A second weaker feature appears centred at $\sim$ 3.40 μm and is identified with the excitation of higher vibrational levels (Barker et al. 1987). There are unconvincing proves of evidence for the other, more weaker emission features at 3.44 and 3.49 μm.
According to laboratory studies concerning the role of the physical environment on the IR spectroscopy of PAHs (Joblin et al. 1994, 1995) and on the basis of the band profile, we suggest that the carriers of the 3.3 μm feature in HD330036 are likely to be large PAH molecules, at rather high temperatures ($\sim$ 800-900 K). Although it is far from being conclusive, it is worth noticing the similarity between the observed "symbiotic" profile and the laboratory one of the ovalene molecule, as reported by Joblin et al. (1994-1995).

The 6.2 μm feature

Even if this region of the spectrum is moderately noisy, we easy recognize the feature at $\sim$ 6.2 μm (preceded by a weak feature at about 6.0 μm) which is the PAH C-C stretching band (Fig. 8.4b). The precise peak position and the width of this emission feature are strongly influenced by several parameters, e.g. molecular size, molecular symmetry, charge status, dehydrogenation, etc.

(Hudgins and Allamandola, 1999; Bakes et al. 2001; Hony et al. 2001).
The overall shape of the profile, peaking at ~ 6.25 μm and rather symmetric, suggests a link with objects such as some post-AGB and emission line stars. According to e.g. Peeters et al. (2002) this symmetry could indicate that the PAH family emitting the band at ~ 6.2 μm has not yet been exposed to a harsh radiation field and its composition still reflects the conditions during the formation at high temperatures.
This last remark, along with the temperature suggested by the 3.3 μm band, is consistent with our scenario proposing that PAHs within HD330036 lie in the inner region (T $\sim$ 850K, r $\sim 2.8\ 10^{13}$ cm) as found by modelling the SED (§8.3).

The 7.7 and 8.6 μm features

The "7.7 μm" feature in HD330036 appears clearly redshifted with respect to standard positions observed in other astronomical sources (Peeters et al. 2002). Its profile seems to show several substructures (Fig. 8.4c); furthermore the peak position is at ~ 8.08 μm, and there is no apparent trace of the two main components seen in the "standard" profiles at ~ 7.6 and ~ 7.8 μm, respectively. The band resembles the one seen in the H-deficient Wolf-Rayet star (WR 48a), hence the whole feature could be a sort of blend of "classical" 7.7 μm PAH feature and of a UIR band whose carriers seem likely to be amorphous carbon dust or large "pure" carbon molecules (Chiar et al. 2002). The band usually ascribed to C-H in plane bending vibrations of probably ionized PAHs at ~ 8.64 μm is also present.

The 11.3 μm feature

The strongest PAH band in HD330036 is that at 11.3 μm, already noticed by Roche et al. (1983). This range of the spectrum (Fig. 8.4d) can show both the bands belonging to PAHs and to silicates; moreover, unfortunately the S/N level of the detector is severely inadequate: therefore any firm conclusion based on the analysis of the profile is precluded. Nevertheless, some "peaks" and a "plateau" do not exclude the presence of some typical, intrinsic substructures.

8.4.3 Crystalline silicates

As stated above, the ISO-SWS spectrum beyond ~ 15 μm shows the presence of bands usually attributed to crystalline silicates.
Despite the S/N level not being sufficiently adequate throughout the whole spectral range (e.g. the instrumental band 3E at 27.5 - 29 μm is known for its mediocre performance) several features are clearly visible on top of the continuum, constraining the chemical compositions and spatial distribution of this symbiotic dust.

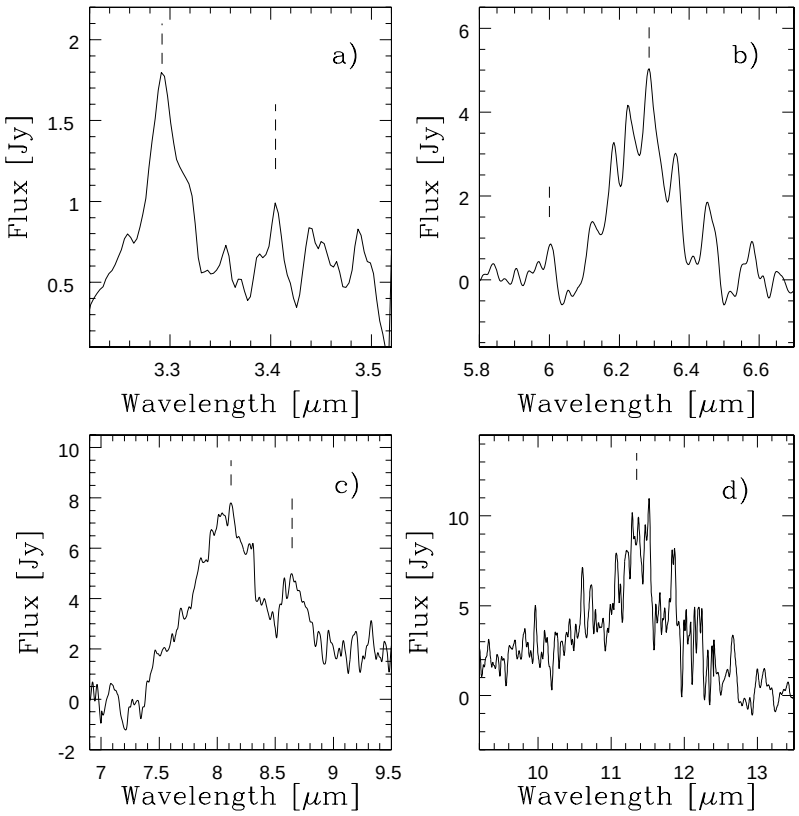

Figure 8.4: The UIR bands in the spectrum of HD330036: a) the 3.3 μm feature; b) the 6.2 μm feature; c) the 7.7 and 8.6 μm features; d) the 11.3 μm feature. The dashed lines indicate the band peak position.

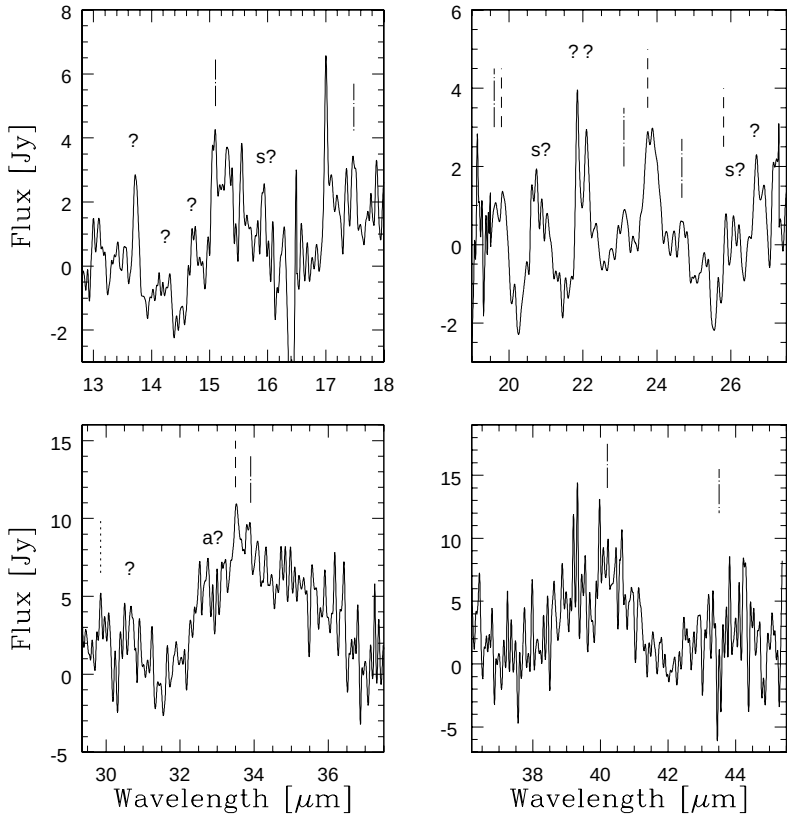

Figure 8.5: Zoom of the spectrum on some interesting crystalline complexes. Short dashed line: fosterite; dot-dashed line: enstatite; dotted line: diopside; s: silica; a: anorthite; ?: bands whose attribution to a specific carrier is still doubtful.

The observed crystalline bands

A zoom on some interesting crystalline complexes is shown in Fig. 8.5.
Most of the bands can be confidently identified with crystalline olivine (i.e. fosterite - Mg_2SiO_4) around 19.7, 23.7 and 33.6 μm and with pyroxenes (i.e. enstatite - $MgSiO_3$) around 23.1, 24.6, 40.5, 43 μm, whereas the features at $\sim$ 15.9, 20.7 and 26.1 μm seem to agree with silica (SiO_2).
Several bands still lack an identification (we label them with question marks in Fig. 8.5), thus suggesting the presence of more features, even though weaker and noisier. As already stressed in §8.4.1, some bands are rather controversial because they could originate from instrumental artifacts (e.g. the 13.8 and 14.2 μm features, with a contribution from enstatite which cannot be excluded). Furthermore, even when the actual origin of the features has been verified, it is not always easy to attribute them to some specific physical carriers (see, Molster et al. 2002b, Table 1): e.g., those at $\sim$ 20, 26, and 32 μm could fit the emission bands of diopside ($CaMgSi_2O_6$), as well as those of anorthite (i.e. at $\sim$ 26). However their relative strengths suggest that they would represent only minor components.
Spectra with a higher S/N ratio, and beyond the wavelength coverage of ISO-SWS, are clearly needed to better constrain this composition insight.

A disk-like geometry for the silicate dust shell

After the end of the ISO mission several studies pointed out that the high abundance of crystalline silicate seems to be related to the geometry of dust shells. In particular, the objects displaying strong crystalline bands (e.g. the olivine 33.6 μm band stronger than 20% over the continuum) are known to have highly flattened dust geometrical distributions (Molster et al. 1999a, 2002). The analysis of the crystalline silicate profiles in HD330036 revealed that not only the olivine 33.6 μm band is stronger than 30% over the continuum, but its profile (with a secondary peak at 34.1 μm), along with the relative strength of the 23.0 and 23.7 μm features, firmly suggest a disk-like geometry of the silicate envelope.

The existence of such a disk is also sustained by dynamical considerations of the orbital parameters of HD330036 as a binary system: in fact, as noticed by Yamamura et al. (2000) for close-binary systems like ours, the massive interaction between the giant and the secondary star strongly affect the local environment, leading to the formation of a massive circumbinary disk in a rather short time. Finally, recall that a disk structure was already proposed for another D' SS (V417 Cen) whose ring nebula has been optically resolved (Van Winckel et al. 1994).

Constraints on dust temperature

All crystalline silicates in evolved stars tend to show low temperatures (<300K; Molster et al. 2002b). We then suggest that the crystalline dust temperature in HD330036 lies close to 100-200K. Otherwise, in stark contrast to the case of

higher temperatures (Molster et al. 2002) the strength ratio of the fosterite band at 33.6 and 23.7 μm would have been < 1. This constraint on the temperature, along with the disk geometry deduced above, indicates that the crystalline silicates reside in the outer large circumbinary envelopes of dust which were found out by modelling the IR SED in §8.3.

Constraints on the mass loss rate of the cool star

As reported in the Introduction, an estimate of the mass loss rate of the cool component of HD330036 is not trivial. As the relations involving stellar atmosphere modelling are not still reliable (Achmad et al. 1997), we endeavor a different method, by exploiting once again the ISO capability along with the presence of crystalline silicate complexes. As a matter of fact, the detection limit of ISO for broad spectral features is - depending on the quality of the spectrum - around 5% of the continuum level. The fact that we clearly recognize several intense crystalline profiles defines a lower limit for the crystallinity (defined as the ratio between the total mass of crystalline silicates over the silicate total mass) and, in turn, an acceptable approximate range for the mass loss rate (Kemper et al. 2001). In particular, the ratio of the $\sim$33 μm fosterite band over the continuum ($\sim$0.4) allows us to suggest that the fosterite mass fraction is greater than 0.15 and that the cool component of the symbiotic star HD330036 loses mass at a rate of $\sim$0.4-1 $10^{-6} M_{\odot}/yr$ (see Fig. 7 of Kemper et al. 2001). Unfortunately the $\sim$43 μm enstatite band is located just to the upper edge of the SWS spectrum, and its exact profile is more ambiguous: nonetheless, a raw estimate of its relative intensity seems to support our evaluation of the HD330036 cool component mass loss.

Crystallization processes

The crystalline grains require a high temperature and a low cooling rate for annealing. Molster et al. (1999a) suggested that in the outflow sources the crystallization of silicates takes place close to the star, i.e. at high temperatures, whereas in a long-term stable disk crystallization occurs slowly at low temperatures under the influence of UV radiation (Sylvester et al. 1999). The temperature required for an effective annealing ($\sim$1000K) which would last long enough to activate the crystallization process can be reached both in the inner region of the outflowing envelope of cool component stars and in the expanding shocked nebula of SS, where colliding winds enable shock waves to compress and heat the dust grains. In effect the shocks could be a very suitable mechanism thanks to the sudden heating and gradually cooling of the grains in the post-shock region, favoring the annealing processes and letting start, in this way, the crystallization path. Such a mechanism has already been suggested with the purpose of explaining the formation of crystalline grains within comets in the protoplanetary solar nebula (Harker & Desch 2002) and claims for a non secondary role of shocks in the dust transformation processes and consequent infrared emission feature.

Our models show that at typical expansion velocities of $\sim$ 15-20 $km\,s^{-1}$, the dust grains formed at T $\sim$ 1000 K would spend 160-320 d at temperatures higher than 900 K: this period is sufficiently long for the annealing and the subsequent crystallization of a significant portion of dust grains. The crystallization process will occur within a distance of $\sim 10^{14}$ cm, which agrees with the size of the outer dust shells.

On the basis of the theoretical Silicate Evolution Index (SEI) proposed by Hallenbeck et al. (2000) and the insight of Harker & Desch (2002), we thus suggest that crystallization processes in HD330036 are triggered by shocks and annealing takes place within the circumbinary disk.

8.5 Discussion and concluding remarks

The analysis of the D' type symbiotic system HD330036 is presented by modelling the continuum SED as well as the line and dust spectra within a colliding-wind binary scenario. The framework is further complicated in D' type systems by the rapid rotation of the cool component which strongly affects the symbiotic environment, leading to a disk-like circumbinary structure where the high gas density enhances grain formation and growth.

We have found (§8.2) that the UV lines are emitted from high density gas between the stars downstream of the reverse shock, while the optical lines are emitted downstream of the shock propagating outwards the system. The models which best explain both the observed UV and optical line ratios correspond to T_*=60,000K; regarding the gas density, in the downstream region of the reverse shock it reaches 10^8 cm^{-3} while it is $\sim 10^6$ cm^{-3} downstream of the expanding shock. Free-free radiation downstream of the reverse shock is self absorbed in the radio, so the data in that range are explained by free-free emission from the nebula downstream of the expanding shock, which becomes optically thick at $\nu \leq 5$ GHz.

The relative abundances of C, N, and O adopted to reproduce the UV line ratios are in good agreement with those obtained by SN93 for symbiotic stars. Particularly, C/O=0.70 indicates a carbon enrichment of the cool star which can be explained by the transfer of matter from the hot component, a former carbon star before becoming a WD. This hypothesis, suggested by SN93, along with the CIII] 1909/SiIII]1892 ratio < 1 predicted by the models, favor a classification of HD330036 as SS more than as PN.

The SED of the continuum (§8.3) has been disentangled in the different gas and dust contributions: the star fluxes, free-free radiation as well as reprocessed radiation by dust from the shocked nebulae. Throughout the modelling we have considered silicate grains with a_{gr}=0.2 μm which correspond to the size of grains generally present in the ISM, and large grains with a_{gr}=2.0 μm which are suitable to become crystalline.
Three shells are identified in the continuum IR SED, at 850K, 320 K and 200

K with radii r = 2.8 10^{13} cm, 4 10^{14} cm, and 10^{15} cm, respectively, adopting a distance to Earth d=2.3 kpc. Interestingly, all these shells appear to be circumbinary.
The consistent modelling of line and continuum emission in the shocked nebulae leads to relatively low dust-to-gas ratios, particularly for large grains. Comparing with D-type SS which are generally rich in dust, HD330036 shows d/g lower by factors > 10. Dust reprocessed radiation at ≤ 100 K downstream of the shock propagating outwards the system cannot be seen in the SED because hidden by the dust shell radiation flux.

The analysis of the ISO-SWS spectrum (§8.4) has revealed that both PAHs and crystalline silicates coexist in HD330036. We suggest that the PAHs are associated with the internal shell at 850 K, while crystalline silicates, which derive from annealing of amorphous silicates at temperatures ≥ 1000 K, are now stored into the cool shells at 320 K and 200 K. Strong evidence that crystalline silicates are in a disk-like structure is derived on the basis of the relative band strengths.
The proposed scenario would link HD330036 to some bipolar Post-AGB stars which have shown such a dichotomy in the dust composition, location and geometrical distribution (Molster et al. 2001, Matsuura et al. 2004).
The presence of such strong crystalline features is intriguing in the light of our colliding-wind model: as a matter of fact, the temperature required for an effective annealing sufficiently long in order to activate the crystallization process could be reached in the expanding nebula of SS, where colliding winds enable shock waves to compress and heat the dust grains. Indeed the shocks can represent a very suitable mechanism to trigger the crystallization processes, principally thanks to the sudden heating and gradually cooling of the grains in the post-shock region, that might favor the annealing processes. We thus suggest that crystallization processes in HD330036 may be triggered by shocks and that annealing may take place within the circumbinary disk.

Our scenario is schematic, of course, and to date should be considered as a mere approximation of the actual physical picture. As a matter of fact, new observations have been revealing the high complexity of these symbiotic environment, where the dynamic of binary components as key parameter is not so trivial to be disregarded entirely.
The VLTI/MIDI proposal (P.I. D'Onofrio - 079.D-0242) based on our model and recently accepted by ESO aims to unveil the HD330036 dust environment by means of IR interferometric observations, constraining the morphology and the emitting properties of the PAH-dust shell.

9

Very Long Telescope Interferometer observations of HD330036

These preliminary results has been presented at the Conference
Cosmic Dust - Near & Far
held from 8th to 12th Sept 2008 in Heidelberg - Germany.

9.1 Interferometric observations of HD330036

HD330036 was observed with MIDI at the VLTI (Fig. 9.1) during ESO Period 79 (spring 2007). Observations were carried out in service mode and we obtained a total of 5 visibility points with different orientations, using Baselines UT2-UT3 and UT3-UT4 (Fig. 9.2). Not all the visibility points are of the best quality, mainly due to poor atmospheric conditions and to the low visibility of our target. However, as it can be seen, the results are as consistent as to make us confident that our following analysis is reliable. In Fig. 9.3 we show the visibility plots of the available observations.

Figure 9.1: The ESO Very Large Telescope.

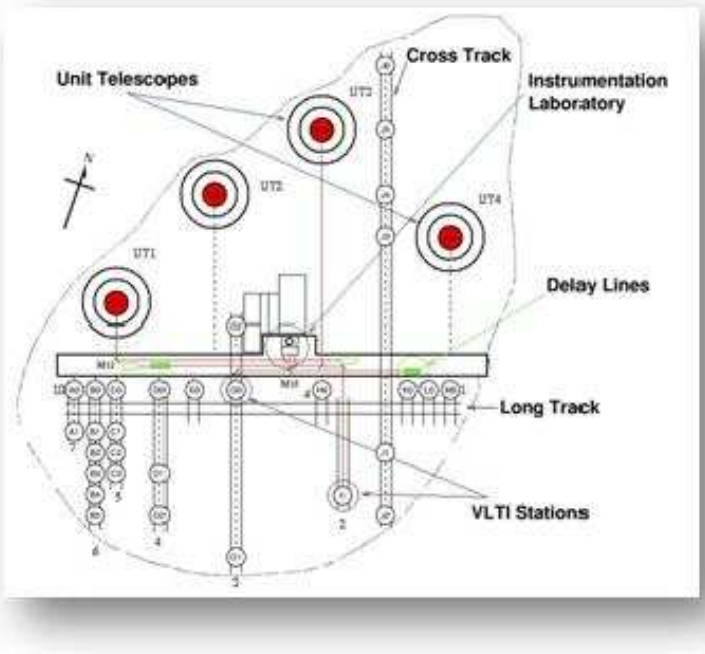

Figure 9.2: The VLT baseline configuration.

9.2 Results

In Fig. 9.4 we show the results of a very simple analysis: for each baseline and for a number of wavelength bins, we computed the Uniform Disk diameter which gives the corresponding value of visibility. Assuming that the geometry of the source is simple enough, this can give us an indication of the size of the object seen at different wavelengths and position angles. We summarized this information in Fig. 9.5. Here we show the UD diameters at the corresponding PA. The inner values correspond to the short wavelengths of the MIDI spectral range, while the outer values are those computed at the long end of the range. We also draw two ellipses to emphasize the fact that the distribution of UD diameters with PA suggests that we are in fact looking at a disk-like structure with the inner parts warmer than the outer parts, as it can be expected in the case of HD330036. Therefore we have an indication of the orientation of the dust disk around the system, as well as of the size of the disk itself. There are large uncertainties on the distance to HD330036; adopting an intermediate value of about 1 Kpc, the observed radius of 18-35 mas is equivalent to 18-35 AU, or 2.7-5.25 10^{14} cm. We plan to obtain more realistic models for the dust

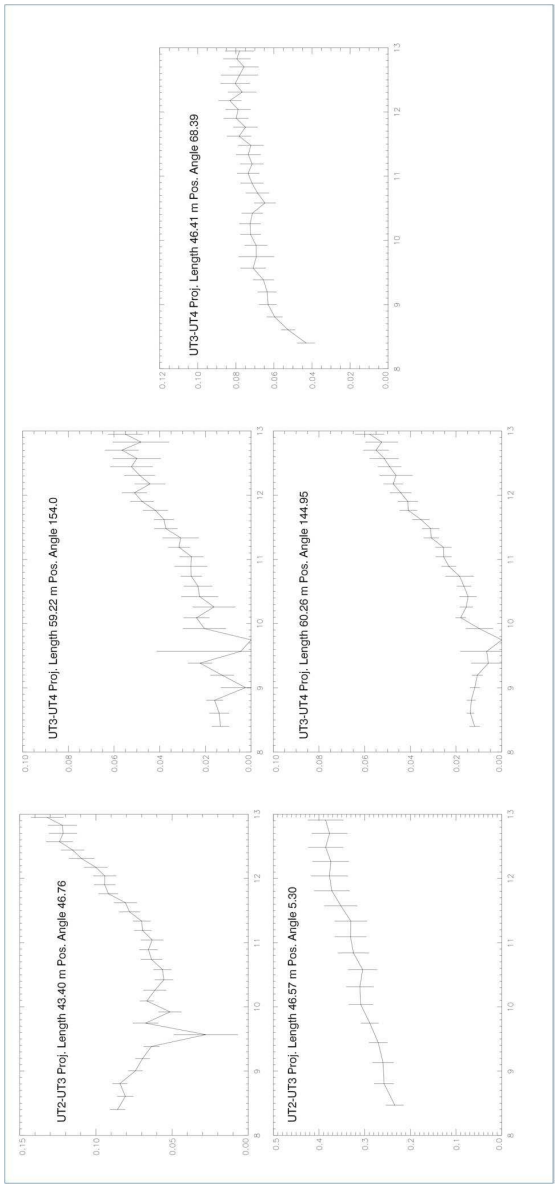

Figure 9.3: Visibility plots for different baselines and position angles. The wavelength is expressed in microns.

distribution and temperature; the simultaneous fitting of the visibilities and SED of HD330036 with these models will give us more detailed information on this object.

An interesting spectral feature in the spectrum of HD 330036 is the PAH emission at 11.3 μm. This feature, well visible in the ISO-SWS spectrum, is also detected in our MIDI observations (Fig. 9.6). However, we notice that, plotting the so-called *correlated flux*, i.e. the flux multiplied by the visibility, which can be interpreted as the flux coming from the more compact regions of the object, the PAH feature is not visible. This could be an indication that the region where the PAH feature is emitted is larger than that of the continuum emission; this conclusion, due to the poor SNR of our visibility data, must be confirmed with further observations. As described in the previous chapter, current models for this kind of objects would expect PAH emission from a more compact region, which is the opposite of what our data indicate.

9.3 Future prospects

The data we obtained are giving us the first indications on the dust distribution in the HD330036 system; however, more work is needed. In particular, we will get additional data with the Auxiliary Telescopes (ATs) during 2009, using the 16m baseline. While the source is at the limit of the MIDI sensitivity using the ATs, we expect to have a much larger visibility thanks to the short baseline. If the observations are successful, we will get a very interesting complementary set of data.
We are in the process of performing detailed numerical models of the dust distribution and comparing different models with the SED and the visibilities observed, with the aim of publishing the results during 2009.

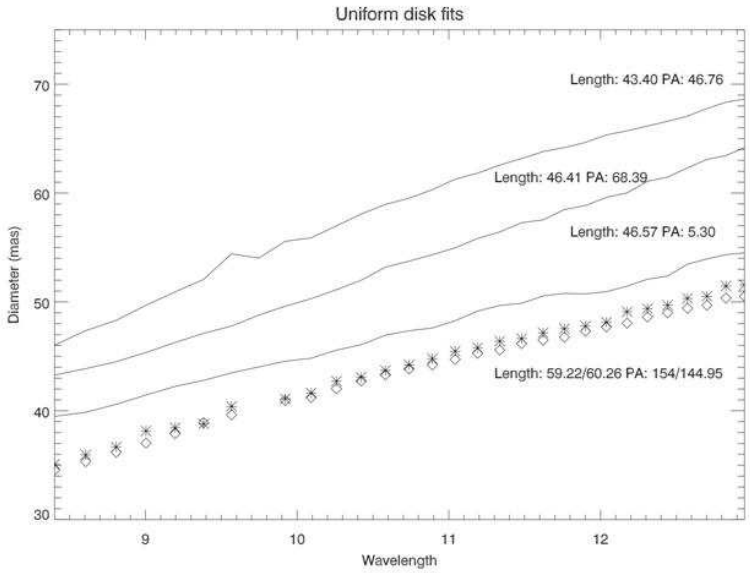

Figure 9.4: Uniform disk fit results for the different visibility points.

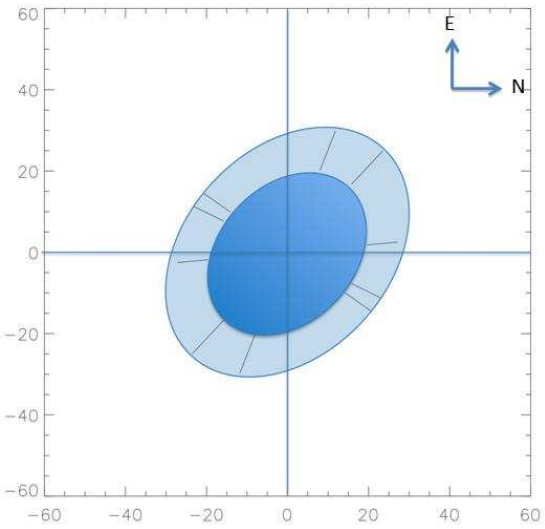

Figure 9.5: HD330036 approximate shape suggested by the visibility analysis.

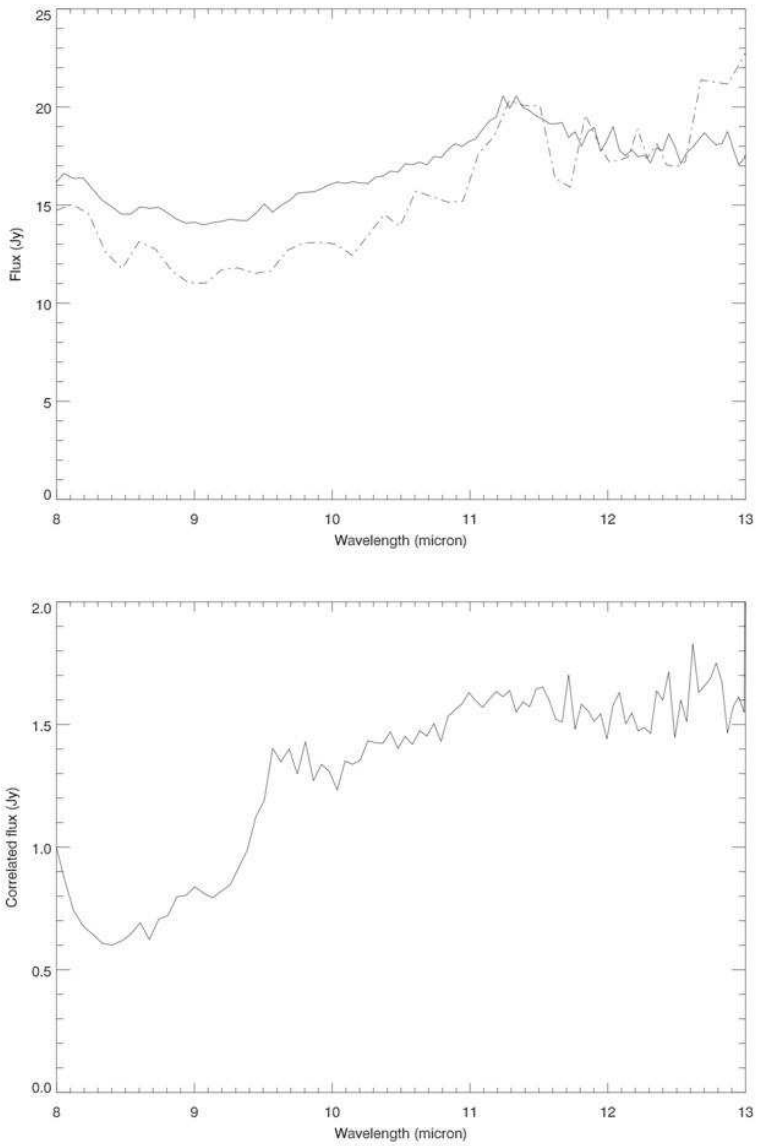

Figure 9.6: Top: MIDI spectrum of HD330036 (continuum line) compared with ISO-SWS spectrum (dash-dotted line). Bottom: one example of correlated flux of HD330036: the 11.3 μm feature is no longer visible.

Part III

Symbiotic Stars in the Magellanic Clouds

10

Symbiotic stars in the Magellanic Clouds An introduction

As we have tried to demonstrate throughout this work, symbiotic spectra tell us a variety of phenomena that are relevant to a number of important astrophysical problems: as a matter of fact, SSs are unique laboratories for studying nova-like thermonuclear outbursts (Munari et al. 1997), colliding-wind processes (Kenny & Taylor 2005, Angeloni et al. 2007a, Contini et al. 2008), formation and collimation of jets (Tomov 2003), bipolar PNe (Corradi 2003), variable X-ray emission (Mukai et al. 2007); they have been even proposed as potential progenitors of Supernovæ *Ia* (Munari & Renzini 1992, Hachisu et al. 1999). Furthermore, SSs offer a powerful benchmark to study the effect of binary evolution on the nucleosynthesis, mixing and dust mineralogy which characterize the AGB companion, that might be different from what expected in single AGB stars (Marigo & Girardi 2007, Marigo et al. 2008).

The energetic operating these binaries is a basic ingredient for a meaningful understanding of the physical processes at work in SSs, but it relies on accurate knowledge of the distance. Unfortunately, the distances to galactic SSs are largely uncertain, and hardly allow reliable calibration of absolute stellar luminosities. Indeed, such luminosities are of vital importance for evaluating the evolutionary state of SSs and the energy budget involved in the observed outbursts.

The specific stellar nature of symbiotic systems places them amongst the intrinsically brightest variable stars, that can be easily detected in nearby galaxies, in particular in the Magellanic Clouds (MCs). At present, 14 SSs are known to belong to the MCs (6 in the Small and 8 in the Large MC). It is clear that observations of Magellanic SSs remove the primary ambiguity in studying these interacting stars, namely the lack of reliable distances. It has been even suggested to use them as standard candles for the calibration of galactic objects (Vogel & Morgan 1994), as already is done with Novæ. Furthermore, Magellanic SSs (MSSs) are also interesting in themselves, because they differentiate from galactic SSs in several aspects.

Figure 10.1: A field view of Magellanic Clouds

SSs have been classified in S- and D-types according to whether the cool star (S-type) or dust (D-type) dominates the near-IR spectral range (Webster & Allen 1975). In our Galaxy, D-type SSs host invariably a Mira variable, while RGB stars are generally found in S-types.

As their galactic cousins, MSSs contains low mass (≤ 3 $M_{\odot}$) giants as cool components. However, in MC systems, only AGB stars are found. 4 out of 8 SSs in LMC are classified as D-type systems (50%, much higher than the galactic ratio $\sim$20%), while no D-types have been found in SMC. These results are intriguing, because *non-dusty S-type* galactic SSs rarely contain AGB stars. Furthermore, the position in the H-R diagram of the symbiotic hot component reveals that in MSS they are amongst the hottest and the brightest within the known symbiotic population (Mikolajewska 2004, Fig.2c).
It is probable that some of these results stem directly from the nature of the present sample, strongly biased towards the brightest objects we have been able to detect so far. Nevertheless, it is worth mentioning that the lack of dusty SSs in SMC may also reflect the very low Z in SMC, and that the galactic SS with the lowest measured $Z \sim 0.002$ - AG Dra - is also amongst the hottest systems.

Another point that makes MSSs interesting to study is that they offer a direct determination of chemical abundances in extragalactic giants: in fact, in a SS the chemical composition of the cool component is reflected in the emission line spectrum of the nebula (Nussbaumer et al. 1988). In the past years, this opportunity triggered several studies which, thanks to new X/UV/optical observations, tempted to constrain the nebular conditions and the chemical

abundances of MSSs (Vogel & Morgan 1994, Vogel & Nussbaumer 1995, Mürset et al. 1996), leading to surprising yet unconfirmed results.

For example, the already mentioned lower Z in MCs with respect to galactic values, along with the suggestions that in several MSSs silicon seems not to be depleted (Vogel & Morgan 1994), has been presented as an indication that none of these systems would have an appreciable amount of dust. Today, this interpretation appears too simplistic, as it has been shown that dust can actually form also at low metallicity (e.g. in globular clusters - McDonald & van Loon 2007 - or in the same MCs - cfr. van Loon et al. 2008).
The truth is that any metallicity effect on the symbiotic phenomenon is virtually unknown.

Therefore, it sounds as a kind of paradox that the only wavelength range where dust can be directly studied, and where a single spectrum may allow a direct investigations of nebular conditions (through emission lines), chemical abundances of stellar components (through absorption and emission lines) and dust properties such temperature and composition (through continuum Spectral Energy Distribution - SED - and dust bands)[1], namely the IR, is also one for which no data exist. The same classification between S- and D-type SSs, that by original definition is based on the SED within the range 1-5 μm, in the case of MSSs is tentatively established on the basis of a few optical emission line ratios, relying on the fact that a larger binary separation (as in D-types) should result into a lower electron density.

The situation is equally regrettable if we consider the issue from another point of view, namely that for a comprehensive and self-consistent modeling of such complex objects, in which so many different physical processes are at work, data along the whole wavelength range is essential (Angeloni et al. 2007b,c).

[1] Cfr. Angeloni et al. (2007a) for a comprehensive analysis of symbiotic ISO-SWS spectra.

11

MASYS
An *AKARI* survey of symbiotic stars in the Magellanic Clouds

MASYS is one of the 11 European proposals
approved for the Phase-3 of the AKARI mission
P.I.: Angeloni

11.1 An introduction to AKARI

AKARI (formerly ASTRO-F), is the first Japanese satellite dedicated to infrared astronomy, from the Institute of Space and Astronautical Science (ISAS) of the Japanese Aerospace Exploration Agency (JAXA). Its main objective is to

perform an all-sky survey with better spatial resolution and wider wavelength coverage than IRAS, mapping the entire sky in six infrared bands from 9 to 180 micron.

AKARI operated with a 68.5 cm-diameter telescope cooled down to 6K (Fig. 11.1, right) and observed in the wavelength range 2-180 μm from a sun-synchronous polar orbit at 700 km altitude. It was successfully launched at 21:28 (UT) on 21 February 2006 by an M-V rocket from the Uchinoura Space Center (USC), Japan. AKARI ran out of its on-board supply of cryogen, liquid Helium at 08:32:40 (UT) on August 26th, 2007, after successful operation and observations that began on May 8th, 2006, achieving the expected lifetime of 550 days. More than 94% of the sky was covered in survey mode.

AKARI also performed more than 5,000 pointed observations over the wavelength range 2-180 μm in 13 bands, providing comprehensive multi-wavelength photometric and spectroscopic coverage of a wide variety of astronomical sources.

AKARI is now in its Post-Helium phase, where imaging and spectroscopic capabilities are available in the 1.8-5.5 micron wavelength range.
10% of the total observing time for pointed observations in this Phase will be dedicated to successful proposals from the dedicated Call for Observation. Proposals have been peer-reviewed by an ESA established Time Allocation Committee, and then merged with those resulting from the parallel Japanese Call. The result of this process has been announced to the proposers[1].

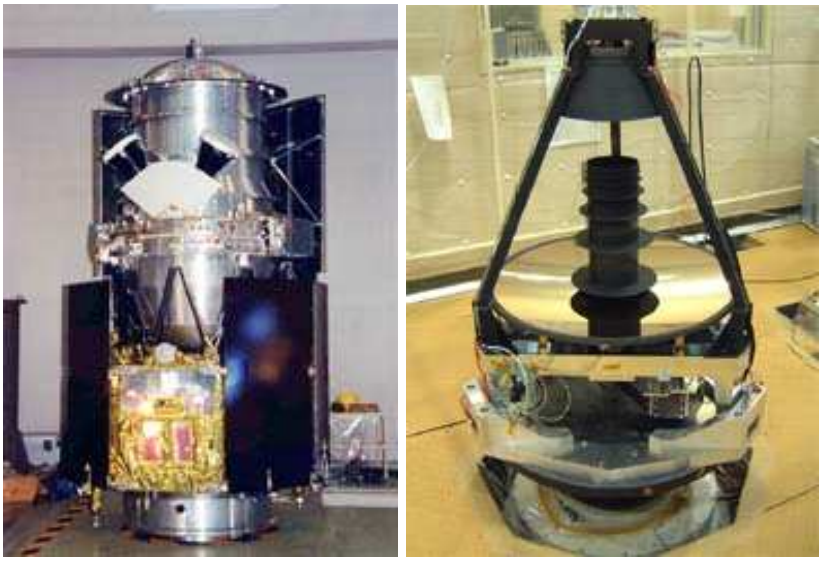

Figure 11.1: Left: AKARI in the lab before launch. Right: the AKARI telescope

[1] http://www.sciops.esa.int/index.php?project=ASTROF&page=OTP3_apprv_ESA

11.2 Description of the proposed program

11.2.1 Objective of Observation

We would like to observe the whole sample of known MSSs, made up of 14 objects (Table 11.1), in both the moderate (NP) and high resolution (NG) spectroscopic mode (AOT IRCZ4) of the NIR channel of the Infra Red Camera (IRC).

AKARI InfraRed Camera			
Camera	NIR	MIR-S	MIR-L
Detector Type	InSb	Si:As	Si:As
Array Format	512x412	256x256	256x256
Field of View(arcmin)	9.5x10.0	9.1x10.0	10.3x10.2
Pixel FOV(arcsec)	1.46	2.34	2.51x2.39

We emphasize that these observations would provide the first ever NIR spectra of Symbiotic Stars in the Magellanic Clouds, and that at the present time only hypothesis can be made about the detectable spectral features, taken into account the diverse morphology of symbiotic spectra in this wavelength region (Figs. 11.2, 11.3, and 11.4).
Specifically, these data would allow to i) trace the NIR continuum between ∼2-5 μm in order to verify whether and to which extent the classification into S- and D-types is actually valid also for MSSs; ii) look for photospheric molecular bands (e.g. OH, HCl, H_2O,CO), that can inform about the nature of the cool component, so far mainly inferred by means of optical spectra; iii) look for emission lines (e.g. [Si VII]@2.48μm, [Fe VII]2.62, H Br γ 2.626, [Mg IV]4.49, [Ar VI]4.52) which help to constrain the physical conditions in the photoionized, shocked nebulæ and give information on the corresponding ionization structure[2] (as done for galactic SSs in Angeloni et al. 2007a); iv) look for specific dust bands (e.g. the PAH bands around 3.3 μm[3]), whose strengths and profiles are capable of revealing the chemical composition of dust grains and the physical conditions of the dust condensation environment.

Eventually, we would like to make some comments about the feasibility of

[2]We use the code SUMA for the interpretation of symbiotic nebular spectra: http://wise-obs.tau.ac.il/ marcel/suma/index.htm
[3]For a detailed discussion of the 3.3 μm PAH band in the spectrum of the galactic SS HD330036, cfr. Angeloni et al. 2007c.

the requested observations. The ecliptic latitude of MCs ensures high visibility for all the objects of the sample: there is no MSS with less than 21 pointing opportunities, more than sufficient for ensuring suitable S/N ratios. No MSS in the target list is duplicated with the blocked target list. Every MSS shows a K mag. compatible with the sensitivity and the saturation limits of the IRC instrument in the AOT IRCZ4 observing mode, as we are going to carefully discuss in the next section.

11.3 Justification of requested observing time, technical feasibility and visibility

As mentioned before, we would like to observe the whole sample of known MSSs in both the moderate (NP) and high resolution (NG) spectroscopic mode (AOT IRCZ4). In the following, we motivate the requested observing time and discuss some related aspects of technical feasibility.

The K band magnitude is known for virtually all MSSs we plan to observe (Table 11.1, col.5). Taking into account that SSs are known to be significantly variable objects, that is the reported values are just a rough indication of the expected fluxes, we see that no object reaches the saturation level of the N3 band (i.e. $\sim$110 mJy). Indeed, this is fundamental in order to acquire the imaging data necessary to determine the wavelength origin in the IRCZ4 mode. Furthermore, the continuum flux is within the continuum sensitivity of the IRC grism.

Since the intensity of emission features (emission lines, dust bands) we want to detect is fairly unknown, we have attempted an estimation of the expected flux in the lines by exploiting the corresponding observed intensities for HM Sge, a representative (galactic) SS. In order to verify whether HM Sge can be considered reliable enough as a "test-symbiotic", we have calculated the K band magnitude of HM Sge (K$\simeq$4.6) at the SMC distance ($\sim$61 kpc): over there, HM Sge would shine with an apparent magnitude of K$\sim$10, namely within the range of values observed for known MSSs. Verified the plausibility of the hypothesis, we have then estimated the expected flux of a few significant IR lines with the same procedure (11.2): as one can see, the values are compatible with the performance by using the IRC grism, for which a line sensitivity of $\sim 5 \times 10^{-18}$ W m^2 has been evaluated. In general, this means that we may require between 3 and 5 pointings for each objects, in order to obtain a suitable S/N.

The visibility of our sources, equally balanced between Phases 3b1 and 3b2, is very high, thus ensuring a comfortable scheduling of the observations.
Eventually, all our targets have passed the Duplication Tool successfully.

Summarizing, it is in the light of these thoughts that AKARI observations of MSSs can give a fundamental and unique contribution to the understanding

Table 11.1: Magellanic Symbiotic Stars in the literature.

Simbad name	Symbiotic name[a]	Type[a]	K mag.[b]	Integrated flux in the K band [mJy]
NAME SMC 1	SMC 1	S	12.64	5.86
NAME SMC 2	SMC 2	S	13.10	3.83
NAME SMC 3	SMC 3	S	10.80	31.9
SV* HV1707	SMC-N60	?	12.62	5.99
RX J0059.1-7505	LIN 358	S	11.46	17.3
LIN 445a	SMC-N73	S	11.6[a]	15.3
2MASS J04515046-7503353	LMC-S154	D	10.1[a]	60.8
(L63) 30	LMC-S147	S	11.9[a]	11.6
LHA 120-N19	LMC-N19	?	-	-
NAME LMC 1	LMC 1	D	10.71	34.8
(KDM2001) 5127	LMC-N67	S	11.4[a]	18.04
NAME Sanduleak's star	Sanduleak's star	D	13.0[a]	4.21
SV* HV 12671	LMC-S63	S	11.33	19.6
SMP LMC 94	SMP LMC 94	?	-	-

[a]from Belczynski et al. 2000;
[b]from 2MASS.

Table 11.2: HM Sge IR emission lines.

λ $[\mu m]$	ID	Transition	Observed flux[a] $[10^{-15}$ W m$^2]$	Estimated flux @ the SMC distance[b] $[10^{-17}$ W m$^2]$
4.052	HI	5-4	5.8±0.6	1.31
4.33	[Ni V]	-	5.1±0.7	1.15
4.5295	[Ar VI]	$^2P_{3/2} - ^2P_{1/2}$	8.7±1.8	1.96

[a]from Schild et al. (2001);
[b]assuming a distance of HM Sge to Earth of 2.9kpc (Mürset et al. 1991).

of the symbiotic phenomenon in its diverse appearance and, in general, of dust properties in complex environment at different metallicities.

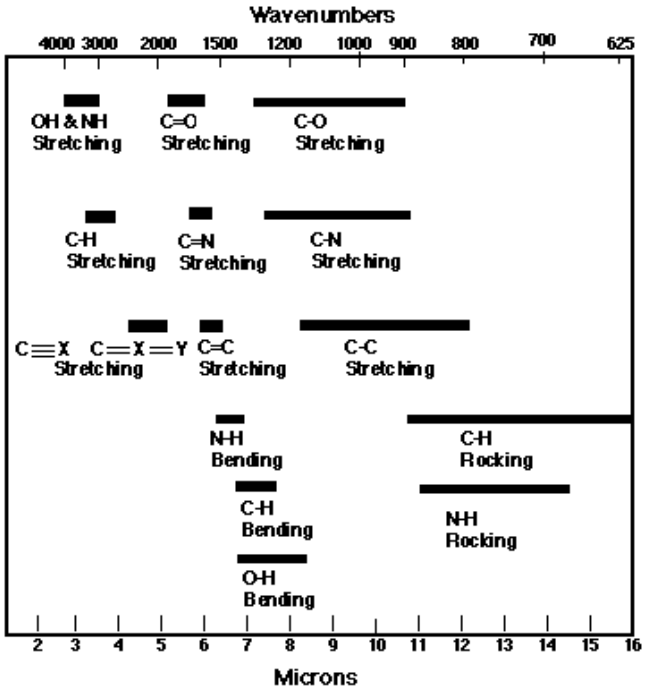

Figure 11.2: The characteristic regions for common infrared stretching and bending vibrations.

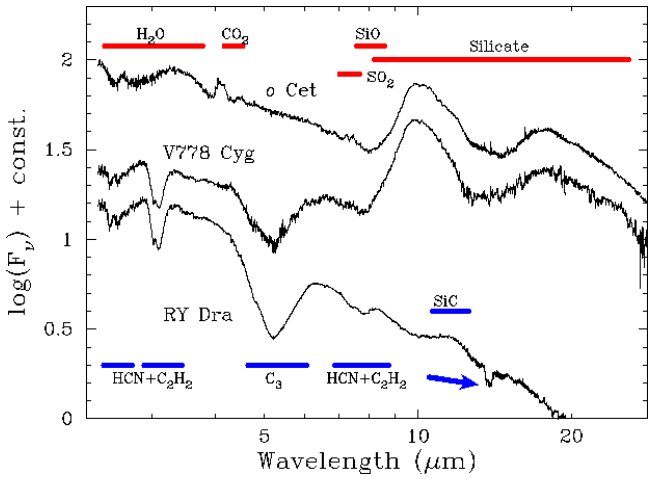

Figure 11.3: ISO-SWS spectral comparison of the O-rich D-type SS o Ceti with the J-type carbon star RY Dra and with the intermediate peculiar star V778 Cyg (from Yamamura et al. 2000).

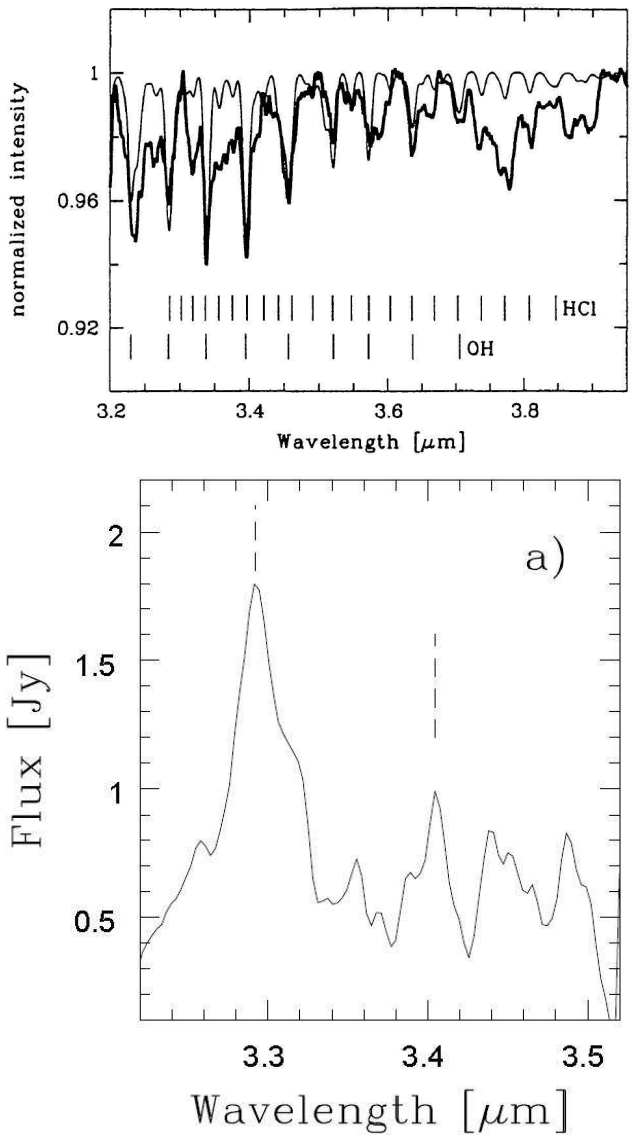

Figure 11.4: ISO-SWS symbiotic spectra around $\sim$3.5 μm. *Top panel*: observed spectrum of CH Cyg (thick line) and single temperature model with the *OH* and *HCl* molecules (from Schild et al. 1999). *Bottom panel*: Dust emission features, usually attributed to the C-H stretching mode ($v = 1 \rightarrow 0$) of highly excited PAHs, in the D'-type HD330036 (from Angeloni et al. 2007c).

12

FUSE observations of symbiotic stars in the Magellanic Clouds

Funded by NASA as part of its Origins program, developed and being operated by the Johns Hopkins University, FUSE[1] - the Far Ultraviolet Spectroscopic Explorer - was launched into orbit aboard a Delta II rocket on June 24, 1999. The FUSE satellite observed light in the far-ultraviolet spectral region, 905-1187 Å, with a spectral resolution of ∼20000. The instrument consisted of four co-aligned prime-focus telescopes and Rowland spectrographs with microchannel plate detectors. Two of the telescope channels used Al:LiF coatings for optimum reflectivity between approximately 1000 and 1187 Å, and the other two channels used SiC coatings for optimized throughput between 905 and 1105 Å.

Within its *Magellanic Clouds Legacy Project*[2] (Fig. 12.2), FUSE was used to observe 187 hot stars in the Large Magellanic Cloud (LMC) and 100 hot stars in the Small Magellanic Cloud (SMC) over its eight years in operations.
A still ongoing archival search, whose aim is to look for complementary data to flank to AKARI upcoming spectra, has allowed to find 12 out of 14 Magellanic symbiotic stars spectra in the FUSE Archive, already public, but still unpublished.
The data reduction and analysis is to start, but a preliminary glance at the raw spectra (Fig. 12.3) gives hope for some promising results.

[1] http://fuse.pha.jhu.edu/
[2] http://archive.stsci.edu/prepds/fuse_mc

Target Name	RA (J2000)	Dec (J2000)	Start Time	Exp Time	Raw Time	Aperture	Archive Date	Release Date
SMC1	7.29825	-74.96128	2004-08-20 13:47:40	15800.000	18818.160	LWRS	2007-10-23 18:56:02	2005-02-27 13:24:09
SMC2	10.700833	-74.70011	2004-08-21 04:32:06	17688.000	19005.830	LWRS	2007-10-23 18:56:34	2005-02-28 23:50:45
SMC3	12.083542	-73.53117	2006-08-07 05:02:17	14678.000	21020.980	LWRS	2008-06-30 23:07:40	2007-11-09 23:11:32
SMC-N60	14.2755	-74.22136	2005-08-22 14:07:49	13727.000	14901.090	LWRS	2008-04-09 01:32:48	2006-03-02 07:43:14
LIN358	14.802125	-75.08822	2005-08-19 21:44:05	32446.000	35132.530	LWRS	2008-04-09 01:42:33	2006-03-02 04:13:24
SMC-N73	16.164917	-75.80681	2005-08-21 18:19:49	28259.000	33644.410	LWRS	2008-04-09 01:52:51	2006-03-16 23:48:25
LMC-S154	72.960042	-75.05969	2004-08-18 07:22:51	21810.000	22985.040	LWRS	2007-10-23 19:06:22	2005-02-28 23:50:53
LMC-N19	75.8499	-67.94306	2004-08-16 14:02:51	18789.000	19897.970	LWRS	2007-10-23 19:07:06	2005-02-28 23:51:22
LMC1	81.2555	-62.48044	2007-07-10 15:21:40	7674.000	20048.340	LWRS	2008-06-19 15:52:44	2008-02-15 22:23:21
LMC-N67	84.032	-64.72291	2005-04-09 02:49:51	16243.000	18625.170	LWRS	2008-03-20 23:21:14	2006-09-03 20:11:53
SANDULEAKS-STAR	86.33225	-71.26883	2004-08-14 09:32:34	22102.000	23181.160	LWRS	2007-10-23 18:14:37	2005-03-01 00:01:22
SMP-LMC-94	88.544292	-73.04672	2004-08-14 01:11:04	19644.000	23340.860	LWRS	2007-10-23 18:24:20	2005-03-01 00:01:52

Figure 12.1: FUSE MSS journal of observations.

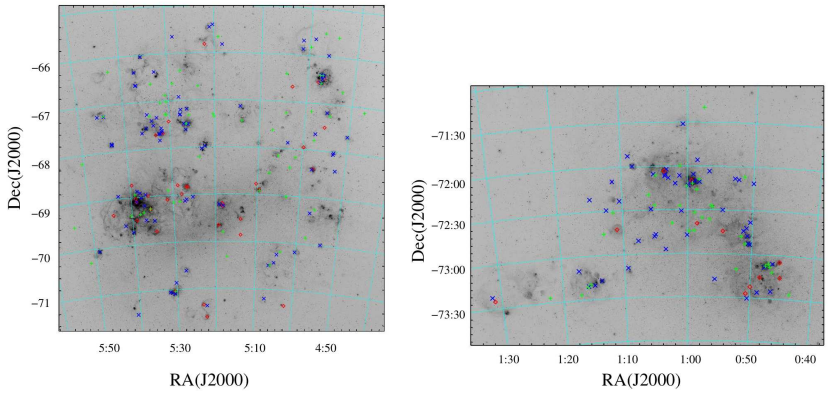

Figure 12.2: B&W background H-alpha images of Magellanic Clouds are shown. The colours indicate the position of FUSE Magellanic Clouds Legacy Project targets. Green = B stars, red = WR+misc stars and blue = O stars.

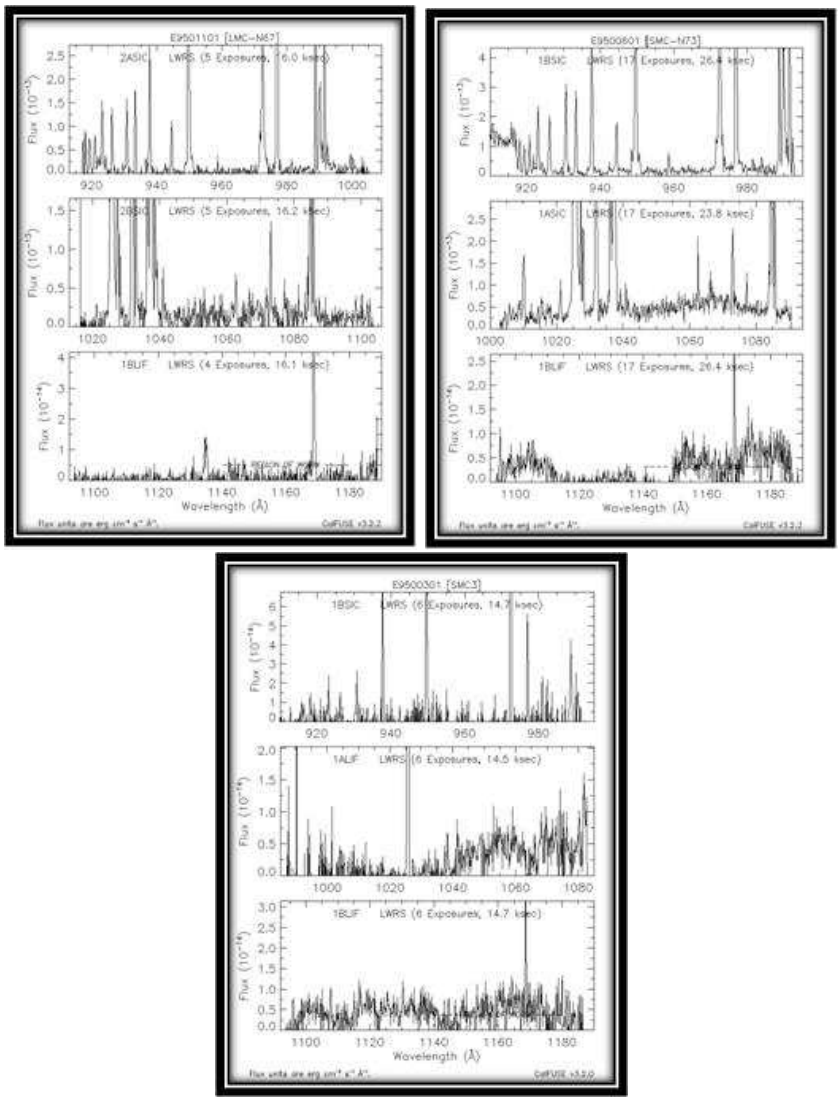

Figure 12.3: Preliminary FUSE spectra of a sample of Magellanic symbiotic stars.

Part IV

APPENDIX

13 SUMA

In this chapter SUMA, a code that simulates the physical conditions of an emitting gaseous cloud under the coupled effect of photoionization from an external source and shocks, is introduced.
Updated information about the code and its development can be found in the official web page at *http://wise-obs.tau.ac.il/∼marcel/suma/index.htm*.

13.1 Introduction

More than 20 years ago, it became clear that radiation processes were not sufficient for predicting the spectra of AGNs, starburst galaxies, SSs, etc., and were unsuitable to calculate the spectra emitted from supernova remnants (SNRs). Collisional processes are important and may be even dominating hydrodynamical regimes where shock waves form. For example, in AGNs, the clouds in the narrow-line region (NLR) move outwards from the galactic center with relatively high velocities (100-1000 $km\,s^{-1}$). In starburst galaxies the shock fronts are created during star formation and destruction phenomena. In SSs shocks form inside and outside the system by collision of the winds from the stars. In SNRs the shocks accompany the blast wave from the supernova explosion.

At the beginning of the 80's, the need for a computer code consistently accounting for the coupled effect of a radiation flux and of shock waves on a gaseous nebula led to the preparation of the first version of the SUMA code (Aldrovandi & Contini 1985, Contini & Aldrovandi 1993). This version was developed at the Instituto Astronômico e Geofísico of the University of São Paulo by Sueli M. Viegas (Aldrovandi) and Marcella Contini from the School of Physics and Astronomy of the Tel-Aviv University. Later on, the code has been constantly updated.

Besides modelling both the emission-line and continuum spectra of various active galaxies, e.g. AGNs (e.g. Contini et al. 1998, Ciroi et al. 2003), LINERs (e.g. Contini 1997, 2004), Starbursts (e.g. Viegas et al. 1999, 2003, Rodriguez-Ardila et al. 2006), and ULIRGs (e.g. Contini & Viegas 2001a, b), detailed

diagnostics of line ratios (Contini & Contini 2003), and continuum spectral energy distribution (SED) of AGN (Contini et al. 2004) were presented for a larger use. In addition, the velocity field prevalent in the NLR of NL-Seyfert 1 galaxies, e.g. Mrk 766 (Contini et al. 2003), Mrk 564 (Rodriguez-Ardila et al. 2005), could be resolved into its various component clouds.

The code was also updated to include the calculation of dust reprocessed radiation consistently with gas emission (Viegas & Contini 1994). In particular, the dust-to-gas ratios *(d/g)* were calculated by SUMA for infrared luminous galaxies (Contini & Viegas 2001a, b). It is also worth noticing the importance of *d/g* in SNR, as for example in the Kepler SNR (Contini 2004).
Regarding SSs, after the seminal models of RH Oph (Contini et al. 1995), HM Sge (Formiggini et al. 1995), AG Peg (Contini 1997, 2003), etc., new studies, from radio frequencies to X-rays, of line ratios and dust bands (Angeloni et al. 2007a, b, c) led to a further update of the code in order to include the calculation of self-absorption of free-free radiation which affects the slope of the radio continuum.

13.2 An overview

The SUMA code simulates the physical conditions of an emitting gaseous cloud under the coupled effect of photoionization from an external source and shocks assuming a plane-parallel geometry. Actually, the use of SUMA in case of spherical shells of gas is justified by large curvature radii (Contini 1997, 2003). Two cases may be considered, corresponding to the photoionizing radiation flux reaching the gas on the same side *or* on the opposite side of the shock front. They are selected at the start of the calculations by the parameter *str = 0* or *str = 1*, respectively.

Results regarding photoionization calculations have been compared with those obtained by other photoionization codes (Ferland 1995).

The main input parameters (see §13.3) are those referring to the shock, as well as those characterizing the source of the ionizing radiation spectrum, those referring to dust, and the chemical abundances of He, C, N, O, Ne, Mg, Si, S, Cl, Ar and Fe, relative to H. The geometrical thickness of the nebula is also an input parameter in the matter-bound case and/or in case str = 1.

The calculations start at the shock front where the gas is compressed and thermalized adiabatically, reaching the maximum temperature ($T \propto {V_s}^2$, where V_s is the shock velocity) in the immediate post-shock region. In each slab compression is calculated by the Rankine-Hugoniot equations (Cox 1972) for the conservation of mass, momentum, and energy. The downstream region is automatically cut in many plane-parallel slabs (up to 300) with different geometrical widths in order to account for the temperature gradient. Thus, the change of

the physical conditions downstream from one slab to the next is minimal. If the primary ionizing radiation reaches the shock-front, the calculations will stop when the electron temperature is as low as 200 K, if the nebula is radiation bound, or at a given value of the nebula geometric thickness, if it is matter bound. In the case where shock and photoionization act on opposite sides of the nebula, the geometrical width of the nebula D is an additional input parameter. Diffuse radiation bridges the two sides, and the smaller D, more entangled are the effects of photoionization and shocks in the middle section of the cloud. In this case, a few iterations are necessary to consistently obtain the physical conditions downstream.

The ionizing radiation from an external source is characterized by its spectrum, which is calculated at 440 energies, from a few eV to KeV, depending on the object. Due to the radiative transfer, the radiation spectrum changes throughout the downstream slabs. Each slab contributes to the nebula optical depth. The calculations assume a steady state downstream. In addition to the radiation from the primary source, the effect of the diffuse radiation created by the gas emission (line and continuum) is also taken into account (Williams 1967), using about 240 energies to calculate the spectrum.

For each slab of gas, the ionic fractional abundances of each chemical element are obtained by solving the ionization equations. These equations account for the ionization mechanisms (photoionization by the primary and diffuse radiation, and collisional ionization) and recombination mechanisms (radiative, dielectronic recombinations) as well as, for charge transfer effects. The ionization equations are coupled to the energy equation (Cox 1972), when collision processes dominate, and to the thermal balance equation if radiative processes dominate. This latter balances the heating of the gas due to the primary and diffuse radiations reaching the slab, and the cooling, due to recombinations and collisional excitation of the ions followed by line emission, as well as collisional ionizations and thermal bremsstrahlung. The coupled equations are solved for each slab, providing the physical conditions necessary for calculating the slab optical depth, as well as its line and continuum emissions. The slab contributions are integrated throughout the nebula.

The effect of dust within the gaseous nebula, characterized by d/g and the initial grain radius, a_{gr}, is consistently taken into account. Dust and gas entering the shock front and downstream are coupled by the magnetic field. The grain radius can be reduced by sputtering depending on the shock velocity and on the gas density. The details of dust temperature calculations are given by Viegas & Contini (1994) and Contini et al. (2004). The grains are heated by the primary and secondary radiation, and by gas collisional processes. When d/g is high, the mutual heating of dust and gas may accelerate the cooling rate of the gas, changing the line and continuum spectra emitted from the gas. The d/g ratios are constrained by the intensity of the continuum IR bump, and the relative abundances of the elements by the line ratios.

13.3 Input parameters

13.3.1 Input parameters depending on the shock

- Shock velocity V_s: although the FWHM of the line profiles indicate the velocity of the emitting gas rather than that of the shock, as a first trial FWHM roughly suggests the $V_s$range.

- Preshock density n_0: for a first trial, it is indicated from the characteristic line ratios (e.g. [SII]6548/[SII]6584), considering, however, that n_0 is by a factor 5-10 less than the density of the downstream gas emitting the lines, depending on V_s.

- Preshock magnetic field B_0: it is generally assumed from the observations related to polarization. Its value is then refined phenomenologically. B_0 is a crucial parameter because a strong filed component transverse to the shock direction can substantially reduce compression.

13.3.2 Input parameters depending on photoionization

Different shapes of the primary radiation can be used:

- *Power-law radiation:* it is characterized by the spectral indexes a_{UV} and a_X, in the UV and in the X-ray domains, respectively, and by F_ν that is the flux intensity at 1 Rydberg, in units of photons $cm^{-2}\ s^{-1}\ eV^{-1}$ and is constrained mainly by the [OIII] 5007/[OII] 3727 line ratios, while the spectral index by the UV line ratios.

- *Black-body radiation:* it is characterized by the stellar temperature T_S, intended as a color temperature, and the ionization parameter U. Both values are strongly constrained by the HeII/HeI line ratios.

- *Black-body + power-law:* the composite spectrum consisting of black-body in the UV and power-law in the X-ray domain is also considered by the code.

13.3.3 Input parameters depending on dust

- *Dust-to-gas ratio (d/g):* it is directly related to the intensity of the infrared peak of the reprocessed radiation by dust, and depends on the ratio of the reprocessed radiation to bremsstrahlung in the IR, throughout the SED of the continuum. Notice that a high *d/g*, speeding up the cooling rate downstream, may change a non-radiative shock into a radiative one.

- *Grain radius (a_{gr}):* the smaller the grains, the higher the temperature reached by radiation heating, and the faster they are eroded by sputtering in grain-gas collisions.

13.3.4 Relative abundance of the elements

The following elements are considered: H, He, C, N, O, Ne, Mg, Si, S, Cl, A, and Fe. They are constrained by the ratios of single element lines. The high abundance of a strong coolant element (e.g. oxygen), affecting the cooling rate, may substantially change both line and continuum spectra.

13.3.5 Geometrical thickness of the nebula

The parameter D (together with the flux intensity and the density) determines whether the model is matter-bound or radiation-bound. In case str=1, a low D reduces the region of relatively low temperature in the internal region of the cloud, and leads to less intense, even negligible, neutral lines (Fig. 13.1).

13.4 Relevant issues

13.4.1 Geometrical thickness of the slabs

In a code accounting for shocks, the choice of the slab thickness cannot be determined *a priori* as an input parameter.

The first slab

The choice of the first slab geometrical thickness is the most crucial: in general, the thinner the better, but it is not always true because you must take into account:

- the equipartition lifetime between ions and electrons;
- the sputtering critical distance against deceleration and stop;
- numerical precision.

High-temperature region

Once having crossed the shock front, the gas is thermalized to a temperature

$$T \approx 1.5\,10^5\,(V_s/100\,km\,s^{-1})^2\;K \qquad (13.1)$$

At high temperatures (T$\geq 10^6$K) recombination coefficients are very low, leading to a low cooling rate. The cooling rate being $\propto n^2$ (n the gas density), the thickness of the first slab depends strongly on the density of the gas.

Intermediate temperatures

At T between 10^4 and 10^5 K the UV lines and the coronal lines in the IR are strong and lead to rapid cooling and compression of the gas. If the cooling rate is

so high as to drastically reduce the temperature eluding intermediate ionization-level lines, the calculated spectrum will be wrong (Fig. 13.2). Therefore, the slab width must be reduced and all the physical quantities recalculated. The choice of the slab width is determined by the gradient of the temperature. This process is iterated until the thickness of the slab is such as to lead to an acceptable gradient of the temperature:

$$T(i-1) - T(i))/T(i-1) \leq 0.1$$

whit $T(i)$ temperature of the slab i.

Beyond the temperature drop

In the radiation-bound case, the gas recombines completely before reaching the edge of the nebula opposite to the shock front (if *str=0*), or the radiation dominated edge (if *str=1*). Thus, as the temperature drops, a large portion of gas is maintained at a temperature of the order of $\approx 10^4$ K by the diffuse (or secondary) radiation. Due to a lower temperature gradient, calculations in this zone proceed throughout wider slabs. This is critical to self-absorption of free-free radiation in the radio domain, in particular for SSs, where the densities are very high and the nebula sizes relatively small. The optical thickness τ of the slab is actually $\propto n^2 dr$, where dr is the geometrical thickness of the slab.

The radiation dominated edge

In the *str=1* case mentioned in the previous section, the edge opposite to the shock front is reached by the photoionizing flux from an external source (AGN center, hot star, starburst, etc.). The geometrical thickness of the slabs cannot be as large as those calculated in the shock dominated case (*str=1* and *U=0*) or in the radiation dominated case (*str=0* and *U≠0*). The effect of the radiation flux on the gas physical conditions has to be accounted for in the subsequent iterations (see below), but the width of the photoionized slabs is evaluated in the first iteration, at the onset of the calculations. Therefore, to improve the precision, it is assumed that the slab width in the radiation dominated edge is a fraction of the total geometrical thickness of the photoionized gas, which is estimated from the ionization parameter and the density. Usually a fraction 1/50 to 1/100 is sufficient to reach a smooth distribution of the physical parameters and a good accuracy for the emission lines.

13.4.2 The compression equation

Very different line and continuum spectra result adopting a pure photoionization code which assumes a constant density throughout the nebula, and a code which accounts for shocks, because compression downstream leads to a different distribution of the physical conditions.

After some algebra, the Rankine-Hugoniot equations for the conservation of mass and of momentum result in the *compression equation*(Cox 1972):

$$[(B_0^2/8\pi)x^2 + n_0 kT(1 + n_e/n)x - P_0]x = -\rho v_0^2 \qquad (13.2)$$

where $x = n/n_0$, $P_0 = \rho v_0^2 + B_0^2/\pi + n_0(1 + f_0/1.16)kT$, f_0 being the initial hydrogen ionization fraction, and ρ the initial mass density.

Eq. 13.2 is a third degree equation which is solved in each slab by a subroutine that finds the roots of a real polynomial using Muller's method of inverse parabolic interpolation, and choosing the adequate solution, as some may be imaginary. Compression strongly affects the cooling rate and, consequently, the distribution of the physical conditions downstream as well as that of the element fractional abundances.

13.4.3 The electron temperature

The temperature in each slab depends on energy gains (G) and losses (L) of the gas. Close to the shock front downstream, collisional mechanisms prevail and the temperature is calculated from the energy equation in terms of the enthalpy change (Cox 1972). In the slabs with temperature $\leq 2\ 10^4$ K, photoionization and heating by both the primary and the secondary radiation dominate and the temperature is calculated by thermal balance (G=L).

Gain

The gains are calculated by the rate at which energy is given to the electrons by the radiation field (Osterbrock 1988). The energy of suprathermal electrons created by photoionization is rapidly distributed among the thermal electrons through collisions, heating the gas.

Losses

Several processes contribute to gas cooling. The cooling components are given by:

$$L = L_{ff} + L_{fb} + L_{lines} + L_{dust}$$

where L_{ff} corresponds to losses due to free-free transitions, particularly strong at high temperatures and high frequencies; L_{fb} to free-bound transitions, being high at temperatures near 10^5 K; L_{lines} is due to line emission mainly between 10^4 and 10^5 K; L_{dust} represents the energy lost by the gas in collisional heating of dust grains, being higher the higher d/g and a_{gr}. Self-absorption of free-free radiation is also included in the calculations.

Ionization equilibrium

The ionization equations are solved for each element up to the maximum ionization level, taking into account all the processes above listed.

13.4.4 Lifetimes

Although the code is built for a hydrostatic regime, the most significant lifetimes must be checked:

- t_{ev} corresponds to the evolution in one slab;
- t_{rad} to the radiative lifetime;
- t_{eq} is the equipartition time between ions and electrons in the first slab downstream;
- t_{sput} is the lifetime against sputtering.

They must satisfy the following relations:

$$t_{ev} \geq t_{rad},\ t_{ev} \geq t_{eq},\ t_{ev} \leq t_{sput}$$

13.4.5 Dust

Dust reprocessed radiation and sputtering of the grains (Fig. 13.3) is calculated consistently with gas emission. A detailed presentation of the equations is given in §3 of Viegas & Contini (1994).

13.4.6 Iterations

The calculations start at the shock front. In the in-falling case, namely shock and photoionization on the same edge, one iteration is enough.
In the ejected case, namely shock and photoionization on opposite edges, the code proceeds through some iterations until convergence of the results (e.g. the distribution of the temperature and of the density throughout the nebula have not changed from the results in the previous iteration).

- *I-iteration:* the calculations start at the shock front and are performed in a shock dominated case (U=0) in which the primary radiation from the external source is neglected. The diffuse radiation from each slab is stored;
- *II-iteration:* the calculations start at the edge reached by the primary radiation. The calculations account for diffuse radiation from both the sides of the nebula. The secondary radiation and the primary radiation fluxes calculated by radiation transfer in each slab in the photoionized zone are stored. In the region close to the shock front the temperature and the density from the I-iteration are used;
- *III-iteration:* the calculations start at the shock front and account for the primary radiation and secondary radiation from the ionized edge which were stored in the previous iteration. The process proceeds by recalculating the physical parameters and the secondary radiation from the slabs

heated by the shock front. The next iterations follow the procedures used in II and III. From II iteration on, the results are compared to those obtained in the previous iterations to check for convergence. Generally three iterations are enough to reach the desired accuracy.

13.5 Applications to astrophysical environments

For examples describing some applications of SUMA to diverse astrophysical environments not directly pertaining to this work - such as AGNs, ULIRGs, SNRs and so on - please refer to the specific web page section:

http://wise-obs.tau.ac.il/∼marcel/suma/applications.htm

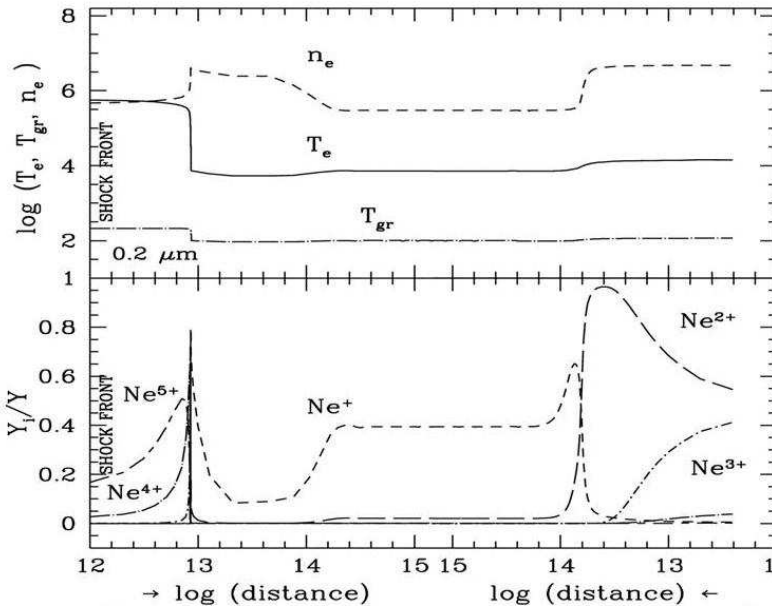

Figure 13.1: The distribution of $\mathrm{T_e}$, $\mathrm{n_e}$, $\mathrm{T_{gr}}$(top panel), and of the fractional abundance of Ne ions (bottom panel) downstream of the expanding shock in the SS HM Sge. Radiation from the hot star reaches the edges of the shocked nebula opposite to the shock front.

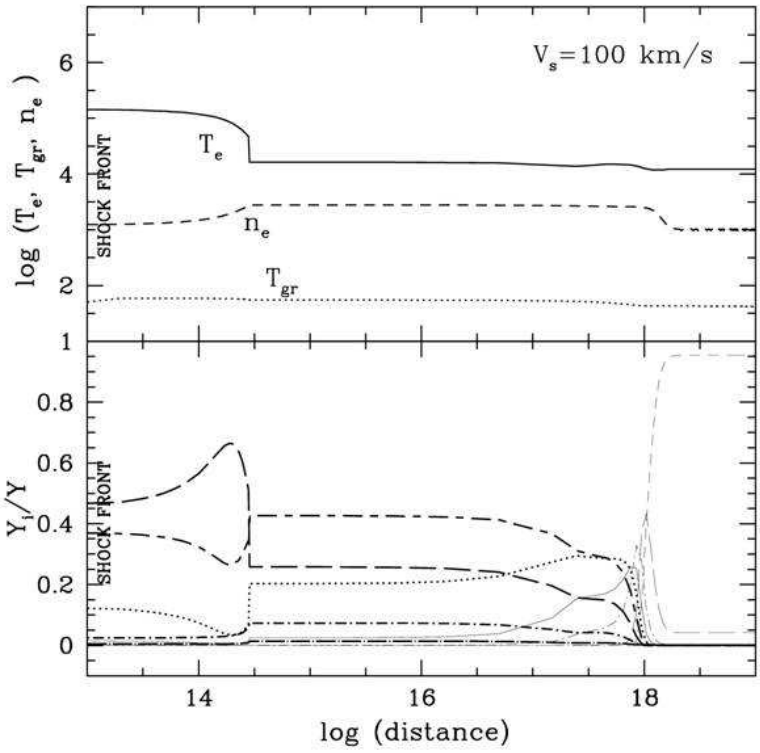

Figure 13.2: Distribution downstream of $\mathrm{T_e}$, $\mathrm{n_e}$, $\mathrm{T_{gr}}$(top panel), and of the fractional abundance of Fe ions (bottom panel) in AGN clouds for V_s=100 $km\,s^{-1}$and V_s=300 $km\,s^{-1}$. For both models, *str=0*, n_0=300 cm^{-3}, $\mathrm{B_0}$=10-4 Gauss, and a_{gr}=0.2 μm. Fractional abundances Fe+ (thin short-dashed), Fe2+(thin long-dashed), Fe3+ (thin dot-short-dashed), Fe4+(thin solid),Fe5+(thick dotted), Fe6+ (thick long-short-dashed),Fe7+(thick long-dashed), Fe8+(thick dot-dashed)Fe9+(thick dot-long- dashed), Fe10+(thick solid), Fe11+(thick short-dashed).

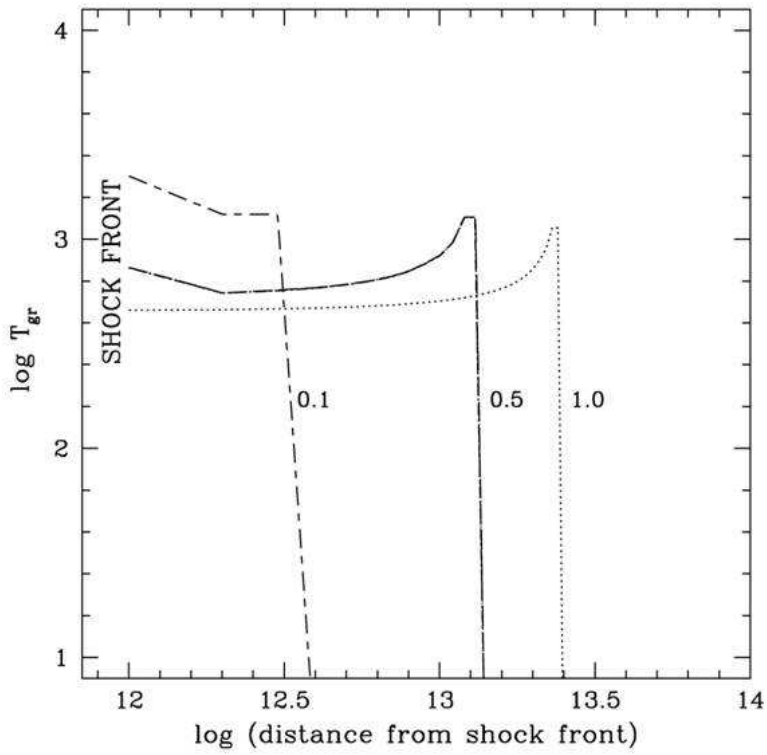

Figure 13.3: Temperatures vs. sputtering distances of grains with 0.1, 0.5, and 1 μm radius. The calculations refer to the reverse shock between the stars in the HM Sge SS (adapted from Angeloni et al. 2007a).

Bibliography

[Aaquist & Kwok(1990)] Aaquist, O. B., & Kwok, S. 1990, A&AS, 84, 229

[Aaquist & Kwok(1991)] Aaquist, O. B., & Kwok, S. 1991, ApJ, 378, 599

[Achmad et al.(1997)] Achmad, L., Lamers, H. J. G. L. M., & Pasquini, L. 1997, A&A, 320, 196

[Allamandola et .(1989)] Allamandola, L. J., Tielens, G. G. M., & Barker, J. R. 1989, ApJS, 71, 733

[Allen(1973)] Allen, C. W. 1973, London:University of London, Athlone Press, 1973, 3rd ed.

[Allen(1974)] Allen, D.A. 1974, Inf. Bull. Var. Stars, 911

[Allen(1981)] Allen, D. 1981, Nature, 293, 99

[Allen(1982)] Allen, D. A. 1982, ASSL Vol. 95: IAU Colloq. 70: The Nature of Symbiotic Stars, 27

[Allen(1983)] Allen, D. A. 1983, MNRAS, 204, 113

[Allen(1984)] Allen, D. A. 1984, Ap&SS, 99, 101

[Allen et al.(1989)] Allen, D. A., Hall, P. J., Norris, R. P., Troup, E. R., Wark, R. M., & Wright, A. E. 1989, MNRAS, 236, 363

[Altenhoff et al.(1994)] Altenhoff, W. J., Thum, C., & Wendker, H. J. 1994, A&A, 281, 161

[Anandarao et al.(1988)] Anandarao, B. G., Taylor, A. R., & Pottasch, S. R. 1988, A&A, 203, 361

[Angeloni et al.(2007a)] Angeloni, R., Contini, M., Ciroi, S., & Rafanelli, P. 2007a, AJ, 134, 205

[Angeloni et al.(2007b)] Angeloni, R., Contini,M., Ciroi, S., & Rafanelli, P. 2007b, A&A, 471, 825

[Angeloni et al.(2007c)] Angeloni, R., Contini,M., Ciroi, S., & Rafanelli, P. 2007c, A&A, 472, 497

[Bakes et al.(2001)] Bakes, E. L. O., Tielens, A. G. G. M., & Bauschlicher, C. W., Jr. 2001, ApJ, 556, 501

[Barker et al.(1987)] Barker, J. R., Allamandola, L. J., & Tielens, A. G. G. M. 1987, ApJL, 315, L61

[Bastian(1992)] Bastian, T. S. 1992, ApJL, 387, L77

[Belczyński et al.(2000)] Belczyński, K., Mikołajewska, J., Munari, ., Ivison, R. J., & Friedjung, M. 2000, A&Ap Suppl. Ser., 146, 407

[Bell(1978)] Bell, A. R. 1978, MNRAS, 182, 147, a

[Bell(1978)] Bell, A. R. 1978, MNRAS, 182, 443, b

[Bhatt & Mallik(1986)] Bhatt, H. C., & Mallik, D. C. V. 1986, A&A, 168, 248

[Bhatt(1989)] Bhatt, H. C. 1989, A&A, 214, 331

[Bhatt & Sagar(1991)] Bhatt, H. C., & Sagar, R. 1991, Journal of Astrophysics and Astronomy, 12, 111

[Biller et al.(2006)] Biller, B. A., et al. 2006, ArXiv Astrophysics e-prints, arXiv:astro-ph/0604336

[Bisikalo et al.(2006)] Bisikalo, D. V., Boyarchuk, A. A., Kilpio, E. Y., Tomov, N. A., & Tomova, M. T. 2006, Astronomy Reports, 50, 722

[Bode et al.(2007)] Bode, M.F. et al. 2007, ApJ, 665, L63

[Bohigas et al.(1989)] Bohigas, J., Echevarria, J., Diego, F., & Sarmiento, J. A. 1989, MNRAS, 238, 1395

[Bowey & Adamson(2002)] Bowey, J. E., & Adamson, A. J. 2002, MNRAS, 334, 94

[Bowey et al.(2002)] Bowey, J. E., et al. 2002, MNRAS, 331, L1

[Chevalier] Chevalier, R.A. 1982, ApJ, 259, L85

[Chiar et al.(2002)] Chiar, J. E., Peeters, E., & Tielens, A. G. G. M. 2002, ApJL, 579, L91

[Collin & Joly(2000)] Collin, S., & Joly, M. 2000, New Astronomy Review, 44, 531

[Contini et al.(1995)] Contini, M., Orio, M., Prialnik, D. 1995, MNRAS, 275, 195

[Contini & Prialnik(1997)] Contini, M., & Prialnik, D. 1997, ApJ, 475, 803

[Contini et al.(1997)] Contini, M., Collodel, L., & Rafanelli, P. 1997, ASSL Vol. 218: Astronomical Time Series, 203

[Contini(1997)] Contini, M. 1997, ApJ, 483, 887

[Contini, Formiggini (1999)] Contini, M., & Formiggini, L. 1999, ApJ, 517, 925

[Contini, M. & Formiggini, L.(2001] Contini, M. & Formiggini, L. 2001 A&A, 375, 579

[Contini et al.(2002)] Contini, M., Radovich, M., Rafanelli, P., & Richter, G. M. 2002, ApJ, 572, 124

[Contini & Formiggini(2003)] Contini, M. & Formiggini, L. 2003, MNRAS, 339, 148

[Contini(2003)] Contini, M. 2003, MNRAS, 339, 125

[Contini(2004)] Contini, M. 2004, A&A, 422, 591

[Contini et al.(2008)] Contini, M., Angeloni, R., & Rafanelli, P. 2008, arXiv:0807.1480

[Contini et al.(2008)] Contini, M., Angeloni, R., & Rafanelli, P. 2008, arXiv:0807.1473

[Corradi et al.(2001)] Corradi, R. L. M., Munari, U., Livio, M., Mampaso, A., Gonçalves, D. R., & Schwarz, H. E. 2001, ApJ, 560, 912

[Corradi, Schwarz (1993)] Corradi, RLM, & Schwarz, H.E. 1993, A&A, 268, 714

[Corradi et al. (1999)] Corradi, R.L.M., Brandi, E., Ferrer, O.E., Schwarz, H.E. 1999, A&A, 343, 841

[Corradi et al. (1999b)] Corradi, R. L. M., Ferrer, O. E., Schwarz, H. E., Brandi, E., & Garcia, L. 1999b, A&A, 348, 978

[Corradi et al.(1999)] Corradi, R. L. M., Brandi, E., Ferrer, O. E., & Schwarz, H. E. 1999, A&A, 343, 841

[Corradi et al.(2003)] Corradi, R. L. M., Schönberner, D., Steffen, M., & Perinotto, M. 2003, MNRAS, 340, 417

[Corradi et al.(2008)] Corradi, R. L. M., et al. 2008, A&A, 480, 409

[Costa & de Freitas Pacheco(1994)] Costa, R. D. D., & de Freitas Pacheco, J. A. 1994, A&A, 285, 998

[Cox(1972)] Cox, D. P. 1972, ApJ, 178, 143

[Crocker et al.(2001)] Crocker, M. M., Davis, R. J., Eyres, S. P. S., Bode, M. F., Taylor, A. R., Skopal, A., & Kenny, H. T. 2001, MNRAS, 326, 781

[De Becker et al.(2007)] De Becker, M., Rauw, G., Pittard, J. M., Blomme, R., Romero, G. E., Sana, H., & Stevens, I. R. 2007, ArXiv e-prints, 709, arXiv:0709.1033

[de Graauw et al.(1996)] de Graauw, T., et al. 1996, A&A, 315, L49

[Deutsch (1964)] Deutsch, A.J. 1964 Ann. Rep. Mt. Wilson and Palomar Obs., 11

[Dwek(1981)] Dwek, E. 1981, ApJ, 247, 614

[Egan et al.(2003)] Egan, M. P., Price, S. D., & Kraemer, K. E. 2003, Bulletin of the American Astronomical Society, 35, 1301

[Eriksson et al.(2007)] Eriksson, M., Veenhuizen, H., & Nilsson, H. 2007, Baltic Astronomy, 16, 95

[Evans et al.(1997)] Evans, A., Geballe, T. R., Rawlings, J. M. C., Eyres, S. P. S., & Davies, J. K. 1997, MNRAS, 292, 192

[Eyres et al.(1995)] Eyres, S. P. S., Kenny, H. T., Cohen, R. J., Lloyd, H. M., Dougherty, S. M., Davis, R. J., & Bode, M. F. 1995, mnras, 274, 317

[Eyres et al.(2002)] Eyres, S. P. S., et al. 2002, MNRAS, 335, 526

[Ezuka et al.(1998)] Ezuka, H., Ishida, M., & Makino, F. 1998, ApJ, 499, 388

[Feast et al.(1983)] Feast, M. W., Catchpole, R. M., Whitelock, P. A., Carter, B. S., & Roberts, G. 1983, MNRAS, 203, 373

[Feibelman(1983)] Feibelman, W. A. 1983, ApJ, 275, 628

[Feibelman(1988)] Feibelman, W. A. 1988, A Decade of UV Astronomy with the IUE Satellite, Volume 2, 2, 179

[Fleming & Pickering(1912)] Fleming, W. P. S., & Pickering, E. C. 1912, Annals of Harvard College Observatory, 56, 165

[Folini & Walder(2000)] Folini, D., & Walder, R. 2000, Ap&SS, 274, 189

[Formiggini et al. (1995)] Formiggini, L., Contini, M., Leibowitz, E.M. 1995

[Friedjung & Viotti(1982)] Friedjung, M., & Viotti, R. 1982, Journal of the British Astronomical Association, 93, 45

[Friedjung et al.(1984)] Friedjung, M., Ferrari-Toniolo, M., Persi, P., Altamore, A., Cassatella, A., & Viotti, R. 1984, Future of Ultraviolet Astronomy Based on Six Years of IUE Research, 305

[Galloway & Sokoloski(2004)] Galloway, D. K., & Sokoloski, J. L. 2004, ApJl, 613, L61

[Gaposchkin(1952)] Gaposchkin, S. 1952 Ann. of Harvard College Obs., 118,155

[Garay et al.(2000)] Garay, G., Mardones, D., & Rodríguez, L. F. 2000, ApJ, 545, 861

[García-Burillo(2000)] García-Burillo, S. 2000, ASP Conf. Ser. 197: Dynamics of Galaxies: from the Early Universe to the Present, 197, 189

[García-Burillo et al.(2001)] García-Burillo, S., Martín-Pintado, J., Fuente, A., & Neri, R. 2001, ApJL, 563, L27

[Giacconi et al.(1974)] Giacconi, R., Murray, S., Gursky, H., Kellogg, E., Schreier, E., Matilsky, T., Koch, D., & Tananbaum, H. 1974, ApJS, 27, 37

[Gillett et al.(1975)] Gillett, F. C., Forrest, W. J., Merrill, K. M., Soifer, B. T., & Capps, R. W. 1975, ApJ, 200, 609

[Ginzburg & Syrovatskii(1965)] Ginzburg, V. L., & Syrovatskii, S. I. 1965, ARA&A, 3, 297

[Girard & Willson] Girard, T., Willson, L.A. 1987, A&A, 183, 247

[Graham & Zhang(2000)] Graham, M. J., & Zhang, Q. 2000, ApJs, 127, 339

[Hachisu et al.(1999)] Hachisu, I., Kato, M., & Nomoto, K. 1999, ApJ, 522, 487

[Hack et al.(1988)] Hack, M., Engin, S., Rusconi, L., Sedmak, G., Yilmaz, N., & Boehm, C. 1988, A&As, 72, 391

[Hallenbeck et al.(2000)] Hallenbeck, S. L., Nuth, J. A., III, & Nelson, R. N. 2000, ApJ, 535, 247

[Harker & Desch(2002)] Harker, D. E., & Desch, S. J. 2002, ApJ, 565, L109

[Haro(1952)] Haro, G. 1952, Boletin de los Observatorios Tonantzintla y Tacubaya, 1, 1

[Harries(1996)] Harries, T. J. 1996, A&A, 315, 499

[He et al.(2005)] He, J. H., Szczerba, R., Chen, P. S., & Sobolev, A. M. 2005, A&A, 434, 201

[Henize,Carlson(1980)] Henize, K.G. & Carlson, E.D. 1980, PASP, 92, 479

[Heng & Sunyaev(2008)] Heng, K., & Sunyaev, R. A. 2008, A&A, 481, 117

[Hinkle et al.(1993)] Hinkle, K. H., Fekel, F. C., Johnson, D. S., & Scharlach, W. W. G. 1993, AJ, 105, 1074

[Hinkle et al.(2009)] Hinkle, K. H., Fekel, F. C., & Joyce, R. R. 2009, American Astronomical Society Meeting Abstracts, 213, #434.10

[Hony et al.(2001)] Hony, S., Van Kerckhoven, C., Peeters, E., Tielens, A. G. G. M., Hudgins, D. M., & Allamandola, L. J. 2001, A&A, 370, 1030

[Hudgins & Allamandola(1999)] Hudgins, D. M., & Allamandola, L. J. 1999, ApJ, 513, L69

[Iijima et al.(1994)] Iijima, T., Strafella, F., Sabbadin, F., & Bianchini, A. 1994, A&A, 283, 919

[Ipatov et al.(1984)] Ipatov, A. P., Taranova, O. G., & Iudin, B. F. 1984, A&A, 135, 325

[Ivison et al.(1991)] Ivison, R. J., Bode, M. F., Roberts, J. A., Meaburn, J., Davis, R. J., Nelson, R. F., & Spencer, R. E. 1991, MNRAS, 249, 374

[Ivison et al.(1992)] Ivison, R. J., Hughes, D. H., & Bode, M. F. 1992, MNRAS, 257, 47

[Ivison et al.(1995)] Ivison, R. J., Seaquist, E. R., Schwarz, H. E., Hughes, D. H., & Bode, M. F. 1995, MNRAS, 273, 517

[Ivison et al.(1995)] Ivison, R. J., Seaquist, E. R., & Hall, P. J. 1995, Ap&SS, 224, 255

[Ivison et al.(1998)] Ivison, R. J., Yates, J. A., & Hall, P. J. 1998, MNRAS, 295, 813

[Jaeger et al.(1994)] Jaeger, C., Mutschke, H., Begemann, B., Dorschner, J., & Henning, T. 1994, A&A, 292, 641

[Jaeger et al.(1998)] Jaeger, C., Molster, F. J., Dorschner, J., Henning, T., Mutschke, H., & Waters, L. B. F. M. 1998, A&A, 339, 904

[Joblin et al.(1994)] Joblin, C., D'Hendecourt, L., Leger, A., & Defourneau, D. 1994, A&A, 281, 923

[Joblin et al.(1995)] Joblin, C., Boissel, P., Leger, A., D'Hendecourt, L., & Defourneau, D. 1995, A&A, 299, 835

[Johansson & Jordan (1984)] Johansson, S. & Jordan, C. 1984, MNRAS, 210, 239

[Jones(1985)] Jones, P. A. 1985, MNRAS, 216, 613

[Karovska et al.(1998)] Karovska, M., Carilli, C. L., & Mattei, J. A. 1998, Journal of the American Association of Variable Star Observers (JAAVSO), 26, 97

[Karovska et al.(2007)] Karovska, M., Carilli, C. L., Raymond, J. C., & Mattei, J. A. 2007, ArXiv Astrophysics e-prints, arXiv:astro-ph/0703278

[Kemper et al.(2001)] Kemper, F., Waters, L. B. F. M., de Koter, A., & Tielens, A. G. G. M. 2001, A&A, 369, 132

[Kemper et al.(2005)] Kemper, F., Vriend, W. J., & Tielens, A. G. G. M. 2005, ApJ, 633, 534

[Kenny et al.(1997)] Kenny, H. T., Taylor, A. R., Kwok, S., Eyres, S. P. S., & Davis, R. J. 1997, High-Sensitivity Radio Astronomy, Proceedings of a meeting held at Jodrell Bank, University of Manchester, January 22-26, 1996. Edited by Davis Jackson, 1996., p.37, 37

[Kenny & Taylor(2005)] Kenny, H. T., & Taylor, A. R. 2005, ApJ, 619, 527

[Kenny & Taylor(2007)] Kenny, H. T., & Taylor, A. R. 2007, ApJ, 662, 1231

[Kenyon & Webbink(1984)] Kenyon, S. J., & Webbink, R. F. 1984, ApJ, 279, 252

[Kenyon et al. (1986)] Kenyon, S.J., Fernandez-Castro, T., Stencel, R.E. 1986, AJ, 95, 1118

[Kenyon(1988)] Kenyon, S. J. 1988, AJ, 96, 337

[Kharchenko(2001)] Kharchenko, N. V. 2001, Kinematika i Fizika Nebesnykh Tel, 17, 409

[Kwok(1988)] Kwok, S. 1988, The Symbiotic Phenomenon, Proceedings of IAU Colloq. 103, held in Torun, Poland, 18-20 August, 1987. Edited by Joanna Mikolajewska, Michael Friedjung, Scott J. Kenyon, and Roberto Viotti. Dordrecht, Kluwer Academic Publishers (Astrophysics and Space Science Library. Volume 145), 1988., p.129, 129

[Lamers & Cassinelli(1999)] Lamers, H. J. G. L. M., & Cassinelli, J. P. 1999, Introduction to Stellar Winds, by Henny J. G. L. M. Lamers and Joseph P. Cassinelli, pp. 452. ISBN 0521593980. Cambridge, UK: Cambridge University Press, June 1999.,

[Leahy & Taylor(1987)] Leahy, D. A., & Taylor, A. R. 1987, A&A, 176, 262

[Lee(1973)] Lee, S.G. 1973, Inf. Bull. Var. Stars, N.813

[Li & Leahy(1997)] Li, P. S., & Leahy, D. A. 1997, ApJ, 484, 424

[Li et al.(1998)] Li, P. S., Thronson, H. A., & Kwok, S. 1998, 1997 Pacific Rim Conference on Stellar Astrophysics, 138, 191

[Little-Marenin & Little(1990)] Little-Marenin, I. R., & Little, S. J. 1990, AJ, 99, 1173

[Lutz(1984)] Lutz, J.H. 1984, ApJ, 279, 714

[Magrini et al.(2003)] Magrini, L., Corradi, R. L. M., & Munari, U. 2003, Astronomical Society of the Pacific Conference Series, 303, 539

[Marigo & Girardi(2007)] Marigo, P., & Girardi, L. 2007, A&A, 469, 239

[Marigo et al.(2008)] Marigo, P., Girardi, L., Bressan, A., Groenewegen, M. A. T., Silva, L., & Granato, G. L. 2008, A&A, 482, 883

[Martin-Pintado et al.(1992)] Martin-Pintado, J., Bachiller, R., & Fuente, A. 1992, A&A, 254, 315

[Matsuura et al.(2004)] Matsuura, M., et al. 2004, ApJ, 604, 791

[McDonald & van Loon(2007)] McDonald, I., & van Loon, J. T. 2007, A&A, 476, 1261

[Medina Tanco & Steiner(1995)] Medina Tanco, G. A., & Steiner, J. E. 1995, AJ, 109, 1770

[Merrill(1919)] Merrill, P. W. 1919, PASP, 31, 305

[Merrill & Humason(1932)] Merrill, P. W., & Humason, M. L. 1932, PASP, 44, 56

[Merrill(1944)] Merrill, P. W. 1944, ApJ, 99, 15 bibitem[Michalitsianos & Kafatos(1988)]1988ASSL..145..235M Michalitsianos, A. G., & Kafatos, M. 1988, IAU Colloq. 103: The Symbiotic Phenomenon, 145, 235

[Mikolajewska et al.(1988)] Mikolajewska, J., Selvelli, P. L., & Hack, M. 1988, A&A, 198, 150

[Mikolajewski et al.(1992)] Mikolajewski, M., Mikolajewska, J., & Khudyakova, T. N. 1992, A&A, 254, 127

[Mikòlajewska(2000)] Mikòlajewska, J. 2000, ASP Conf. Ser. 199: Asymmetrical Planetary Nebulae II: From Origins to Microstructures, 199, 431

[Mikołajewska et al.(2002)] Mikołajewska, J., Ivison, R. J., & Omont, A. 2002, Advances in Space Research, 30, 2045

[Mikołajewska(2004)] Mikołajewska, J. 2004, Revista Mexicana de Astronomia y Astrofisica Conference Series, 20, 33

[Morris(87)] Morris,M. 1987, PASP¡ 95, 1115

[Milne & Aller(1982)] Milne, D. K., & Aller, L. H. 1982, A&AS, 50, 209

[Min et al.(2003)] Min, M., Hovenier, J. W., & de Koter, A. 2003, A&A, 404, 35

[Min et al.(2006)] Min, M., Waters, L. B. F. M., de Koter, A., Hovenier, J. W., Keller, L. P., & Markwick-Kemper, F. 2006, ArXiv Astrophysics e-prints, arXiv:astro-ph/0611329

[Molster et al.(1999)] Molster, F. J., et al. 1999, Nature, 401, 563

[Molster et al.(2001)] Molster, F. J., Yamamura, I., Waters, L. B. F., Nyman, L.-Å., Käufl, H.-U., de Jong, T., & Loup, C. 2001, A&A, 366, 923

[Molster et al.(2002)] Molster, F. J., Waters, L. B. F. M., Tielens, A. G. G. M., & Barlow, M. J. 2002, A&A, 382, 184

[Molster et al.(2002)] Molster, F. J., Waters, L. B. F. M., & Tielens, A. G. G. M. 2002, A&A, 382, 222

[Molster et al.(2002)] Molster, F. J., Waters, L. B. F. M., Tielens, A. G. G. M., Koike, C., & Chihara, H. 2002, A&A, 382, 241

[Monnier et al.(1998)] Monnier, J. D., Geballe, T. R., & Danchi, W. C. 1998, ApJ, 502, 833

[Mürset et al.(1996)] Mürset, U., Jordan, S., & Wolff, B. 1996, Supersoft X-Ray Sources, 472, 251

[Muerset et al.(1997)] Muerset, U., Wolff, B., & Jordan, S. 1997, A&A, 319, 201

[Mukai et al.(2007)] Mukai, K., Ishida, M., Kilbourne, C., Mori, H., Terada, Y., Chan, K.-W., & Soong, Y. 2007, PASJ, 59, 177

[Munari et al. 1992] Munari, U. et al. 1992, A&A Suppl. 93, 383

[Munari & Renzini(1992)] Munari, U., & Renzini, A. 1992, ApJL, 397, L87

[Munari et al.(1996)] Munari, U., Yudin, B. F., Kolotilov, E. A., & Tomov, T. V. 1996, A&A, 311, 484

[Munari et al.(1997)] Munari, U., Renzini, A., & Bernacca, P. L. 1997, Hipparcos - Venice '97, 402, 413

[Munari et al.(2001)] Munari, U., et al. 2001, A&A, 369, L1

[Nichols et al.(2007)] Nichols, J. S., DePasquale, J., Kellogg, E., Anderson, C. S., Sokoloski, J., & Pedelty, J. 2007, ArXiv Astrophysics e-prints, arXiv:astro-ph/0701336

[Nussbaumer et al.(1988)] Nussbaumer, H., Schmid, H. M., Vogel, M., & Schild, H. 1988, A&A, 198, 179

[Nussbaumer & Vogel(1989)] Nussbaumer, H., & Vogel, M. 1989, A&A, 213, 137

[Nussbaumer & Vogel (1990)] Nussbaumer, H., & Vogel, M. 1990, A&A, 236, 117

[Nussbaumer & Walder(1993)] Nussbaumer, H., & Walder, R. 1993, A&A, 278, 209

[Vogel & Nussbaumer(1994)] Vogel, M., & Nussbaumer, H. 1994, A&A, 284, 145

[Nussbaumer et al.(1995)] Nussbaumer, H., Schmutz, W., & Vogel, M. 1995, A&A, 293, L13

[Nussbaumer(2000)] Nussbaumer, H. 2000, Thermal and Ionization Aspects of Flows from Hot Stars, 204, 317

[Nuth & Hecht(1990)] Nuth, J. A., III, & Hecht, J. H. 1990, Ap&SS, 163, 79

[Osterbrock(1988)] Osterbrock, D.E. 1988 in Astrophysics of Gaseous Nebulae and Active Galactic Nuclei, University Science Book

[Peeters et al.(2002)] Peeters, E., Hony, S., Van Kerckhoven, C., Tielens, A. G. G. M., Allamandola, L. J., Hudgins, D. M., & Bauschlicher, C. W. 2002, A&A, 390, 1089

[Pégourié & Papoular(1985)] Pégourié, B., Papoular, R. 1985, A&A, 142, 451

[Penston(1987)] Penston, M. V. 1987, MNRAS, 229, 1P

[Pereira(1995)] Pereira, C. B. 1995, A&AS, 111, 471

[Pereira et al.(1998)] Pereira, C. B., Landaberry, S. J. C., & Junqueira, S. 1998, A&A, 333, 658

[Pereira et al.(2005)] Pereira, C. B., Smith, V. V., & Cunha, K. 2005, A&A, 429, 993

[Posch et al.(1999)] Posch, T., Kerschbaum, F., Mutschke, H., Fabian, D., Dorschner, J., & Hron, J. 1999, A&A, 352, 609

[Prialnik(2000)] Prialnik, D. 2000, An Introduction to the Theory of Stellar Structure and Evolution, by D. Prialnik. Cambridge, UK: Cambridge University Press, 2000.,

[Prialnik & Kovetz(1995)] Prialnik, D., & Kovetz, A. 1995, ApJ, 445, 789

[Purton et al.(1977)] Purton, C. R., Allen, D. A., Feldman, P. A., & Wright, A. E. 1977, MNRAS, 180, 97P

[Purton et al.(1982)] Purton, C. R., Feldman, P. A., Marsh, K. A., Allen, D. A., & Wright, A. E. 1982, MNRAS, 198, 321

[Puget & Leger(1989)] Puget, J. L., & Leger, A. 1989, ARA&A, 27, 161

[Ramos-Larios & Phillips(2005)] Ramos-Larios, G., & Phillips, J. P. 2005, MNRAS, 357, 732

[Richards et al.(1999)] Richards, A. M. S., Bode, M. F., Eyres, S. P. S., Kenny, H. T., Davis, R. J., & Watson, S. K. 1999, MNRAS, 305, 380

[Robinson et al.(1989)] Robinson, K., Bode, M. F., Meaburn, J., & Whitehead, M. J. 1989, Dynamics of Astrophysical Discs, 85

[Roche et al.(1983)] Roche, P. F., Aitken, D. K., & Allen, D. A. 1983, MNRAS, 204, 1009

[Rossi (1988)] Rossi, C., Altamore, A., Ferrari-Toniolo, M., Persi, P., Viotti, R. 1988, A&A, 206, 279

[Russell et al.(1975)] Russell, R. W., Soifer, B. T., & Forrest, W. J. 1975, ApJL, 198, L41

[Schild et al.(1999)] Schild, H., Dumm, T., Folini, D., Nussbaumer, H., & Schmutz, W. 1999, The Universe as Seen by ISO, 427, 397

[Schild et al.(2001)] Schild, H., Eyres, S. P. S., Salama, A., & Evans, A. 2001, A&A, 378, 146

[Schilke et al.(1997)] Schilke, P., Walmsley, C. M., Pineau des Forets, G., & Flower, D. R. 1997, A&A, 321, 293

[Schmeja, Kimeswenger (2001)] Schmeja, S. & Kimeswenger, S. 2001, A&A, 377, L18

[Schmid(1989)] Schmid, H. M. 1989, A&A, 211, L31

[Schmid & Nussbaumer(1993)] Schmid, H. M., & Nussbaumer, H. 1993, A&A, 268, 159

[Schmid et al.(2001)] Schmid, H. M., Kaufer, A., Camenzind, M., Rivinius, T., Stahl, O., Szeifert, T., Tubbesing, S., & Wolf, B. 2001, A&A, 377, 206

[Schmidt et al.(2006)] Schmidt, M. R., Začs, L., Mikołajewska, J., & Hinkle, K. H. 2006, A&A, 446, 603

[Schwarz & Corradi(1992)] Schwarz, H.E. & Corradi, R.L.M. 1992, A&A, 265, L37

[Schulte-Ladbeck & Magalhaes(1987)] Schulte-Ladbeck, R. E., & Magalhaes, A. M. 1987, A&A, 181, 213

[Seaquist & Gregory(1973)] Seaquist, E. R., & Gregory, P. C. 1973, Nature, 245, 85

[Seaquist et al.(1984)] Seaquist, E. R., Taylor, A. R., & Button, S. 1984, ApJ, 284, 202

[Seaquist et al.(1993)] Seaquist, E. R., Krogulec, M., & Taylor, A. R. 1993, ApJ, 410, 260

[Sedov(1959)] Sedov, L. I. 1959, Similarity and Dimensional Methods in Mechanics, New York: Academic Press, 1959

[Selvelli, P.-L. & Hack, M.(1952)] Selvelli, P.-L. & Hack, M. 1985 ESASP.236, 207

[Selvelli & Hack(1985)] Selvelli, P. L., & Hack, M. 1985, Recent Results on Cataclysmic Variables. The Importance of IUE and Exosat Results on Cataclysmic Variables and Low-Mass X-Ray Binaries, 236, 207

[Sigut & Pradhan(2003)] Sigut, T. A. A., & Pradhan, A. K. 2003, ApJS, 145, 15

[Shore et al.(1996)] Shore, S. N., Kenyon, S. J., Starrfield, S., & Sonneborn, G. 1996, ApJ, 456, 717

[Shull(1978)] Shull, J. M. 1978, ApJ, 226, 858

[Siodmiak & Tylenda(2001)] Siodmiak, N., & Tylenda, R. 2001, VizieR Online Data Catalog, 337, 31032

[Skopal et al.(1996)] Skopal, A., et al. 1996, MNRAS, 282, 327

[Skopal(1997)] Skopal, A. 1997, Informational Bulletin on Variable Stars, 4495, 1

[Skopal et al.(1998)] Skopal, A., Bode, M. F., Lloyd, H. M., & Drechsel, H. 1998, A&A, 331, 224

[Skopal et al.(2000)] Skopal, A., Pribulla, T., Wolf, M., Shugarov, S. Y., & Jones, A. 2000, Contributions of the Astronomical Observatory Skalnate Pleso, 30, 29

[Skopal et al.(2002)] Skopal, A., Vanko, M., Pribulla, T., Wolf, M., Semkov, E., & Jones, A. 2002, Contributions of the Astronomical Observatory Skalnate Pleso, 32, 62

[Skopal et al.(2004)] Skopal, A., Pribulla, T., Vaňko, M., Velič, Z., Semkov, E., Wolf, M., & Jones, A. 2004, Contributions of the Astronomical Observatory Skalnate Pleso, 34, 45

[Skopal(2005)] Skopal, A. 2005, A&A, 440, 995

[Skopal et al.(2007)] Skopal, A., Vaňko, M., Pribulla, T., Chochol, D., Semkov, E., Wolf, M., & Jones, A. 2007, Astronomische Nachrichten, 328, 909

[Sloan & Price(1995)] Sloan, G. C., & Price, S. D. 1995, ApJ, 451, 758

[Sloan & Price(1998)] Sloan, G. C., & Price, S. D. 1998, ApJS, 119, 141

[Sloan et al.(2003)] Sloan, G. C., Kraemer, K. E., Price, S. D., & Shipman, R. F. 2003, ApJS, 147, 379

[Smith et al.(2001)] Smith, V. V., Pereira, C. B., & Cunha, K. 2001, ApJ, 556, L55

[Snijders(1987)] Snijders, M. A. J. 1987, Ap&SS, 130, 243

[Sofia et al.(2006)] Sofia, U. J., Gordon, K. D., Clayton, G. C., Misselt, K., Wolff, M. J., Cox, N. L. J., & Ehrenfreund, P. 2006, ApJ, 636, 753

[Soker(2002)] Soker, N. 2002, MNRAS, 337, 1038

[Sokoloski & Kenyon(2003)] Sokoloski, J. L., & Kenyon, S. J. 2003, ApJ, 584, 1021

[Sokoloski(2006)] Sokoloski, J. 2006, Chandra Proposal, 2059

[Solf (1987)] Solf, J. 1987, A&A, 180, 207

[Speck et al.(2000)] Speck, A. K., Barlow, M. J., Sylvester, R. J., & Hofmeister, A. M. 2000, A&AS, 146, 437

[Stevens et al.(1992)] Stevens, I. R., Blondin, J. M., & Pollock, A. M. T. 1992, ApJ, 386, 265

[Sylvester et al.(1999)] Sylvester, R. J., Kemper, F., Barlow, M. J., de Jong, T., Waters, L. B. F. M., Tielens, A. G. G. M., & Omont, A. 1999, A&A, 352, 587

[Tamanai et al.(2006)] Tamanai, A., Mutschke, H., Blum, J., & Meeus, G. 2006, ApJL, 648, L147

[Taranova & Iudin(1988)] Taranova, O. G., & Iudin, B. F. 1988, Ap&SS, 146, 33

[Taranova & Yudin(1992)] Taranova, O. G., & Yudin, B. F. 1992, Soviet Astronomy, 36, 132

[Taranova & Shenavrin(2004)] Taranova, O. G., & Shenavrin, V. I. 2004, Astronomy Reports, 48, 813

[Taranova & Shenavrin(2007)] Taranova, O. G., & Shenavrin, V. I. 2007, Astronomy Letters, 33, 531

[Taylor & Seaquist(1984)] Taylor, A. R., & Seaquist, E. R. 1984, ApJ, 286, 263

[Taylor & Seaquist (1985)] Taylor, A.R. & Seaquist, E.R. 1985, IAU circular No. 4055

[Taylor et al.(1986)] Taylor, A. R., Seaquist, E. R., & Mattei, J. A. 1986, Nature, 319, 38

[Taylor(1988)] Taylor, A. R. 1988, ASSL Vol. 145: IAU Colloq. 103: The Symbiotic Phenomenon, 77

[Tielens(1990)] Tielens, A. G. G. M. 1990, From Miras to Planetary Nebulae: Which Path for Stellar Evolution?, 186

[Tomov & Mikolajewski(1992)] Tomov, T., & Mikolajewski, M. 1992, Informational Bulletin on Variable Stars, 3721, 1

[Tomov (2003)] Tomov, T. 2003 in Symbiotic Stars Probing Stellar Evolution, ASP Conference Series, Vol. 303, 2003, Corradi, R.L.M., Mikolajewska, J., Mahoney, T.J. eds.

[Usero et al.(2006)] Usero, A., García-Burillo, S., Martín-Pintado, J., Fuente, A., & Neri, R. 2006, A&A, 448, 457

[van Diedenhoven et al.(2004)] van Diedenhoven, B., Peeters, E., Van Kerckhoven, C., Hony, S., Hudgins, D. M., Allamandola, L. J., & Tielens, A. G. G. M. 2004, ApJ, 611, 928

[Van Winckel et al.(1994)] Van Winckel, H., Schwarz, H. E., Duerbeck, H. W., & Fuhrmann, B. 1994, A&A, 285, 241

[Vandenbussche et al.(2004)] Vandenbussche, B., Dominik, C., Min, M., van Boekel, R., Waters, L. B. F. M., Meeus, G., & de Koter, A. 2004, A&A, 427, 519

[van Loon et al.(2005)] van Loon, J. T., Cioni, M.-R. L., Zijlstra, A. A., & Loup, C. 2005, A&A, 438, 273

[van Loon et al.(2008)] van Loon, J. T., Cohen, M., Oliveira, J. M., Matsuura, M., McDonald, I., Sloan, G. C., Wood, P. R., & Zijlstra, A. A. 2008, A&A, 487, 1055

[Viegas & Contini(1994)] Viegas, S. M., & Contini, M. 1994, ApJ, 428, 113

[Verner et al.(2000)] Verner, E. M., Verner, D. A., Baldwin, J. A., Ferland, G. J., & Martin, P. G. 2000, ApJ, 543, 831

[Véron-Cetty et al.(2004)] Véron-Cetty, M.-P., Joly, M., & Véron, P. 2004, A&A, 417, 515

[Vogel & Morgan(1994)] Vogel, M., & Morgan, D. H. 1994, A&A, 288, 842

[Vogel & Nussbaumer(1995)] Vogel, M., & Nussbaumer, H. 1995, A&A, 301, 170

[Wachter et al.(2002)] Wachter, A., Schröder, K.-P., Winters, J. M., Arndt, T. U., & Sedlmayr, E. 2002, A&A, 384, 452

[Watson et al.(2000)] Watson, S. K., Eyres, S. P. S., Davis, R. J., Bode, M. F., Richards, A. M. S., & Kenny, H. T. 2000, MNRAS, 311, 449

[Webster & Allen(1975)] Webster, B. L., & Allen, D. A. 1975, MNRAS, 171, 171

[Weidemann(2003)] Weidemann, V. 2003, NATO ASIB Proc. 105: White Dwarfs, 3

[Welty et al.(2001)] Welty, D. E., Lauroesch, J. T., Blades, J. C., Hobbs, L. M., & York, D. G. 2001, ApJL, 554, L75

[Wheatley & Kallman(2006)] Wheatley, P. J., & Kallman, T. R. 2006, MNRAS, 372, 1602

[Whitelock et al. (1983)] Whitelock, P.A., Feast, M.W., Roberts, G., Carter, B.S., Catchpole, R.M., 1983, MNRAS, 205, 1207

[Whitelock(1987)] Whitelock, P. A. 1987, PASP, 99, 573

[Williams(1967)] Williams, R. E. 1967, ApJ, 147, 556

[Willson et al.(1984)] Willson, L. A., Salzer, J., Wallerstein, G., & Brugel, E. 1984, A&A, 133, 137

[Wright & Barlow(1975)] Wright, A. E., & Barlow, M. J. 1975, MNRAS, 170, 41

[Yamamura et al.(2000)] Yamamura, I., Dominik, C., de Jong, T., Waters, L. B. F. M., & Molster, F. J. 2000, A&A, 363, 629

[Yaron et al.(2005)] Yaron, O., Prialnik, D., Shara, M. M., & Kovetz, A. 2005, ApJ, 623, 398

[Yoo(2006)] Yoo, K. H. 2006, New Astronomy, 11, 359

[Yoo(2007)] Yoo, K. H. 2007, New Astronomy, 12, 569

[Zamanov et al.(2006)] Zamanov, R. K., Bode, M. F., Melo, C. H. F., Porter, J., Gomboc, A., & Konstantinova-Antova, R. 2006, MNRAS, 365, 1215

List of Figures

List of Tables